DOCTOR OF ENGINEERING (ENGD)

Coastal protection and nearshore evolution under sea level rise

Bayle, Paul

Award date:
2020

Awarding institution:
University of Bath

Coastal protection and near-shore evolution under sea level rise

Paul Bayle

A thesis presented to the Faculty of Engineering & Design of the University of Bath in partial fulfillment of the requirements for the degree of Doctor of Philosophy

Bath, September 2020

Water Informatics Science & Engineering (WISE)
Water Innovation and Research Centre (WIRC)
Centre for Infrastructure, Geotechnical and Water Engineering (IGWE)
Faculty of Engineering & Design
University of Bath, UK

Coastal protection and nearshore evolution under sea level rise

Supervisors:

Dr. Chris Blenkinsopp	Senior Lecturer at University of Bath, UK
Dr. Alan Hunter	Senior Lecturer at University of Bath, UK

Examination committee:

Dr. Kevin Briggs	Lecturer at University of Bath, UK
Dr. José Alsina	Senior Researcher at Universitat Politècnica de Catalunya, Spain

Author declarations:

This thesis is composed of my original work and contains no material previously published or written by another person except where due reference has been made in the text. The contributions by others to the Journal articles used in this thesis is clearly stated in my thesis. The work published in the thesis was carried out since the commencement of my Research degree at the University of Bath and do not include any other work submitted to qualify for another degree or diploma at any other institution.

This work was financially supported by the Water Informatics: Science and Engineering Centre for Doctoral training.

Copyright:

Acknowledgements

I am writing these lines after my successful viva and after addressing all my corrections. I am in a relieved and exited state, as working on this PhD over the last 4 years was a hard work and a very rich experience. I am also writing this just before leaving the UK after spending 5 years living in this beautiful country, so I am also a bit nostalgic and sad. I am going to try to translate this combination of feelings in the best way, and thank all the persons involved in this journey, without forgetting anybody I hope!

Nothing could have been possible without you Chris! From our first exchange before even applying to WISE, you have always been very enthusiastic about working with me, and this was very motivating for me. I have told you this many times, but you are the best version of a supervisor that a PhD student could dream of. You were available, responsive, supportive and you knew how to structure and shape my work while leaving me enough freedom in my research which surely contributed to the person and scientist I am today. Besides the valuable time we had together at work, you also became a friend, who with I enjoyed sharing a beer (s), a nice meal and obviously, surfing (both in the field and the new lab in Bristol...). There is not enough space here to describe all your amazing work and support, but I hope you know how grateful I am, and I hope you will remain the same all along your career, with all your future students. I know we will keep collaborating, and try to organise research visits in each other's universities as much as we can (depending on the forecast...), so I know this is just the beginning of a long and nice collaboration. Thanks!

I want to thank all the person in charge of WISE, especially Tom Arnot for recruiting me and trusting a french guy over a skype from a hut in Malaysia. This program is particularly complete, inclusive and inspiring, and my PhD outside of this scheme would definitely not have been the same. Thank you for giving me the chance to be part of this journey. I also want to thank all my cohort (cohort 2, the best one): it was very nice to spend the first year in Exeter with you all, I think we were a nice mix of personalities, and a few of you are now friends for life (they will recognise themselves).

I want to thank the Aussie team with Tom Baldock, Ian Turner and Tom Beuzen, who were present all along my PhD (mainly because I am slow at writing papers), especially Tom Baldock who spent a lot of time with me during his sabbatical in Bath. I want to thank the Plymouth team, with Daniel Conley and Gerd Masselink for their help during DynaRev1. The french team, represented by Rafael Almar only: merci pour le temps passé

au téléphone à m'expliquer les bases du fonctionnement d'une caméra. And obviously the Bath team with Chris, but also Alan Hunter and Oscar Bryan.

The North Cove field experiment was one of the richer experiences of my PhD, and this would have not been possible without you George. Thank you for trusting a french lad met at a conference, and inviting him for a two-week field trip with your team. More generally, thanks for being such a passionate and interesting person, I learnt a lot with you. I also thank all the persons involved in this experiment, which made me aware of the impact and application of my work: David Cottrell (a real genius), Heather Weiner, Connie Allen, Richard Harris and all the local community who welcomed me.

Kevin, tu es la personne parfaite pour faire la liaison entre mes remerciements liés au travail, et les remerciements pour les proches. Tu m'as énormement apporté niveau recherche et tu as toujours pris le temps de m'expliquer les choses, j'ai beaucoup appris, merci! J'espère que cela restera pareil dans nos collaborations futures. Mais bien entendu, tu es plus un ami qu'un collègue, et j'espère qu'on arrivera à profiter du temps sur Bordeaux, surtout pour se remettre au squash.

I want to thanks all the amazing people who I shared my office and corridor space with: Ioanna, Olivia, Naomie, Russell, John, Keveh, Badr, Astrid, Valentina, Zaharatu, Gwyn, Emily, James, Erwin, Aurelie, Mahan... William Bazeley, for being such a good mate in the lab, and outside. Mehrnaz, it was great to do my PhD at the same time as you, we will stay friend. Marianno and Marios, thanks for being such great volleyball and basketball mates.

My PhD in Bath would have not been the same without the best rugby club in the country, Avonvale RFC, and all its members. I enjoyed every single moment in this club, until the last memorable send off party. You will all stay forever in my heart, but I am sure I will see you on many tours in the future. Special thanks to Wedgie, Archie, Marcus, Jonny, Donald, Josh, Moggy and Steve for your great welcome at the club and generally as part of your life for the last 4 years.

Merci à mes parents pour leur éternel soutien et confiance. L'amour et l'éducation que vous m'avez donné sont les principaux facteurs de cet accomplissement. Merci Justine d'être la meilleure soeur du monde. Je vous aime tout les trois très fort.

Merci à tous mes amis francais. Peu d'entre vous savent ce que je foutais vraiment en Angleterre pendant 5 ans, mais peu importe. Votre amitié est et sera toujours le pilier principal de ma vie.

Julia, mon petit calin, merci de m'avoir supporté pendant le lockdown, et plus géneralement dans la vie. Tu as une place speciale dans mon coeur!

Summary

Coastlines are extremely valuable assets for many countries as they play a major role in the national and local economy. In this context, sandy coastlines are particularly challenging as they are one of the most developed types of coast but also one of the most vulnerable in terms of erosion risk. The threat of erosion is mainly driven by storms, including storm surge and waves, and long term sea level rise which is expected to increase in rate with the on-going climate change. In response to this forcing, sandy beaches have been and will be protected in many areas. However, most of the coastal defences, whether hard or soft, are not designed to face the combination of these threats, with storms acting on a higher water level. Therefore, there is a need to develop a sustainable coastal protection which would take these threats into account to provide a reliable protection level. In this context, dynamic cobble berm revetments which mimic natural composite beaches that consist of a lower sandy beach and a back-shore gravel ridge, seem to be a promising solution. The potential of this structure has not been studied in depth, and therefore their performance, behaviour and dynamics remain unclear. To study these aspects and get a better understanding of their capacity to protect the coast and improve their design, one laboratory and one field experiment were undertaken on two different types of dynamic revetment. Under energetic waves and increasing water level conditions, dynamic revetments are able to protect the hinterland by reducing the wave runup and excursion. They also protect the underlying beach by armouring the sand and protecting it from backwash erosion. While protecting the coast, dynamic revetments show a dynamic stability as their particles are constantly mobilised by swashes but the overall structure maintains a coherent shape. Revetments are also able to quickly reach a stable state at both the intra- and inter-tidal timescale, but the overall stable state is only attained when the internal sand becomes stable. The volume of dynamic cobble berm revetments can vary through time, mainly caused by sand volume variations driven by water level and offshore wave conditions, and is able to rapidly recover from periods of erosion. In summary, dynamic cobble berm revetments are relatively inexpensive, easy to install and in many cases the material can be locally sourced. Further improvements in our understanding of dynamic revetments can be achieved through additional laboratory experiments, and a new scaling method is developed to compare distorted experiments. The scaling method is valid for both fixed and increasing water level experiments, and is used to better understand the beach profile evolution under rapid sea level rise.

Contents

List of Figures

List of Tables

Chapter 1

Introduction

1.1 Coastal adaptation

Coastlines are the bases of cultural, social and environmental assets which contribute significantly to many national economies. Many coastlines are currently under threat from waves and storm surges, which can create coastal erosion and flooding. These coastal threats will likely intensify under climate change, which is expected to cause an increase in the sea level rise rate and storm intensity (Church et al., 2013). This is particularly true for sandy beaches, the most vulnerable type of beach with respect to erosion, which cover more than 30 % of the world's coastlines (Vousdoukas et al., 2020). As a consequence, many sandy coastlines have been protected, and although they do not all require the same level of protection (from "nothing" to "hold the line", Krebs et al., 2013b), they are and will still need to be protected against wave attack and erosion. Moreover, according to (Vousdoukas et al., 2020), there is a risk that half of the sandy beaches vanish by the end of this century due to accelerated erosion if sustainable and adaptive protections are not implemented. However, most of the existing protection methods, whether hard or soft engineering, are not designed to cope with the combination of rapid sea level rise and storms, and therefore will likely fail if not modified or renewed. There is therefore a need to develop a sustainable protection which would take these threats into account and reliably protect sandy beaches against erosion. While hard engineering structures, which provide close to 100 % protection, are required in highly developed areas of locations with essential infrastructure, in other locations where the level of protection required does not necessitate hard engineering, lower cost, more sustainable and adaptable novel soft engineering methods could be a suitable alternative.

While many types of soft engineering exist, using different approaches and providing different levels of protection (French, 2001), dynamic cobble berm revetments seem to have a high potential for coastal protection and adaptation (Komar and Allan, 2010). Dynamic cobble berm revetments are essentially a gravel ridge or berm built in the back-shore, directly on top of an existing sand beach. This creates an artificial composite beach, which consists of a lower tide terrace (*i.e.*, surf zone) and fore-shore of sand, and a back-shore gravel ridge or berm. Dynamic cobble berm revetments are by definition dynamic in a sense that they are not static structures and are mobilised and reshaped under waves and

swashes. Therefore, they are expected to change and adapt to forcing conditions while providing overtopping protection to the hinterland. These expectations are based on our understanding of the natural behaviour of composite beaches, which are recognised as a natural form of coastal protection and have shown good adaptability under sea level rise and storm waves (Komar and Allan, 2010). However, very few studies have investigated the dynamics and behaviour of such beaches, and even fewer have focused on dynamic revetments. Furthermore, the existing examples of dynamic revetments significantly differ in terms of their design and material used, which further complicate any analysis of them. As a consequence, the potential of this type of protection is yet to be fully explored, and its functionality as a sustainable coastal protection is yet to be proven.

To better understand dynamic cobble berm revetments, it is important to investigate their dynamic behaviour and capacity to protect the hinterland under increasing water level and energetic conditions. This can be achieved by performing a thorough analysis of the overall behaviour, including sediment dynamics and response to different forcing conditions. The sustainability and performance of dynamic cobble berm revetments as a coastal protection also need to be investigated to strengthen the level of confidence in these structures. In parallel, the understanding of sandy beach profile evolution under sea level rise needs to be enhanced in order to adopt appropriate coastal adaptation under the increasing climate change threat.

1.2 Experimental options to study coastal adaptation

In the area of coastal engineering and oceanography, experimental studies can be performed using three main approaches: numerical, laboratory and field experiments. However, as no commonly used numerical model has been validated with composite beaches (McCall et al., 2019), only the two latter options are considerable. Laboratory experiments, and more specifically laboratory flume experiments, allow the number of environmental forcing variables to be reduced by assuming processes only occur in a 2-D plane and by controlling the wave conditions. In addition, they enable a large number of instruments to be deployed easily and safely and therefore can provide comprehensive datasets over a short period. Field experiments are more complex in the sense that they deal with nature and all the associated variability. They can be used to study a specific site, under specific conditions at a specific time of the year. They are also used to study long term coastal trends, which can be applied to larger areas. However, the collection of data requires a lot of labour, environmental conditions are sometimes hard to forecast and the desired conditions may not occur. Therefore, choosing between one or the other option should be motivated by the specific research questions to be solved.

1.3 Research objectives and thesis outlines

Coastal adaptation under sea level rise is a critical area of coastal engineering and can be approached on both the long term (*e.g.*, natural and anthropogenic sea level rise) and short term (*e.g.*, tides, storm surges, El Nino/La Nina cycles). Although the present work

mainly focuses on the short-term sea level rise aspects, through both a laboratory and field experiments, longer term sea level rise is considered throughout and most short term findings remain valid in the long term. Dynamic cobble berm revetments and beach profile evolution under storm surge-equivalent sea level rise will be investigated in a laboratory flume. In the field, a dynamic revetment will be investigated during a spring tidal cycle and storm conditions. To better understand dynamic cobble berm revetments and improve understanding of coastal adaptation under sea level rise, the following research objectives and questions are formulated:

Objective 1. Investigate the performance of dynamic cobble berm revetment as a coastal defence structure, under energetic conditions and sea level rise

- Can a dynamic cobble berm revetment protect the hinterland against wave attack? What level of protection is provided and what mechanisms are key to the structure's function?
- Can a dynamic cobble berm revetment protect the sandy beach on which it is placed? What level of protection is provided and what mechanisms are key to the structure's function?
- Can a dynamic cobble berm revetment withstand energetic conditions and water level changes? Can the structure recover following energetic periods?
- Can some preliminary guidelines be defined for the design and maintenance for dynamic revetments?

Objective 2. Investigate the behaviour of a dynamic cobble berm revetment under energetic conditions and water level changes, at a range of temporal and spatial scales

- How does the dynamic cobble berm revetment structure change under energetic conditions and water level increase? Does the revetment retreat and keep its shape under sea level rise?
- Is the revetment stable? How is this stability expressed at different spatial and temporal scales?
- How is the revetment influenced by hydrodynamics and swash interactions?
- How does the revetment integrate with the underlying sand? How does the whole system work?

Objective 3. Develop a new scaling approach to compare distorted laboratory flume beach profiles under a fixed and increased water level, in order to increase the number of datasets available to study sediment dynamics associated with dynamic revetment and beach profile evolution

- Can a method to compare distorted flume experiments be developed? What kind of comparison can be performed with such datasets? Can it be used to study dynamic revetment characteristics?

- How do sandy beach profiles evolve under increasing water level? Do they follow the empirical rules for long term evolution under sea level rise?

Note that in this alternative format thesis, a specific literature review and methodology is contained in each chapter (*e.g.*, paper). For this reason, there is no standalone methodology section. Moreover, the literature review, in **Chapter 2** aims to present the general scientific background to the reader, explain the reasoning which led to this study of dynamic revetments and beach profile evolution and highlight the research gaps which will be filled. The thesis is then composed of four results chapters, all associated with a preamble which puts the work presented into context, and a concluding remarks which act as a transition to the next chapter. **Chapter 3** presents the prototype scale experiment performed at the GWK large wave flume in Hannover, Germany which tested the performance of a dynamic cobble berm revetment as a coastal protection. The dynamic behaviour of the revetment under increasing water level and energetic waves is investigated, and some preliminary design guidelines are proposed. **Chapter 4** presents a field experiment on the dynamic revetment in North Cove, USA. The results focus on the behaviour of the revetment under both cross-shore and longshore sediment transport, and its performance as a coastal protection structure. The internal sand dynamics of the revetment are also investigated in details, and a model is presented. A preliminary nourishment guideline is proposed. In **Chapter 5**, lidar data obtained during the North Cove field experiment are used to explore net cross-shore sediment fluxes at the swash-by-swash scale. The distribution of swash-induced fluxes and swash depths are investigated to better understand swash interactions with the revetment and morphodynamic processes. **Chapter 6** is separated into two parts: in the first, a new scaling approach is developed to compare distorted beach profiles from different flume scales, under both a fixed and increasing water level. The approach is developed with three datasets, including the one obtained at the GWK (Chapter 3), and validated with two further published datasets; in the second part, the scaling approach is used to study beach profile evolution under sea level rise, and compare the results with empirical rules for long term sea level rise. Finally, **Chapter 7** concludes this study by addressing each research objective and suggesting future work required to further investigate dynamic revetments and composite beaches.

Chapter 2

Literature review

2.1 Coastal threat and climate change

2.1.1 Beaches as natural coastal protection

Coastlines around the world face a wide variety of stresses from both natural and anthropogenic factors, including agriculture, industry, tourism, urbanisation and nearshore processes. Although all of these factors are inter-related, the work presented in this thesis focuses on the latter stress, and therefore particular attention is given to the physical processes generally involved in coastal erosion, flooding and retreat.

The coast can be separated into two areas: the beach and the hinterland. The beach can be considered as the border between the sea and the hinterland, providing a form of natural coastal defence. In consequence, the beach can also be defined as a volume of sediment, acting as a buffer, which must be maintained to ensure robust protection (Vousdoukas et al., 2020). However, this volume constantly varies due to ongoing wave-driven sediment transport punctuated with storm events which can remove large volumes in hours/days. This dynamic and evolving volume of sediment is localised between the nearshore – characterised by a zone where the wave energy is progressively transferred and dissipated – and the hinterland, which is more stable and only periodically directly influenced by coastal processes during extreme events. Therefore, in the context of coastal protection, the beach is one of the key areas that must be managed in order to prevent nearshore and coastal processes from damaging the hinterland, which may host natural assets such as ecological habitat, or economical assets like infrastructure or agriculture. This vision of the beach as a volume of sediment protecting the hinterland is crucial in coastal engineering and allows the threats to be easily identified. Anything reducing the active volume of sediment between the nearshore and the hinterland can be seen as a threat. This includes waves, wave-induced currents and longshore drift which can create erosion, hence a reduction of the total volume of sediment. It also includes tides and storms surge as they reduce the active part of the beach by inundating a proportion of beach area and therefore reduce the active volume of sediment in the shore.

2.1.2 Sea level rise predictions and consequences

The threats previously defined are very likely to worsen under Sea Level Rise (SLR), and therefore the understanding of this on-coming issue is important to correctly assess the type of coastal protection that need to be developed. According to Bindoff et al. (2013), anthropogenic climate change inducing ocean warming and glacier mass loss has very likely contributed to global SLR during the latter half of the 20^{th} century. Global mean sea level increased at a rate of 1.8 mm/yr between 1880 and 2010 (Rhein et al., 2013). This rate accelerated between 1993 and 2010, reaching a value of 3.2 mm/yr (Church et al., 2013). A comparable rate was used by Antonov (2005) to determine the thermosteric contribution to global mean sea level.

Church et al. (2013) predicted SLR under four carbon emission scenarios, known as RCP (Representative Carbon Pathways) scenarios. The most optimistic model (RCP2.6) predicts a SLR of 0.44 metres by 2100, whereas the most pessimistic model (RCP8.5) predicts a SLR of 0.74 metres by 2100. However, the SLR forecast models derived from these RCPs only take into account the thermosteric and glacier components responsible of SLR. DeConto and Pollard (2016) estimated that the melting of the Antarctica ice-sheet could contribute to a further rising of 0.77 metres by 2100 in the worst case scenario. In this case, the rate of global sea level rise would exceed 4cm/yr at the end of the century. Moreover, although no studies have been able to precisely calculate the contribution of Greenland ice-sheet, it will likely worsen the predictions.

Church et al. (2013) state that there is a high confidence level that extreme events will increase with SLR. They explained that storms will be more severe on a given coast mainly because they will act on a higher water level. Therefore, SLR is a crucial component to be taken into account in the design of coastal protection and more generally in coastal management as it will enhance the risk of coastal hazards through two main mechanisms: the wave energy received by the beach will be increased under SLR, with more frequent and intense storms which will directly affect the beach sediment volume; relative to a fixed coast, a higher water level reduces the active volume of sediment able to act as a protection. The development of sustainable protection taking into account these components is therefore a key concern for coastal engineering in the oncoming decades.

The evolution of the beach profile morphology under SLR has been largely studied (Bruun, 1954; Dean, 1973; Bruun, 1962, 1983; Rosati et al., 2013; Atkinson et al., 2018; Beuzen et al., 2018). Although it has sometimes been a subject of controversy (SCOR Working Group, 1991; Cooper and Pilkey, 2004), the long–term morphological changes of a beach profile driven by SLR are now generally accepted. However, the existing models only take into account the profile evolution from one equilibrium state to another one, and neglect short term morphological changes. The understanding of rapid SLR-induced short term changes are important in the context of storm surge as a SLR. It is therefore crucial to identify the beach profile evolution under rapid SLR to correctly evaluate the resulting threat to the coast.

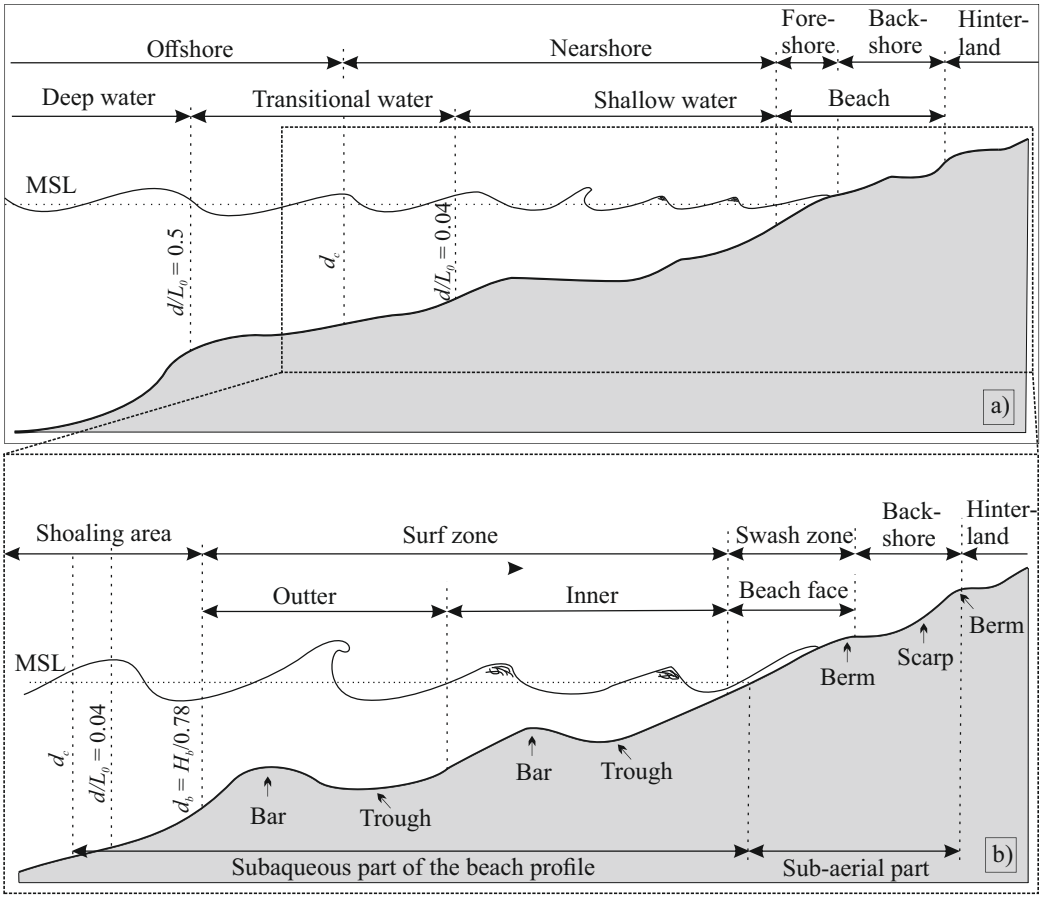

Figure 2.1: Description and terminology of the coastal areas used in this thesis. (a) Shows the entire nearshore area and extends beyond the depth of closure. (b) encompasses the area landward of the depth of closure.

2.2 Beach processes

As detailed in Section 2.1, beaches are a form of natural coastal protection, however the resilience of this buffer varies with changing wave conditions. As a result it is essential to understand and be able to predict the response of beaches to waves, and use recognised parameters to describe them. The following section outlines the general knowledge and terminology used in this thesis, and present a critical analysis of some existing parameters used to describe them.

2.2.1 Beach and nearshore processes

Beaches are commonly described using a wide range of terminology which describes different prominent features. Furthermore, they are typically divided into regions dependent on morphodynamic and/or hydrodynamic characteristics. The terminology used in this thesis is shown in Figure 2.1.

The offshore zone includes the deepwater area in which waves are free to propagate without being affected by the seabed. The deepwater region is bounded by a limit defined as $d/L_0 = 0.5$ (Dyer, 1989; Dean and Dalrymple, 2002). The subscript "0" is used to indicate that a parameter is taken in the deepwater region. Waves in this area are linear and their surface can be reconstructed using the well-established linear wave theory (Dean and Dalrymple,

2002). The separation of the offshore and nearshore zones occurs in the transitional water region, at the depth of closure (d_c). From offshore to nearshore, it corresponds to the depth at which wave driven flows start affecting the bed morphology. This depth depends on the wave orbital velocity and is therefore related to the height, and period of the waves. While the real value of the depth of closure varies with every single wave, empirical equations are available in the literature to calculate a time-averaged representative value (*e.g.*, Kraus et al., 1998). This limit also marks the beginning of the active beach profile, which is composed of a sub-aqueous and sub-aerial part. The separation between the transitional and the shallow water regions is defined as $d/L_0 = 0.04$ (Dyer, 1989; Dean and Dalrymple, 2002), with shoaling occurring in both areas. The shoaling process is the transformation of the wave signal assuming a conservation of energy from the deepwater to the wave breaking area, where $d_b = H_b/0.78$ (Dyer, 1989; Dean and Dalrymple, 2002). During shoaling, the speed, wave height and wavelength vary (the wave period being conserved), until the wave reaches a limiting steepness and breaks, dissipating energy. In the nearshore area, waves are non-linear and can be approximated using non-linear wave theories (numerous theory are presented in Dean and Dalrymple (2002)), and the recently developed non-linear, weakly dispersive approach from Bonneton et al. (2018) (see applications for the shoaling zone in Mouraghes et al. (2019), and for the surf zone in Martins et al. (2020)). Wave breaking marks the beginning of the surf zone which can be separated into an outer and an inner area (Dean and Dalrymple, 2002). The outer surf zone is the region in which waves undergo rapid changes after breaking, and energy dissipation is dominated by the wave breaking process. The main breaker bar (or outer bar) and trough are typically located in this region. In the inner surf zone, waves become quasi-steady propagating bores and energy dissipation occurs mainly due to turbulence associated with roller processes and bed friction. The inner surf zone sometimes hosts an inner bar and trough. The point that separates the nearshore and shore is tide dependent, but is generally defined by the shoreline position at low tide. The fore-shore is the most active part of the shore where the beach face, which extends from the minimum rundown to the maximum runup, is reshaped by swash (see Section 2.2.3 and Figure 2.3) and therefore, is also tide dependent. The high tide berm created by swash processes can be considered as the separation between the fore-shore and the back-shore. Back-shore features are very site-specific and include relic berms, sand scarps and dunes. Finally, the hinterland encompasses anything located landward the back-shore area including natural habitats or man-made infrastructure.

The beach profile is a 2D slice through the beach, encompassing the sub-aerial and sub-aqueous regions of the nearshore (Figure 2.1b). Beach profiles shape can change very rapidly in response to individual waves (Blenkinsopp et al., 2011), however beach profiles are typically inherently stable and oscillate around long term state of equilibrium. The concept of the equilibrium beach profile was first presented in Johnson (1919), as the beach profile that would naturally develop to a stable state under given wave forcing – *i.e.*, no significant change in the profile evolution with time. While complete and stable equilibrium cannot be achieved in nature or in the laboratory for sandy beaches forced

Table 2.1: Empirical parameters commonly used in coastal engineering for beach classification. H_0 is the deepwater significant wave height (m), H_b is the wave breaking height, H_s is the significant wave height at the toe of the beach profile (m), T_p the mean wave period (s), L_0 is the deepwater wavelength (m), β is the fore-shore slope angle, w_s is the sediment settling fall velocity (m/s) and g is the acceleration due to gravity (m/s^2). The lower case "b" indicates that the parameter is assessed at the break point.

Parameter name	**Parameter symbol**	**Parameter equation**
Surf similarity or Iribarren number (Battjes, 1974)	ξ_0	$\tan\beta/\sqrt{H_0/L_0}$
Dimensionless fall velocity (Gourlay, 1968; Nayak, 1970; Dean, 1973)	Ω_0	$H_0/(w_s T_p)$
Surf scaling (Wright et al., 1979)	ϵ_b	$H_b 2\pi^2/(gT_p^2(\tan\beta)^2)$

by erosive random waves, the rate of morphological change can be observed to decrease over time. When this rate is small and reaches a certain threshold of change, the profile state is defined as "quasi-equilibrium" (Grasso et al., 2009; Moore, 1982; Rector, 1954; Wang and Kraus, 2005; Baldock et al., 2017; Beuzen et al., 2018; Atkinson et al., 2018). Accretive profiles tend to be more stable than erosive profiles with respect to an equilibrium state since breaker bars do not exist (Swart, 1974; Atkinson et al., 2018), but the evolution time-scale to approach equilibrium is comparable for a similar wave height (Baldock et al., 2010).

2.2.2 Sandy beach state, classification and interaction parameters

Nearshore hydrodynamics and morphology are often described using three empirical parameters (Table 2.1). These parameters use wave characteristics, such as the wave height and period to parameterise the forcing conditions along with morphological characteristics of the beach, such as the beach slope, to understand how the actual beach is going to change in response to the wave forcing. Note that in Table 2.1, while the parameters are shown with their original variable (*e.g.*, the dimensionless fall velocity was originally defined using the wave breaking height H_b), they have often been derived with different variable (*e.g.*, H_0 or H_s can be used as an alternative to H_b).

Numerous observations and long-term monitoring of the nearshore zone have revealed the wide range of shapes that nearshore sandbars can attain (Wright and Short, 1984). Although sandbar configurations are unique and continuously change in shape under the influence of waves and currents, a certain regularity in sandbar morphology has been observed. As a result, sandbar morphologies are typically associated with several discrete sandbar states, often related to the energy of the incoming wave field. For single-barred beaches, Wright and Short (1984) developed the most widely accepted beach state classification model, based on observations of beaches with contrasting environmental conditions over a period of three years Figure 2.2.

Wright and Short (1984) identified two distinct end states, the dissipative and the reflective state, which were found to be related to persistent high and low energy wave conditions respectively. A sandbar is generally found in the intermediate states, identified as longshore bar and trough, rhythmic bar and beach, transverse bar and rip and low tide terrace, resulting in a total of six beach states.

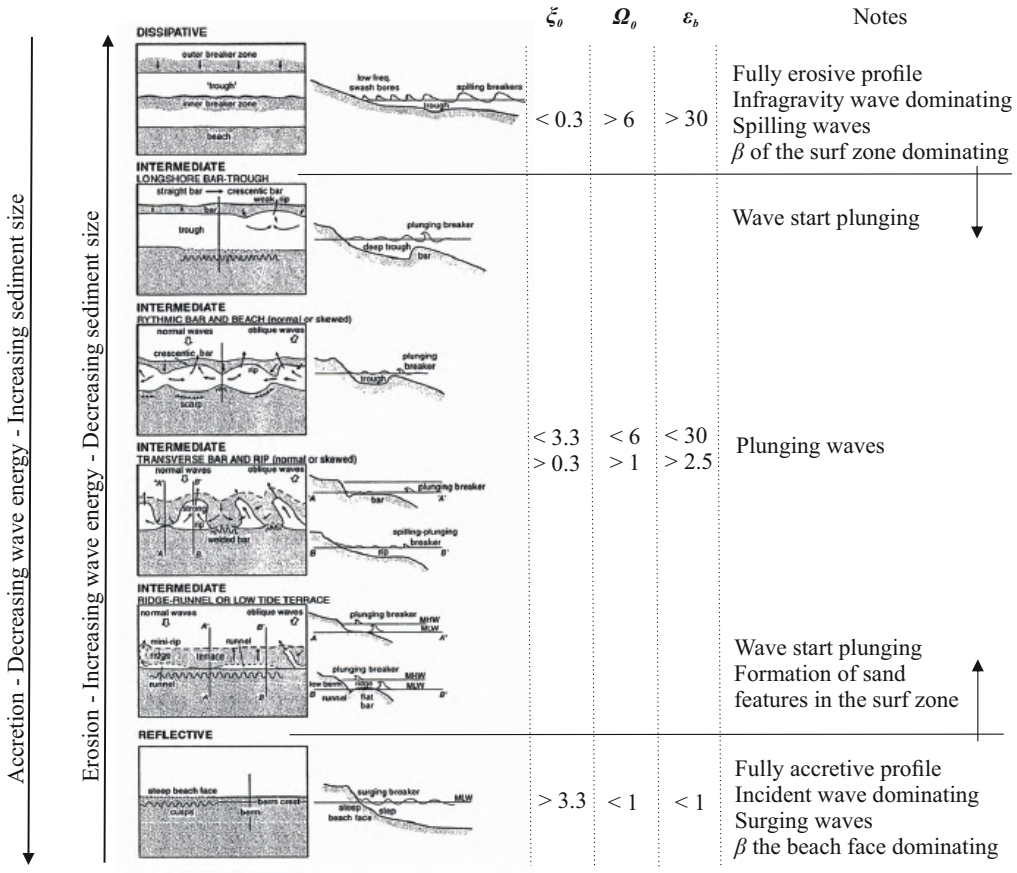

Figure 2.2: Beach profile classification (extracted from Wright and Short (1984), Fig.2) associated with the threshold values of the three parameters presented in Table 2.1.

During an accretionary (downstate) sequence (Short, 1979), associated with low-energy conditions, a bar mostly advances through each of the intermediate states toward the reflective state over a period of days to weeks (Ranasinghe et al., 2004). However, the larger amount of energy needed for erosional (upstate) sequences (Short, 1979; Short and Masselink, 1999) often causes the bar to jump to a higher state within hours (Lippmann and Holman, 1990; van Enckevort and Ruessink, 2003; Ranasinghe et al., 2004), with the bar briefly acquiring the erosional intermediate states described by Short (1979). An erosional sequence where all pre-existing alongshore variability is erased, resulting in the alongshore-uniform longshore bar and trough state, is often referred to as a morphological reset.

The relationship between the three parameters shown in Table 2.1 and the beach states is shown in Figure 2.2. The threshold values given in Figure 2.2 indicate the values at a quasi-equilibrium beach state. If the profile is not at the state indicated by the value, then the value indicates the direction of change in terms of wave breaking type and sediment transport. Therefore, it can be expected that for some given wave conditions, the equilibrium state (*i.e.*, stable state) should be the same regardless of the initial shape of the profile. This was demonstrated by Eichentopf et al. (2018) which showed that the same wave forcing leads to the same profile, regardless of its initial shape. Consequently, a given wave condition can

either yield to onshore or offshore sediment transport to reach a final profile (see Figure 2.2), depending on the initial beach state. In consequence, the intermediate states by which the beach profile goes through must also be different depending on the initial beach state. This was studied by Baldock et al. (2017) who defined the morphological hysteresis as the effect of the preceding beach profile changes and wave conditions on the evolution path followed by the beach profile toward its equilibrium state. For example, wave conditions that would be expected to lead to accretion according to the empirical parameters can cause shoreline erosion if the crest of the breaker bar is too low for the new waves to break, meaning the majority of wave energy is dissipated at the shoreline. As a consequence, although parameters in Table 2.1 can still help to assess the current and future beach state as shown on Figure 2.2, it is important to bear in mind that the real-time changes are more complex. Nevertheless, the dissipative and reflective end states are supposed to be unchanged and reliably predictable with these parameters.

2.2.3 Wave runup and overtopping

As mentioned in Section 2.1, the energy of waves propagating toward the shore is conserved through the deepwater and shoaling area. This energy is dissipated in the surf zone under breaking and bed friction processes as the wave propagates toward the shore. The remaining energy is dissipated as waves run up and down the beach in the swash zone. The swash zone is recognised as the most dynamic part of the nearshore in terms of morphology changes (Phillips et al., 2019) and swash flows can lead to damaging wave overtopping and coastal flooding. Figure 2.3 illustrates the components of which contribute to the total water level on beaches.

When a broken wave in the surf zone reaches the swash zone, the entire volume of water flowing landward (up-slope) on the beach face is called the uprush. This volume of water then flows seaward (down-slope), referred to the backwash, and reaches a seaward limit called the run-down, defined vertically below water level. Wave runup, R is the vertical elevation difference between the Still Water Level (SWL) and the highest instantaneous shoreline elevation for a single wave (Sorensen, 1997). Wave run-down is the vertical elevation difference between the SWL and the lowest instantaneous shoreline elevation between two swash event. It also corresponds to the position where the bore collapses, which is the process of the swash front breaking on a dry bed (Bergsma et al., 2019). Wave setup and set-down are intrinsic contributions to wave runup and run-down. They are wave-induced mean water level variations, over time and space (Longuet-Higgins and Stewart, 1964). Wave setup is an increase in mean water level due to wave breaking while wave set-down is a decrease in mean water level before the wave breaks. The wave runup R for each consecutive wave is different, however engineers are typically concerned only with extreme events. Consequently, wave runup for engineering design is typically represented as $R_{2\,\%}$, which corresponds to the elevation exceeded by 2 % of runup events. On this basis, a large number of empirical equations have been developed to predict the $R_{2\,\%}$ on sand and gravel beaches as a function of the offshore wave conditions and beach slope. This will be

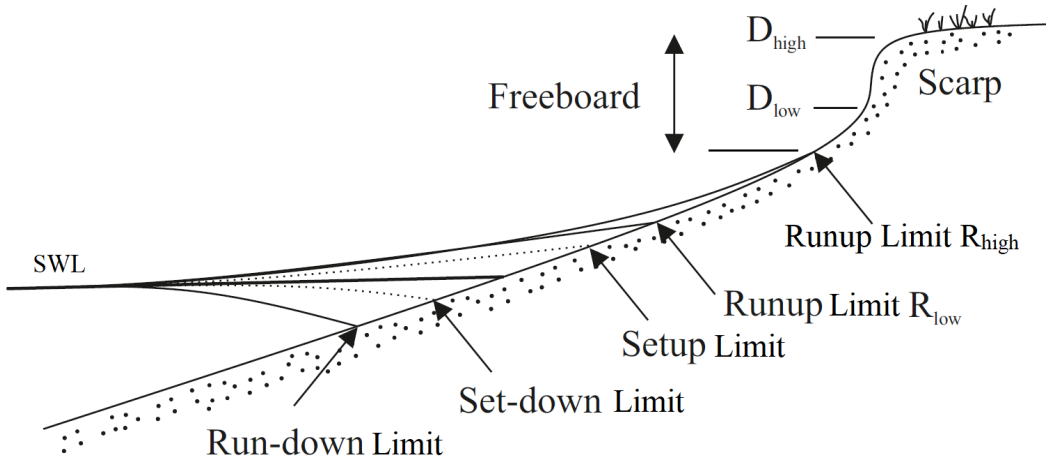

Figure 2.3: Definition sketch for the variables used in the Storm Impact Scale model, from Sallenger (2000). The dashed lines represent the setup and set-down. R_{high} is the maximum runup limit, (vertical maximum runup being equal to SWL + tide + surge + set-up + R) and R_{low} the minimum runup limit (vertical minimum runup being SWL + tide + set-up + R). The rundown is also calculated from the still water line.

further detailed in Section 2.4.2.2.

A wave overtops a structure or a beach feature when the runup exceeds the elevation of that feature. Generally, overtopping discharge either occurs because of waves running up the face of a feature and passing its crest, or because of waves breaking on the seaward face of the structure and producing significant volume of splash (Van der Meer et al., 2018). Overtopping is usually given as a volume of flux passing the feature crest, but can also be defined as a percentage given as the number of waves overtopping the feature over the total number of waves measured over time. To be statistically significant, the percentage of overtopping should be calculated over a minimum of 1000 waves (Gallach-Sanchez, 2018).

The Storm Impact Scale (SIC) model developed by Sallenger (2000) was defined for sandy beaches and barriers response to storms, but its terminology can be applied to any feature on any type of beach. Figure 2.3 shows the definition sketch of this model, using a sand scarp as back-shore feature. Using this principle, the model defines four storm impact regimes:

- Swash regime: this is defined for $R_{high} < D_{low}$. The runup occurs in the fore-shore area and does not reach the back-shore.
- Collision regime: this is defined for $D_{high} > R_{high} > D_{low}$. The back-shore feature (dune, scarp, berm) is reached by runup and slumps may occur.
- Overwash regime: this is defined for $R_{high} > D_{high}$. The back-shore feature is often overtopped by wave runup.
- Inundation regime: this is defined for $R_{low} > D_{high}$. All runup excursions overtop the back-shore feature, and may lead to drowning, breaching or failure of that feature.

Orford et al. (2003) developed a similar model for gravel barriers, using the term “freeboard" to characterise the elevation of the barrier crest above the maximum run-up (Figure 2.3). The transition between the collision regime and the overwash regime is marked by overtopping. In overall, it appears that limiting beach runup, and minimising

the overtopping are the two main objectives of coastal protection, to both protect the beach against erosion under swashes, and prevent the hinterland from being flooded.

2.2.4 Experimental investigation of beach processes and coastal protection

To investigate beach processes and coastal protections, one approach in coastal engineering is to perform field experiments. Field experiments allow to get a complete set of data, including all the natural processes occurring at a specific site, over a short or long period of time. However, due to the complexity of natural environments, which can combine cross-shore and longshore waves and currents, wind, river discharge, infrastructure and urbanisation, they not always allow to investigate only one specific aspect of a problem. Furthermore, it is not always easy to find a suitable study site for a research project, especially in the area of coastal protection. In consequence, laboratory experiments, and more specifically wave flumes, are very much used in the area of coastal engineering, as they allow to undertake experiment under controlled conditions, and limit the amount of processes involved. Wave flumes are by essence only two dimensional, and therefore exclude longshore sediment transport. Moreover, there are a lot of flumes of very different sizes around the world, ranging from a few meters to hundreds of metres. In consequence, undergoing test in such facilities generally introduce scale effects between model and nature, but also between models of different scales. This problem limits the use of non scaled experiments together, and therefore limits the amount of data that could be compared across existing projects. There is therefore the need to develop a scaling method which would allow distorted experiments (*i.e.*, not scaled to each other) to be compared. This would significantly increase the amount of beach profile data available, and enable past and future datasets to be combined and compared to answer research questions.

2.3 Existing coastal protection methods and their adaptability to a changing climate

In the context of coastal threat presented in Section 2.1, many different approaches have been used to protect the beach and/or the hinterland against erosion and flooding. These approaches can be classified into two categories: “hard" and “soft" engineering techniques.

2.3.1 Hard coastal engineering

Hard engineering techniques such as seawalls and revetments are generally used to protect highly urbanised areas where coastal retreat is not acceptable (Dean and Dalrymple, 2002; Cartwright et al., 2008; Hudson et al., 2008). These methods consist of building a wall at the shore, typically from either concrete or rock, to protect the volume of sediment, directly protect the hinterland, or both. Although quite efficient at protecting the hinterland against wave attack, they often create scouring and may interfere with local sediment transport (Longuet-Higgins and Stewart, 1988; Kraus and McDougal, 1996; McDougal et al., 1996). According to Boorman et al. (1989), many existing seawalls will become obsolete under the expected SLR as they do not have sufficient foundations to support further upgrading.

Another common hard engineering protection are groynes which are used to control longshore sediment transport on sedimentary coastlines. Groynes consist of shore perpendicular barriers, built to maintain and increase the volume of sediment at a specific location. Groynes can be considered as a longshore sediment trap, able to store sediment which is mobilised by longshore drift. This technique interrupts the natural sediment flow by accumulating sediment upstream and depleting the downstream coastline, hence moving erosion problems elsewhere (Dean and Dalrymple, 2002; Cartwright et al., 2008; Hudson et al., 2008; French, 2001). They do not provide any direct protection to the hinterland other than by partially maintaining the sediment buffer in localised areas. Under SLR, the level of protection that existing groynes provide will be reduced as they may end up relatively lower and seaward as the shoreline retreats (Dean and Dalrymple, 2002).

Another hard engineering protection, which may significantly affect the beach amenity, is the detached breakwater. It consists of a wall constructed parallel to the beach in the nearshore zone, either in the transitional or shallow water zone. The concept is to break the wave energy before it reaches the shore, hence reducing the threat to the hinterland. It generally promotes lateral sediment transport between unprotected and protected area due to wave energy gradient, hence accretion of sediment in the surf zone and on the subaerial beach (leading to a salient or tombolo). Breakwaters can be implemented on every kind of coast and are locally efficient against storms waves. However, they tend to reduce the longshore sediment transport as sand accretion increases, and may completely stop it if a tombolo is formed (Cartwright et al., 2008; Hudson et al., 2008). Under SLR and shoreline retreat, the relative distance from the coast to the structure and the freeboard are likely to increase, potentially requiring expensive realignment works to maintain functionality.

Submerged offshore reefs are artificial reefs, made of sandbags, natural or artificial rocks (*e.g.*, dolos) placed in the surf zone at a depth designed to force incident waves to break consistently further offshore. The wave energy is therefore dissipated further from the shore, which allows more time and space for the energy to dissipate, reducing erosion potential at the shoreline. These structures are mainly used to protect sedimentary coasts, as similarly to the offshore breakwater, it promotes the accretion of sediment in its vicinity (Ranasinghe and Turner, 2006; Ranasinghe et al., 2010). However, among the existing prototypes of submerged artificial reefs, there are as many which have led to erosion as accretion in their lee (Dean and Dalrymple, 2002; Cartwright et al., 2008; Hudson et al., 2008; French, 2001). The crest elevation below the mean water level is the key design parameter for these structures. Consequently under SLR, the depth of the structure crest will increase, leading to reduced wave breaking over the structure, hence a decrease in performance. The recent top-up campaign of the Narrowneck artificial reef (Brown et al., 2011) has demonstrated the complexity, high cost and timing of a maintenance works, which discourage future employment of this method with our knowledge on SLR.

Krebs et al. (2013b) have stated that based on historical data, hard engineering techniques used to stop local erosion are effective in the short term but may not be suitable in the longer-term. In many areas, they are unnecessary and cause adjacent effects sometimes

worse than the problem they are trying to solve, and even if costly maintenance is undertaken, they are at risk of breaching or overtopping under SLR. Important for minimizing such negative impacts is the testing of “soft" engineering alternatives that attempt to replicate nature by slowing the erosion to an acceptable rate while eliminating or reducing scour and beach sediment losses.

2.3.2 Soft coastal engineering

Soft engineering techniques are opposed to hard engineering techniques, in a sense that they are not rigid and static and aim at protecting the coast in a more natural way, and accounting for natural dynamic of coastlines. The most widely used soft engineering method is beach nourishment where a volume of sediment, either sand, gravel or a mixture of both, is added artificially to the submerged and/or sub-aerial beach profile. As such, a renourishment is a direct way to increase the shore sediment volume, enhancing the natural coastal protection function of the sediment buffer which protects the hinterland. It represents an artificial and instantaneous sediment stock contributing to wave energy dissipation under future extreme events (Seymour et al., 1995; Dean and Dalrymple, 2002; Cartwright et al., 2008). However, because the added sediment is mobile, renourishments can be only a short term buffer which can sometimes be removed with a few large storm events. As a consequence, beach nourishments are generally performed on timescales of years to decades, which is a short enough interval to adapt the maintenance work to long term SLR (Hudson et al., 2008; French, 2001). However, they appear more as a short term treatment than a sustainable solution to protect the coast, with generally a high economical and ecological cost.

Vegetation planting is recognised as one of the most eco-friendly and sustainable soft engineering methods. It consists of planting vegetation to stabilise the sediment and prevent it from being eroded by waves, currents and wind. The large varieties of available species allow this technique to be suitable for a large range of coast types. Although relatively inexpensive, this approach requires a high level of maintenance as the performance of this protection relies on the growth rate. The main weakness of this approach is SLR. If the sediment on which they grow does not move under SLR, the vegetation and the sediment are lost underwater, and the volume of sediment remaining on the beach is reduced, increasing the risk to the hinterland. Therefore, vegetation can be associated with beach nourishment to maintain the volume of sediment, or be implemented to protect potential accommodation space – area previously attributed to the hinterland, which is accepted to be lost under coastal retreat, and therefore attributed to the beach to compensate for any lost volume (French, 2001; Policy Research Corporation, 2004).

A more technical method is beach drainage, which consists of installing drains within the beach sediment to desaturate the beach and lower the water table. Used on sedimentary coasts, this method aims to increase sediment deposition during the swash uprush and reduce the hydraulic pressure head which causes erosion during the backwash (French, 2001; Policy Research Corporation, 2004). Beyond the fact that the systems often get clogged

up, they are very expensive to install, run and maintain. They also tend to increase the saline content of the ground which negatively affects the ecosystem. Under SLR, these drains will need to be relocated, if they are proved to be efficient, and therefore they do not prevent shore sediment volume to be significantly eroded (Dean and Dalrymple, 2002; Cartwright et al., 2008).

More recently developed protection methods include floating breakwaters and some types of wave energy converters. The principle of these devices is to dissipate the wave energy offshore of the coast by absorbing the energy through platform movement, and in some cases, transform this energy into electricity. As they are deployed offshore, they can be used on any type of coast and have limited adverse effects (French, 2001). However, at the current state-of-the-art, these types of device are not operational under storm waves and have limited spatial coverage (Ruol et al., 2011; Zanuttigh et al., 2010). Consequently, although they would still be operational under SLR, they would not protect the coast against the associated threats.

A promising soft engineering technique, which will be developed further in Section 2.4.3, is a cobble berm, generically called a dynamic revetment. While there are a large variety of dynamic revetment designs, with different modes of construction and purposes, they are generally used on sedimentary beaches and consist of a gravel ridge composed of sediment larger than the natural beach sediment, and placed on the back-shore. The added gravel increases the volume of sediment at the shore, but also provide direct protection to the hinterland by dissipating the wave energy (Komar and Allan, 2010). Maintenance is still required as sediment volume losses are expected due to longshore sediment transport. Under SLR, they are expected to behave similarly to natural gravel and composite beaches (see Section 2.4.2.2), retaining their resilience. Combined with extra accommodation space, these structures have the potential to be used to naturally manage the realignment of the coast while providing protection to the hinterland.

Krebs et al. (2013a) presented soft engineering techniques as more suitable than hard engineering approaches in the medium to long term. However, the majority of the existing structures, whether soft or hard, are not designed to deal with a rapid SLR. Most will not be efficient under SLR whereas others will need to be modified. In parallel, soft engineering techniques are based on natural processes, and are therefore often considered as “work with nature" approaches (see Section 2.4). In consequence, the analysis of natural beaches and their response to storms and SLR appears to be a good approach to find opportunities of improvement and development of soft engineering techniques.

2.4 “Work with nature" coastal defence solutions

Using beach as defined in Section 2.1.1, it appears that the concept of soft coastal protection can be summarised as the utilisation of the beach in the ’best’ possible way to maintain or increase its volume and its capacity to act as a barrier and protection to the hinterland. The challenge is, however, to be able to interpret the word ‘best’ in the previous sentence using a multifactorial approach. This includes the factors defined in the first paragraph of

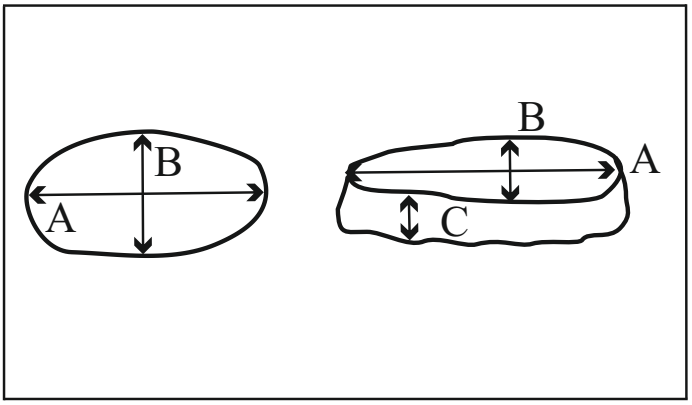

Figure 2.4: Illustration of the three orthogonal axes measured on a sediment particle.

Section 2.1.1, and particularly deals with the ecology, economy, feasibility and sustainability of a coastal protection. One possible approach to address these concerns is to better understand the dynamics of natural beaches and assess their natural ability to protect the hinterland. This whole system understanding will allow to identify potential improvement of coastal protection techniques able to face the coastal threats presented in Section 2.1.1 and Section 2.1.2, taking into account the natural resilience of a given beach. The application of such a method is referred to as a “work with nature" approach, and this idea is critical to this study.

The first step before defining a potential “work with nature" approach is to classify the existing types of beach, analyse their vulnerability and assess their behaviour under the coastal threats presented in Section 2.1 (waves, currents and SLR). But first of all, it is important present the way sediments and beaches are classified.

2.4.1 Sediment classification and measurement

A sediment particle is characterised by the length of three orthogonal axes Figure 2.4: the longest axis (A), the intermediate axis (B) and the short axis (C) (Pettijohn, 1975). These three measurements are used to compute all shape indexes and classifications found in the literature, including the roundness (Wentworth, 1919; Wadell, 1922), the sphericity (Wadell, 1922; Krumbein, 1940), the Zingg shape classification (Zingg, 1935), the Sneed and Folk sphericity-form diagram (Sneed and Folk, 1958), the Cailleux flatness index (Cailleux, 1945) and the Powers’s scale of roundness (Powers, 1953). These shape-based indexes and classifications are useful to compare different types of sediment and highlight differences that could not be identified with only the primary axis length. The classification of sediment used in this thesis is that defined by Wentworth (1922) (Table 2.2). Sediments are classified according to their sieve size. The sieve size corresponds to the length of the intermediate axis (B), because on a two-dimensional sieve grid, two of the particle’s axes must be smaller than the grid cell for the grain to pass through. The intermediate axis (B) is considered to be the representative diameter for the sediment particle, and is referred to as the grain diameter.

The classification shown in Table 2.2 is theoretically valid only for a single particle.

Table 2.2: Nomenclature of sediment grain size, as defined by Wentworth (1922). Note that the size corresponds to the length of the intermediate axis (B).

Size	<3.9 um	3.9 - 63 um	63 um - 2 mm	2 – 64 mm	64– 256 mm	>256 mm
Name	Clay	Silt	Sand	Gravel		
				Pebble	Cobble	Boulder

However, the classification of a sediment is more complex due to the heterogeneous composition of most natural sediments. Indeed, when measuring the sieve size of a volume of sediment, different sizes of grain will be found and in different quantities. Therefore, the size characteristics of a sediment are defined as a cumulative density function, as illustrated in Figure 2.5.

In sediment transport research, particle size is most commonly represented by the median or 50^{th} percentile diameter, D_{50} (here 0.33 mm) of the whole sediment. However for coarse sediment, the 15^{th} and 85^{th} percentile particle diameters (D_{15} and D_{85}) are also of interest, as they are used in the description of gravel sorting (Section 2.4.2.2)

2.4.2 Beach types

The four types of beach present in nature according to the mixed sand and beach classification developed by Jennings and Shulmeister (2002) are schematised and illustrated in Figure 2.6. The different types of beach are classified in terms of the amount and location of sand and gravel contained in their volume with the sand concentration increasing from Figure 2.6a to Figure 2.6d.

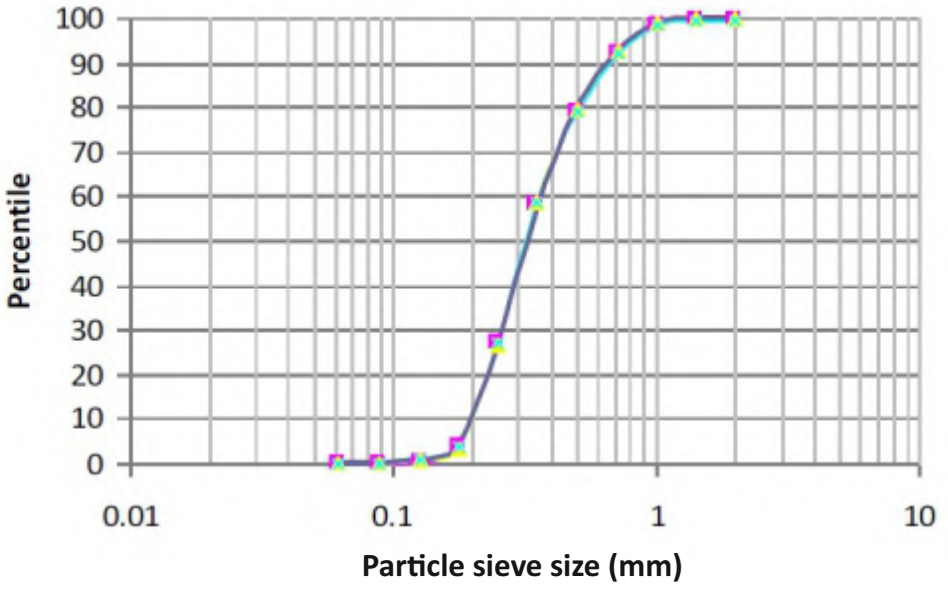

Figure 2.5: Cumulative density function representing the percentage of grain diameters smaller than sieve size value, on a logarithmic scale in millimetres. Note that the data used here is for the sand used in the laboratory experiment described in Chapter 3.

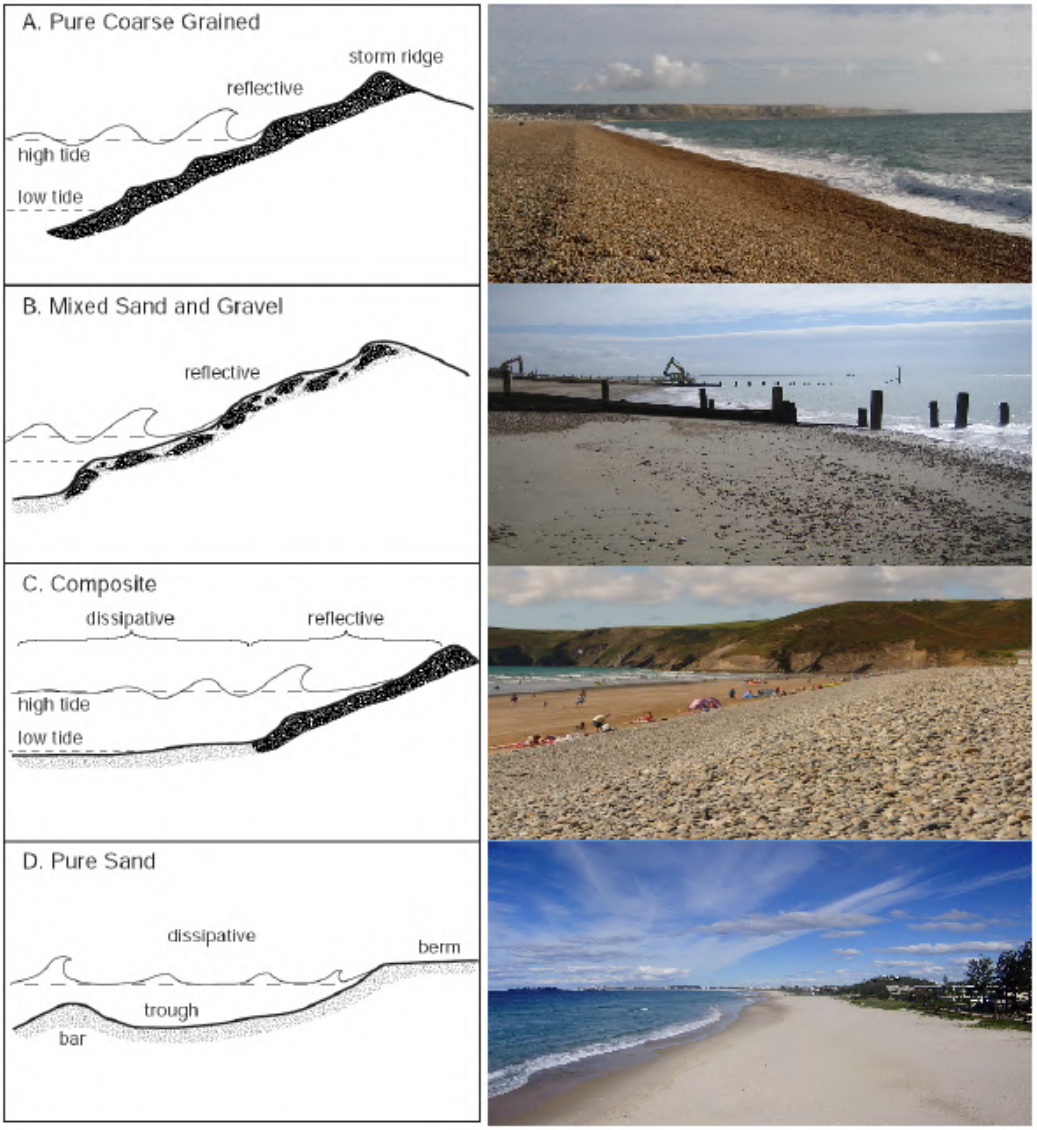

Figure 2.6: Schematic representation of the four types of beach (extracted from Council (2007), Figure 5-1), associated with a representative photograph – (a) Chesil Beach, UK; (b) Hayling Island UK; (c) Newgale, UK; (d) Currimbin, Australia. Note that the “mixed sand and gravel beach" will be referred to as “mixed beach" for the rest of the thesis.

2.4.2.1 Sandy beaches

Pure sandy beaches (Figure 2.6d) are present worldwide and are the most studied and protected type of beaches (Dean and Dalrymple, 2002), as they are highly prized for their aesthetic qualities and leisure opportunities and represent a valuable economic asset. A sandy beach is characterised by a median grain diameter D_{50} smaller than 2 mm (the limit between sand and gravel, see Table 2.2) and can be composed of a uniform sand size or a mixture of sand sizes. This type of beach has a relatively dissipative beach profile and therefore tend towards the dissipative end state in the Wright and Short (1984) classification (Figure 2.2), though they can form almost all of the different states.

The runup, R is independent of the grain diameter. It can be determined using the

offshore wave conditions through one of the many empirical runup equations developed from laboratory flume experiments (*e.g.*, Hunt, 1959; Battjes, 1974; Mase, 1989; van der Meer and Stam, 1992; Hedges and Mase, 2004; Hughes, 2004; Blenkinsopp et al., 2016) or from field data (*e.g.*, Guza and E, 1982; Holman, 1986; Nielsen and Hanslow, 1986; Ruggiero et al., 2004; Stockdon et al., 2006; Voudoukas et al., 2012; Power et al., 2013). All of these parameterisations take a form similar to that developed by Hunt (1959):

$$R = 2.3H_0 \tan\beta / (\sqrt{H_0/L_0}) = 2.3\xi_0 H_0 \tag{2.1}$$

where H_0 is the deepwater significant wave height, L_0 the deepwater wavelength, β the beach slope and ξ_0 the Iribarren number for deepwater conditions.

As noted, this equation forms the basis of all runup parameterisations. However, it is noted that the other equations predict the $R_{2\,\%}$ value for given wave and beach characteristics, rather than R for a single wave with the given characteristic. The selection of a runup equation for a particular site should take into account the environmental conditions in which the equation was developed and ideally be tested against observations.

Sandy beaches are the most vulnerable to coastal threats as they are very mobile and highly dynamic under both cross and longshore sediment transport. They have not demonstrated a great level of adaptation under long term SLR (Dean and Dalrymple, 2002), and are inclined to vanish under a rapid long term SLR (Vousdoukas et al., 2020). Due to this vulnerability, a lot of sandy coastlines are currently protected, and future coastal management scheme will need to maintain this level of protection in a sustainable way to cope with the expected threats driven by climate change (Section 2.1.2). Kriebel and Dean (1985) found that for the same forcing conditions, sandy beaches erode more than coarser sediment beaches. Furthermore, the inertia makes coarse-grained barrier stronger than sandy ones, as the bed shear tress needed to move a single particle as well as the whole formation is large (Orford et al., 2003). This suggests that learning from coarse sediment beach types may be a good approach to develop sustainable “work with nature" approaches.

2.4.2.2 Gravel beaches

Pure gravel beaches Figure 2.6a are the second most studied type of beach in the literature, and are also present along many coastlines. A gravel beach can be composed of any mixture of pebbles, cobbles or boulders and should contain no more than 5 % of sand (Table 2.2). Due to the coarse material these beaches are composed of, the beach profile is typically steeper than a pure sandy beach and therefore gravel beaches tend toward the reflective end state in Figure 2.2. To assess the heterogeneity of sediment composing a gravel beach, the grading coefficient defined as the ratio D_{85}/D_{15} (van der Meer, 1988; Powell, 1990) is generally used. The natural process of abrasion under waves and currents rounds the gravels over time, leading to most gravel beaches being composed of rounded gravels (shingle). However, angular material can be found on gravel beaches when they

are naturally fed by the erosion of a rocky cliff. Gravel beaches are also very dynamic and their morphology can significantly vary over both short and long time scales.

A number of authors have developed empirical runup equations (Powell, 1990; van der Meer and Janssen, 1994; Stockdon et al., 2006; Polidoro et al., 2014; Poate et al., 2016). The parameterisation which will be used in this thesis is the most recent one developed by Poate et al. (2016), given as:

$$R_{2\,\%} = 0.21 D_{50}^{-0.15} (\tan\beta)^{0.5} T_{m_{-1}m_0} H_s \tag{2.2}$$

where D_{50} is the nominal grain diameter, $tan\beta$ is the slope of the beach face, $T_{m_{-1}m_0}$ is the mean spectral period and H_s is the offshore significant wave height.

Unlike for sandy beaches, this runup equation incorporates the sediment diameter D_{50}. This is not the case in the other runup equations for gravel beaches cited above, which then questions the relevance and influence of the particle diameter on the runup. Poate et al. (2016) also proposed a variation of the equation without the diameter variable, and found a similar match between the measured and predicted runup values. The resulting deviation of this alternative equation was mainly attributed to data points corresponding to small pebbles, close to coarse sand. Therefore, it seems that for large gravel, the runup is independent from the sediment diameter.

Pure gravel beaches have shown greater resilience than sand beaches under both energetic waves and SLR. Trueba and Andrew (2014) explain that geological records show that pure gravel barriers have mainly moved landward (retreat) due to the Holocene sea level rise and kept pace with this SLR, with the sediment rolling-over the top of the barrier (overwash process) leading to an upward and landward profile movement. A similar observation was made by Storms et al. (2008). This mechanism of transport is referred to as rollover transport for the rest of the thesis and is well illustrated in Scott et al. (2015). This process was also observed on shorter timescales by Wright et al. (1982), who observed that gravel-dominated barriers build up during storm events. According to Carter and Orford (1984), there is no mechanism that can balance the landward transport of gravel barriers, any wave action tends to move the crest upward, landward and steepen the front slope making the barrier more reflective and less likely to erode. This reflectiveness of pure gravel beaches was also mentioned by Powell (1988) who found that on average, 10 % of the wave energy is reflected and 90 % is dissipated by gravel beaches. The particle diameter and the slope appear to not significantly affect the energy dissipation, meaning that the wave breaking and frictional losses on the beach are the main factors leading to energy dissipation. The negative aspect of pure gravel beaches is that because they can form a steeper gradient, waves can travel further inshore before breaking and the energy dissipation is concentrated over a narrower area, which can increase risks for the hinterland (Watt, 2006).

2.4.2.3 Composite beaches

Unlike pure sand and gravel beaches, composite beaches have received little attention in the literature, and have not been investigated through long-term (decades) field surveys or laboratory experiments. Composite beaches (Figure 2.6c) consist of a lower dissipative foreshore of sand and a reflective back-shore ridge composed of gravels. Composite beaches have a higher proportion of sand than gravel, and there is a distinct observable boundary between the sand and gravel parts of the beach (Pye and Blott, 2018). The cobble ridge is generally exposed at all stages of the tide when the tidal range and wave conditions are small. For larger wave conditions and particularly during spring tides, the ridge is exposed to swash processes and may be overtopped during particularly energetic events (Everts et al., 2002; Allan and Komar, 2004). The clear separation between the gravel and sand is a natural sorting process, which transport larger particles landward and upward. This is explained by the high porosity of a gravel ridge which significantly reduces the volume of surface run-off water during the backwash flow. This pattern is enhanced by the fact that in the swash zone, the uprush bed-shear stress is two to four times larger than the backwash bed-shear stress (Masselink and Hughes, 1998), which further limit backwash sediment fluxes as gravels do not undergo suspended sediment transport. Therefore, generally speaking, swashes have a higher capacity to transport gravels landward than seaward. This explains the general composition of composite beaches, which can also be found at the gravel ridge scale. However, this sorting process only occurs when the uprush is strong enough to move all types of particle present on the beach. On many composite beaches, very large gravels are present and can only be mobilised under extremely energetic events (generally combined with high tide). As a consequence, sediment sorting on the gravel ridge tends to move the smallest gravel to the top and the larger material is found at the bottom of the ridge. This has been observed by many geologists interested in the sorting of gravel particles across beach profiles (Bluck, 1967; Orford, 1975; Williams and Caldwell, 1988) who generally observed an onshore, up-slope decrease in grain size that reflects the decreasing energy of swash flows.

Composite beaches are generally considered to be very stable as they represent the two most stable ends of the Wright and Short (1984) classification (dissipative sand slope and reflective gravel ridge). Nonetheless, both the fronting sand beach and gravel ridge can undergo short and long term changes, and sand transfer between the primarily sandy and gravel parts of the beach has been observed, although this is not well understood due to the lack of studies of composite beach dynamics. Nevertheless, it is recognised that sand can be transported over the ridge and infiltrate into the gravel as the water percolates into the ridge. The sand then becomes packed into the gravel ridge due to the vibratory swash mechanism, called kinetic sieving (Wright et al., 1982). This shear mechanism also entrains the small gravels below the larger ones, which naturally create a vertical sorting of the ridge. This mechanism is well known by the geologists as it occurs during soil liquefaction and debris flow. As a result of the sand intrusion, the hydrostatic porosity and permeability of the ridge decrease.

To the author's knowledge, there is currently no runup equation available for composite beaches and no existing numerical model has been shown to robustly predict morphology change on composite beaches (McCall et al., 2019). The complex processes occurring within the gravel ridge and the exchange between the sandy part of the beach and the ridge need to be better understood before any significant progress can be made in numerical modelling.

Composite beaches have received little attention in the literature, but they have long been recognised as an effective form of natural coastal protection (Allan et al., 2015), showing a great degree of stability and adaptability in the face of wave attack. Van Rijn (2010) studied coarse clastic beaches behaviour, and found that a sandy beach with a minimal coarse gravel component would be composed of a back gravel ridge fronted by a low-tide terrace of sand, and therefore confirmed the physical processes involved in the formation of a composite beach. The stable nature of composite beaches is a result of the morphology of the entire beach profile. Composite beaches have a dissipative sandy surf zone and a reflective gravel beach face. As a consequence, they combine the wave energy dissipation processes of the pure sand and pure gravel beaches: energy is dissipated in the surf zone through waves breaking and roller energy dissipation; while in the swash zone, energy is dissipated through bed friction over a reflective porous beach face, with a high permeability reducing the backwash flow. As a result, incident wave energy is dissipated over a larger area. Furthermore, rollover transport occurs over the gravel ridge, which prevents the gravels from moving seaward.

2.4.2.4 Mixed beaches

Mixed shingle beaches are not well studied mainly because of their relatively restricted distribution throughout the world (Watt, 2006). These beaches are composed of a mixture of sand and gravel, with a similar proportion of each (Figure 2.6b). The difference between composite and mixed beaches is not always easy to identify, especially if a composite beach is nearly saturated with sand. For this reason, some papers in the literature refer to mixed beaches whereas they actually investigate composite beaches (*e.g.*, Dornbusch, 2017; Stark and Hay, 2016). A review of mixed beach literature (*e.g.*, Frandsen et al., 2015; Matsumoto and Young, 2018) highlights that beyond the larger proportion of sand present in mixed beaches than in composite beaches, mixed beaches contain smaller gravels (not larger than pebbles) and the sand component is typically relatively coarse. As a result, the difference between the sand and the gravel particle size is typically small meaning that they behave in a similar manner under the same wave conditions, explaining why the natural sorting process does not occur. Therefore a combination of both a large amount of sand and a small range of sediment diameters means that the sand and gravel are mixed together throughout the beach volume and generally create a reflective beach profile, although the outer surf zone is likely mainly composed of sand.

As for composite beaches, no existing runup equation or predictive models currently exist. This type of beach has nonetheless been more studied than composite beaches, as they are associated with beach nourishments (see Section 2.3.2). Indeed, a lot of beach

nourishments use a sediment different to that found locally, and thus the nourishment creates an artificial mixed beach. This was studied through laboratory experiments by Frandsen et al. (2015) and Roman-Blanco et al. (2006).

Table 2.3: List of laboratory experiment referring to dynamic revetments.

Flume	Type of test	Reference
Delft Hydraulics, medium scale	Artificial gravel beach	van Hijum and Pilarczyk (1982)
Delft Hydraulics, small scale	Artificial gravel beach	Pilarczyk and Boer (1983)
HR Wallingford, large scale	Coarse grain beach for coastal protection	Powell (1988)
USACE Coastal Engineering Research Center's (CERC's), medium scale	Small gravel placed on a concrete bottom	Ahrens (1990)
USACE Coastal Engineering Research Center's (CERC's), medium scale	Small gravel placed on a concrete bottom	Ward and Ahrens (1992)
Delft Hydraulics, small scale	Shingle beach placed on a concrete bottom	van der Meer and Pilarczyk (1986)
Delft Hydraulics, small scale and medium scale	Cobble and mixed beaches	van Gent (2010)

According to Watt (2006), mixed beaches are very effective natural defences against wave attack as they are able to dissipate more than 90 % of wave energy. The key differences between mixed beach and single grain size beaches are summarised in Watt (2006), the main point being the high porosity and hydraulic conductivity, hence the high permeability of mixed beaches. Mixed beaches are more inclined to erosion than pure gravel and composite beaches, primarily because when the volume consists of more than 30 % of sand, the hydraulic conductivity of the bulk sediment is equal to sandy beaches (Watt, 2006). This explains why under a combination of high water levels and waves, these beaches can be strongly eroded (Miller et al., 2011) and even drown, as rollover transport does not occur on this type of beaches. As a consequence, although they can efficiently dissipate wave energy, they appear less sustainable and adaptive than composite beaches.

2.4.3 Dynamic cobble berm revetment

The fact that the volume of a composite beach is mainly composed of sand, and the fact that sandy beaches are very vulnerable, open the possibility to protect sandy beaches and their hinterland by building an artificial composite beach. This rather efficient type of protection has the potential to fulfill the requirements of a "work with nature" approach, as long as it is proved to be efficient when artificially installed. In parallel, dynamic revetment (refsec232) can be effective in dissipating the wave energy and protecting shore-front properties and infrastructure under the threat defined in Section 2.1, while maintaining its shape and a natural appearance. Dynamic revetments are considered to be highly adaptive and have a high potential for coastal protection. However, knowledge on dynamic revetment

possibilities are relatively poor, and therefore, there are opportunities for improvement and development to maximise their performance.

Table 2.4: List of field experiment referring to dynamic revetments.

Site	Type of protection	Reference
North Cove, Washington, USA	Cobble berm on sandy beach	Weiner et al. (2019)
Columbia river south jetty, Oregon, USA	Cobble berm fronting a dune	Allan and Gabel (2016)
Yaquina Bay, Oregon, USA	Artificial gravel beach	Allan et al. (2012)
Cape Lookout State Park, Oregon, USA	Cobble berm on sandy beach	Komar and Allan (2010)
Port of Rotterdam, The Netherland	Artificial gravel beach, combined with artificial submerged reef	Loman et al. (2010)
Bari, Italy	Multi-layer capping composed of geotextile, calcareous gravel, local stone and cobbles	Tomasicchio et al. (2010)
Washdyke beach in South Canterbury, New Zealand	Gravel ridge on top of a nourished sandy berm	(Kirk, 1992)
Flathead Lake, Montana, USA	Perched gravel beach, with underlying boulders	Lorang (1991)
Great Lakes, USA	Artificial gravel beach	Johnson (1987)
University of British Columbia, Canada	Cobble berm along a sand cliff	Downie and Saaltink (1983)
Surfer's Point, Ventura, California	Cobble mattress in the back-shore, with sand dune reconstruction	ESA (2016)

Over the last few decades, a few dynamic revetments have been tested in laboratory and field experiments. Table 2.3 lists the dynamic revetments tested in laboratory flume while Table 2.4 lists the dynamic revetment installed in the field. These tables aim at providing a concise list of references of the existing experiments on dynamic revetment. A more precise description of each experiment can be found in Chapter 3. Generally, Table 2.3 shows that most of the dynamic revetments tested in laboratory corresponded to pure gravel beach. Concerning field experiment, Table 2.4 shows that existing revetment have been used for different purposes on very different coastlines, with no consistent approach and design. In consequence, most of the existing revetments differ in terms of concept and design, except the North Cove, Columbia river south jetty, Cape Lookout State Park and Surfer's Point which mimic a composite beach. For these reasons, the type of dynamic revetment illustrated by these examples, which are in essence the construction of an artificial composite beach, are named 'dynamic cobble berm revetment' to identify them from the rest of the dynamic revetment family. This is the type of protection that will be investigated in this study, as it combines all the natural and engineering aspect of an efficient work with nature approach. However, due to the lack of post-construction monitoring of these revetments, their performance, behaviour and adaptability under coastal threat are very unclear. Getting a better understanding of the behaviour, sediment transport process and

performance as a coastal protection would be valuable to the coastal engineering science, as it would both inform on the capacities of dynamic cobble berm revetment, and improve our understanding of composite beach dynamics.

Chapter 3

Performance of a dynamic cobble berm revetment for coastal protection, under increasing water level

This chapter is based on the research article published in Coastal Engineering, and usable in this thesis: "Use by an author [$\cdots$] inclusion in a thesis or dissertation, [$\cdots$] (with full acknowledgement of the original publication of the Article)" (Source: https://authors.elsevier.com/authorform/staticpage/definitions.do?lang=English# prePrint).

Paul M. Bayle, Chris E. Blenkinsopp, Daniel Conley, Gerd Masselink, Tomas Beuzen and Rafael Almar (2020). Performance of a dynamic cobble berm revetment for coastal protection, under increasing water level. *Coastal Engineering*, 159.
DOI: 10.1016/j.coastaleng.2020.103712

Abstract

In a changing climate, sea level rise and projected regional-scale changes in storminess may increase the vulnerability of sandy coastlines to coastal erosion and flooding. As a result, there is increased interest in the development of adaptable, sustainable and effective coastal protection measures to protect these highly variable sandy coastlines. One such example is a dynamic cobble berm revetment; a “soft-engineering" solution (*i.e.*, not fixed) consisting of a cobble berm constructed around the high tide wave runup limit, that has the potential to stabilise the upper beach, provide overtopping protection to the hinterland and translate with water level rise. However, there have been limited applications of dynamic cobble berm revetments to date, and there is a lack of understanding about the efficacy of this coastal protection to current and changing waves and water levels. This study details a prototype-scale experiment conducted to test the behaviour and performance of a dynamic cobble berm revetment as a form of coastal protection against erosive waves and water level increase. Results from the experiment showed that the revetment was “dynamically stable" under wave action as a consistent global shape was retained even though individual cobbles were mobilised under every swash event. Although the front slope and the crest responded to the incident wave condition, the net rate of change was always an order of magnitude lower than the gross rate of change. Tracking of individual cobbles using Radio Frequency Identification (RFID) technology showed that stability of the revetment was likely maintained by rollover transport of cobbles onto the crest, as the revetment moved upward and landward under water level rise. The presence of the revetment reduced the vertical and horizontal runup as well as the retreat of the upper beach. The experimental results presented suggest that a dynamic cobble berm revetment could be a cheap, efficient and low environmental impact engineering solution for protecting sandy coastlines in a changing climate. Some preliminary design guidelines for coastal engineers are also drawn from this experiment.

Declaration concerning the article used for this Chapter:

Title	Performance of a dynamic cobble berm revetment for coastal protection, under increasing water level
Status	Published in Coastal Engineering (Elsevier)
Details	Paul Bayle, Chris E. Blenkinsopp, Daniel Conley, Gerd Masselink, Tomas Beuzen and Rafael Almar (2020). Performance of a dynamic cobble berm revetment for coastal protection, under increasing water level. *Coastal Engineering*, 159. DOI: 10.1016/j.coastaleng.2020.103712
Contribution from the authors	P.M. Bayle: Planning/Collection/Processing/Analysis of data; Manuscript (70%) C.E. Blenkinsopp: Collection/Assistance with analysis of data; Edited drafts of manuscript (15%) D. Conley: Collection; Edited drafts of manuscript (6%) G. Masselink: Collection; Edited drafts of manuscript (3%) T. Beuzen: Collection; Edited drafts of manuscript (3%) R. Almar: Collection/Analysis of data (3%)
Statement	This paper reports on original research I conducted during the period of my Higher Degree by Research candidature.
Date and Signature	

Preamble

The data presented in this chapter was collected during the DynaRev laboratory flume experiment, completed as part of the European Union's Horizon 2020 research and innovation programme, Hydralab+. The DynaRev experiment was performed over 7 weeks, from the 14/08/2017 to the 29/09/2017, in the Großer Wellenkanal, GWK large wave flume. During the first year of my PhD, I designed and planned most of this experiment in coordination with all research partners. I also conducted and managed the full experiment on-site, from installation to decommissioning. The description and goals of the complete experiment can be found in Blenkinsopp et al. (In review) in the Appendix. In this chapter, only the data related to the study of the dynamic cobble berm revetment are presented and used. As explained in Chapter 1 and 2, the access to a laboratory flume was a great opportunity to test specific research questions which could not be addressed in a field experiment. The experiment was therefore designed to address the following main research questions/objectives:

1. Can the dynamic cobble berm revetment keep pace with SLR by self-maintaining its relative elevation to the water level? How does it behave under increasing water level and energetic wave conditions?
2. Is a dynamic cobble berm revetment efficient as a coastal protection structure? How does it protect the beach and/or the hinterland?
3. Plan and conduct a large scale experiment to address the above points.

The questions listed under point 1 above are motivated by the natural behaviour of gravel and composite beaches, which tends to be dominated by rollover transport driving upward and landward transport (Scott et al., 2015). It is therefore hypothesised that a dynamic cobble berm revetment is able to move landward and upward under SLR, keeping its crest at the same relative elevation to the water level. This theory is illustrated in Figure 3.P1: under the action of waves and swashes, the revetment particles rollover the crest (shown in red on Figure 3.P1b,c). This rollover transport is intensified under increasing water level, and it is hypothesised that the structure would end up in a higher and more landward position, with a similar shape and relative elevation to the mean water level (Figure 3.P1c). To test this hypothesis, a model revetment was constructed on a sandy beach profile after it had been shaped to an approximately natural profile by 20 hours of waves. Four incremental water level increases of 0.1 m., with 7 to 14 hours of waves at each water level were then used to test the coastal protection function and water level rise response.

To test the performance of the revetment, and answer the question under point 2 above, it is necessary to compare erosion parameters, such as erosion volume, shoreline retreat and wave runup, between an unprotected sandy beach and a sandy beach with a dynamic cobble berm revetment. Therefore, the experiment was split into two phases with identical waves, water levels and run time, for an unprotected beach and a beach protected by a dynamic revetment. By doing so, a direct and objective assessment of the dynamic

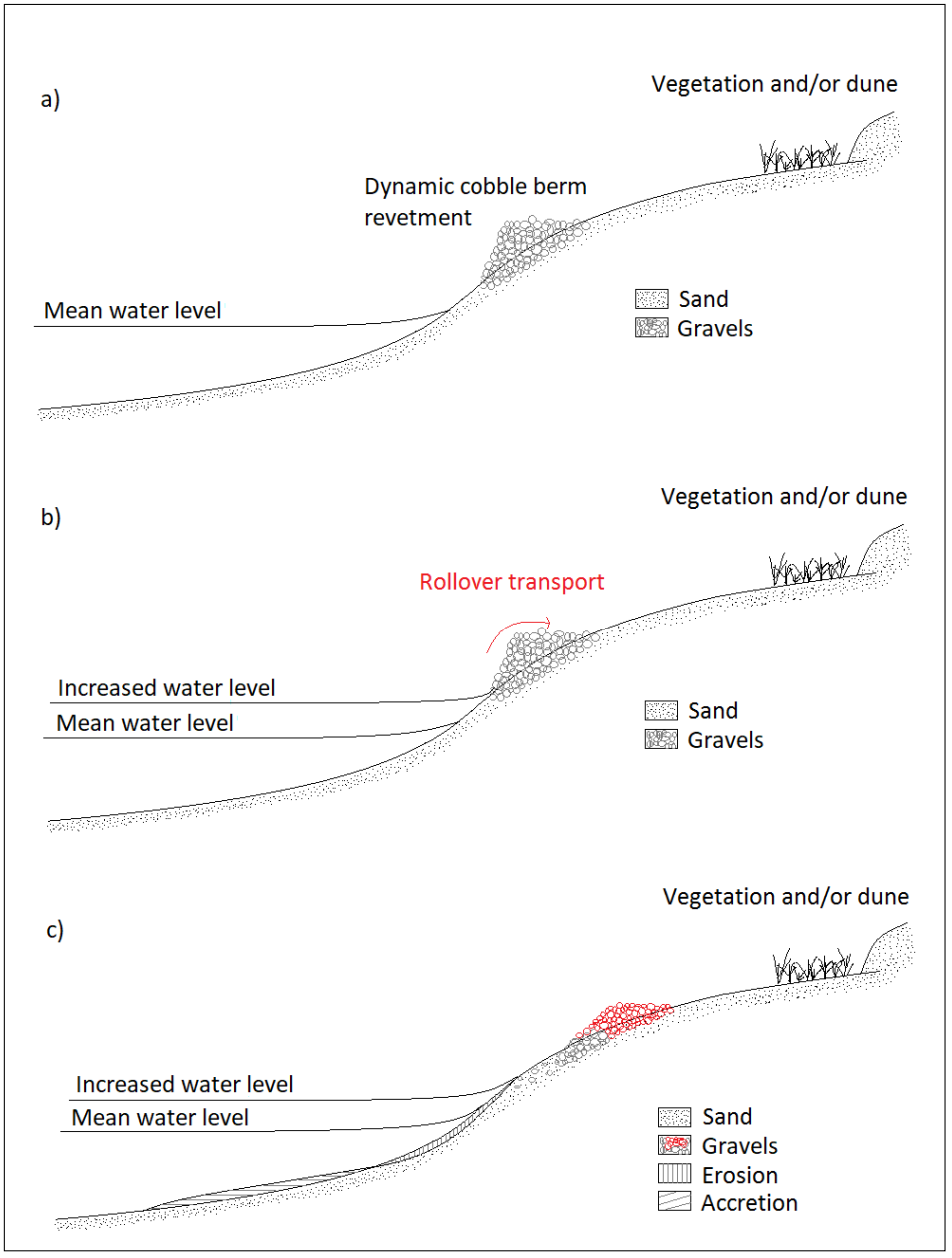

Figure 3.P1: Schematic drawing of the expected dynamic revetment behaviour under sea level rise.

revetment as a coastal protection can be performed.

3.1 Introduction

Coastal areas are home to cultural, social and environmental assets which contribute significantly to the national economies in many countries. They are all different in terms of their geology, habitat and urbanisation characteristics and are one of the most threatened environments from climate change induced sea level rise (SLR) and increasing storm severity (DeConto and Pollard, 2016). In light of these threats, the need to protect the coast from erosion and flooding is only expected to increase and there is a need to consider new approaches to coastal management and new types of coastal structures to ensure the sustainability of our coasts.

One promising structure, with respect to its potential for adaptation to a changing climate, is a dynamic cobble berm revetment. There have been several studies examining dynamic cobble berm revetments, and related structures, in the field and in small-scale laboratory experiments (van Hijum and Pilarczyk, 1982; Downie and Saaltink, 1983; Pilarczyk and Boer, 1983; Johnson, 1987; van der Meer and Pilarczyk, 1986; Powell, 1988; Ahrens, 1990; Lorang, 1991; Ward and Ahrens, 1992; Kirk, 1992; Allan et al., 2006; Komar and Allan, 2010; Loman et al., 2010; Allan et al., 2012, 2006; Allan and Gabel, 2016). However to date, there has been no detailed study into the performance of dynamic cobble berm revetments under controlled conditions at prototype scale, and in particular under changing water levels. In this paper, we investigate the performance and resilience of a dynamic cobble berm revetment under water level changes for a range of wave conditions in a large scale laboratory flume. This work presents new information about the application of such structures for coastal protection under energetic conditions and for a rising water level.

The paper is structured as follows: Section 2 presents a background of coastal protection and a detailed literature review of existing studies and applications of dynamic cobble berm revetments. Section 3 details the methodology used in the large scale laboratory flume experiment undertaken to test the performance of the prototype structure. Section 4 investigates the behaviour and performance of the dynamic cobble berm revetment as a coastal defence. Section 5 discusses the results and limitations, focusing on maintenance and application of such a structure. Section 6 presents a preliminary guidance on the implementation of a dynamic cobble berm revetment as a coastal protection. Section 7 concludes the study and introduces future work.

3.2 Background and literature review

3.2.1 Coastal protection techniques

Coastal protection methods can be divided into hard and soft engineering techniques (Dean and Dalrymple, 2002; Cartwright et al., 2008; Hudson et al., 2008). Hard engineering techniques consist of building fixed structures to counteract natural processes and protect the coastline; soft engineering consists of implementing less rigid techniques which are usually integrated and work with natural processes to protect the coastline.

Hard engineering structures often have a negative impact on beach amenity and the natural landscape. From an engineering prospective, existing hard engineering structures need to be maintained to continue to provide protection under new design wave and water level conditions associated with a changing climate. Such maintenance works can be done for structures like submerged artificial reefs but can be more complex for seawalls as the foundations are not designed to withstand additional loads. In all cases, such modifications are likely to be expensive. Revetment and rock armour upgrades are hard to achieve as the addition of an extra layer of material usually creates planes of weakness (Howe and Cox, 2018). Howe and Cox (2018) suggested that efficient top-up maintenance could be achieved using a higher density layer, however this method is only at the prototype testing stage.

Existing hard engineering protections have rarely been designed to face extreme and long-term water level changes; thus, soft engineering could become a sustainable alternative for areas where the required level of protection does not necessitate hard engineering. Classic soft engineering techniques like beach or dune nourishment and submerged nourishment are expensive and can be destructive to the ecosystem (Seymour et al., 1995). In addition, they generally have a short life span (depends on the quantity of nourished sediment). However, because they are maintained or re-implemented at least every decade, they can be modified to cope with changes in design conditions (Dean and Dalrymple, 2002; Cartwright et al., 2008; Hudson et al., 2008; French, 2001; Sorensen, 2006).

3.2.2 Composite beach

In this paper, we investigate the performance of a “dynamic cobble berm revetment" (Figure 3.1b) defined here as a cobble ridge constructed around the wave runup limit on sandy beaches to mimic natural composite beaches (Jennings and Schulmeister, 2002). Composite beaches (Figure 3.1a) consist of a lower foreshore of sand and a backshore ridge composed of gravel or cobbles which stabilises the upper beach and provides overtopping protection to the hinterland. Like gravel beaches, they have long been recognised as an effective form of natural coastal protection (Allan et al., 2006), showing a great degree of stability and adaptability in the face of wave attack by reshaping and self maintaining their relative elevation to the water level. On composite beaches, the cobble ridge is generally exposed at all stages of the tide when the tidal range and wave conditions are small. For larger wave conditions and particularly during spring tides, the ridges are exposed to swash processes and may be overtopped during particularly energetic events (Everts et al., 2002; Allan and Komar, 2004). Unlike pure and mixed sand-gravel type of gravel beaches, composite beaches have received little attention in the literature and have not been investigated using long-term (decades) field surveys or laboratory experiments. A dynamic cobble berm revetment is designed to mimic the cobble ridge of a natural composite beach. These structures contrast with static coastal defence structures as they are “dynamic” and are expected to reshape under wave attack and retreat as the sea level rises.

(a)

(b)

Figure 3.1: (a) Photo of a natural composite beach, at Kalaloch, Washington State, the USA. Cobbles are relatively similar in shape and size to those in this study. Note that drift wood is regularly deposited on the upper part of the beach at this location. (b) Photo of the dynamic cobble berm revetment as built during the DynaRev experiment. *Photo from Paul Bayle*.

3.2.3 Review of dynamic cobble berm revetment

The concept of a dynamic cobble berm revetment is not new, and previous research has investigated a range of structures with similarities to that explored here which have been variously termed “dynamic revetment", “cobble berms", “gravel ridge" or “artificial cobble beaches" (Lorang, 1991; Kirk, 1992; Allan et al., 2012; Allan and Gabel, 2016). In many cases however, there have been significant differences in the form and function of these structures and only a few examples of the structure type that is the subject of this paper exist.

The most recent example of what is termed here a “dynamic cobble berm revetment" was installed in North Cove, Washington State, USA in 2017. The community of North Cove has a history of rapid coastal erosion, with a 2 km length of coast eroding by around 13 m per year. In order to slow this erosion, the local population have gradually implemented a dynamic revetment composed of locally-sourced, inexpensive, poorly sorted angular material, ranging in size from D_{50} = 1 cm to D_{50} = 80 cm. The material was randomly placed in an ad hoc manner over time along the back of the beach, especially when and where the erosion sand scarp was exposed. The revetment has been seen to mitigate the effect of storm erosion and protect the hinterland (Weiner et al., 2019).

A dynamic cobble berm revetment was installed to provide coastal protection along a 300 m stretch of the highly vulnerable sandy beach of Cape Lookout State Park, Oregon, USA (Komar and Allan, 2010). The revetment was completed in December 2000, and was designed to protect the hinterland. It consisted of a ridge of cobbles backed by an artificial dune reinforced with geotextile sand bags to protect the hinterland against storm waves. Such beaches are relatively common on many coasts, so the placement of a cobble berm could be considered to be a more natural and aesthetic solution than a conventional revetment or seawall. Although the hybrid dynamic revetment/dune was not constructed to the design height to protect the hinterland against extreme winter waves and water levels by the contractors, it remained stable and provided overtopping and erosion protec-

tion for almost two decades. Over time however, longshore transport has moved cobbles northward, leading to depletion of the revetment in the southern end of the beach (Allan et al., 2006).

Another example of a dynamic cobble berm revetment was installed at the Columbia River south jetty in October 2013 to protect the foredune and prevent the spit from breaching (Allan and Gabel, 2016). The structure was constructed using 3 different layers: a bedding filter layer on the excavated sand bed using angular gravel (D_{50} = 2.5 cm); a core layer made of angular gravel (D_{50} = 2.5 cm to D_{50} = 20.3 cm), which was expected to become sub-rounded by wave action in 2-5 years; and an upper layer of rounded cobbles (D_{50} = 2.5 cm to D_{50} = 20.3 cm). The structure had a front slope of 1:5 and the crest height was set to 6.7 m based on a study of wave runup. The berm width, which was identified as a key parameter, was set to 19.8 m, in agreement with previous observations of the Cape Lookout dynamic revetment and natural gravel beaches in Oregon. The storm response of this revetment was monitored along 780 m of beach, using 28 surveyed transects 25 m to 40 m apart, with 10 monitoring campaigns from the end of its construction to September 2015. Primary analysis showed that sediment is moving slowly southward. Due to this longshore transport, maintenance work is expected to be required every 10-15 years in order to keep the revetment operational for its expected life of 30-50 years.

The oldest example of a dynamic cobble berm revetment is the one installed in 1981 along 300 metres of the sand cliffs forming the westerly boundary of the University of British Columbia, Canada (Downie and Saaltink, 1983). In 1981, an artificial cobble beach was constructed over 300 m. It consisted of drift sills made of heavy boulders (D_{50} = 150 cm diameter) and oriented perpendicular to the coast. They were then filled and covered with smaller cobbles (D_{50} = 10 cm). The structure extended from 0.6 m contour elevation up to the berm elevated to 6.4 m, with a 1:15 slope. The width of the berm extended back to the toe of the cliff talus. This flat area was also covered with sand and vegetated to satisfy the beach users. The subtidal zone was composed of natural river sand exposed at low tide. In this case, the structure goal was to protect the cliff against storm induced waves and drift logs movement, as well as retaining the talus' sand falling from the cliff. Overall, the protection was a success as it maintained the recreational area while stabilising the talus. However, the sills reduced in height by 0.6 m, and therefore, a lot of material bypassed southward. It was observed that storm waves tended to push the cobbles up to the beach, with the crest forming above the original berm level. The slope also changed from 1:15 to 1:3 during energetic conditions.

At Washdyke beach in South Canterbury, New Zealand, through a beach reconstruction and renourishment scheme, an experimental gravel ridge was constructed over a 300 m long section of coastline significantly affected by erosion, flooding and retreat (Kirk, 1992). The local beach material was first reworked and reshaped as a berm to raise the overall

crest height by 2.00-2.5 m. The reformed crest was then capped by $9,800\,m^3$ of coarser river gravel which was expected to be much more resistant to erosion than the fine beach grain. The revetment was built in 1980 and monitored for 5 years. During this period, the crest of the protected area remained static while the adjacent unprotected section experienced a retreat of 11.5 m to 22.5 m. In addition, the overall erosion rate was reduced by 55 %, and no overtopping induced flooding was recorded.

While different to the dynamic cobble berm revetments that are the focus of this paper, a variety of similar structures have been discussed in the literature. Several authors describe the installation of a full gravel beach extending below the level of Minimum Low Water Shoreline (MLWS) to protect a given asset. The few examples of application of this type are well summarised by Allan and Gabel (2016). Johnson (1987) discusses a series of artificially constructed gravel beaches which they termed “dynamic revetments" and were installed in the Great Lakes after realising that the eroded copper mine tailings naturally spread and formed a gravel beach which significantly reduced the erosion of the area.

At Flathead Lake in Montana, a perched gravel beach (Lorang, 1991) was constructed using a stable base of boulders overlain by cobbles to mitigate shoreline erosion. This type of design makes the revetment dynamic with respect to the motion of cobbles on the front slope, but the underlying boulders keep the whole structure static and prevent it from adjusting its position in the cross-shore. The structure was found to reduce erosion, but material was transported away from the protected area under oblique wave induced longshore currents.

A gravel beach (Allan et al., 2012) was installed in March 2007 at Yaquina Bay, Oregon where the erosion due to ebb and flood tide created critical damage to a path and threatened the assets of the Hatfield Marine Science Centre. The structure was installed in the north part of the area, and was shown to stabilise the shoreline and walking path. After erosive events in winter 2009-2010, an additional gravel beach was installed in November-December 2011 to stabilise the southern part of the area. The structure acted as a buffer and protected the foot path behind. It also showed a dynamic behavior with the revetment profile changing both alongshore and cross-shore while remaining fairly stable.

A gravel beach (Loman et al., 2010) was used as part of the coastal protection for the Port of Rotterdam expansion in 2008. This artificial gravel beach differs slightly from those discussed above because it is combined with a submerged artificial reef. The gravel beach was composed of a thick layer of cobbles and placed to form a typical gravel beach-dune profile (Loman et al., 2010). This approach of combining a cobble beach with an underwater breakwater was also used on the Adriatic coast of Italy, near Bari (Tomasicchio et al., 2010). A multi-layer capping composed of geotextile, calcareous gravel, local stone and cobbles was used for reclaiming contaminated coastal areas. The role of the breakwater was to decrease the wave energy reaching the coastline, while the cobble top layer of the capping was designed to dissipate the swash energy through dynamic motion.

A number of laboratory experiments have been undertaken that are relevant to the different types of dynamic revetment structure discussed above. For example, van Hijum and Pilarczyk (1982) and Pilarczyk and Boer (1983) investigated the design of artificial gravel beaches, while Powell (1988) studied the potential use of a coarse grain beach for coastal protection in place of a conventional revetment. Ahrens (1990) and Ward and Ahrens (1992) (see also Tomasicchio et al. (1994)) conducted a flume experiment to assess the performance of a coastal structure, which consisted of small rocks placed on a concrete bottom and extending offshore beyond the shoreline. Ahrens (1990) introduced the concept of critical mass, which is the mass of stones needed to maintain stability under a given wave condition. The experiment showed that while the gravel beach slope was dependent on wave conditions, there was almost no difference between equilibrium profiles formed from different initial beach profiles under same wave conditions. This was also observed by van der Meer and Pilarczyk (1986) through a similar laboratory experiment of a shingle beach for deep water wave conditions. This work suggests that it may not be necessary to precisely place the material forming dynamic revetment-type structures as long the required crest height is built and sufficient volume is provided.

3.3 Methodology

3.3.1 Experimental facility

The DynaRev experiment took place in the Großer Wellenkanal, GWK large wave flume, during August and September 2017. The flume is situated at the Forschungszentrum Kuste (FZK Coastal Research Centre), which is a joint institution between the University of Hanover and the Technical University Braunschweig located in Hanover, Germany. The flume is 309 m long, 7 m deep and 5 m wide and is equipped with a combined piston-flap-type wave paddle. Reflected waves and low frequency resonance (*e.g.*, seiche) are damped at the paddle using an Automatic Reflection Compensation (ARC). A large-scale facility was necessary for this experiment due to the bimodal nature of the beach-revetment system. Scaling sediments to work in a smaller scale facility while retaining the particle diameter ratio of the cobbles and sand would result in cohesive sediment on the sand beach. It is noted that the 2D nature of this facility does not allow us to consider the influence of longshore sediment transport or short crested waves on the revetment performance.

The coordinate system is defined as follows: the vertical elevation, z is defined positive upwards from the base of the flume; the cross-shore coordinate system, x has its origin at the wave paddle and is positive in the direction of the beach. A sandy beach with an initial plane slope of 1:15 was installed on a permanent asphalt slope with a gradient of 1:6 located at the far end of the flume. The sand used to form the beach had the following characteristics: D_{50} = 0.33 mm, D_{90} = 0.65 mm and D_{10} = 0.20 mm. The beach was constructed to an elevation of 6.8 m above the flume bed. A 0.5 m thick layer of sand extending 25 m from the toe of the beach was placed to provide an additional store of sand seaward of the main beach slope (Figure 3.2). Therefore, the toe of the beach slope was

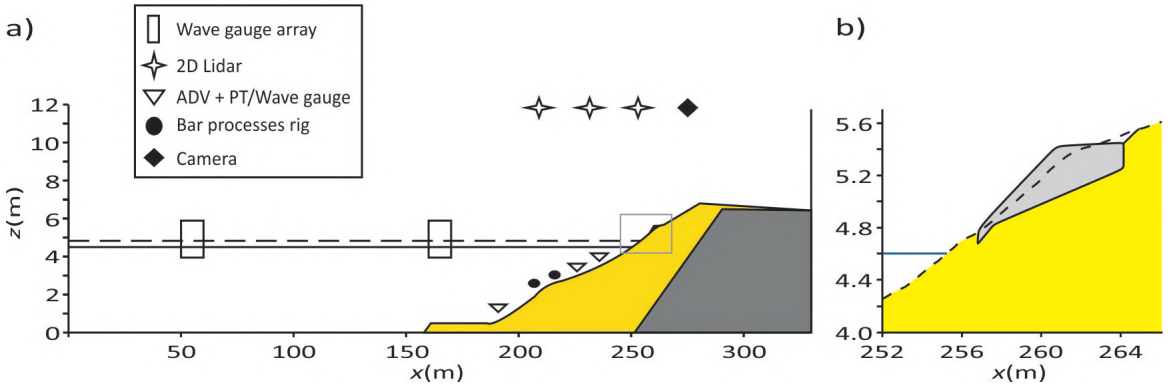

Figure 3.2: a) Schematic of flume setup showing primary instrument locations. The yellow shaded area represents the sand volume and the dark grey shaded area is the permanent 1:6 impermeable slope. The black solid and dashed horizontal lines indicate the minimum (h = 4.5 m) and maximum (h = 4.9 m) water levels. b) Close up of the dynamic revetment geometry after construction, corresponding to the grey box in (a). The light grey region indicates the dynamic revetment and the dashed line shows the beach profile prior to revetment construction.

located at x = 188.5 m and the top of the beach at x = 283 m. The total amount of sand required to build the beach was 1660 m^3.

3.3.2 Experimental set-up and instrumentation

A mechanical profiler was used to measure the beach profile after each run (see terminology in Section 3.3.3.1 and Section 3.3.3.2). It consists of a mechanical roller attached to an overhead mobile trolley running along the flume side walls. The system enables measurements of the complete bed profile to approximately 1 − 2 cm vertical accuracy.

An array of three SICK LMS 511 Lidar scanners was used to measure the time-varying water surface elevation along an 80 m transect on the flume centreline. All three Lidars were sampled by a single computer at a scan rate of 25 Hz and angular resolution of 0.166 deg. Each Lidar is capable of obtaining measurements within a 190 degree field of view, though here we consider only the central 150 degrees within which valid water surface measurements were obtained. The Lidars were mounted in the flume roof at z = 11.80 m, (7.3 m above the initial still water line) at cross-shore locations x = 230 m, x = 242 m and x = 255 m and looked vertically down (Figure 3.2).

A high definition IP camera was mounted in the flume roof at z = 11.8 m and x = 272 m, and was facing the wave paddle. A series of ground control points (GCPs) were positioned within the camera field of view in order to rectify the generated timestack images of the swash zone. In combination with the most landward Lidar, the timestack images of swash flow can be used to infer the time-varying shoreline.

The movement of individual cobbles within the dynamic revetment was monitored using a Radio Frequency Identification (RFID) tracking system similar to that used by Allan et al. (2006). The RFID system consists of three components: Passive Integrated Transponder (PIT) tags, a module reader and a detection antenna. A total of 97 cobbles were fitted with transponders: 20 were painted in pink and placed on the bottom layer of the revetment (at the sand interface), from x = 257.4 m to x = 259.8 m; 30 were painted in orange and placed 20 cm above the bottom of the revetment (mid layer), from x = 258.6 m

to x = 262.2 m; 47 were painted in green and placed at the toe and on the top layer of the revetment, from x = 257 m to x = 262.6 m. Cobbles placed in the middle layer started further landward than in the other layers, as the revetment has a triangular shape and becomes thick enough only around x = 258.6 m. They were all positioned along the centreline of the revetment in groups of 3 cobbles – except at the toe, where 7 cobbles where placed – at 40 cm intervals. As the wave flume is effectively 2 dimensional, the centreline was considered to be representative of the profile, and sediment transport assumed to be only cross-shore.

3.3.3 Experimental procedure

The main objective of the experiment was to quantify the performance of a dynamic revetment under varying wave and water level conditions. This was done by obtaining two comparable datasets of a sandy beach only (named phase SB) and a sandy beach protected by a dynamic revetment (named phase DR) under the same wave conditions and water level changes.

3.3.3.1 Phase SB: morphological response of a sandy beach

Run names for this phase are given as SB(E,A)<WL increment>–<Run No.>, where E and A stand for Erosion and Accretion respectively, water level (WL) increments are numbered 0 for the initial water level of h = 4.5 m to 4 for h = 4.9 m and run numbering is started from 1 for each WL increment. For example, SB1-2 corresponds to second run for the first water level rise for the Sandy Beach (SB) Phase. Runs had different durations, varying from 20 minutes up to 3 hours. Starting with a water level of 4.5 m, a standard wave case with a significant wave height H_s = 0.8 m (at the wave paddle), and a peak period T_p = 6 s was run for 20 hours. Time series of 2 hours of irregular waves were created from a JONSWAP spectrum (using a peak enhancement coefficient of 3.3), and were repeated every 2 hours. This allowed the waves to reshape the beach profile to a developed beach profile approaching equilibrium (Table 3.1). The second part of Phase SB consisted of a series of 4 incremental water level increases of 0.1 m using the standard wave conditions (Table 3.1). At the final water level, z_{wl} = 4.9 m, 2 erosive cases (labelled SBE) and 1 accretive case (labelled SBA) were run as part of a 'resilience test' (Table 3.1).

3.3.3.2 Phase DR: morphological response of a sandy beach with a dynamic cobble berm revetment

Run names for this phase are given as DR(E,R)<WL increment>–<Run No.>. For example, DR4-3 corresponds to third run for the last water level rise for the Dynamic Revetment (DR) Phase. Runs had different durations, varying from 20 minutes up to 3 hours. Before starting Phase DR, the beach was manually reshaped to the original 1:15 planar slope. Starting with a water level of z_{wl} = 4.5 m, the initial case of Phase SB was repeated with 20 hours of the standard wave conditions to obtain a developed beach profile approaching equilibrium that was almost identical to that at the end of SB0 (Table 3.2). Once the developed beach profile was reached, and before building the revetment, the beach was first flattened to 1:15 at

Table 3.1: Overview of the test programme for Phase SB: H_s is the significant wave height at the wave paddle; T_p is the peak period; Ω_0 is the dimensionless fall velocity (also called Dean's number, $\Omega_0 = H_0/w_s T_p$, (Dean, 1973; Gourlay, 1968)) calculated using offshore significant wave height (H_0); and wave energy is given in MJ per metre of wave crest.

Test	**Duration (hr)**	H_s **(m)**	T_p **(s)**	**Water level** z_{wl}**(m)**	Ω_0	**Energy (MJ)**
Approach Equilibrium						
SB0	20	0.8	6	4.5	3.38	0.78
Water Level Changes						
SB1	7	0.8	6	4.6	3.38	0.78
SB2	7	0.8	6	4.7	3.38	0.78
SB3	7	0.8	6	4.8	3.38	0.78
SB4	17	0.8	6	4.9	3.38	0.78
Resilience test						
SBE1	2	1	7	4.9	3.51	1.23
SBE2	4	1.2	8	4.9	3.54	1.76
SBA1	6	0.6	12	4.9	1.02	0.44

the revetment location to ensure a sufficient volume of cobbles could physically be placed (see Blenkinsopp et al., In review). The revetment was placed by dumping stones and then reshaping to the required profile using a front-end loader and manual profiling. The dynamic revetment was constructed using rounded granite cobbles from local supplier, with the following characteristics (intermediate axis): D_{max} = 90 mm, D_{min} = 50 mm, D_{50} = 63 mm, D_{85}/D_{15} = 1.32 and a minor axis dimension of 30 mm on average. This well sorted material was close enough from the wanted design size, and had a density of 2700 kg/m^3 and a bulk density of 1600 kg/m^3, giving a porosity of 0.41. Based on previous studies of slope steepness (*e.g.*, Komar and Allan, 2010; van Hijum, 1976; Powell, 1988; Roman-Blanco et al., 2006), the front slope of the revetment was set to 1:6.3, in agreement with the cobble characteristics (Powell, 1993). The toe of the revetment was located at x = 256.8 m, and z = 4.77 m, roughly corresponding to the predicted shoreline position (water level intersection) for test DR3 (z_{wl} = 4.8 m). The predicted $R_{2\,\%}$ runup height for the standard wave condition was calculated as 0.72 m using the equation developed by Poate et al. (2016) for gravel beaches. Therefore, the crest was built at z = 5.42 m, putting the crest 0.65 m above the toe, at x = 260.7 m. This elevation corresponds to the predicted value of R_2 % for DR2 (z_{wl} = 4.7 m) and so consequently, it was expected that the revetment crest would be overtopped by approximately 2 % of waves during testing at this water level increment. The crest of the revetment was horizontal until it intersected with the sand slope, at x = 264.1 m. Therefore, the total cross-shore length of the revetment was 7.3 m. The volume of the revetment was 9.375 m^3 with a total weight of 15 tonnes.

Following construction of the revetment, the procedure used for tests SB1 to SB4 described in Section 3.3.3.1 was repeated, with the same water level elevations and run durations (Table 3.2).

The resilience test in Phase DR was modified from that used in Phase SB (Table 3.2) to investigate the relationship between the revetment front slope and wave period. A series of erosive tests with increasing wave energy were completed, followed by a two hour case using the standard wave condition, in order to observe the process of recovery after

Table 3.2: Overview of the test programme for Phase DR: H_s is the significant wave height at the wave paddle; T_p is the peak period; Ω_0 is the dimensionless fall velocity (also called Dean's number, $\Omega_0 = H_0/w_s T_p$, (Dean, 1973; Gourlay, 1968)) calculated using offshore significant wave height (H_0); and wave energy is given in MJ per metre of wave crest.

Test	**Duration (hr)**	H_s **(m)**	T_p **(s)**	**Water level** z_{wl}**(m)**	Ω_0	**Energy (MJ)**
Approach Equilibrium						
DR0	20	0.8	6	4.5	3.38	0.78
Construction of the dynamic revetment						
Water Level Changes						
DR1	7	0.8	6	4.6	3.38	0.78
DR2	7	0.8	6	4.7	3.38	0.78
DR3	7	0.8	6	4.8	3.38	0.78
DR4	17	0.8	6	4.9	3.38	0.78
Resilience test						
DRE1	2	0.9	6	4.9	3.69	0.99
DRE2	2	1	7	4.9	3.51	1.23
DRE3	1	1	8	4.9	3.08	1.23
DRR1	2	0.8	6	4.9	3.38	0.78

Table 3.3: Overview of the test programme for the recharged revetment testing at the maximum water level $z_{wl} = 4.9$ m: H_s is the significant wave height at the wave paddle; T_p is the peak period; Ω_0 is the dimensionless fall velocity (also called Dean's number, $\Omega_0 = H_0/w_s T_p$, (Dean, 1973; Gourlay, 1968)) calculated using offshore significant wave height (H_0); and wave energy is given in MJ per metre of wave crest.

Test	**Duration (hr)**	H_s **(m)**	T_p **(s)**	**Water level** z_{wl}**(m)**	Ω_0	**Energy (MJ)**
DRN1	2	0.8	6	4.9	3.38	0.78
DRN2	0.66	1	8	4.9	3.08	1.23
DRN3	2	0.8	6	4.9	3.38	0.78
DRN4	0.66	1	9	4.9	2.73	1.23
DRN5	0.33	1.2	8	4.9	3.54	1.76
DRN6	1	0.8	6	4.9	3.38	0.78

energetic conditions (Table 3.2).

Following the completion of the resilience testing, an extra 2.50 m^3 of material was added to the front slope of the revetment to increase the thickness of the revetment slope and crest width. The extra cobbles were placed with the same slope as the reshaped revetment (around 1:3.2) while retaining the same crest height. After renourishment of the revetment, a series of different wave cases were run to investigate the short-term response of the revetment front slope, at water level $z_{wl} = 4.9$ m (Table 3.3).

3.3.4 Data Processing

3.3.4.1 Volume of the revetment during the experiment

The thickness of the revetment was measured after each water level change test, after the erosive tests and after the recovery test. Revetment thickness was established by digging a series holes in the revetment which could be refilled without damaging the initial revetment shape. This technique allowed the depth to the sand to be measured manually with a vertical accuracy of $1 - 2$ cm. Holes were dug approximately every 0.5 m cross-shore. The position of the toe and the back of the revetment were also surveyed during

these measurements. A linear interpolation was used to obtain the interface between the revetment and the sand for the entire revetment width and this data combined with profiler measurements of the revetment surface were used to estimate the volume and shape of the revetment. At the end of the experiment, a channel was excavated along the centreline of the revetment to expose the sand-cobble interface and enable a complete profile to be measured. This enabled the revetment volume at the end of the experiment to be accurately determined and suggests that the technique described above is able to estimate revetment volume within 5 % ($0.4\,m^3$) of the actual volume.

3.3.4.2 Swash detection

Timeseries of beach profile and swash surface elevation were obtained from the most landward Lidar, which was located directly above the exposed beach, using a method similar to that presented by Almeida et al. (2015). The raw lidar measurements capture the nearest surface, beach profile or swash surface, without any distinction between the two. To separate topography from the swash surface over time at each cross-shore position, the Lidar data was sub-sampled onto a 0.1 m horizontal grid and a moving-average window of 2 s with a mean variance threshold was applied to all measurements. This method of separating the stationary bed level (referred to here as the 'bed') from the non-stationary water surface (wave or swash, here referred to as the 'swash') is similar to that used by Turner et al. (2008) for data collected using ultrasonic bed-level sensors. Using this method, Lidar data were separated into timeseries of "swash" and "bed" elevation which can be analysed independently. Therefore, a timeseries of the shoreline position, defined by the location of the most landward "swash" position at every timestep, could be extracted. These runup data obtained from the Lidar were validated against visual *in situ* observations, and by plotting the shoreline timeseries on top of rectified timestacks generated by the HD camera (Section 3.3.2).

3.3.4.3 Gross and net change rates

Using the "bed" timeseries extracted from the Lidar data it is possible to capture the exposed beach profile at high temporal resolution (25 Hz). From this dataset, a representation of the gross and net rates of change of the revetment volume were calculated.

Revetment profiles were extracted from the Lidar data every 6 seconds (approximately every wave) at a spatial resolution of 0.1 m. These data were used to calculate both the net and gross rate of absolute volume change per metre width between profiles by applying the trapezoidal rule and summing the absolute values.

Specifically, the rate of absolute volume change per metre width was calculated between each consecutive profile, and then averaged every 10 minutes to give an indicative rate of short-term volume change, ignoring the direction of change. The averaged value was finally divided by 6 to give the gross volume change (per metre width) per second, denoted $\overline{dV}$. Here, the gross rate of revetment volume change per metre width $\overline{dV}$ represents the rate at which the volume of the revetment is changing over short timescales.

In contrast, the rate of absolute volume change per metre width was calculated between profiles separated by 10 minutes, and then divided by this duration. This is hereafter named the net volume change (per metre width) per second, and is denoted dV_{10}. This value simply represents the mean rate of change over a 10 minute period.

3.4 Results

3.4.1 Revetment behaviour

3.4.1.1 Comparison of Phase SB and DR

Figure 3.3 shows the overall evolution of the bed relative to the original planar profile. Bed elevation was extracted from the profiler and Lidar data, and bed changes relative to the initial planar profile were computed at every second throughout the experiment, for Phase SB (Figure 3.3a) and Phase DR (Figure 3.3b). Note that the revetment was built at $t = 0$ h on Figure 3.3b. This explains the sudden accretion between $x = 259$ m and $x = 262.5$ m showing the revetment installation, and the sudden erosion between $x = 262.2$ m and $x = 264.8$ m showing the sand compaction during cobble placement.

Bed evolution during the first 20 hours (from $t = -20$ h to $t = 0$ h) was almost identical for Phase SB (Figure 3.3a) and Phase DR (Figure 3.3b), suggesting that laboratory experiments investigating morphological change are repeatable at this scale. Differences in bed change can be observed between Phase SB and Phase DR once the revetment is installed, and particularly around the beachface. The shoreline and the berm (small sand berm in light blue around $R_{2\%}h$ on Figure 3.3a; cobble berm in light blue in Figure 3.3b) retreated further landward during Phase SB than Phase DR, leading to reduced horizontal runup excursions during Phase DR (Section 3.4.3 and Section 3.4.4). The presence of the revetment limited the erosion of the beachface during energetic conditions (runup data not available) and altered the evolution of the outer bar, which appears more stable during Phase DR than Phase SB.

These differences are also seen on Figure 3.3c which shows a series of profiles comparing the response of the beach with and without the revetment. It is clear that the profile at the start of SB1 and DR1 are very similar, with the exception of the revetment area. Over the course of the water level increments, the offshore bar in Phase DR tends to be a little higher, and later in the tests, further landward than in Phase SB. During the water level changes, the defined trough and inner bar evident landward of the outer bar at the start of the first water level increment (SB1, DR1) are smoothed out and become less pronounced. Between the shoreline and the sandbar, sand ripples with a wavelength greater than one metre are evident in all profiles. During Phase SB, the bed elevation in this region rises by approximately 0.20 m as the water level increases by 0.4 m. This is not the case for the Phase DR testing, and the bed between the revetment toe and the bar remains at approximately the same elevation. At the end of testing, the main difference between the two tests is the erosion area directly adjacent to the revetment toe, as well as the ripple area in inner surf zone. In this region, profile DR4 is approximately 0.25 m lower than profile SB4 $x = 252$ m

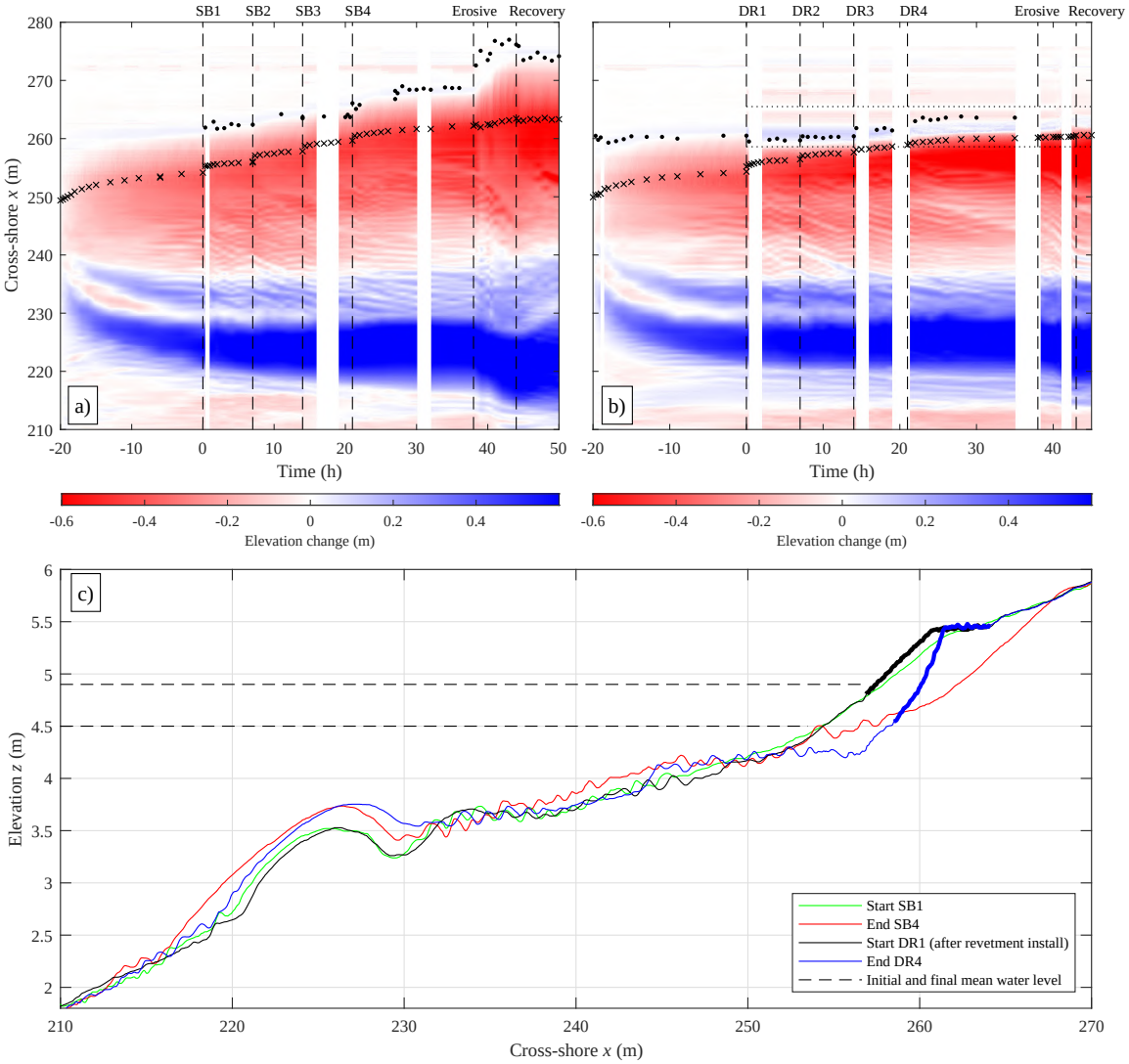

Figure 3.3: Bed elevation change relative to the original planar profile, for (a) Phase SB and (b) Phase DR. Red represents erosion and blue accretion. The vertical dashed lines mark the beginning of a new water level (*e.g.*, DR1, DR2,...) and resilience test cases (*e.g.*, erosive and accretive). The black dots represents $R_{2\%}h$, which is the horizontal runup limit exceeded by 2 % of the wave runup (note that data are not available for all runs). The black crosses represent the shoreline position, taken at the end of each run. The horizontal and parallel dotted lines on (b) mark the most seaward and landward limit of the revetment. (c) shows the beach profile at the beginning of SB1 (initial water level of 4.5 m) in green and DR1 in black; and at the end of SB4 (final water level of 4.9 m) in red and DR4 in blue. The revetment surface is marked with a thicker line.

and $x = 258$ m. This local erosion may be influenced by the increase in wave reflection caused by the presence of the revetment in Phase DR. The coefficient of reflection at the end of SB0 and DR0 was around 0.200. At the end of the final water level increment, the coefficient of reflection decreased to 0.180 for SB4 whereas it increased to 0.225 for DR4.

Significant erosion of the sand beachface is observed during the Phase SB testing (Figure 3.3a and c). The shoreline retreated (due to both water level rise and sand loss) by 12.8 m over the course of the water level increments, and erosion was observed up to $x = 268$ m. The presence of the revetment slowed this retreat considerably, with the shoreline retreating by approximately 9.7 m (Figure 3.3b and c). Over the course of the water level increases, the revetment crest elevation was relatively stable but it retreated by 0.9 m overall. Additionally, the toe of the revetment retreated by approximately 1.7 m

and lowered by 0.28 m. This led to an overall steepening of the revetment from 1:6.3 to 1:2.3. Although the crest of the cobble structure was overtopped completely by multiple waves, the horizontal runup extent was greatly reduced when compared to the SB cases (Section 3.4.3), and no beach change is observable in the profile measurements landward of the back of the revetment at $x = 265$ m.

3.4.1.2 Evolution of the revetment

During DR1 ($z_{wl} = 4.6$ m) and DR2 ($z_{wl} = 4.7$ m), the original crest was not overtopped (Figure 3.6). The maximum $R_{2\,\%}$ limit is shown by a blue dot in Figure 3.4b and Figure 3.4c, and it is observed that a small intermediate berm was created just below this elevation. The majority of morphological change occurred around the toe and lower part of the front slope of the revetment (below the intermediate berm), causing steepening in this region. At the end of DR2, the toe of the primary revetment volume is located 7 cm lower than the original elevation, at $z = 4.69$ m (Figure 3.5a), and has moved 0.9 m landward (Figure 3.5b). In addition, a mixed layer of cobbles and sand was formed at the toe (shown in green on Figure 3.4a and Figure 3.4b), and extends to the original toe position at $x = 256.8$ m. Globally, the crest and the centroid remain stable in elevation and horizontal position (Figure 3.5a, Figure 3.5b), although the landward movement of the toe brings the centroid slightly landward by 16 cm. This caused the revetment to shorten by 0.7 m in cross-shore extent (Figure 3.5c), and increase in height from 0.65 m to 0.76 m (Figure 3.5c).

At the end of DR3 ($z_{wl} = 4.8$ m), after 7 hours of waves (Figure 3.4d), the original crest started to be overtopped by around 10 % of wave runup events (Figure 3.6). The maximum $R_{2\,\%}$ limit is now landward the crest, at $x = 261.6$ m (Figure 3.4d). A lot of water percolated through the structure during the overtopping events, which transported sand seaward from beneath the revetment and caused the front slope to steepen further. This steepening again occured primarily in the lower and mid swash, although the intermediate berm observed previously is now indistinct. The region of sparse cobbles and sand lengthened (Figure 3.4d). As shown in Figure 3.5b, the revetment crest, centroid and toe retreated by 0.4 m, 0.3 m and 0.9 m respectively. Therefore, the cross-shore length of the revetment decreased to 5.6 m. The revetment was observed to sink slightly due to the sand erosion occurring underneath, so the crest and centroid elevation decreased by 1 cm and 2 cm respectively (Figure 3.5a). The total revetment height fluctuated between 0.65 m and 0.74 m during DR3 (Figure 3.5c). This was mainly driven by the variation of the toe elevation (Figure 3.5a).

As soon as the water level was raised to $z_{wl} = 4.9$ m (DR4), the percentage of overtopping increased significantly, up to 65 % (Figure 3.6) and the maximum $R_{2\,\%}$ limit moved further landward. This caused steepening over the entire front slope of the revetment which seemed to approach an equilibrium with a value of 1:2.3 at the end of DR4 (Figure 3.4f). Toward this equilibrium, the crest, toe and centroid positions retreated (Figure 3.5b). The elevation of the toe and centroid dropped while the elevation of the crest increased (Figure 3.5a). As mentioned before, this lowering is due to the sinking process caused by the sand erosion

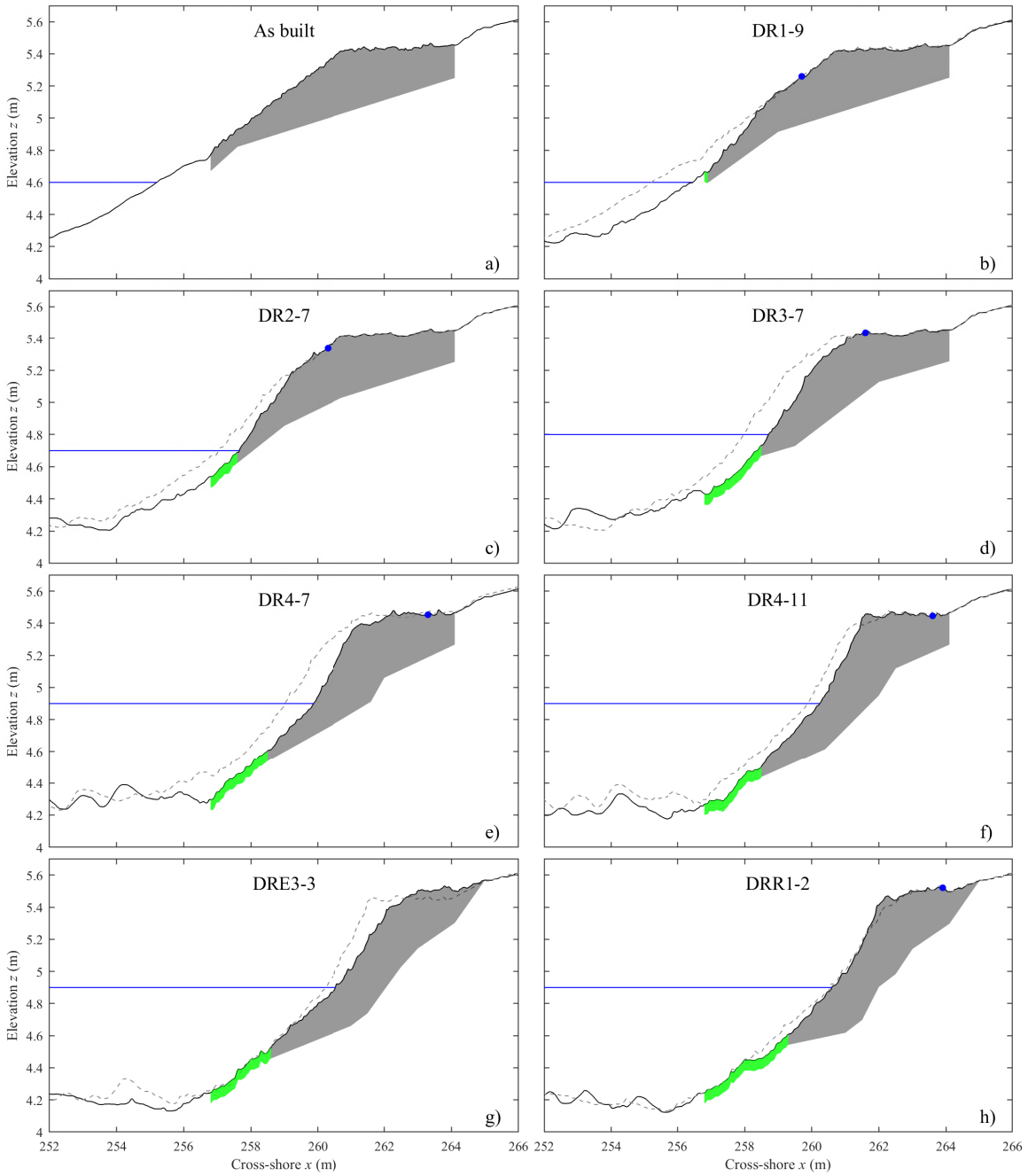

Figure 3.4: Shape of the dynamic cobble berm revetment, showing: (a) revetment shape as built, DR1-0; (b) revetment shape after 7 hours of testing at z_{wl} = 4.6 m water level, DR1-9; (c) revetment shape after 7 hours of testing at z_{wl} = 4.7 m water level, DR2-7; (d) revetment shape after 7 hours of testing at z_{wl} = 4.8 m water level, DR3-7; (e) revetment shape after 7 hours of testing at z_{wl} = 4.9 m water level, DR4-7; (f) revetment shape after 17 hours of testing at z_{wl} = 4.9 m water level, DR4-11; (g) revetment shape after the 2 erosive cases of the resilience test, DRE3-3 (5 hours); (h) revetment shape after the recovery case of the resilience test, DRR1-2 (2 hours). The grey areas represent the part of the revetment composed of cobble only (no mixing with sand). The green layer areas represent a single layer of cobble mixed with sand. The boundary between the grey and green shading corresponds to the toe of the primary revetment volume. The blue dot represents the maximum cross-shore position exceeded by 2 % of wave runup. The dashed line shows the surface of the revetment as on the previous panel.

occurring underneath the structure as the backwash percolates through it. In the meantime, it was observed that cobbles were being pushed over the crest, rolling upward and landward through rollover transport. It is suggested that this rollover transport counter-acts the

sinking process, maintaining the crest at an almost constant elevation with a little gain in elevation at the end of DR4 (Figure 3.5az. Without this rollover transport it is hypothesised that the structure crest would be much lower. It is unclear at present what are the main drivers of this sand erosion. Nonetheless, this sinking process needs to be considerate for revetment design and will be further discussed in Section 3.7. Overall, sand erosion and rollover transport led to an increase in total revetment height from 0.68 m to 0.95 m, and a stabilisation of the revetment length around 5.6 m (Figure 3.5c).

After 38 hours, a series of erosive tests with increasing wave energy were completed as part of the resilience testing, followed by a two hour case using the standard wave condition (Table 3.2). At the end of DRE3 (z_{wl} = 4.9 m), increased runup was measured along with more frequent overtopping which spread the cobbles beyond the original landward limit of the revetment through rollover transport. This process flattened the revetment to a 1:3.15 slope and caused the overall length to increase to 6.4 m (Figure 3.4g;Figure 3.5c). It was observed (see Section 3.4.2) that cobbles from the toe were pushed onto the crest and beyond, thus the single cobble layer lengthened (Figure 3.4g). The crest, centroid and toe of the revetment retreated by 1.40 m, 0.10 m and 0.35 m respectively (Figure 3.5b). The crest

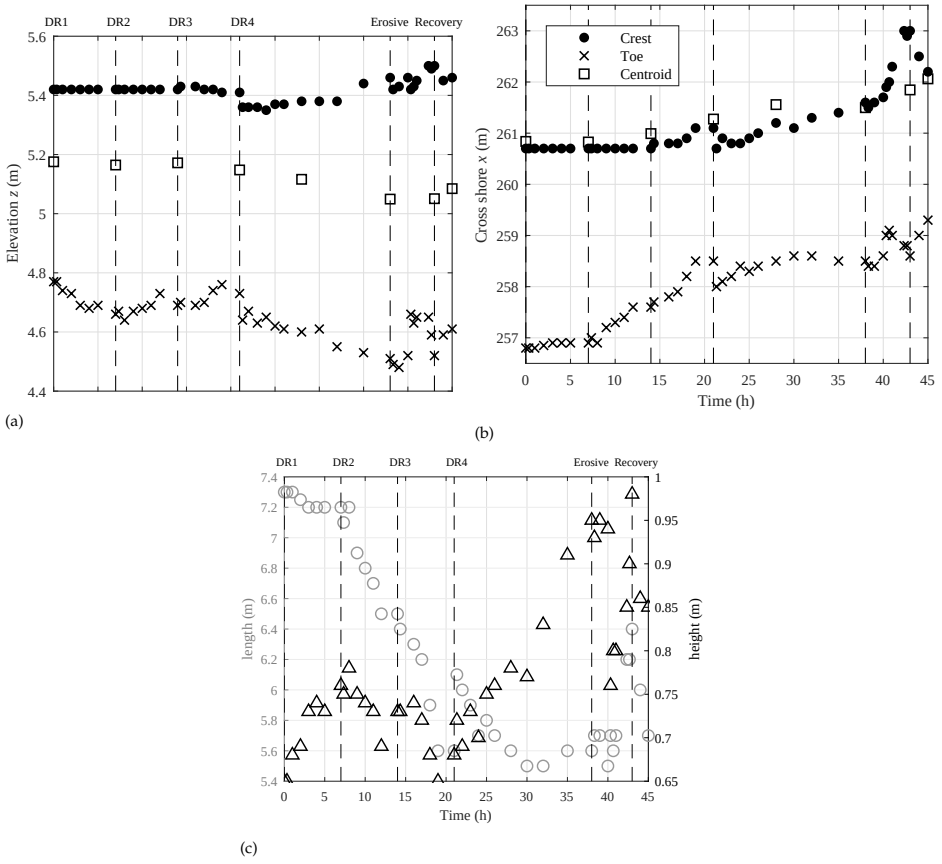

Figure 3.5: (a) Vertical, and (b) horizontal evolution of the crest, toe and centre of gravity of the revetment through time. The crest (dots) height is defined as the averaged elevation of the flat area at the top of the revetment. The toe (cross) is defined as the toe of the cobble body, corresponding to the toe of the grey area on Figure 3.4. The centroid (square) is defined as the centre of mass of the cobble body. Each cross and dot corresponds to a run. The squares correspond to the end of the runs showed in (Figure 3.4). (c) Evolution of the cross-shore extent (length) and height of the revetment through time. Each grey circle (length) and black square (height) corresponds to a run.The dashed lines marks the beginning of a new water level (*e.g.*, DR1, DR2,...) and resilience test cases (*e.g.*, erosive and recovery).

became higher by 4 cm, whereas the centroid remained at the same elevation (Figure 3.5a). The toe elevation was highly variable, but ended at the same position as at the end of DR4, at $z = 5.52$ m. Overall, the height of the revetment increased to 0.98 m respectively, but was variable (±10 cm) throughout the runs.

The recovery test (DRR) was observed to reshape the structure to its previous shape and slope of 1:2.3 (Figure 3.4h). The maximum $R_{2\,\%}$ limit was located slightly further inland than at the end of DR4, at $x = 263.9$ m (Figure 3.4f). A lot of material was brought upward from the toe during the previous energetic conditions, making it available for rollover transport. As a result, both the toe and the centroid increased in elevation to their final position at $z = 4.61$ m and $z = 5.08$ m respectively (Figure 3.5a). They also both retreated, by 0.20 m for the centroid and 0.7 m for the toe (Figure 3.5a). The crest location ended up slightly lower and more seaward than its previous position. This is mainly due to the method of measuring its position, which averaged the elevation of the flat area at the top of the revetment. Figure 3.5. The revetment is back to what seems to be its equilibrium length of 5.7 m, for a height of 0.85 m (Figure 3.5c).

3.4.1.3 Revetment stability

The global changes in revetment profile observed in the previous section are the integrated result of smaller and rapid changes in beach profile. This can be observed and measured by the Lidar on a wave by wave basis. As described in Section 3.3.4.3, the gross rate of volume change, $\overline{dV}$ and the net rate of volume change, dV_{10} were calculated over the revetment area using the Lidar data. It is important to note that these estimates include the elevation changes due to sand erosion occurring underneath the structure.

Figure 3.6a and Figure 3.6b indicate that overtopping started to occur during test DR3 ($z_{wl} = 4.8$ m) but rates remained smaller than 10 %. A sudden increase to around 50 % of waves overtopping the structure crest was observed during DR4 when the water level was raised to $z_{wl} = 4.9$ m.

The net rate, dV_{10} was observed to increase with each water level increment as more of the revetment was exposed to swash flows (Figure 3.6b). During DR4, although overtopping remained around 50 %, the net rate was observed to decrease approximately linearly to around $0.005\,m^2/s$. It is suggested that this is evidence that the revetment is approaching an equilibrium and this will be discussed further in Section 3.7. During the erosive runs of the resilience testing, the net rate increased, however when the standard wave case was used again in run DRR1, a net rate of $0.005\,m^2/s$ was measured in agreement with that at the end of DR4.

The gross rate of change throughout runs DR1 to DR4 are relatively stable at approximately $0.07\,m^2/s$, with small changes occurring with each water level increment as the position of the swash zone changes (Figure 3.6a). During the energetic runs of the resilience testing (DRE1, DRE2, DRE3) higher rates of gross change are measured. However when the wave energy is reduced again to the standard test case (DRR1), the gross change rate returns to approximately $0.07\,m^2/s$ suggesting that this gross rate of change is primarily

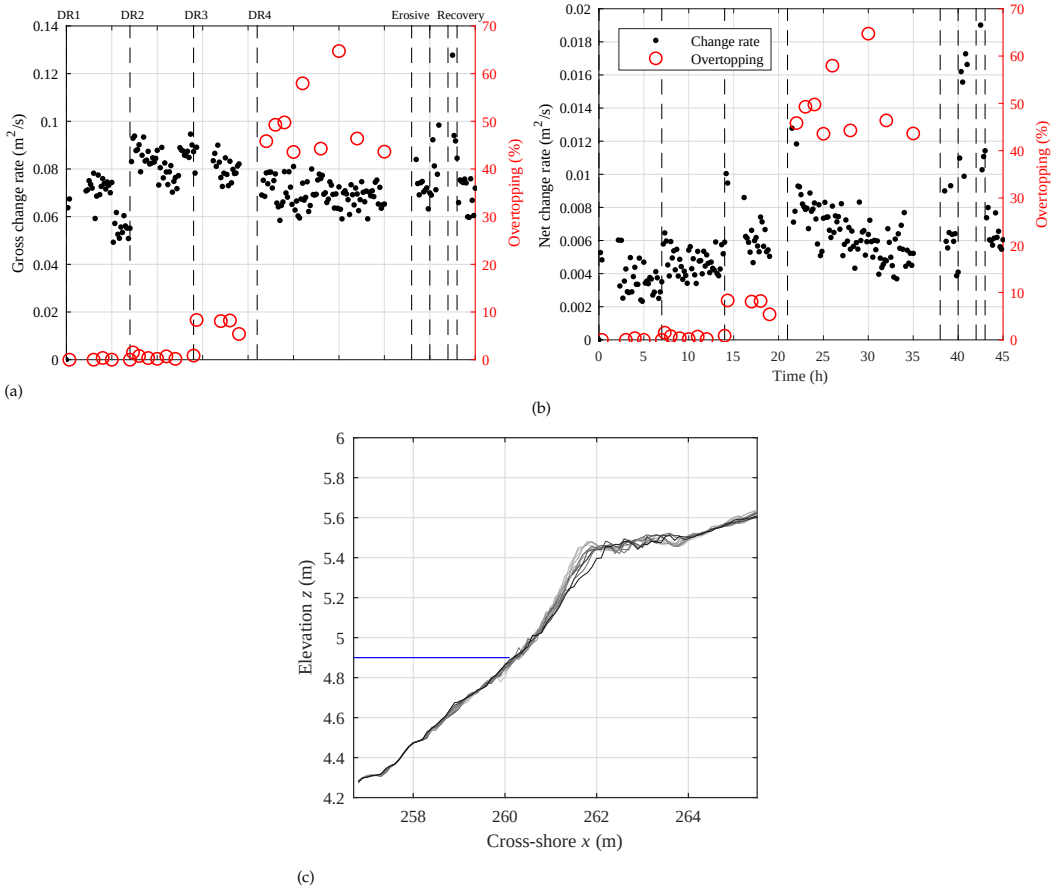

Figure 3.6: *Left axis*: (a) Gross rate of volume change per second $\overline{dV}$ (black dots): The change of revetment volume per metre width was calculated every 6 seconds (so roughly every wave), as the sum of the absolute difference between consecutive profiles. An average value was then calculated every 10 minutes to give the average per second volume change over this period. The percentage of overtopping is shown by the red circles. (b) Net rate of volume change per second dV_{10} (black dots): The change of revetment volume per metre width was also calculated every 10 minutes, as the sum of the absolute difference between 2 bed profiles. A mean rate of change per second over the whole 10 minute period was then calculated. The dashed lines marks the beginning of a new water level (*e.g.*, DR1, DR2,...) and resilience test cases (*e.g.*, DRE1, DRR1,...). The percentage of overtopping is shown by the red circles. (c) Profile of the revetment plotted each 5 minutes for DRE2 (1h test). Light grey corresponds to the beginning of the run, and dark the end.

dependent on the wave energy. This is supported by the fact that there appears to be no effect of the high rates of overtopping during DR4 on the measured gross rates of volume change.

Figure 3.6 indicates that the gross rate of volume change is an order of magnitude larger than the net rate. This suggests that the revetment surface is highly dynamic, moving significantly with every wave, while the overall shape of the revetment remain stable.

During the resilience testing it is noticeable that the revetment shape (including the front slope and crest position) responds rapidly to changes in wave conditions. Figure 3.6c shows the profile of the revetment every 5 minutes during test DRE2 where it is observed that the top of the slope flattens, leading to a landward migration of the crest over just 1 hour. A clear relationship was identified between the revetment face gradient and the offshore incident wave steepness (Figure 3.7), with the slope increasing with offshore incident wave

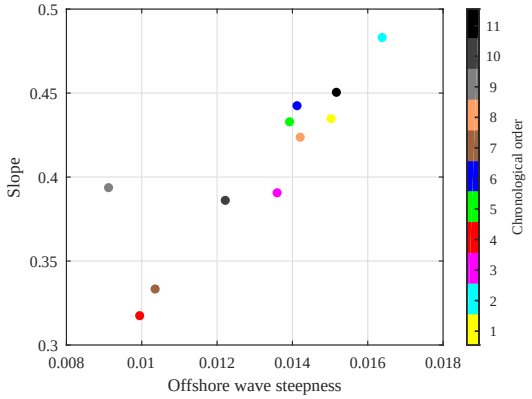

Figure 3.7: Revetment face slope as a function of the offshore wave steepness. The colours represent the chronological order of the observed slopes.

steepness. This was not influenced by the previous state of the revetment and suggests that an equilibrium revetment slope exists for a given wave condition, at least for this type of material.

3.4.2 Cobble tracking

Instrumented cobbles were initially placed along the centreline of the flume, at different elevation within the revetment (layers, see Section 3.3.2) and in groups of 3 – except at the toe where 7 cobbles were placed. This initial setup can be seen in Figure 3.8, and corresponds to the circle at $t = 0$ ('Start DR1'). The position of the instrumented cobbles was then measured after each change in water level or wave conditions (Figure 3.8). Note that the cobbles in the top and bottom layers extended to the initial revetment toe, however the first group of cobbles in the middle layer was 1.2m landward of the toe. Additionally the cobbles in the middle and top layers extended further landward than the bottom layer

Figure 3.8a shows that 4 of the cobbles initially placed around the toe ($x = 257\,\text{m}$ to $x = 258.2\,\text{m}$) moved offshore between $x = 252.8\,\text{m}$ and $x = 255\,\text{m}$ over the course of the experiment and did not return to the revetment structure. These cobbles were lost offshore primarily during DR1 and account for 4 % of the total number of instrumented cobbles. Figure 3.8a also indicates a second group of cobbles between $x = 256.2\,\text{m}$ and $x = 257.4\,\text{m}$, which were moved offshore of the initial toe during the experiment and formed the single layer of mixed sand and cobbles discussed in Section 3.4.1.2 (see green region in Figure 3.4). Of these cobbles some remained in this region for the remainder of the experiment, while some were subsequently transported landwards back onto the main revetment structure. This single layer area is also visible in Figure 3.8b and Figure 3.8c.

Figure 3.8 shows that landward cobble transport was often characterised by large cross-shore 'jumps' whereas seaward cobble transport is characterised by more progressive movements. There is also evidence that once cobbles were transported over the crest, they tended to remain there causing cobbles, particularly those initially in the top layer, to collect on the crest over the course of the experiment. Figure 3.8 also shows that this rollover transport was intensified with wave energy, with the energetic runs of the resilience test mainly causing landward transport. While cobble movement is most evident in the top

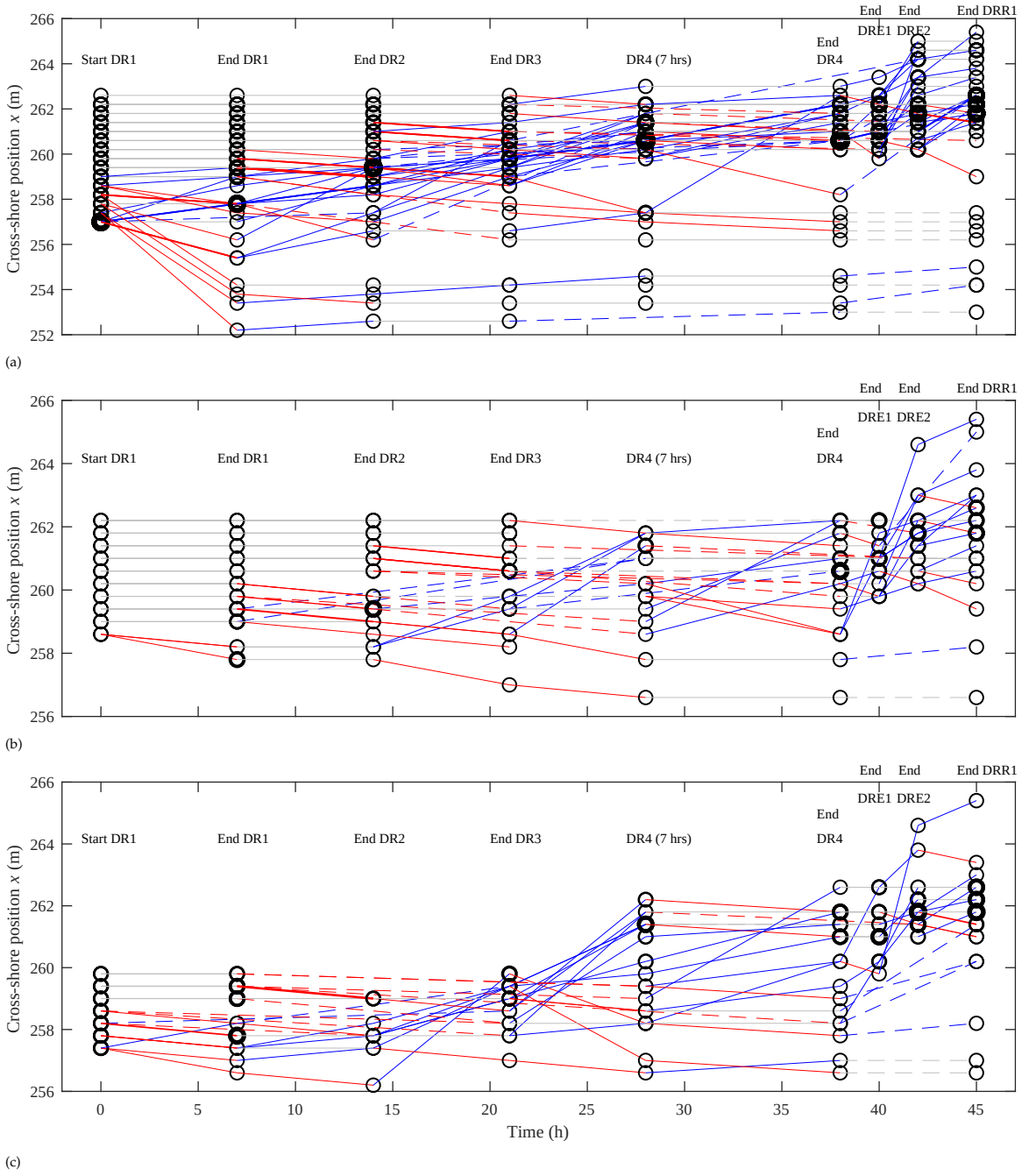

Figure 3.8: Cross shore position of the 97 tagged cobbles as a function of time, and for the three different layers (Section 3.3.2): (a) top layer; (b) middle layer; and (c) bottom layer (sand-gravel interface). The position of the cobbles was measured to the nearest 0.4 m in the cross-shore direction at the end of every water level increment and after each resilience test (except DRE3). The black circles represent the instrumented cobbles at each 0.4 m cross-shore increment and the thickness of the circle is relative to the number of cobbles at each location. Plain red lines correspond to seaward transport. Plain blue lines correspond to landward transport. Plain grey lines correspond to no transport. The thickness of the lines is relative to the number of cobbles moving along a particular path. The dashed lines indicate that a cobble was not detected for at least one detection survey, but was found again later. The same colour and thickness principles apply for the dashed lines.

layer as expected, all cobbles in the mid and bottom layers were mobilised over the course of the experiment as they became directly exposed to swash once cobbles previously present on their seaward side were transported landward. Figure 3.8 indicates that most cobbles in all layers were initially transported seaward a short distance, before moving landward.

A possible reason for this is that cobbles initially rolled seaward down the revetment slope under gravity before being pushed landward by wave runup. As a result, the overall transport motion appeared to be dominated by landward transport.

Overall, at the end of DR4, 74 (76.3 %) cobbles were detected and of these, 42 (56.7 %) cobbles had moved landward (upward), 28 (37.8 %) had moved seaward (downward) from their original position and 4 (5.5 %) cobbles remained at their original locations. A total of 23 cobbles (23.7 %) were not detected: they could have been deeply buried within the structure, or the their signal might have interfered with another one, or they could have simply been missed during the survey.

At the end of the resilience tests, 81 (83.5 %) cobbles were detected and of these, 59 (72.8 %) cobbles had moved landward (upward) and 19 (23.5 %) had moved seaward (downward) from their original position and 3 (3.7 %) cobbles had remained at their original locations. A total of 16 (16.5 %) cobbles were not detected.

3.4.3 Wave Runup

Figure 3.9 shows a comparison of the measured 2 % exceedance vertical ($R_{2\%}v$) and horizontal ($R_{2\%}h$) runup limits for each run and water level during phase SB and DR (the value is given with respect to the used water level). The presence of the revetment reduced the vertical runup by 17 %, 20 %, 27 % and 39 % for DR1, DR2, DR3 and DR4 respectively (Figure 3.9a). It is evident that for Phase SB, there is a direct relationship between $R_{2\%}v$ and the horizontal runup extent – *i.e.* as the water level rises, the vertical ($R_{2\%}v$) and horizontal ($R_{2\%}h$) runup increase. This is not the case for Phase DR because the flat revetment crest leads to a physical limit for the runup height ($R_{2\%}v$) but has a smaller influence on horizontal excursion ($R_{2\%}h$). This is particularly noticeable during DR4 when there is a reduction in $R_{2\%}v$ but the horizontal excursion continues to increase. Comparing Phases SB and DR, the presence of the revetment reduced the horizontal runup by 2.4 m, 3.3 m, 4.3 m and 4.9 m for DR1, DR2, DR3 and DR4 respectively. It seems that the horizontal runup is minimised when the interaction between swash, cobbles and interstices is maximised, as is the case during DR4. In addition, the coefficient of reflection is at its maximum during DR4 and at its minimum during SB4. Therefore, the total energy reaching the beach is smaller for DR4 than SB4, and this can explain the trend of runup differences between the 2 phases.

3.4.4 Shoreline retreat

Figure 3.10 shows the evolution of the horizontal position of: (1) the intersection between the water level and sand beach during Phase SB, (2) the intersection between the water level and revetment surface during Phase DR, (3) the intersection between the water level and sand interface beneath the revetment during Phase DR (Figure 3.10a; (4) the berm, taken as the highest point on the beachface (Figure 3.10b). The locations of these interfaces are shown at the end of each water level increment and after the beach has received the same amount of energy from waves within the resilience test (the resilience test being different for each phase). For both the measured shoreline and sand interface underneath the structure, the presence of the revetment slowed down their retreat under wave action.

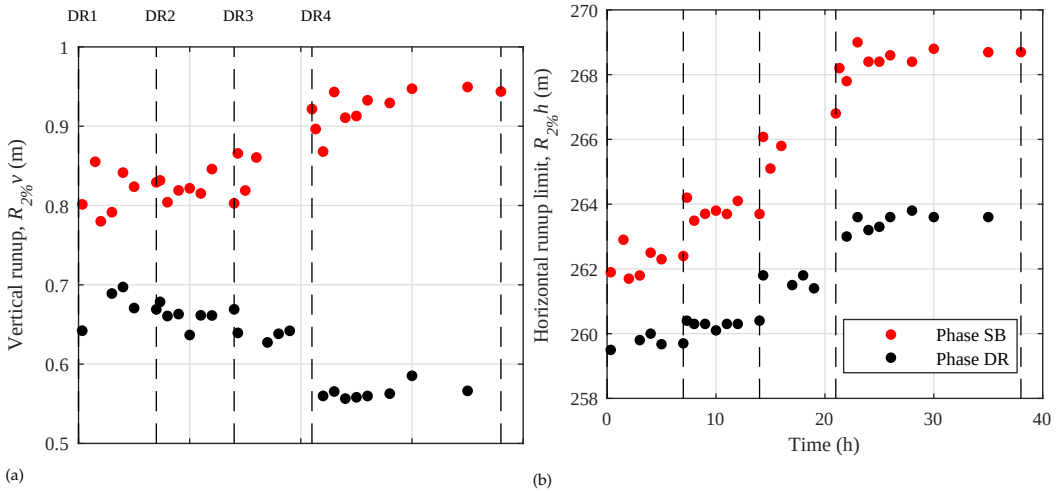

Figure 3.9: Comparison of (a) the $R_{2\%}v$ vertical runup height and (b) $R_{2\%}h$ horizontal runup limit for Phase SB (red dots) and Phase DR (black dots). Note that values from the resilience tests are not shown. The dashed lines marks the beginning of a new water level (*e.g.*, DR1, DR2,...).

For Phase DR, the sand interface under the revetment was interpolated from *in-situ* measurements, and the estimated sand shoreline is presented in Figure 3.10a. The sand depletion at the beginning of DR1, corresponding to the manual adjustment of the slope before the construction of the revetment, is evident (see Section 3.3.3.2). Despite this lack of sand at the beginning of the revetment testing, the sand interface retreated more slowly during Phase DR than during Phase SB. Indeed, even though the sand interface at the start of DR1 starts 0.8 m landward of that at the beginning of SB1, the final position shown in Figure 3.10a is 0.5 m further seaward for Phase DR. The ratio of the volume of sand on the sub-aerial beach for Phase DR to that for Phase SB is 1.0673 at the end of DR4/SB4, and 1.0964 at the final position shown in Figure 3.10a, meaning that there is respectively 6.73 %

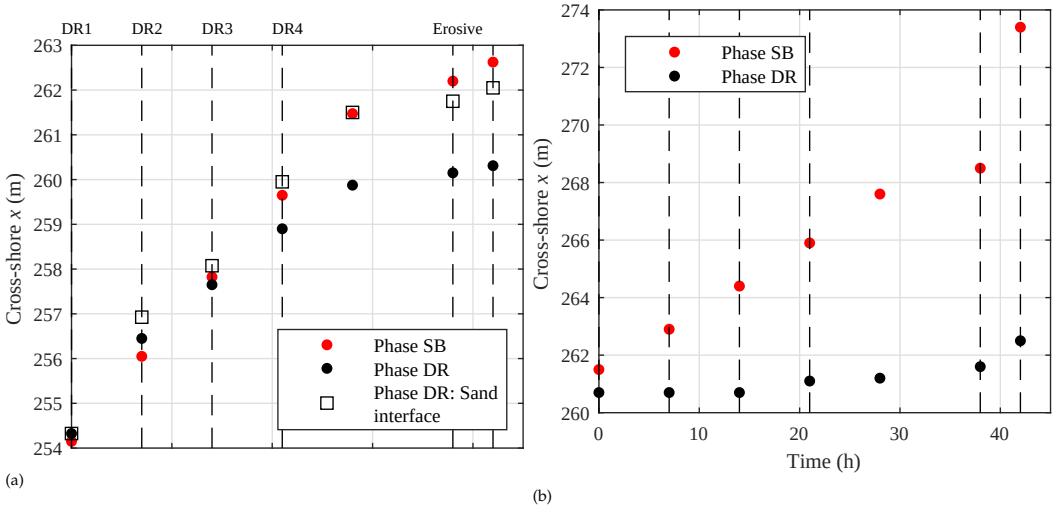

Figure 3.10: a) Comparison of the evolution of the horizontal position of: *red circle*: the intersection between the water level and sand beach during Phase SB; *black circle*: the intersection between the water level and revetment surface during Phase DR; *black square* the intersection between the water level and sand interface beneath the revetment during Phase DR. The sand interface under the revetment is obtained from *in-situ* measurements which were interpolated to estimate the position of the sand surface. The dashed lines marks the beginning of a new water level (*e.g.*, DR1, DR2,...) or resilience test case (*e.g.*, erosive). b) Comparison of the evolution of the berm position during Phase SB (red dots) and Phase DR (black dots).

and 9.64 % more sand on the sub-aerial beach when the revetment is present. Similarly, the berm position moved further landward during Phase SB than Phase DR (Figure 3.10b). The revetment limited the total berm retreat to 2 m while the unprotected beach experienced a total retreat of about 10 m. The smaller berm retreat observed during Phase DR is a primary reason for the significant reduction in horizontal runup excursion discussed above.

3.5 Discussion

As with all flume experiments, the 2D nature of this experiment brings some limitations. Longshore sediment transport, short crested waves and oblique waves could not be tested, and therefore their impact on the processes presented in the results could not be explored. Longshore sediment transport, which is present on most coastlines, is expected to have an impact on cobble movement and the long-term resilience of dynamic revetments. However, at most locations it is expected that cross-shore processes will most strongly influence the revetment evolution during storms, as welll as the sediment transport at the sand-cobble interface. It is suggested that future work should investigate the effect of longshore processes on composite beaches and dynamic revetments in the field. In particular, longshore transport of cobbles should be considered when designing dynamic cobble berm revetments for coastal protection and a replenishment programme would likely be required to maintain structure volume over time. The rate of replenishment can potentially be estimated by using one of the longshore transport equations developed for gravel (Kamphuis, 1991; CERC, 1984; van Wellen et al., 2000; McCarroll et al., 2019) or for sand, gravel and shingle (Tomasicchio et al., 2013, 2015; van Rijn, 2014). Furthermore, it is suggested that future efforts focus on the development of a numerical model for composite beach and dynamic revetment. An initial investigation into modelling composite beach behaviour using the XBeach-G gravel beach model is presented by McCall et al. (2019), which highlighted the importance of accurately representing the sand erosion happening within the cobble berm to obtain robust predictions.

Figure 3.4 showed the global behavior of the dynamic cobble berm revetment as a coherent structure. The core body of the revetment represented in grey is always composed of at least 87 % of its original volume. Therefore, the retreat of the crest, toe and centroid of the revetment shown in Section 3.4.1.2 represents the retreat of almost the whole structure. This retreat was driven by two main processes:

1. the erosion of sand underneath the structure caused by water percolating through the cobbles and transporting sand seaward during swash backwash. This process caused the revetment to sink and steepen.
2. the rollover transport: RFID demonstrated that 70 % of the instrumented cobbles ended up landward of their original position by the end of the resilience testing, and a large number of these were transported onto the revetment crest.

While rollover transport is a well-known phenomena for gravel beaches and berms (Lorang, 1991; Allan et al., 2006; Almeida et al., 2015), the sand erosion phenomena oc-

curring underneath the cobbles has not been observed during monitoring of previously installed cobble berm revetments in the USA (Downie and Saaltink, 1983; Lorang, 1991; Allan et al., 2006; Komar and Allan, 2010; Allan and Gabel, 2016) and it is not an obvious feature on composite beaches. However, the lack of long term monitoring or field experiments on existing dynamic revetments and composite beaches partly explains the absence of information regarding this process. It is important to note that existing monitoring has only focused on surface changes and volume losses, with no measurements of the sand-cobble interface beneath the cobbles. However, van Gent (2010) undertook a laboratory experiment investigating the behaviour of a beach profile consisting of sand overlain by a uniform layer of gravel (porosity = 0.4) which extended the full length of the profile (test series S1). A profile shape similar to that observed during DR4 developed with an accretive berm and erosion below the SWL. However, no observations of the evolution of the sand-gravel interface were reported and it is possible that sand erosion underneath the gravel may have contributed to the observed erosion around the SWL.

Under water level increases, the sandy beach during Phase SB eroded as it evolved toward a new equilibrium (Figure 3.3c). A similar process appears to be happening to the sand underneath the revetment in Phase DR (Figure 3.4), with the sand profile beneath the revetment evolving in a similar manner to the sand beach in Phase SB but at a slower rate. Note that in the present experiment, in order to get significant interaction between waves and cobbles, the revetment was placed at the location of the natural sand berm developed during DR0. Therefore, it was placed in an area which is prone to erosion as the water level is increased. As a result, the erosion demand occurring between $x = 255$ m and $x = 266$ m was at the location of the revetment. Similar sand erosion, as well as accretion, may occur in the field under changing hydrodynamic conditions. Future field work is required to understand how the combination of sand dynamics and rollover transport drives the overall change of a cobble berm over time.

As it retreated, the revetment remained a coherent structure with the majority of the individual cobbles remaining within the primary structure. Thus, despite being composed of relatively small cobbles which moved with every wave, the overall shape of the revetment structure was retained at all times during testing and the structure is considered dynamically stable. At the end of the resilience testing, the main body of the revetment retained 90 % of its original volume. In addition, the single mixed layer of sand and cobbles, represented in green on Figure 3.4, increased through the experiment and at the end of the resilience test, this layer accounted for a further 9 % of the original volume. As the revetment retreated, this layer remained attached to the structure, and is directly available to form part of the revetment under accretive conditions. Nevertheless, it is conservative to assume that this material is not part of the active protection anymore. The remaining 1 % is considered as lost offshore. Thus the results from the current experiment suggest that assuming at least 10 % loss of cobble volume from the main structure due to

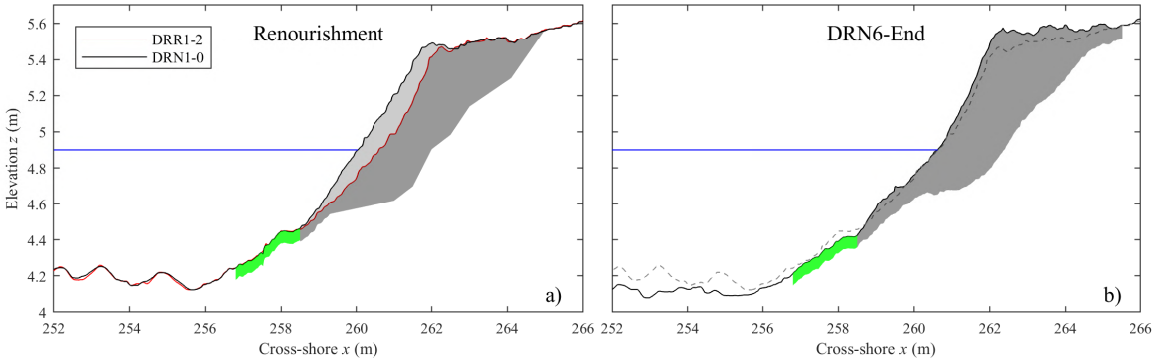

Figure 3.11: Profile of the dynamic cobble berm revetment after adding an extra 2.50 m^3 of identical material (renourishment) and running different wave conditions at 4.9 m water level: (a) the revetment shape after the addition of the extra material to the front slope, DRN1-0; (b) the revetment shape after all the runs (Table 3.3), DRN6.

cross-shore processes is advisable. Of course further, temporary cross-shore loss of cobbles following large energy events may also occur but this has not been observed in the current testing, even under energetic waves with large overtopping rates.

The observed dynamic stability of the revetment was also illustrated in Figure 3.6 where it was observed that the gross rate of volume change (per metre width), $\overline{dV}$ was 10 times bigger than the net rate dV_{10}. The relatively large gross rate of change suggests that there was significant cobble movement on a wave-by-wave basis, hence the structure was dynamic. However, the net rate of change was small, which means the overall effect of this large gross change (cobble activity) over many waves was small, leading to minimal overall impact on the revetment morphology. This observation is directly comparable to the sandy beach field measurements of Blenkinsopp et al. (2010a) who demonstrated that the volume of sediment transported by single waves can be comparable to the net transport which occurs over several hours. This suggests that beaches can be very dynamic over short timescales, but over multiple waves, cross-shore sediment fluxes approximately balance leading to minimal net transport. Here, a large value of the gross volume change rate and a small value of net volume change rate would indicate that the revetment volume fluctuates significantly over short timescales, but that these changes balance out over longer timescales and lead to minimal overall net volume change in a 10 minute period. Section 3.4.1.3 showed that during runs DR1 to DR4, the gross and net rates of change remain relatively constant with only small changes each time the water level was changed and more of the revetment was exposed to swash processes. There was some evidence that rates of change decreased with time at each water level, regardless of the percentage of overtopping. This suggests that the revetment was approaching an equilibrium with the wave and water level conditions – this was most evident for run DR4 (Figure 3.6).

Beyond demonstrating that the transport of cobbles was predominantly landward and hence upward, RFID detection showed a rotational motion of particles within the revetment body. Within the parts of the revetment most strongly influenced by swash motions (toe and lower slope), the instrumented cobbles tended to move seaward by

rolling down the slope due to both backwash flows and gravity. Once they reached the active area of the toe and seaward of the toe, they were pushed landward by the uprush and transported onto the structure and over the crest through rollover transport. After further wave actions and mobilisations, cobbles on the upper part of the revetment face became buried by newly transported cobbles, and were eventually exposed as the face of the revetment retreated. It is important to bear in mind that the rollover process can only occur because of the revetment porosity, which yields to a weaker backwash than uprush. This overall rotational motion occurs within the retreating structure, and the combination of gravity and swash effectively induces the overall landward motion.

Accretion of the crest would be expected under rollover transport, particularly as the water level increased and more cobbles were transported onto the crest, however this was counterbalanced by the observed loss of sand from beneath the revetment during the first 28 hours. During DR4, the rate of rollover transport increased due to higher overtopping rates, leading to only a small, 4 cm increase in crest height during this water level increment. While loss of sand is thought to be the major reason for the minimal increase in crest height, van der Meer (1988) and Powell (1990) found that for gravel beaches, a low value of the grading coefficient D_{85}/D_{15} (corresponding to well-sorted material as used here) leads to a lower crest elevation. During DRE1, DRE2 and DRE3 (energetic conditions of the resilience test), landward cobble transport was significantly intensified (Figure 3.8). As a result, cobbles were pushed on top of the revetment and beyond (Figure 3.4g). This suggests that rollover transport may be expected to maintain and indeed increase crest elevation (to keep a positive freeboard) during storm events, particularly if sand loss from beneath the structure is a minor issue as is generally observed in field monitoring of existing composite beaches.

Rollover transport during DR4 and the resilience testing caused an accumulation of material on the revetment crest and a relatively small revetment thickness on the front slope. In response to this, the revetment slope was opportunistically “nourished" by adding an extra 2.50 m^3 of cobbles on the front slope, as shown on Figure 3.11. Following this renourishment, the revetment response was measured for a range of different wave conditions during test series DRN (Table 3.3). Figure 3.11a shows the revetment after nourishment and Figure 3.11b at the end of test series DRN (Table 3.3). During these tests, the crest retreated by 0.10 m, moving from $x = 262.2$ m to $x = 262.3$ m (Figure 3.12b). The toe maintained a constant cross-shore position but moved down slightly (Figure 3.12). However, due to rollover transport onto the crest, the centroid moved 0.47 m landward (Figure 3.12b) and 0.07 m higher (Figure 3.12a). The crest elevation increased from $z = 5.46$ m to $z = 5.56$ m, increasing the height of the revetment (Figure 3.12a). With the extra material, the crest of the revetment increased in overall height due to rollover transport, better maintaining its relative elevation to water level than prior to nourishment. This suggests that the designed volume of the revetment may have been too small, meaning not enough material

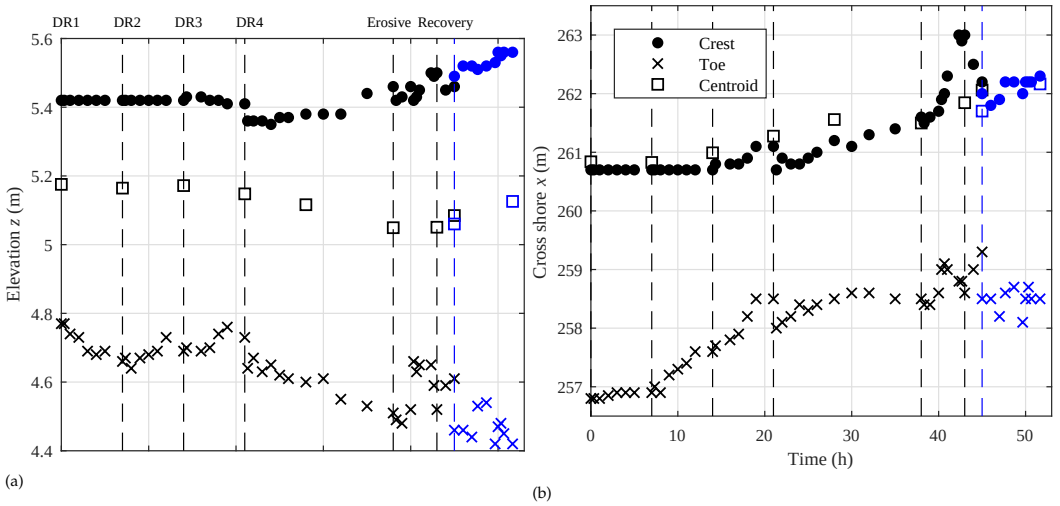

Figure 3.12: Evolution of the crest, toe and centre of gravity of the revetment through time, in terms of: (a) elevation; (b) cross-shore position. The crest height (dots) is defined as the average of the elevation of the flat area at the top of the revetment. The toe (crosses) is defined as the toe of the cobble body, *i.e.* the seaward limit of the grey area in Figure 3.4 and Figure 3.11). The centroid (squares) is defined as the centre of mass of the cobble body. Note that until 45 hours, the data shown in black is identical to that shown in Figure 3.5 with the extra blue points indicating post-renourishment values. The dashed lines mark the beginning of a new water level (*e.g.*, DR1, DR2,...), resilience test cases (*e.g.*, erosive and accretive) and the blue dashed line indicates the time of renourishment.

was available to maintain the front slope and increase crest elevation due to rollover. It is suggested that the critical mass criteria defined in Ahrens (1990) may be suitable for estimating a minimum stable design volume (V_d).

The increase in reflected wave signal over the course of water level increases likely contributed to the local erosion at the toe of the revetment between $x = 253$ m and $x = 258$ m, shown in Figure 3.3. Similar localised erosion was also observed by Beuzen et al. (2018) in front of a seawall and rubble mound revetment for a rising water level, and interpreted as a transfer of the erosion demand from the sub-aerial beach to the available sand in front of the structure. It is likely that increased wave reflections would lead to more suspended sediment seaward of the revetment toe and in a 3D situation, this sand would become available for longshore transport. However, the total amount of sand available for longshore transport is reduced due to the presence of the revetment which has been shown to retain sand on the subaerial beach.

The presence of the dynamic cobble berm revetment reduced the vertical (Figure 3.9a) and horizontal (Figure 3.9b) runup. It was also seen that this reduction was enhanced as the water level was raised – *e.g.*, the horizontal runup was reduced by 2 m during DR1 but by 4 m during DR4. This reduction was likely due to the swash occurring on the porous cobble slope. The measured $R_{2\%}$ (Figure 3.9a) runup was always smaller than the calculated value of 0.72 m used for the design of the crest elevation using the pure gravel beach formula developed by Poate et al. (2016). This suggests that under the same wave conditions, a beach with a dynamic cobble berm revetment (or a composite beach) is likely to experience smaller runup events than a pure gravel beach (and also a sandy beach). This can be

qualitatively explained by the fact that a composite beach is composed of a dissipative sandy surf zone and a reflective, dynamic and porous cobble beach face, whereas a gravel beach has a less dissipative surf zone. At present, no specific runup equation for composite beaches exists, and such an equation is likely to be complicated due to the variability in the position of the cobble berm toe, relative sand and cobble gradients and cobble sizes. Further measurements of runup on composite beaches and dynamic revetments would be beneficial, and aid the development of an approach to estimate wave runup to inform revetment crest elevation design.

Due to the flat crest of the revetment, the vertical runup height is not considered representative of the extreme swashes (Section 3.4.3). The horizontal runup limit which is more representative of the swash excursions, was reduced by the presence of the revetment (Figure 3.9b). Therefore, as the water level increased (*e.g.*, during a storm surge) the beach behaved more and more like a composite beach and the runup height was reduced accordingly. It is therefore considered that under increasing water level and energetic wave conditions, the crest (hence the revetment) up-graded to a higher level of protection than it was at before (relative to WL3 for instance). Figure 3.10a showed that the presence of the revetment slowed down the shoreline retreat as well as the underlying sand interface retreat (the sand is either protected from erosion by the cobbles, or gets deposited by the swash percolating through the cobbles and accumulates within the revetment; further field work is required to fully understand this process). However, differences remain between these two types of retreat and it highlights the fact that the shoreline may not be a suitable parameter to compare the retreat. Figure 3.10b showed that the sandy beach berm retreated 8 m more than the cobble berm under the same wave energy and water level forcing (Figure 3.3). It therefore appears that assessing the retreat using the berm position is more appropriate for a dynamic cobble berm revetment. In addition, the berm retreat is directly linked to the horizontal runup excursion shown in Figure 3.9b (also seen in Figure 3.3).

Dynamic cobble berm revetments effectively create and artificial composite beach and are characterised by an inherent dynamic stability. The 2D results do not show obvious localised scouring or increase erosion of the sandy component of the beach through cross-shore processes. Beyond the performance of this structure regarding coastal protection, it is important to mention that dynamic cobble berm revetments are likely to be low cost structures compared to traditional coastal protection structures, particularly where cobbles can be locally sourced. They do not require any foundation preparation or specialist equipment or expertise for installation which makes them an interesting alternative for developing nations.

3.6 Preliminary design guidelines

The data collected in this experiment are not sufficient to provide complete revetment design guidance. Only one type of material, one revetment position and initial geometry

and a narrow range of hydrodynamic conditions were tested. In addition, the 2D nature of the flume experiment limited the analysis to cross-shore processes only. Nevertheless, some basic design suggestions can be drawn from this experiment to be used by practical engineers as the basis for the design of dynamic cobble berm revetments.

The primary objective of a dynamic cobble berm revetment is to limit wave runup and overtopping and to protect the hinterland during extreme storms which are associated with large waves and extreme water levels. For these reasons, dynamic revetments have the potential to provide coastal protection for a wide range of coastlines, ranging from natural habitats to urbanised coasts. The size and volume of the material can be adapted depending on design conditions, from estuaries to open coasts. As observed in the experiment, dynamic revetments do not provide a fixed, hard barrier but evolve and retreat gradually under wave action. As such, any revetment is ideally placed above the natural high tide berm where it will only interact with waves during elevated high tides when waves are relatively large. If sinking of the revetment can be minimised through further research and development, in this configuration the revetment would be expected to evolve, gradually retreat and self-adapt to sea level through rollover transport. To allow this, some accommodation space is required between the initial position of the revetment and the landward asset to be protected.

The crest elevation is a site-specific parameter which is dependent on the predicted wave runup for a given design wave and water level condition. While no wave runup equation for composite beaches or dynamic revetments currently exists, the work presented here suggests that existing gravel beach runup equations provide an overestimate of wave runup and so could be used for conservative design.

To estimate the minimum revetment volume per unit width, the critical mass criteria developed by Ahrens (1990) for artificial gravel beaches is suggested. However, as this criteria has not been robustly tested for dynamic cobble berm revetments, at least an extra 10 % of material should be added to account for cross-shore losses. It is also necessary to account for losses due to gradients in longshore transport which could be estimated using existing gravel beach longshore transport equations (Kamphuis, 1991; CERC, 1984; van Wellen et al., 2000; McCarroll et al., 2019; Tomasicchio et al., 2013, 2015; van Rijn, 2014). Post-construction monitoring of the revetment, combined with estimates of longshore cobble transport should be used to plan cobble renourishments over the life of the revetment.

The results presented here demonstrate that the gradient of the revetment front slope is controlled by the short term wave conditions (Figure 3.7, Figure 3.6c). Thus there is no need to carefully design the gradient of the revetment slope. It is recommended simply that sufficient volume is placed in front of the crest to form the lowest expected gradient based on historical wave steepness data. For conservative design, it is suggested that this

volume should be in addition to the critical mass value calculated using Ahrens (1990).

In the experiment, the revetment was placed by dumping stone and then reshaped to the required profile using a front-end loader and manual profiling. It is suggested that a similar process be used in the field and no specialist equipment is necessary. Indeed, as it was observed that wave action will rapidly reshape the revetment to a new profile after a change in wave conditions, it may be sufficient to simply place the required volume of cobbles to achieve the design crest height and minimum revetment slope and then allow wave action to shape the seaward face of the revetment.

Results from pure gravel beaches (van der Meer, 1988; Powell, 1990) suggest that material with a high grading coefficient, D_{85}/D_{15} should lead to a higher crest. This suggests that it may be beneficial to used poorly sorted material with a lower porosity than used in the current experiment. However, at this stage, no conclusion can be drawn regarding the size, type and shape of the material to be used for given design conditions. Future work is needed to study the performance of different cobble sizes, shapes and sorting for varying wave conditions.

3.7 Conclusion

Dynamic cobble berm revetments are inspired by natural composite beaches, and are expected to mimic their behaviour to provide coastal protection. The few existing examples of dynamic cobble berm revetments presented in Section 3.2.3 motivated the DynaRev large scale laboratory flume experiment, performed at the GWK flume (Germany). Within the limitations of a 2D laboratory flume, this experiment was designed to better understand the behaviour of a dynamic cobble berm revetment, and assess its performance as a coastal protection structure under wave attack and a rising water level.

The dynamic cobble berm revetment demonstrated a remarkable dynamic stability, as cobbles within the structure moved with every wave but the global shape of the revetment remained stable with net the rate of bed evolution an order of magnitude lower than the gross rate. Net changes were predominantly localised in the front face of the revetment, mainly due to the underlying erosion of sand caused by the backwash percolating through the structure. The revetment toe, crest and centroid also retreated landward and moved slightly upward under water level rise. This translation was driven by rollover sediment transport which moved more than 70 % of the instrumented cobbles landward. This rollover transport played a major role in maintaining the revetment elevation, while the sand underneath was washed away due to the high porosity of the material used.

The presence of the dynamic cobble berm revetment reduced the shoreline and berm retreat, decreased the amount of sand moving from the sub-aerial to sub-aqueous beach and significantly reduced the vertical and horizontal runup, hence the potential for erosion of the hinterland. Wave reflection was increased by the presence of the revetment, and this played a role in the erosion of sand seaward of the revetment toe.

Based on this experiment, dynamic cobble berm revetments appear to be a sustainable and affordable option for many locations experiencing coastal erosion where complete protection from coastal hazards is not needed and some coastal retreat is acceptable – *i.e* accommodation space available. Some basic design guidelines are provided as a first step for practical engineers to design dynamic cobble berm revetments. Nevertheless, further research into composite beach and dynamic revetments needs to be done before comprehensive guidance can be provided. Future work includes development of a numerical model that can predict revetment behaviour, field experiments at composite beaches and dynamic revetment sites including measurements of longshore cobble movement, and investigation of different material types, sizes and grading.

Acknowledgements

The DynaRev project has received funding from the European Union's Horizon 2020 research and innovation programme under grant agreement No 654110, HYDRALAB+. Paul Bayle is supported by a PhD scholarship through the EPSRC CDT in Water Informatics: Science & Engineering (WISE).

The authors gratefully thank Matthias Kudella, Stefan Schimmels, and all staff and technicians from the Groβer WellenKanal (GWK) flume for their support before, during and after the DynaRev experiment. They also thank Isabel Kelly and Emily Gulson for their help and enthusiasm during the experiment. Finally, they want to thank William Bazeley, Neil Price, Robert Dyer and David Surgenor from the University of Bath for their technical support during the experiment preparation; and Peter Ganderton from the University of Plymouth for their technical support during the experiment.

References

Ahrens, J. P. (1990). Dynamic revetment. *Coastal Engineering* 138, 1837—1850.

Allan, J. C. and Gabel, L. L. (2016). *Monitoring the response and efficacy of a dynamic revetment constructed adjacent to the columbia river south jetty, Clatsop county, Oregon.* Tech. rep. O-16-07. Oregon Department of Geology and Mineral Industries.

Allan, J. C., Harris, E., Stephensen, S., Politano, V., Laboratory, H., Folger, C., and Nelson, W. (2012). *Hatfield Marine Science Center Dynamic Revetment Project*. Tech. rep. Hatfield Marine Science Center, Oregon State University.

Allan, J. C., Hart, R., and Tranquili, J. V. (2006). The use of Passive Integrated Transponder (PIT) tags to trace cobble transport in a mixed sand-and-gravel beach on the high-energy Oregon coast, USA. *Marine Geology* 232.

Allan, J. C. and Komar, P. (2004). Environmentally compatible berm and artificial dune for shore protection. *Shore and Beach* 721, 9—16.

Almeida, L. P., Masselink, G., Russel, P. E., and Davidson, M. A. (2015). Observations of gravel beach dynamics during high energy wave conditions using a laser scanner. *Geomorphology* 228, 15—27.

Beuzen, T., Turner, I. L., Blenkinsopp, C. E., Atkinson, A., Flocard, F., and Baldock, T. E. (2018). Physical model study of beach profile evolution by sea level rise in the presence of seawalls. *Coastal Engineering* 136, 172—182.

Blenkinsopp, C. E., Bayle, P. M., Conley, D., Masselink, G., Gulson, E., Kelly, I., Ganderton, P., Almar, R., Turner, I. L., Baldock, T. E., Beuzen, T., McCall, R. T., Renier, A., Troch, P., Sanchez, D. G., Hunter, A., Bryan, O., Hennessey, G., McCarroll, J., Barrett, A., Schimmels, S., and Kudella, M. (In review). High-resolution, prototype-scale laboratory measurements of nearshore wave processes and morphological evolution of a sandy beach and dynamic cobble berm revetment. *Scientific Data*.

Blenkinsopp, C. E., Mole, M. A., Turner, I. L., and Peirson, W. L. (2010a). Measurements of the time-varying free-surface profile across the swash zone obtained using an industrial LiDAR. *Coastal Engineering* 57, 1059—1065.

CERC (1984). *Shore Protection Manual*. 4th ed. Vol. 2. U.S. Government Printing Office, Washington, D.C.: U.S. Army Waterways Experiment Station.

Cartwright, A., Brundrit, G., and Fairhurst, L. (2008). *Global Climate Change and Adaptation – A Sea-Level Rise Risk Assessment*. Tech. rep. Cape Town, South Africa: LaquaR Consultant CC.

DeConto, R. M. and Pollard, D. (2016). Contribution of Antarctica to past and future sea-level rise. *Nature*, 591—597.

Dean, R. G. (1973). Heuristic model of sand transport in the surf zone. *Proceedings of engineering dynamics in the surf zone, Institute of Engineers, Australia*.

Dean, R. G. and Dalrymple, R. A. (2002). "Coastal Processes with Engineering Applications". Cambridge University Press. Chap. 3, 35—65.

Downie, K. A. and Saaltink, H. (1983). An artificial cobble beach for erosion control. *Coastal Structure '83*. Reston, Va., American Society of Civil Engineers, 846—859.

Everts, C. H., Eldon, C. D., and Moore, J. (2002). Performance of cobble berm in Southern California. *Shore and Beach* 704, 4—14.

French, P. W. (2001). *Coastal defences : processes, problems and solutions*. London: London : Routledge.

Gourlay, M. R. (1968). *Beach and Dune Erosion Tests*. Tech. rep. M935/M936. Delft Hydraulic Laboratory, the Netherlands.

Howe, D. and Cox, R. (2018). Upgrading Breakwaters in response to sea level rise: practical insights from physical modelling. *Proceedings of the 36th International Conference*.

Hudson, T., Keating, K., and Pettit, A. (2008). *Delivering benefits through evidence. Coast estimation for coastal protection - summary of evidence*. Tech. rep. SC080039/R7. Environment Agency, Bristol: Environmental agency.

Jennings, R. and Schulmeister, J. (2002). A field based classification scheme for gravel beaches. *Marine Geology* 186, 611—228.

Johnson, C. N. (1987). Rubble beaches versus revetments. *Coastal Sediments '87*. Reston, Va., American Society of Civil Engineers, 1217—1231.

Kamphuis, J. W. (1991). Alongshore sediment transport rate. *Journal of Waterway, Port, Coastal and Ocean Engineering* 117, 624—640.

Kirk, R. M. (1992). Experimental beach reconstruction-renourishment on mixed sand and gravel beaches, Washdyke Lagoon, South Canterbury, New Zealand. *Coastal Engineering* 17, 253—277.

Komar, P. and Allan, J. C. (2010). "Design with Nature strategies for shore protection - The construction of a cobble berm and artificial dune in an Oregon State Park". *Puget Sound Shorelines and the Impacts of Armoring—Proceedings of a State of the Science Workshop*. U.S. Geological Survey Scientific Investigations Report 2010-5254, 117—126.

Loman, G. J. A., van Gent, M. R. A., and Markvoort, J. W. (2010). Physical model testing of an innovative cobble shore, Part I: Verification of cross-shore profile deformation. *Third International Conference on the Application of Physical Modelling to Port and Coastal Protection*.

Lorang, M. S. (1991). An artificial perch-gravel beach as a shore protection structure. *Coastal Sediments '91*. Vol. 2. Reston, Va., American Society of Civil Engineers, 1916—1925.

McCall, R., Rijper, H., and Blenkinsopp, C. (2019). Towards the development of a morphological model for composite sand-gravel beaches. *Coastal Sediment 2019*, pp. 1889–1900.

McCarroll, R. J., Masselink, G., Wiggins, M., Scott, T., Billson, O., Conley, D. C., and Valiente, N. G. (2019). High efficiency gravel longshore sediment transport and headland bypassing over an extreme wave event. *Earth Surface Processes and Landforms* 0.

Pilarczyk, K. W. and Boer, K. D. (1983). *Stability and profile development of coarse material and their application in coastal engineering*. Tech. rep. Delft Hydraulics.

Poate, T. G., McCall, R. T., and Masselink, G. (2016). A new parameterisation for runup on gravel beaches. *Coastal Engineering* 117, 176—190.

Powell, K. A. (1988). The dynamic response of shingle beaches to random waves. *Coastal Engineering* 130, 1763—1773.

Powell, K. A. (1990). *Predicting Short Term Profile response for shingle beaches.* Tech. rep. SR 219. HR Wallingford, Oxfordshire, UK.

Powell, K. A. (1993). *Dissimilar Sediments: Model tests of replenished beaches using widely graded sediments*. Tech. rep. SR 250. HR Wallingford.

Roman-Blanco, B. L. D. S., Coates, T. T., Holmes, P., Chadwick, A. J., Bradbury, A., Baldock, T. E., Pedrozo-Acuna, A., Lawrence, J., and Grüne, J. (2006). Large scale experiments on gravel and mixed beaches: experimental procedure, data documentation and initial results. *Coastal Engineering* 53, 349—362.

Seymour, R. J., Bockstael, N. E., Campbell, T. J., Dean, R. G., Komar, P. D., Pilkey, O. H., Pratt, A. P., Snow, M. R., van Dolah, R. F., Weggel, J. R., and Wiegel, R. L. (1995). "Beach Nourishment and Protection". Washington, DC: The National Academies Press. Chap. 5, 107—126.

Sorensen, R. M. (2006). *Basic coastal engineering*. 3rd ed. New York, London : Springer.

Tomasicchio, G. R., D'Alessandro, F., Barbaro, G., and Malara, G. (2013). General longshore transport model. *Coastal Engineering* 71, 28—36.

Tomasicchio, G. R., D'Alessandro, F., Barbaro, G., Musci, E., and Giosa, T. M. D. (2015). Longshore transport at shingle beaches: An independent verification of the general model. *Coastal Engineering* 104, 69—75.

Tomasicchio, G. R., D'Alessandro, F., and Musci, E. (2010). A multi-layer capping of a coastal area contaminated with materials dangerous to health. *Chemistry and Ecology* 26, 155—168.

Tomasicchio, G. R., Lamberti, A., and Guiducci, F. (1994). Stone movement on a reshaped profile. *Proceedings of the 24th International Conference on Coastal Engineering. ASCE, Kobe.* 1625—1640.

Turner, I. L., Russel, P. E., and Butt, T. (2008). Measurement of wave-by-wave bed-levels in the swash zone. *Coastal Engineering* 55, 1237—1242.

Ward, D. L. and Ahrens, J. P. (1992). *Laboratory study of a dynamic berm revetment*. Tech. rep. US Army Corps of Engineers.

Weiner, H. M., Kaminsky, G. M., Hacking, A., and McCandless, D. (2019). *North Cove Dynamic Revetment Monitoring: Winter 2018-2019*. Tech. rep. 19-06-008. Shorelands and Environmental Assistance Program, Washington State Department of Ecology.

van Gent, M. R. A. (2010). Dynamic cobble beaches as sea defence. *Proceedings of the Third International Conference on the Application of Physical Modelling to Port and Coastal Protection, Barcelona.*

van Hijum, E. (1976). Equilibrium profiles and longshore transport of coarse material under oblique wave attack. *Coastal Engineering* 74, 1258—1276.

van Hijum, E. and Pilarczyk, K. W. (1982). *Equilibrium Profile and Longshore Transport of Coarse Material Under Regular and Irregular Wave Attack*. Publication (Waterloopkundig Laboratorium (Delft, Netherlands)). Delft Hydraulics Laboratory.

van Rijn, L. C. (2014). A simple general expression for longshore transport of sand, gravel and shingle. *Coastal Engineering* 90, 23—39.

van Wellen, E., Chadwick, A. J., and Mason, T. (2000). A review and assessment of longshore sediment transport equations for coarse grained beaches. *Coastal Engineering* 40, 243—275.

van der Meer, J. W. (1988). "Rock slopes and gravel beaches under wave attack." PhD thesis. University of Technology, Delft.

van der Meer, J. W. and Pilarczyk, K. W. (1986). Dynamic Stability of Rock Slopes and Gravel Beaches. *Coastal Engineering* 125, 1713—1726.

Chapter concluding remarks

In this chapter, we saw that the dynamic cobble berm revetment maintained its shape and behaved as a coherent structure under wave attack and water level changes. The structure demonstrated a dynamic stability, showing constant particle motion but limited shape change, and managed to recover from periods of large, energetic waves. However, although it retreated under water level increases, the expected behaviour presented in Figure 3.P1 was not fully observed as the sand erosion underneath the revetment appeared to play a major role, leading to underlying sand profile change and revetment sinking. The fact that the sand beneath the cobbles was only eroded, yielding to revetment sinking, was the main weakness of the structure. This sinking process significantly slowed down over time, showing that the underlying sandy was approaching a stable state. Nonetheless, the cobble dynamics was dominated by rollover transport which maintains most of the structure shape and allowed the revetment to retreat, but at a slower pace than the water level increase rate. The experiment also revealed that the revetment was able to significantly reduce the wave runup, shoreline retreat and sand volume eroded, hence demonstrating a capacity to armour the underlying sand while protecting the hinterland. The experiment also enabled some preliminary guidelines for the design and installation of a dynamic cobble berm revetment to be proposed. The obtained results are valid for the type of material tested. In addition, as they were obtained in a 2-D laboratory with all of the simplifications inherent to those facilities, further work is required to confirm this behaviour and performance on the field. The role and contribution of longshore sediment transport also needs to be assessed. The observed revetment sinking and sand erosion beneath the cobbles raised a question about the importance of internal sand dynamics, and assessing this in the field would be valuable towards a better understanding of dynamic revetments. For this reason, the following chapter details a field experiment on a dynamic cobble berm revetment.

Chapter 4

Behaviour and performance of a dynamic cobble berm revetment during a spring tidal cycle in North Cove, Washington State, USA

This chapter is based on the research article submitted in Coastal Engineering, and currently under review.

Paul M. Bayle, Chris E. Blenkinsopp, George Kaminsky, Heather Weiner and David Cottrell (In review). Behaviour and performance of a dynamic cobble berm revetment during a spring tidal cycle in North Cove, Washington State, USA. *Coastal Engineering*.

Abstract

In many places, sandy coastlines and their associated assets are at high risk of erosion and flooding, with this risk increasing under climate change and sea level rise. In this context, dynamic cobble berm revetments appear to be a sustainable protection technique to armour sandy beaches, reduce wave runup and protect the hinterland against wave attack. However, the behaviour and performance of such structures is not well understood. The dynamic revetment located in North Cove, WA, USA, was monitored over a spring tidal cycle in January 2019. A representative 60 metre alongshore section was monitored over 10 days, using 2D laser scanner (lidar) measurements, GPS ground elevation surveys, Radio Frequency Identification of individual cobbles and revetment thickness measurements. These data were used together to assess the behaviour and dynamics of the revetment throughout the experiment. Over the course of the experiment, the surface elevation changed by up to $\pm 0.5\,m$, and the revetment lost on average $0.67\,m^3/m$. These changes were found to be caused by relatively large high tide water level and offshore wave energy. The revetment demonstrated a dynamic stability and the capacity to quickly reshape under changing hydrodynamic conditions. Longshore transport was found to be important for local and small scale cobble changes, while cross-shore transport dominated the overall structure changes, both for sand and cobbles. Under longshore and cross-shore transport, the instrumented cobbles accumulated at the toe of the revetment, but were never transported seaward of the toe. The revetment also managed to recover some of the lost volume under moderate hydrodynamic conditions. The revetment behaviour was found to be influenced by variation in the cobble-sand matrix. The underlying sand dynamics – *i.e.*, accumulation or removal of sand within the cobbles – were found to govern the overall volume changes and were important to the overall stability of the revetment. Seven possible transport regimes were identified, and a model of the internal sand dynamics was developed. Overall, based on measurements during the spring tidal cycle, the low-cost revetment protected the sand scarp and prevented flooding of the hinterland, while capturing and armouring the underlying sand. Over time, renourishment will likely be required due to strong longshore sediment transport, and preliminary guidelines for this are suggested

Declaration concerning the article used for this Chapter:

Title	Behaviour and performance of a dynamic cobble berm revetment during a spring tidal cycle in North Cove, Washington State, USA
Status	Submitted in Coastal Engineering (Elsevier), and currently under review
Details	Paul M. Bayle, Chris E. Blenkinsopp, George Kaminsky, Heather Weiner and David Cottrell (In review). Behaviour and performance of a dynamic cobble berm revetment during a spring tidal cycle in North Cove, Washington State, USA. *Coastal Engineering*.
Contribution from the authors	P.M. Bayle: Planning/Collection/Processing/Analysis of data; Manuscript (70%) G. Kaminsky: Collection/Suggestions for analysis; Edited drafts of manuscript (12%) C.E. Blenkinsopp: Suggestions for analysis; Edited drafts of manuscript (12%) H. Weiner: Collection/Processing; Edited drafts of manuscript (5%) D. Cottrell: Edited drafts of manuscript (2%)
Statement	This paper reports on original research I conducted during the period of my Higher Degree by Research candidature.
Date and Signature	

Preamble

In Chapter 3, the results of the Dynarev laboratory experiment were presented, particularly focusing on the revetment behaviour and performance. The main observations were that the revetment actively reduced the runup excursion and shoreline retreat, while maintaining an overall coherent shape and armouring the sub-aerial sand. While the revetment demonstrated a dynamic stability, it was noted that the sand underneath the structure was not fully protected and was eroded by the water which infiltrated into the structure and then flowed back offshore. The sand erosion, hence revetment sinking, reduced over time as the underlying sand profile reached a more stable state and therefore the crest built significantly after the material added during the renourishment was placed. As a consequence, the underlying sand played an important role in the overall behaviour. However, it is unclear if this underlying sand dynamic observed was a laboratory effect due to the sudden revetment placement, or if it also happens in the field under changing water level and wave conditions. Furthermore, the data obtained in the laboratory were very useful to compare a protected and unprotected beach under the same conditions. The limited amount of forcing was an advantage in this aspect, but it also prevented from understanding the complete morphodynamics associated with a natural environment. For these reasons, the monitoring of an existing dynamic cobble berm revetment during a period of expected erosion and high water levels and comparison with lab results is valuable for the general understanding of dynamic cobble berm revetments.

The above narration can be summarised in the following research questions/objectives:

1. How does a revetment behave under energetic wave conditions and changing water level in the field? What are the importance of cross- and longshore sediment transport?
2. Is the underlying sand dynamic important in the field, and what role does it play in the overall morphodynamic changes?
3. Plan and conduct a field experiment to address the above points.

To address the above research points, during the third year of my PhD, I designed, planned and conducted a 2–week experiment to monitor the dynamic cobble berm revetment in North Cove, Washington, USA. The objective of the experiment was to intensively survey a section of the dynamic revetment during an energetic spring tidal cycle. The North Cove revetment is one of the few such structures currently installed and is ideal for the current study as it is located in a zone of high coastal erosion, with a very large wave climate and large tidal range.

Chapter 4.

4.1 Introduction

Coastlines and their associated cultural and economical assets are exposed to waves, storm surge and Sea Level Rise (SLR) which present a risk of erosion. Under on-going climate change scenarios, many coastal environments are likely to be severely affected by these factors (Church et al., 2013; DeConto and Pollard, 2016). In response, it is expected that the need to protect the coast from erosion and flooding will only increase with time, and future coastal protection action will likely have to consider new approaches and solutions to ensure sustainable coastal management.

In this context, soft engineering techniques with the potential to be highly adaptable, such as dynamic cobble berm revetments (or dynamic revetments), appear to be a promising alternative in some situations. A dynamic revetment consists of a gravel ridge constructed around the high tide wave runup limit. These structures mimic composite beaches which consist of a lower fore-shore of sand and a back-shore ridge, constructed of gravels, which stabilises the upper beach and provides overtopping protection to the hinterland. Therefore, like the ridges of composite beaches, dynamic revetments are composed of three layers: 1) A layer of pure gravels, which generally behaves like a pure gravel beach. This layer is dominated by cross-shore transport which over time, tends to lead to a net landward transport (Carter and Orford, 1984). Cross-shore sorting of particles in the pure gravel layer is common, with the direction of sorting depending on the hydrodynamic capacity of the swash to bring the largest particles into motion (Bluck, 1967; Orford, 1975; Williams and Caldwell, 1988). 2) A layer of mixed gravel and sand, composed of coarse sand and small pebbles. This layer is vertically sorted, with particle size decreasing with depth (Pye and Blott, 2018). 3) A layer of pure sand. The presence of these three layers is important in the understanding of dynamic revetment behaviour as it makes their dynamics more complex than pure sand or gravel beaches.

Dynamic revetments contrast with static coastal defence structures as they are "dynamic" and are expected to reshape under wave attack. However, although this type of structure has been studied through small scale laboratory experiments (*e.g.*, van Hijum and Pilarczyk, 1982; Downie and Saaltink, 1983; van der Meer and Pilarczyk, 1986; Powell, 1988; Ahrens, 1990; Lorang, 1991; Ward and Ahrens, 1992), real applications (*e.g.*, Kirk, 1992; Allan et al., 2006; Komar and Allan, 2010; Loman et al., 2010; Allan et al., 2012; Allan and Gabel, 2016) and most recently through a large scale laboratory flume experiment (Bayle et al., 2020), their response to storm conditions have not been thoroughly addressed. The few post-construction monitoring and observations of existing dynamic revetments (*e.g.*, Weiner et al., 2019; Allan and Gabel, 2016) show promising results. However, the performance and behaviour of such structures is yet to be fully understood and this is necessary if such structures are to be used more widely as a reliable coastal engineering solution.

A detailed review of existing field and laboratory experiments was presented by Bayle et al. (2020). They also presented the main results of the DynaRev large scale experiment undertaken to study the behaviour and performance of a dynamic cobble berm revetment under controlled conditions. The tested revetment demonstrated a dynamic stability un-

der energetic waves and water level increase – *i.e.*, the global shape of the revetment was conserved as it moved landward by rollover transport. Furthermore, the presence of the revetment decreased the vertical and horizontal runup ($R_{2\,\%}$) and retained additional sand on the sub-aerial part of the beach. However, the limitations inherent in a 2-D laboratory experiment do not allow a perfect representation of the hydro- and morphodynamic processes occurring under field conditions. Therefore, in order to better understand the dynamics of such structures, a series of field measurements were undertaken at a dynamic revetment in North Cove, Washington State, USA. The experiment was performed during an energetic spring tidal cycle in January 2019, in a location at high risk of erosion. Therefore, the current experiment provides a novel dataset for the analysis of dynamic cobble berm revetment behaviour and performance under severe conditions.

The paper is structured as follows: Section 2 presents the methodology including a description of the study area, the instruments used for data collection, the environmental conditions during the surveys and the data processing techniques. Section 3 presents the results and discusses the behaviour of the dynamic revetment and the sediment dynamics associated with it. Section 4 discusses the main findings, and presents a model of internal sand dynamics for dynamic revetments and composite beaches. Section 5 presents some preliminary guidelines for maintenance and nourishment of a beach with a dynamic revetment. Finally, section 6 concludes and suggests future research directions.

4.2 Methodology

4.2.1 Study Site

The dynamic revetment at North Cove, Washington State, USA is used as a case study to better understand the behaviour and sediment dynamics of a dynamic cobble berm revetment. The town of North Cove is situated on the U.S. Pacific Northwest coast along the northern shore of the Willapa Bay entrance in Washington State (see Figure 4.1). This coast is directly exposed to the predominant winter waves from the southwest. At least once per year, winter storms produce deep-water significant wave heights greater than 10 m (Allan and Komar, 2002). In general, winter months (from November to February) are characterised by high mean-water levels, high and long-period waves averaging around 3 m in height and 12 – 13 s in period, and approaching from the west–southwest. In contrast, summer months (from May to August) are characterised by lower mean water levels (approximately 30 cm lower than during winter), weaker winds and smaller waves (1.2 m and 8 s) approaching from the west–northwest (Ruggiero et al., 2005). As a result, the exposed coastline mainly experiences offshore and northward sediment transport in winter, and onshore and southward sediment transport in summer (Ruggiero et al., 2005; Kaminsky et al., 2010; Michalsen, 2018). Semi-diurnal tides dominate this part of the coastline, with a tidal range ranging from 2 to 4 m (Kaminsky et al., 2010).

The naturally sandy (D_{50} = 0.18 mm) North Cove coastline is oriented northwest-southeast (120°N-310°N), near the north channel of the Willapa Bay inlet (Kaminsky et al., 2010; Michalsen, 2018). Therefore, ocean waves entering the bay drive longshore

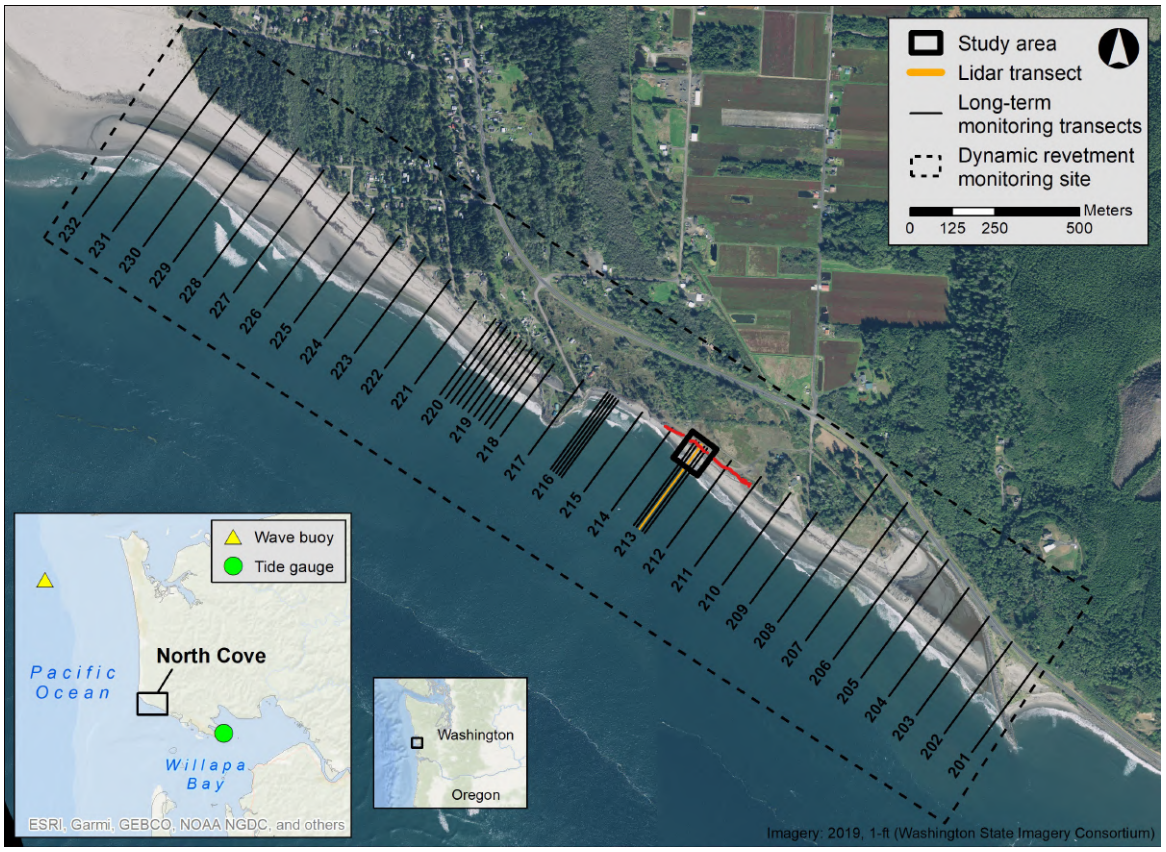

Figure 4.1: Geographical location of the North Cove dynamic cobble berm revetment. The long-term revetment monitoring site extends along more than 3 km of coast (dashed square). The red line represents the 318 m–long revetment section referred to Table 4.1. The study area (black square) is a representative section of the dynamic revetment, which was intensively monitored over the spring tidal cycle for this study. The Grays Harbor waverider buoy is shown as a yellow triangle, and the Toke Point tide station as a green circle in the bottom left map.

sediment transport toward the southeast, which may be aided by the flood tide. Wind waves from the south generated within the bay can drive nearshore sediment transport toward the northwest, aided by the ebb tide (Lesser, 2009). The combination of energetic hydrodynamics, storm events and northward migration of the main tidal channel within the inlet has led to chronic coastal erosion at North Cove over several decades. Kaminsky et al. (2010) revealed that the southern coastline of North Cove retreated by an average of 20 m/yr between 1950 and 1999, with a maximum rate of 37.3 m/yr between 1963 and 1974 (Figure 4.2). The shoreline recession rate was about 13 m/yr at the beginning of the 21^{st} century. As shown on Figure 4.2, many properties and assets have already been washed away by the ocean, leading to significant environmental, social and economic issues for the local community. In an attempt to resolve this issue, the local community began in February 2017 to incrementally build a dynamic revetment, along the 3–km long coastline delimited by the dashed black rectangle on Figure 4.1, using material from a local quarry. They built it based on existing examples constructed on the Oregon coast (Allan and Gabel, 2016; Allan et al., 2012, 2005). Table 4.1 details the volumes, dates and cost of material placed to date along the 318 m–long coastline section shown by the red line on Figure 4.1. At this location, the erosion of the coastline was defined by an abrupt sand scarp at the

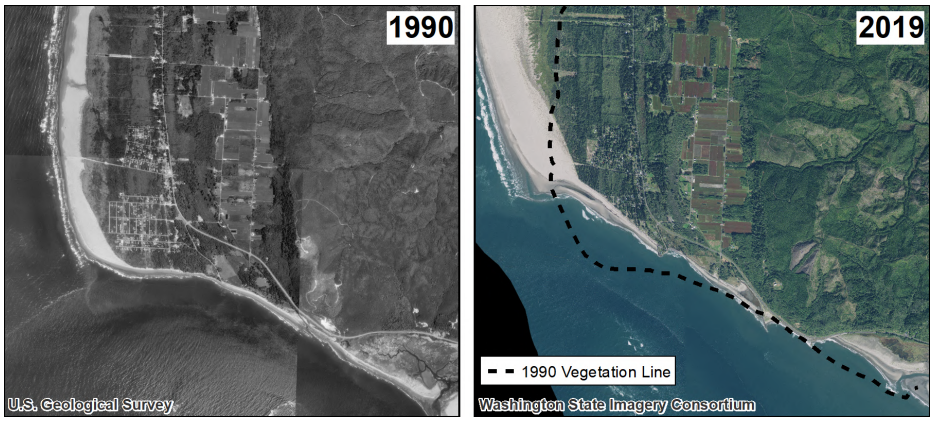

Figure 4.2: Aerial photographs of North Cove in 1990 (*left*) and 2019 (*right*), showing the shoreline retreat over 29 years. For more illustrations and information on the historical shoreline retreat at North Cove, see Kaminsky et al. (2010).

back of the beach prior to revetment construction (Figure 4.3a).

The first placement of revetment material within the study area was completed on 14^{th} February, 2017 in front of the sand scarp to protect it from direct wave attack. As shown on Figure 4.3a, the material was roughly placed along the scarp face and toe with no specific design. This low-cost and convenient method was applied for each material placement. At the time of this study, between 16^{th} January, 2019 and 28^{th} January, 2019, the total volume of the revetment was 5195.62 m^3 over a 318 m–long section (red line on Figure 4.1) including the study area (Table 4.1), corresponding to an average of 16.23 m^3/m (Figure 4.3b). The material used to construct the revetment is angular and poorly sorted, with a diameter range varying from a few centimetres to almost one metre (D_{50} = 15 cm) and is primarily basalt with a bulk density of 1830 kg/m^3, although other mineralogy can be found. The hardness of the material means that it tends to break down into smaller pieces, reducing the D_{50} over time, and adding coarse sand to the material range. For the remainder of this paper, the construction material will be referenced as 'cobbles', as this characterises the predominant material size within the revetment.

After installation, the revetment was reshaped by wave action and spread across shore, leading to a reduction in revetment slope (Figure 4.3b,c). With the revetment in place, the beach is considered to be an artificial composite beach: from mid to high tide, swash motions occur on the gravel ridge with swash events reaching the sand scarp during

Table 4.1: Volumes and dates of material placement along the 318 m–long coastlines section, including the study area.

Date	m^3	m^3/m	**Rock ($)**	**Labor ($)**
14/02/2017	395.02	1.23	50.98	64.50
15/02/2017	87.78	0.27	886.46	966.00
18/02/2017	131.67	0.41	738.72	805.50
23/02/2017	109.73	0.34	1,034.21	1,127.00
26/11/2017	153.62	0.48	3,965.76	4324.00
01/11/2018	2651.76	8.29	17,324.60	18,871.25
05/01/2019	1666.04	5.21	11,609.78	15,822.25
Total	**5195.62**	**16.23**	**35,610.51**	**41,980.5**

Figure 4.3: Photographs of the revetment within the study area, showing: (a) the sand scarp and the first material placement in February 2017; (b) the dynamic revetment on 24th January, 2019 at low tide. At that time, the total volume of the revetment over a 318 m–alongshore distance including the study area was 5195.62 m^3. The drift logs and large woody debris placed on top of the scarp are also visible; (c) the dynamic revetment on 21st January, 2019 at mid-tide; and (d) the dynamic revetment on 21st January, 2019 at high tide. Note for this particular high tide, waves also interacted with the large woody barrier dune on top of the scarp. *Photos taken by David Cottrell and Paul Bayle*

extreme events at high tide (Figure 4.3c and Figure 4.3d); between low and mid tide, the shoreline is seaward of the revetment toe and swash motions occur on the sandy part of the beach (Figure 4.3b).

Note that in addition to the revetment construction, available drift logs and large woody debris were placed at the back of the revetment, on top of the sand scarp in order to provide additional overtopping protection during extreme events. This large woody barrier dune was placed in September 2018 and is visible in Figure 4.3c and Figure 4.3d. Note large drift wood accumulation on top of beach berms is a common natural feature along the U.S Pacific Northwest beaches.

4.2.2 Data Collection

The field experiment was performed over ten days, between 16th January and 28th January, 2019, over approximately a spring tidal cycle. Three different types of data were collected: Global Positioning System (GPS) data over the study area (Weiner et al., 2019); Light Detection And Ranging (Lidar) measurements of swash motions and revetment surface elevation along a single cross-shore transect (Blenkinsopp et al., 2010a; Bayle et al., 2020); and Radio Frequency Identification (RFID) data to track individual cobbles (Allan et al., 2006; Weiner et al., 2019). The data collection dates are shown in Table 4.2.

Table 4.2: Recording dates for each type of dataset.

Date	GPS surveys	GPS profiles	Lidar measurements	RFID surveys	Cobble layer measurements
16/01/2019			✓		
17/01/2019	✓	✓	✓	✓	✓
18/01/2019			✓		
19/01/2019	✓	✓	✓	✓	✓
20/01/2019			✓		
21/01/2019			✓		✓
22/01/2019			✓		✓
23/01/2019			✓		✓
24/01/2019	✓	✓	✓	✓	✓
25/01/2019			✓		✓

4.2.2.1 GPS surveys and transects

GPS surveys were completed on three occasions during the experiment (Table 4.2) by walking on the beach at low tide (Figure 4.4b), carrying a backpack- mounted Real-Time Kinematic, Global Navigation Satellite System (RTK-GNSS) receiver to collect profile data along five defined cross-shore transects (referred to as GPS profiles, and shown in Figure 4.4a) and over the entire revetment area, including the toe and top of the revetment (referred to as GPS survey). A base station was set up on a local survey monument, allowing real-time data collection within $2 - 3$ cm accuracy. The GPS data collection was completed as part of the long-term monitoring of the revetment being undertaken by Washington State Department of Ecology, which started in June 2018 and is repeated every 2-3 months.

4.2.2.2 Lidar transect

A SICK LMS 511 lidar scanner was mounted on top of a 6 m pole strongly attached to a large drift log at the top of the revetment. The pole and lidar were anchored with four ropes making it almost completely immobile even in strong winds (Figure 4.4b and c). The lidar collected swash surface elevation and topographic measurements along a 20 m-long cross-shore transect on the cobble revetment for approximately six hours around each high tide (three hours before and after) to capture interactions between waves and cobbles. The lidar sample rate was 25 Hz with an angular resolution of 0.1667° across a 150° field-of-view. Note that the transect measured by the lidar is almost perfectly aligned with transect 213 (Figure 4.4a).

4.2.2.3 RFID

Radio Frequency Identification (RFID) surveys were completed on two occasions during the experiment to track the movement of individual cobbles using a tracking system similar to that of Allan et al. (2006). Passive Integrated Transponders (PIT), each with a unique

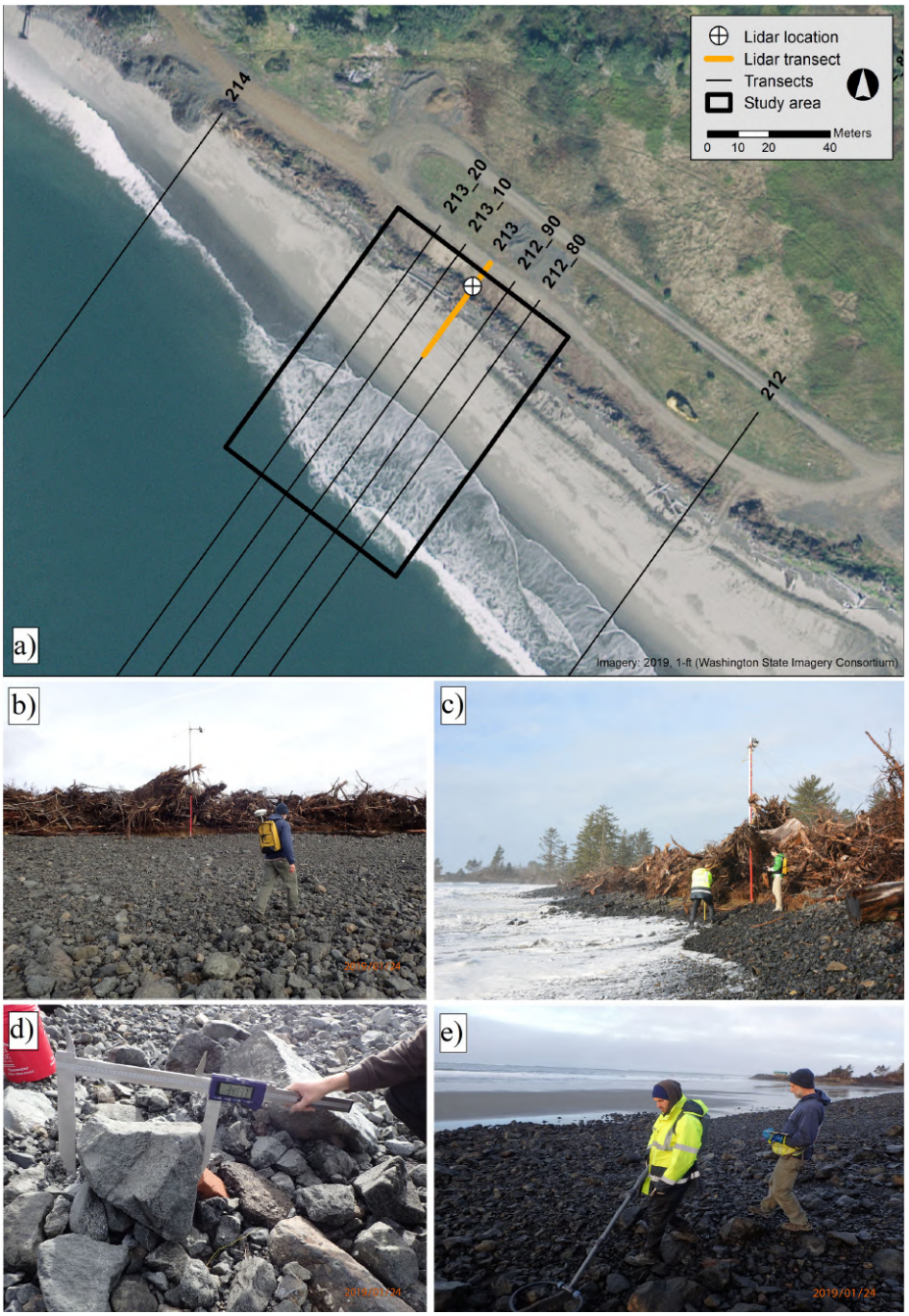

Figure 4.4: (a) Aerial photograph of the study area, showing the lidar location and the GPS transects (212_80, 212_90, 213, 213_10, 213_20). Note that the photograph was taken on 30^{th} September, 2019 when the revetment was covered with sand. This figure also shows photographs of (b) a GPS survey; (c) side view of the lidar deployment; (d) caliper measurement of an instrumented cobble (34 cm); and (e) RFID detection using the antenna and module reader. *Photos taken by George Kaminsky, Heather Weiner and Paul Bayle*

identification (ID) number, were installed inside 70 cobbles with a wide range of sizes and placed at the study site. The largest tagged cobble had an intermediate axis of 28.3 cm. The average intermediate axis of all tagged cobbles was 14.4 cm, with a standard deviation of ±4.3 cm. The smallest cobble tagged had a diameter of 7.7 cm. All instrumented cobbles were placed on the revetment along the five GPS transects on 17^{th} January (Figure 4.4a) in groups of three or five cobbles, every 0.5 m in elevation from 2.5 to 4 m NAVD88 (North

American Vertical Datum of 1988) and the positions were measured using GPS. RFID surveys (Table 4.2) were undertaken by using a portable Oregon RFID mobile reader to detect each cobble, their new positions were then recorded using GPS. The RFID reader antenna is able to detect a PIT within a 2 m horizontal range at depths of up to 1 m.

4.2.2.4 Pure cobble layer thickness

The thickness of the upper layer of the revetment, which consisted purely of cobbles, was measured almost everyday at multiple points on the revetment profile (Table 4.2) by digging a series of holes in the revetment. The holes were dug so they could be refilled without significantly altering the revetment profile. Thickness measurements were taken along a cross-shore line adjacent to the lidar measurement transect, at 1 m, 4.4 m, 9.4 m and 14.4 m seaward of the lidar location. The thickness of the pure cobble layer was defined as the distance from the surface to the point where the material becomes a mixture of sand and cobble (*i.e*, first trace of sand). This measurement technique is estimated to give a local thickness measurement with an accuracy of approximately $1-2$ cm, however inhomogeneity in the cobble layer thickness was evident. A linear interpolation was used to obtain the interface between the pure cobble layer and the underlying mixed layer across the entire revetment width. These data, combined with lidar measurements of the revetment surface, were used to estimate the pure cobble thickness over the cross-shore section of the revetment. The position of the exposed toe was also surveyed. Note that although GPS, lidar and RFID surveys ended by 25^{th} January, observation, digging and photos were undertaken until 28^{th} January.

4.2.3 Environmental Conditions

Revetment morphology change is expected to be primarily driven by wave action superimposed on tidally varying water levels. Secondary effects due to aeolian processes transporting sand into/out of the revetment structure may also be present during periods of high wind speed, particularly during low tide.

The environmental conditions during the experiment were obtained from publicly available continuously operating stations. Validated water level, wind speed and wind direction data were obtained from the Toke Point station (ID. 9440910; Figure 4.1) via the NOAA Tides and Currents open data platform. Wave height, period, and direction were obtained from the Coastal Data Information Program (CDIP) Grays Harbor waverider buoy (NDBC 46211; Figure 4.1) via the NOAA National Data Buoy Center open-source platform. Figure 4.5 shows the time series of wave, wind and water level data for the duration of the field experiment.

4.2.4 Data processing

4.2.4.1 Coordinate system

GPS data coordinates, including surveys and transects, were recorded in North American Datum of 1983 (NAD83), giving a Northing and an Easting for each data point collected.

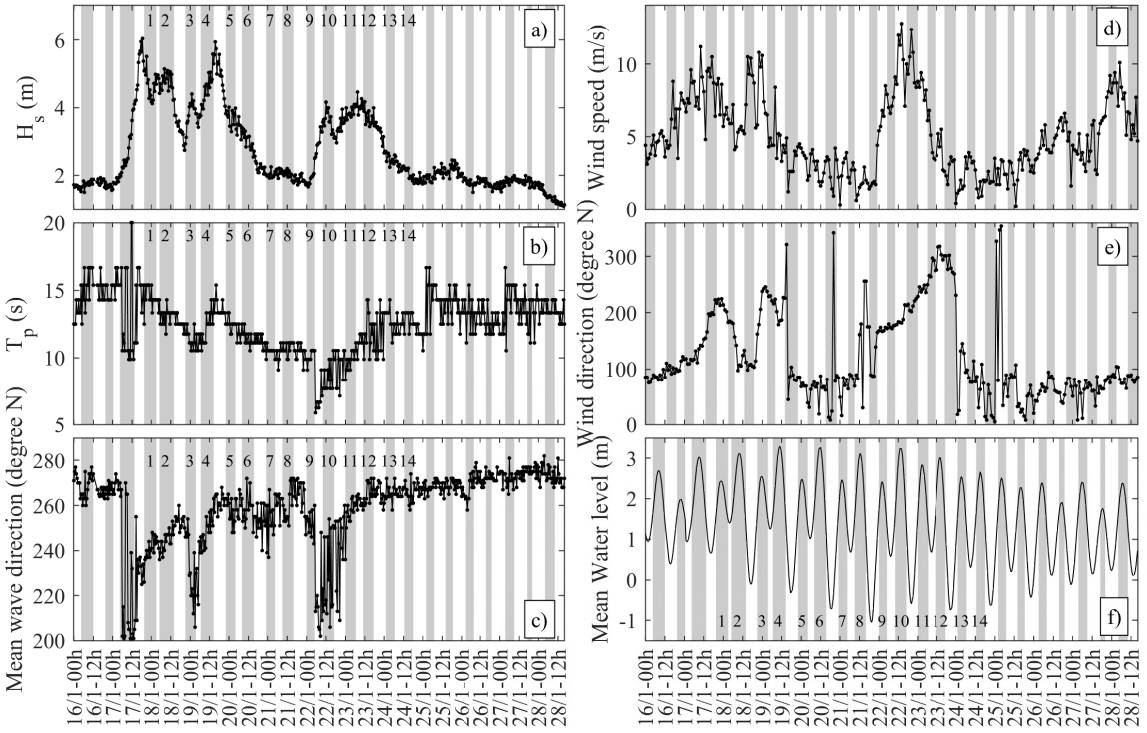

Figure 4.5: Time series of: (a) Significant wave height, H_s (m); (b) Peak wave period T_p (s); (c) Mean wave direction from North (degrees); (d) Wind speed (m/s); (e) Wind direction from North (degrees); and (f) Mean Water level (m), using the validated version of the data. Wave data were available every half hour; wind data every hour; and water level data every six minutes. The shaded areas on Figure 4.5a, b, c, f indicate when the lidar was recording swash processes occurring on the revetment at mid- and high tide. The numbers within each shaded area indicate the tide numbering system used in this paper. In Figure 4.5d, e, the shaded areas represent the periods when the tide was low and there was potential for aeolian transport of sand into the revetment structure. Times are given in Pacific Time (GMT-8). Elevation is given relative to the North American Vertical Datum of 1988 (NAVD88) (see Section 4.2.4).

The lidar was geolocalised using GPS–surveyed objects within the field of view as ground control points. All data were transformed and normalised relative to the lidar position with the x and y coordinates representing the cross-shore and longshore directions respectively. The cross-shore distance x is positive seaward and longshore distance y is negative north-west and positive southeast. All elevation data is given relative to the North American Vertical Datum of 1988 (NAVD88). Ground-based beach topography data were combined onto a 0.5 m grid (using MatlabR2019b) to form a surface elevation map of the studied site. In parallel, lidar data were first despiked and interpolated into a 0.1 m grid spacing (*e.g.*, see Martins et al., 2016; Martins et al., 2017b), giving a more detailed cross-shore profile along the lidar transect.

4.2.4.2 Bed and swash detection: lidar dataset

Using the despiked and gridded lidar data, hydrodynamic (broken waves or swashes) and topographic data points were separated following Almeida et al. (2015) and Martins et al. (2016). This methodology, based on the technique proposed by Turner et al. (2008) for ultrasonic bed-level sensors, applies a threshold on the variance computed over a moving 4 s window to extract raw bed points at each cross-shore location. The stationary bed level (referred to as the “bed") is separated from the non-stationary water surface (wave or

swash, here referred to as the “swash") to obtain a complete timeseries of bed elevation. This method also allows the instantaneous shoreline position, which is defined as the most landward wet point, to be tracked in both time and space enabling extraction of the runup and rundown limits.

4.3 Results

As shown in Table 4.2 and Figure 4.5, GPS surveys, GPS transects and RFID deployment/detection were completed during the evening low tide on 17^{th} January (*i.e.*, 17/1, hereafter “survey 1"), 19^{th} January (*i.e.*, 19/1, “survey 2") and 24^{th} January (*i.e.*, 24/1, “survey 3"). As a result, the following analysis focuses on the periods between consecutive surveys.

4.3.1 Revetment behaviour: GPS and RFID analysis

4.3.1.1 Global revetment elevation changes

It is important to bear in mind that the dynamic revetment is expected to reshape in response to waves, but retaining a coastal protection function by dissipating the wave energy and armouring the sand below. Figure 4.6a shows the bed-level changes between surveys 1 and 3. Note that over this period, there were 14 high tide (Figure 4.5). It shows that while the surface elevation of the revetment changed by up to ± 0.50 m over the course of the experiment, the whole revetment remained a coherent structure. It is also apparent that erosion and seaward transport dominated over the spring tidal cycle, with a clear longshore transport component.

Figure 4.6b shows the bed-level changes between surveys 1 and 2 and it is notable that the patterns of erosion and accretion are comparable to those over the entire survey period shown in Figure 4.6a. It can be seen that erosion occurred in the upper part of the revetment, from $x = 0$ m to $x = 8$ m and $y = -20$ m to $y = 10$ m. The erosion is particularly evident in front of the lidar, with about $0.45 - 0.5$ m of erosion occurring over two days (the equivalent of four high tides). The lower part of the revetment, from $x = 8$ m to $x = 18$ m shows a general accretion almost over the entire longshore section displayed. In the meantime, the revetment toe limit (*i.e.*, visual cross-shore delimitation of cobble and sand) moved seaward over the entire longshore section. This new revetment area between the initial and final toe limit is dominated by erosion, as is the area of sand located seaward of the toe.

Figure 4.6c shows the bed-level changes between surveys 2 and 3. The zones previously characterised by erosion on Figure 4.6b show accretion between survey 2 and survey 3. This is particularly true for the upper part of the revetment, between $x = 0$ m and $x = 5$ m and $y = -20$ m and $y = -5$ m, and between $x = 3$ and $x = 7$ m and $y = 24$ m and $x = 30$ m, as well as the lower part of the toe, between $x = 18$ m and $x = 20$ m. Furthermore, the zone between $x = 8$ m and $x = 18$ m and $y = -20$ m and $y = 20$ m which showed erosion in Figure 4.6b, is characterised by accretion between surveys 2 and 3. Although the period covered by Figure 4.6c includes ten high tides, the toe location did not vary significantly.

Overall, Figure 4.6 shows that the dynamics of the bed-level are complex and variable through time. The similarity between Figure 4.6a and Figure 4.6b indicates that most of the

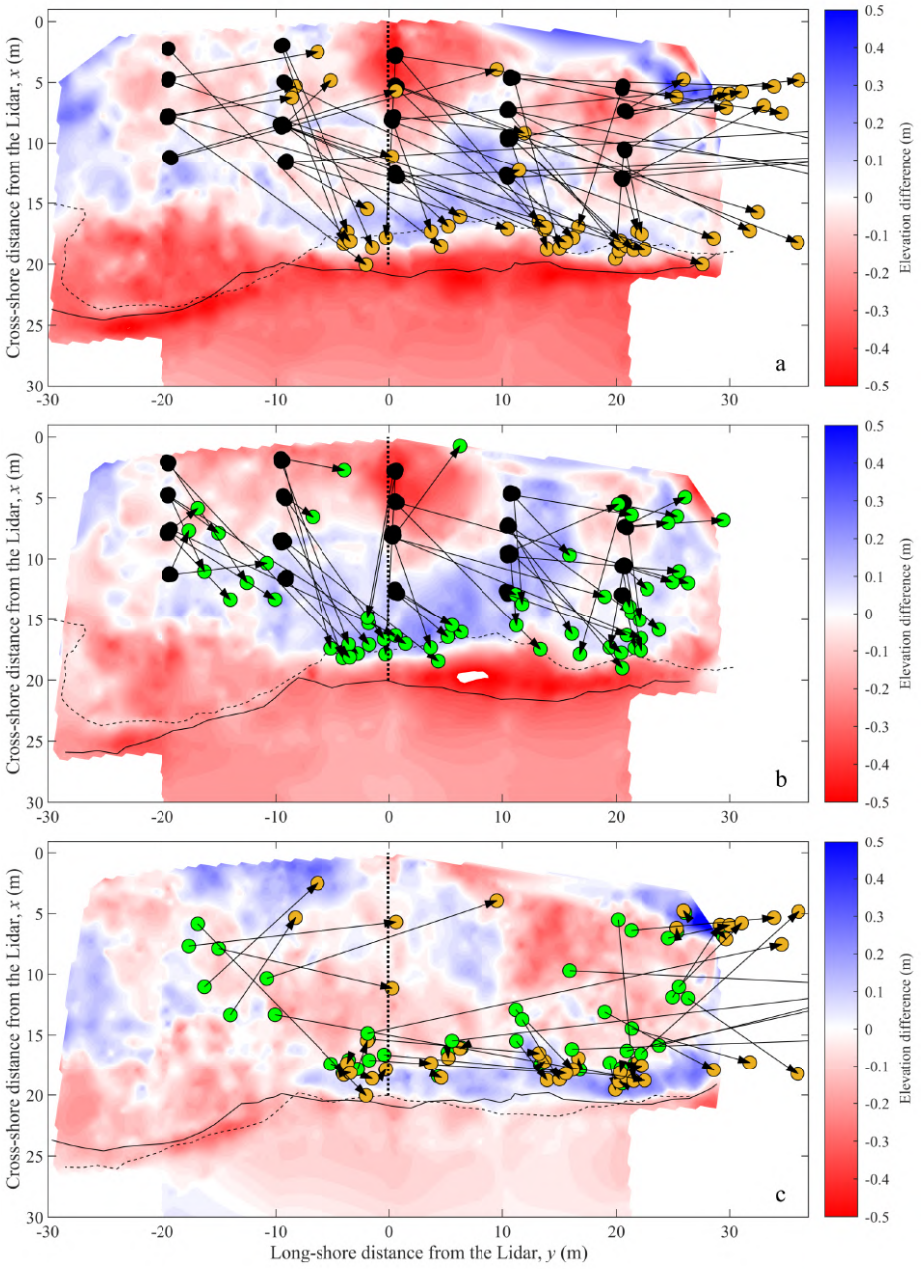

Figure 4.6: Revetment bed-level changes (in metres) between (a) survey 1 and survey 3, (b) survey 1 and survey 2 and (c) survey 2 and survey 3. The dashed and plain black lines represent the cobble–sand cross-shore limit at the beginning and end of the period respectively. The vertical dotted line shows the lidar measurement transect. Note that the lidar position is the origin of the coordinate system. The instrumented cobbles were placed at the locations marked by black dots. The cobbles found by Radio Frequency Identification (RFID) during survey 2 and survey 3 are shown in green and orange respectively.

bed-level changes observed over the entire experiment were generated between surveys 1 and 2, so over the first four tides. The only changes occurring between surveys 2 and 3 which substantially influence the net change over the experiment are the erosion between $x = 5\,\text{m}$ and $x = 10\,\text{m}$ and $y = 10\,\text{m}$ and 17 m, and accretion between $x = 3\,\text{m}$ and 7 m and $y = 24\,\text{m}$ and 30 m. According to Figure 4.5a, the four high tides between the evening low tide on 17/1 and the evening low tide on 19/1 are marked by very large wave height, with H_s varying from 4 to 6 m (Figure 4.5). The following ten tides also experienced a similar peak of

wave height, hence energy, occurring between 19/1 and 20/1, but are generally characterised by milder wave conditions. This shows the capacity of the revetment to rapidly adapt to changes in forcing. After a period of calm weather prior to 17/1 (Figure 4.5), the revetment rapidly and significantly changed under the first large waves to reach an approximately stable state with the new higher energy conditions. As a consequence, the second peak of wave height had much less influence on the revetment shape. This rapid adaption of the structure to the hydrodynamic condition was noted by Bayle et al. (2020), who found through large scale laboratory experiments that revetment slope changed rapidly (within 20 minutes) as a function of the offshore wave steepness.

Taking the revetment limits as $x = 0.7\,\text{m}$ and $x = 19.5\,\text{m}$ and $y = -30\,\text{m}$ and $y = 30\,\text{m}$, the volume of the revetment above the NAVD88 datum was calculated, thus measuring the volume of the entire ridge with no differentiation between cobbles and sand. The revetment volume decreased by $40\,m^3$ between surveys 1 and 3, with $30\,m^3$ lost between surveys 1 and 2 and only $10\,m^3$ between surveys 2 and 3. This volume loss, corresponding to $0.67\,m^3/m$, along the 60 metres of the study area is very small in comparison with the overall volume of gravel placed (3 % of the $16.23\,m^3/m$). However, the initial volume accounts only for the cobbles placed, and not for the entire sediment volume down to the NAVD88 datum. Consequently, the actual volume loss should be smaller than 3 %, but cannot be estimated as no survey data are available immediately prior to the first cobble placement.

4.3.1.2 Instrumented cobble transport

As previously highlighted, the original position of the instrumented cobbles was recorded during survey 1, and RFID detection surveys were performed during surveys 2 and 3. A total of 70 cobbles were placed during survey 1, 57 cobbles were found during survey 2 and 59 during survey 3, corresponding to 81 % and 84 % recovery, respectively. These percentages are similar to that reported by Allan et al. (2006) for a similar beach in Oregon, and that reported for a large scale laboratory flume experiment (83.5 % Bayle et al., 2020). Figure 4.6 shows that the RFID cobble tracking technique is able to identify the main zones of accretion and erosion on the revetment. Indeed, the instrumented cobbles were globally transported away from the zones of erosion, and toward the main zones of accretion. This is particularly true for the depleted area in front of the lidar in Figure 4.6b, and for the accumulation zone at the toe of the revetment in Figure 4.6b, c. The cobbles located beyond $y = 30\,\text{m}$ on Figure 4.6c cannot be correlated to accretion or erosion due to the absence of bed-level data in this area, but it seems that a region of accretion was created between survey 2 and 3, between $x = 3\,\text{m}$ and $7\,\text{m}$ and $y = 20\,\text{m}$ and $y = 35\,\text{m}$. Note that some cobbles were transported up to $y = 50\,\text{m}$.

Figure 4.7 presents the elevation of the instrumented cobbles relative to NAVD88 after surveys 2 (Figure 4.7a) and 3 (Figure 4.7b) as a function of the total distance moved between survey 1 and 2 (Figure 4.7a) and survey 2 and 3 (Figure 4.7b). On both figures, the grey area represents the revetment toe elevation change between surveys. It therefore corresponds to the seaward advance of the toe, which is characterised by erosion in Figure 4.6 especially

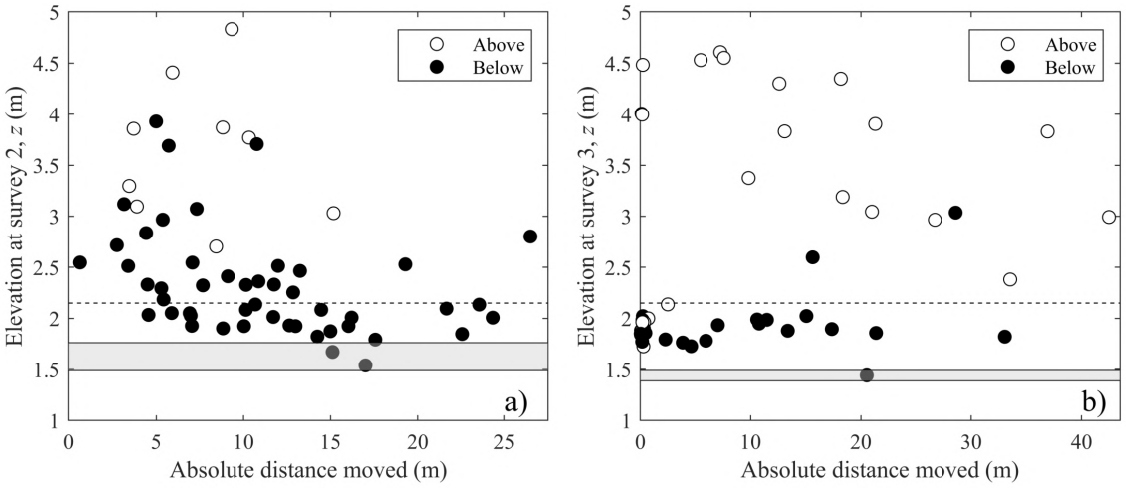

Figure 4.7: Elevation of each instrumented cobble (in metres relative to NAVD88) during (a) survey 2 and (b) survey 3 as a function of the absolute distance moved (metres) between (a) surveys 1 and 2 and (b) surveys 2 and 3. Cobbles transported above their initial location are displayed as empty circles while those transported below are marked as filled black circles. The dashed black line marks the elevation $z = 2.15$ m representing the upper bound of the toe area. The grey area represents the revetment toe shift between consecutive surveys (seaward in both cases).

between survey 1 and 2 (Figure 4.6b). Almost no cobbles were transported into this area, as shown by the RFID elevation (Figure 4.7) and location (Figure 4.6) data. Consequently, the advancement of the revetment toe limit is likely due to the erosion of sand covering the cobbles. Even if some cobbles were transported into this area, visual observations of cobble and sand on site suggest that the majority of cobbles which became visible at the toe were already there, but became exposed as the sand covering them was eroded. Furthermore, it is also conceivable that these newly exposed cobbles contributed to the region of accretion located between $x = 16$ m and $x = 20$ m and $y = -10$ m and $y = 30$ m (Figure 4.6c) if they moved onshore after being exposed. However, this cannot be verified as the monitoring of these initially buried cobbles was not possible.

The RFID data shown in Figure 4.6 revealed that the dominant longshore transport is in the positive y-direction, corresponding to a South-Easterly transport, which is expected in this area (Section 4.2.1). Figure 4.7 shows that the transport distances can be significant (*e.g.*, up to 50 m) after only a few tides. Figure 4.7 also reveals that none of the instrumented cobbles were transported seaward of the toe, showing that the dynamic revetment material is unlikely to be lost offshore, which contributes to the observed dynamic stability of the structure. This observation was also made in the laboratory by Bayle et al. (2020), where less than 1 % of the revetment volume was found seaward of the initial toe. The evidence of longshore transport presented in Figure 4.6 may partly explain the overall loss of volume observed through the experiment if more cobbles are transported out of the study area than arrive from upstream. However, there is no clear evidence of a consistent longshore transport gradient (either within the data or through observations during the experiment) and at a larger scale, the longshore fluxes are expected to be less important than cross-shore fluxes in the observed cross-shore variations (Masselink and Van Heteren, 2014). As a result, the volume loss is mainly attributed to sand removal from within and underneath the cobble berm, and this will be studied in more detail in Section 4.3.3.1 and Section 4.3.3.3.

4.3.1.3 Detailed analysis of instrumented cobble behaviour

Figure 4.7a shows that the majority of cobbles moved seaward of their original position (*i.e.*, transported below their initial position) between survey 1 and 2 (only nine moved landward). In contrast, 29 cobbles moved upward between surveys 2 and 3. Although the manual placement of the instrumented cobbles during survey 1 may bias this comparison, it seems that the cobbles significantly moved down slope between surveys 1 and 2 (*i.e.*, when the majority of morphological changes occurred, Section 4.3.1.1), while numerous cobbles were transported to a position relatively high on the revetment between surveys 2 and 3 (*i.e.*, when less morphological change occurred, Section 4.3.1.1).

Figure 4.7b shows that 68 % of the instrumented cobbles were located between z = 1.45 m and z = 2.15 m (dashed black line on Figure 4.7b) during survey 3, with 42 % already within these boundaries during survey 2 (Figure 4.7a). These elevations correspond respectively to x = 19.5 m, the most landward location of the sand–cobble boundary within the study area, and x = 17 m. This can be seen as a 2.5 m wide band representing the revetment toe area. Therefore, the majority of cobbles which moved to the toe area between surveys 1 and 2 remained in this zone between surveys 2 and 3 (Figure 4.7).

Figure 4.8a, b display the change in cobble elevations between surveys 2 and 3 as a function of the absolute distance moved and cobble size. Note that this analysis is not performed between surveys 1 and 2 because the manual placement of cobbles during survey 1 introduces a bias. Figure 4.8a does not display any obvious relationship between cobble size and the distance moved or elevation change. Figure 4.8b displays a zoom around the origin of the plot, and shows that regardless of their size, the majority of the cobbles that moved by less than 0.5 m were initially within the toe area during survey 2 (shown by black circles). Figure 4.8a also shows that the cobbles already in the toe area which moved by more than 10 m are smaller than 15 cm. Therefore, while larger cobbles already in the toe area are less mobile, those originally above the toe area (shown by empty circles) seem to be less restricted in motion. This restriction of motion for the cobbles located at the toe of the revetment is confirmed by the numerous small and medium-size cobbles within the toe area (black circles) which did not move by more than 4 m (*i.e.*, are near the origin of the graph).

Figure 4.8c and Figure 4.8d indicate that except for a few cobbles, the distance moved by cobbles is primarily in the longshore direction resulting in Figure 4.8c being very similar to Figure 4.8a. Therefore, similar observations can be drawn from Figure 4.8c, d: cobbles located in the toe area are more restricted in motion than those outside, regardless of their size. However, these data should be used with care: where the cumulative absolute longshore transport is likely well represented by the net longshore distance moved over time due to the uni-directional nature of longshore sediment transport at this site, the cumulative absolute cross-shore transport is significantly underestimated due to the two-directional nature of this process. Therefore, although net longshore distances are larger than net cross-shore distances (Figure 4.8c and Figure 4.8d), gross cross-shore transport remains larger on dynamic revetments as on gravel and composite beaches (Masselink and

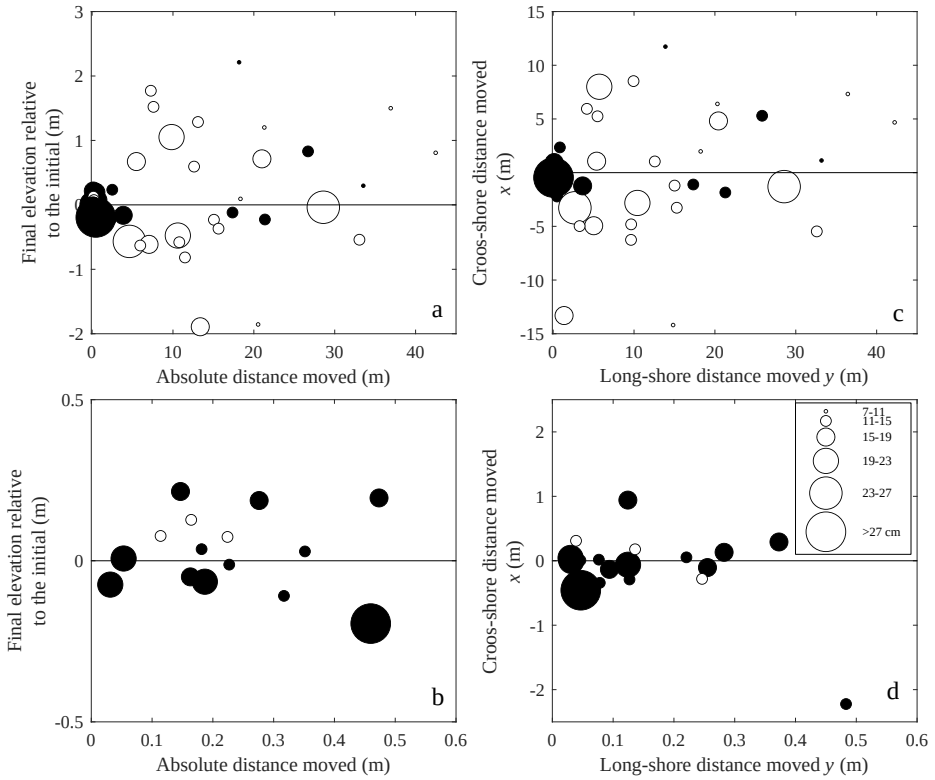

Figure 4.8: (a) and (b): Change in cobble elevation between surveys 2 and 3 as a function of the absolute distance moved. (c) and (d): Cross-shore distance moved by each cobble between surveys 2 and 3 as a function of longshore distance moved. Note that (a) and (c) show the entire range of distances while (b) and (d) display a zoom around the origin of the plot. Cobbles initially located (so survey 2) between $z = 1.45$ m and $z = 2.15$ m (*i.e.*, the toe area) are shown as full black circles while those originally outside this area are shown as empty circles. The size of the circles represents the length of the intermediate axis for each cobble in centimetres.

Van Heteren, 2014).

Overall, from the discrete data collected using RFID and visual observation of the revetment, the toe area is composed of larger cobbles (Figure 4.8) which may prevent some large and small cobbles from moving due to strong interlocking. In contrast, as the toe area is at a low elevation, it lies within the swash zone for longer periods and small cobbles are transported over longer distances than for similar size cobbles located higher on the revetment (Figure 4.8a, c). Therefore, the trend suggests that cobble transport is limited by size (and weight) and also by their location within the revetment structure over time. However, the hydrodynamic conditions could also cause this accumulation, as the small and medium cobbles may move landward and seaward within the revetment profile during a tide, but end up at the bottom after the tide has receded. Both hypotheses are plausible, and it would be necessary to monitor individual cobble movement in real time to conclude which process occurs.

4.3.2 Continuous revetment dynamics along the lidar profile

4.3.2.1 Importance of the local water level

The previous 3D analysis highlighted the importance of both the cross-shore and longshore processes in the revetment dynamics. The 2D profile measured with the lidar along a

single transect is considered as a representative profile where both long- and cross-shore transports cause changes, although during large events, it is expected that cross-shore transport dominates. Using the “bed" time series (Section 4.2.4.2), net bed-level changes relative to the initial beach face morphology (either survey 1 or survey 2) were computed at each cross-shore position on the 0.1 m grid, and at every second. Note that the y axis on the lidar data presented in this section does not quite extend to the revetment toe located at $x = 20$ m from the lidar, as the quality of the data recorded further than $x = 18$ m was inconsistent. Bed-level changes in Figure 4.9, Figure 4.10 and Figure 4.11 are generally shown from the time where swash events start to interact with the revetment. However, for some tides (*e.g.*, 2 and 4), the lidar was started too late. Note that the sand scarp and the large woody debris barrier at $x = 0$ m were often reached by the swash, as shown by the maximum runup line (dashed line in Figure 4.9a) going beyond the displayed revetment area ($x < 0.7$ m).

Figure 4.9a shows the evolution of the revetment surface elevation over time relative to survey 1 along the lidar profile, between surveys 1 and 2. Consequently, the final bed-elevation on 19/1-13h corresponds to the bed-elevation along the lidar transect shown on Figure 4.6b, and the same erosion and accretion areas are visible. Figure 4.9a illustrates that the evolution of the bed was not constant and homogeneous over time. For these four tides, it appears the zones of accretion were always located below the mean shoreline position (MSP), in the lower swash, with more accretion during tides 2 and 4. The revetment surface in the upper swash zone eroded two to three times more during tides 2 and 4 than 1 and 3. Most of the final bed-level changes observed on 19/01-13h were caused during tides 2 and 4. Over the time shown in Figure 4.9a, tides 2 and 4 were characterised by a higher high tide shoreline position and an average wave energy of $28.8\,kJ/m^2$ and $26.4\,kJ/m^2$ respectively, which was slightly higher than the average wave energy of $25\,kJ/m^2$ measured between survey 1 and 2. Tides 1 and 3 were characterised by a relatively low high tide shoreline position and an average wave energy of $27.8\,kJ/m^2$ and $18.8\,kJ/m^2$ respectively. Therefore, although the wave conditions during tide 1 were similar to those during tides 2 and 4, bed-level changes were significantly smaller which highlights the importance of the water level in morphodynamic processes on the revetment.

Figure 4.9b confirms this observation, as the revetment profile is relatively constant during tides 1 and 3, while the slope changes considerably during tides 2 and 4. As shown by the RFID data on Figure 4.7a, cobbles were transported seaward in the toe area, which contributed to the overall gentling of the slope. The thickness of the pure cobble layer generally decreased between survey 1 and 2 (Figure 4.9b), principally caused by longshore sediment transport as very few, if any cobbles were transported seaward of the revetment toe (Section 4.3.1.3, Bayle et al., 2020)).

Figure 4.10a shows the evolution of the revetment surface elevation relative to survey 2, over the ten high tides between surveys 2 and 3. The final bed-level elevation on 24/1-17h matches the bed-elevation along the lidar transect shown in Figure 4.6b. The separation between the zone of accretion and erosion by the MSP is not as clear as in Figure 4.9a,

but the parts of the revetment located below the MSP consistently show large bed-level changes. However, the upper part of swash can also drive substantial bed-level changes as illustrated by tide 5 and 11 (accretion during the rising tide in this case). These two tides are related to high level of wave energy ($17.5\,kJ/m^2$ and $18.8\,kJ/m^2$ for tide 5 and 11 respectively) and are the most energetic tides between survey 2 and 3.

The profiles in Figure 4.10b reveal four tides which led to significant profile change: tide 6, 8, 10 and 12. Tide 6 led to erosion over almost the entire profile (Figure 4.10b, b-6). Unfortunately, data are missing for this tide when much of this change was occurring.

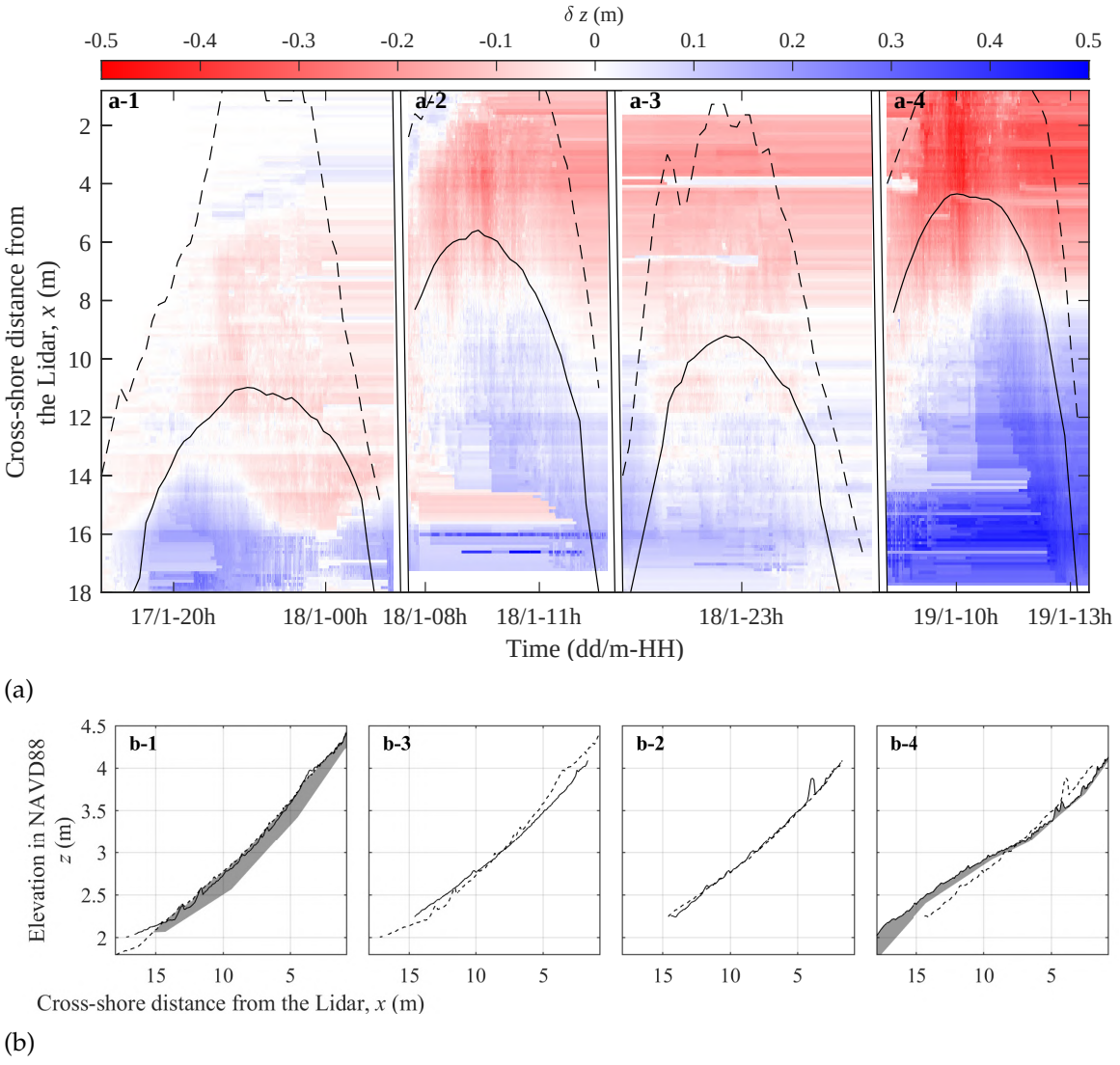

Figure 4.9: Bed-level changes for tides 1-4 (between surveys 1 and 2 – 17/1 to 19/1) (a) Change in bed-level elevation through the swash zone over time. The dashed and solid lines represent the run-up limit and the mean shoreline position respectively. The mean shoreline position was calculated using the instantaneous shoreline timeseries derived from lidar measurements, and averaged over 10–minute windows. The colour scheme represents net bed-level change in metres (measured every second) relative to the beach face morphology during survey 1. Breaks in time where no lidar data are available (generally when no interaction) are shown by two close parallel lines. (b) Revetment profiles obtained using the lidar at the start (dashed) and end (solid) of each high tide measurement period. For some tides (Table 4.2), the thickness of the pure cobble layer is shown in grey. The thickness was obtained as described in Section 4.2.2. Note that the lump observed during tide 3 at x = 4 m is caused by a large cobble manually placed during the calibration of the lidar, and which was removed during tide 4.

During tide 8 the profile steepened, with erosion at the bottom of the revetment and accretion at the top (Figure 4.10b, b-8). Tide 10 led to accretion over the entire width of the revetment (Figure 4.10b, b-10), with the thickness of the pure cobble layer slightly

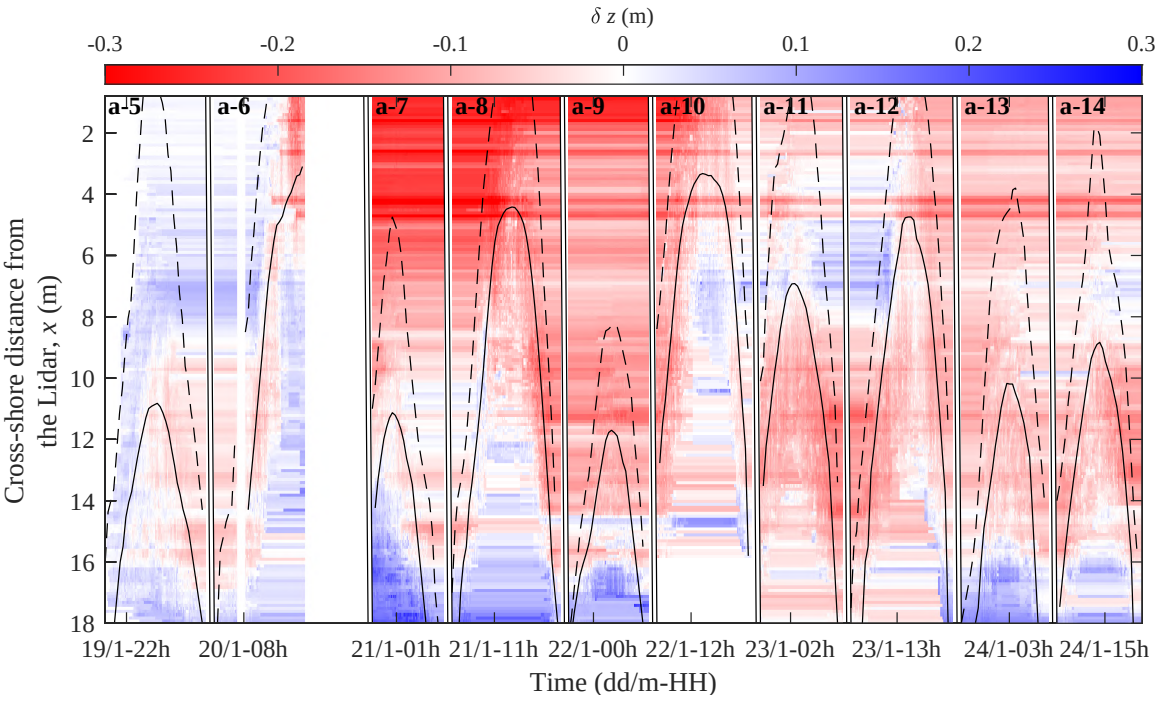

(a)

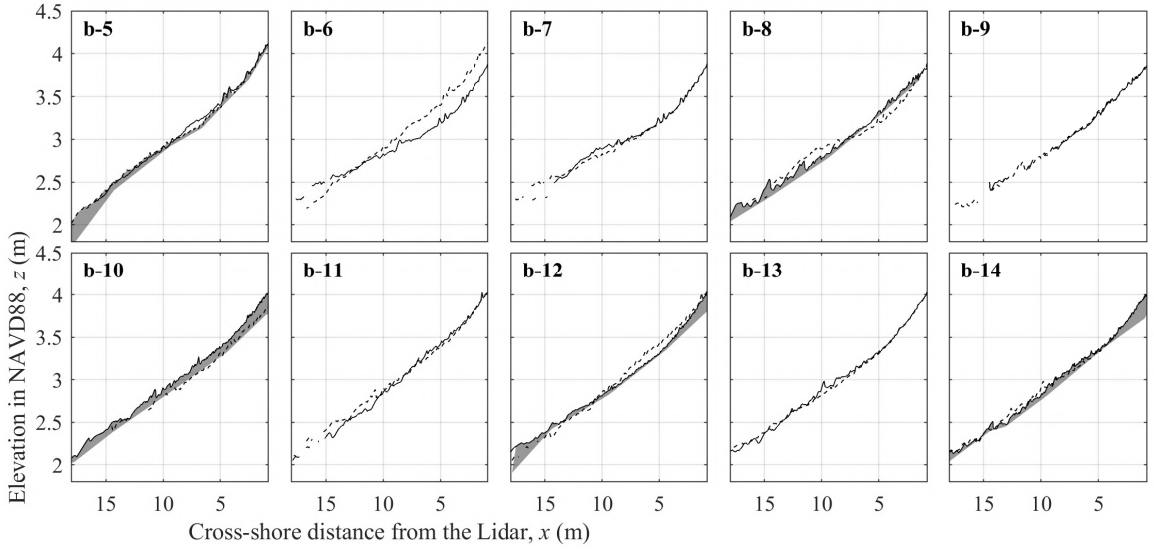

(b)

Figure 4.10: Bed-level changes for tides 5-14 (between surveys 2 and 3 – 19/1 to 24/1) (a) Change in bed-level elevation through the swash zone over time. The dashed and solid lines represent the run-up limit and the mean shoreline position respectively. The colour scheme represents net bed-level change in metres (measured every second) relative to the beach face morphology during survey 2. Note that the bed-level changes scale range is smaller than in Figure 4.10. Breaks in time where no lidar data are available (generally when no interaction) are shown by two close parallel lines. Note that the band of erosion visible on tide 6-14 around x = 4.4 m is caused by a large cobble manually removed. (b) Revetment profiles obtained using the lidar at the start (dashed) and end (solid) of each high tide measurement period. For some tides (Table 4.2), the thickness of the pure cobble layer is shown in grey. Note that the initial profile and thickness corresponds to the final values in Figure 4.9b, b-4.

increasing from its previous measured state after tide 8. Tide 12 showed erosion in the upper part of the revetment between $x = 3$ m and $x = 10$ m, and accretion in the lower part (Figure 4.10b, b-12). Tides 6, 10 and 12 (not tide 8) had wave conditions above the average wave energy of 11.1 kJ/m^2 measured between survey 2 and 3. Furthermore, they were all associated with the four highest water levels (above 3 m) during this period. Therefore, even though tide 8 was not associated with high energy waves, it led to important changes as the water level was high, meaning longer and more energetic interaction between swash flows and the revetment, and deeper swashes in the mid and upper part of the revetment. This suggests that for dynamic revetments used as coastal protection, high tide water level, hence storm surge can drive greater changes than storm waves with the combination of both driving the most significant changes.

4.3.2.2 Revetment dynamics toward a stable state

Figure 4.9 shows that during tide 4, the bed-level is almost unchanged during the last 3 hours of measurement, after 19/1-10h30. Most of the changes were achieved during the rising tide, and minimal net bed-level change is observed during the falling tide. This observation is true for most of the observed tides, and suggests that under new conditions, the bed-level is able to rapidly change and reach a relatively stable state for the forcing conditions at the intra-tidal time scale.

Figure 4.11 shows the bed-level changes during tide 1, 4, 5 and 14 relative to the initial profile measured during survey 1. It shows that most of the final bed-elevation changes occurred during tide 4, and that the bed-level changes observed between survey 2 and 3 (Figure 4.10) did not affect the overall final shape. Following the large changes measured during Tide 4, the revetment then remained relatively stable with the profile oscillating around this quasi-stable state (note the colour scale used in Figure 4.10 has a smaller range than Figure 4.9 and Figure 4.11) and indeed returning to almost the same profile again during Tide 14. Therefore, it seems the revetment also reached a stable state at the inter-tidal time scale, and that this state was reached during tide 4, which confirms the observation made in Section 4.3.1.1 and Figure 4.6.

The inter-tidal stable state is confirmed by Figure 4.12a which shows the initial revetment profiles and the profile at the end of tides 1, 4, 5 and 14. It shows a significant tilt in the revetment face, with the slope decreasing during tide 4. After tide 4, the variations in final profile shape and slope measured from tide-to-tide were significantly smaller (Figure 4.12a), which confirms that most of the net changes occurred between survey 1 and 2, and that the changes observed between survey 2 and 3 were mostly limited to oscillations around this stable state. The cobbles kept moving and the overall revetment remained dynamic, but its global shape did not significantly change.

Figure 4.12a allows the difference in revetment volume per metre to be estimated based on the lidar data. Using the same cross-shore revetment limits as in Section 4.3.1.1 as $x = 0.7 - 19.5$ m, the volume of the revetment ridge was calculated from the NAVD88 datum, with no distinction between sand and cobbles. The volume differences obtained

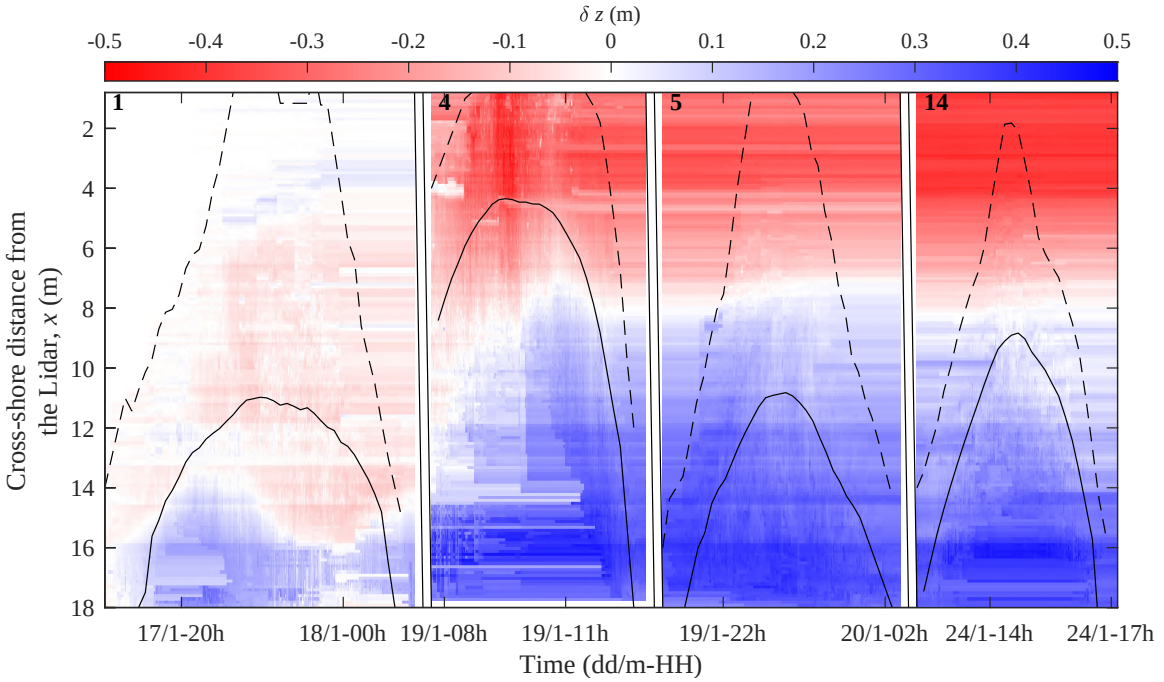

Figure 4.11: (a) Change in bed-level elevation through the swash zone measured relative to the initial profile at that start of tide 1 (survey 1) for tides 1, 4, 5 and 14. These tides were choosen as they represents the beginning and end of Figure 4.9 and Figure 4.10. The dashed and solid lines represent the run-up limit and the mean shoreline position respectively. The colour scheme represents net bed-level change in metres (measured every second). Note that the scale used is the same as in Figure 4.9, which is larger than the one used in Figure 4.10.

are counter intuitive and are not in agreement with those calculated in Section 4.3.1.1 over the whole study area, with the revetment gaining 0.30 m^3/m between survey 1 and 2, and losing 0.87 m^3/m between survey 2 and 3. This leads to a total loss of 0.57 m^3/m between surveys 1 and 3, which is similar the overall loss of 0.67 m^3/m measured over the entire surveyed revetment section (Section 4.3.1.1). Therefore, when net bed-level changes were large and the revetment shape changed substantially between survey 1 and 2, its volume increased by a relatively small amount along the lidar transect; whereas when the revetment was relatively stable between survey 2 and 3, its volume decreased by a relatively larger amount. This apparent discrepancy can partly be explained by local longshore gradient creating longshore inhomogeneity, as the thickness of the pure cobble layer decreased through the experiment between surveys 1 and 3 (Figure 4.12b). However, the volume of the pure cobble layer decreased by 1.96 m^3/m between survey 1 and 3, with the thickness of the pure cobble layer varying from a few centimeters to 30 cm. Although the measurement of this volume is coarse as it relies on interpolation, and noting that the revetment toe was covered in sand up to x = 15 m during survey 1 (17/1), this value is almost four times larger than the total volume loss of 0.57 m^3/m between survey 1 and 3. Therefore, the cobble loss must have been compensated by some incoming material not counted in the pure cobble layer. This analysis highlights the complex morphodynamics of a cobble ridge, and this is explored in the next section.

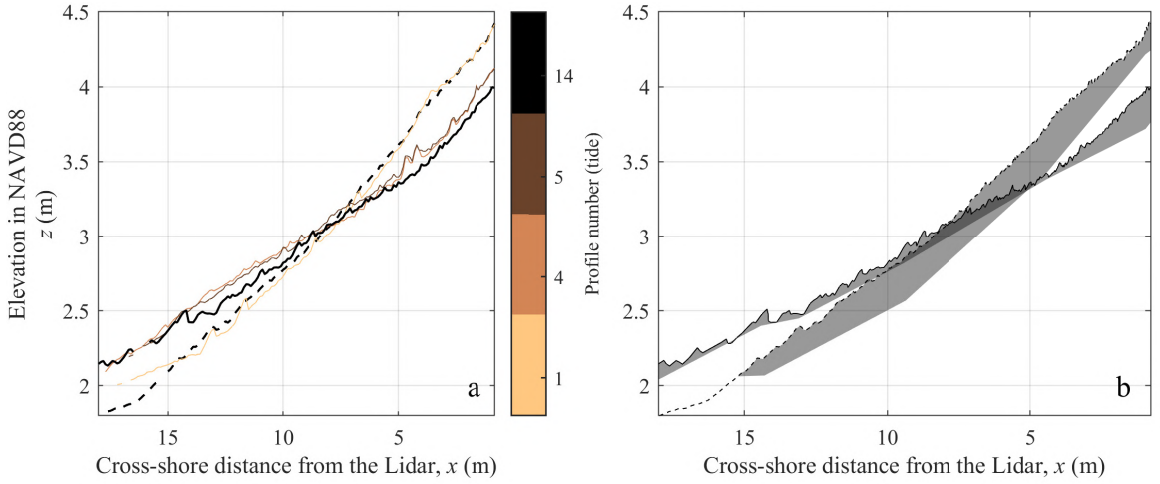

Figure 4.12: (a) Evolution of the cross-shore bed-elevation of the lidar-measured profile, for tide 1, 4, 5 and 14 (survey 3). The dashed black line represents the initial profile during survey 1, and the profile at the end of each displayed high tide is shown with a color, from light copper to black. (b) Revetment profile and pure cobble layer thickness during survey 1 (dashed line) and 3 (plain line).

4.3.3 Sand dynamics

4.3.3.1 Cobble layer and internal sand dynamics

The grey areas shown in Figure 4.9b and Figure 4.12 represent the layer of pure cobbles only. Underneath this layer lies a layer of mixed sand and cobbles, typically composed of smaller cobbles with size decreasing with depth. Pure sand is then found below the mixed layer (Section 4.1). As observed in Figure 4.9b and Figure 4.10b, the thickness of the pure cobble layer varied significantly between surveys. However, it seems that the pure cobble layer thickness does not always follow the bed-elevation variations detected by the lidar and this is investigated in Figure 4.13. This figure compares the revetment surface elevation change to the pure cobble layer thickness change at four locations on the revetment. Circles define surface accretion (erosion) when located on the right (left) hand side of the vertical axis, and pure cobble layer thickness increase (decrease) when located above (below) the horizontal axis. As a consequence, they define sand accretion (erosion) beneath the pure cobble layer when located below (above) the 1:1 dashed line. A simple equation can be written to which captures this relationship:

$$\Delta z_s = \Delta z_r - \delta_c \tag{4.1}$$

where Δz_s represents the sand sub-surface elevation change, Δz_r the revetment surface elevation change and δ_c the change in pure cobble layer thickness.

As a result, seven different possible regimes of change are identified, numbered in Figure 4.13, and defined as follows:

1. Surface erosion less than cobble layer thickness decrease , which requires sand accretion beneath the pure cobble layer.
2. Surface erosion greater than cobble layer thickness decrease , which requires sand erosion beneath the pure cobble layer.

3. Surface erosion with cobble layer thickness increase dominated by sand erosion beneath the pure cobble layer; possible cobble erosion or accretion.
4. Surface accretion less than cobble layer thickness increase, which requires sand erosion beneath the pure cobble layer.
5. Surface accretion greater than cobble layer thickness increase, which requires sand accretion beneath the pure cobble layer.
6. Surface accretion with cobble layer thickness decrease dominated by sand accretion beneath the pure cobble layer; possible cobble accretion or erosion.
7. Surface change = cobble layer thickness change, defined by the thick black dashed line.

The manual measurement of the pure cobble thickness has a measurement accuracy of $1-2$ cm (Section 4.2.2). As a result, points which are away from a line by this order of magnitude cannot be confidently associated with a regime. Nonetheless, regimes 2, 3, 5, 6 and 7 seem to dominate the dynamics of the revetment over the tidal cycle.

To help the reader understand this figure, the "t-1/t-4" plot in Figure 4.13 which compares the cobble layer profiles between tide 1 (t-1) and tide 4 (t-4) (marked as grey shaded regions in Figure 4.9b) is described here as an example. Starting from the uppermost measurement location ($x = 1$ m, blue), the "t-1/t-4" plot shows that the bed-elevation dropped by 0.3 m while the cobble layer thickness decreased by 0.10 m. Thus the cobble layer erosion accounts for only one third of the total surface erosion and therefore sand erosion within the revetment, beneath the pure cobble layer, must have occurred at this location (regime 2). The green marker at $x = 4.4$ m is near the 1:1 line, so could be associated with regime 7 meaning the pure cobble layer thickness change balanced the revetment surface elevation change. The measurement location at $x = 9.4$ m (red) is located near the seaward limit of the accretion zone observed between $x = 8$ m and $x = 18$ m in Figure 4.6b and Figure 4.9a, which explains the surface elevation increase of 0.10 m. However, the cobble layer thickness decreased by more than 0.20 m. Therefore, sand accretion beneath the pure cobble layer must have occurred at this location (regime 6). Finally at $x = 14.4$ m (black), the exposed surface increased in elevation, but with almost zero change in cobble thickness, meaning sand accreted beneath the pure cobble layer. This result can be associated with regime 5 or 6, but the accuracy of the measurement does not enable this to be determined with confidence.

Using the above example of plot "t-1/t-4", it becomes possible to better understand the changes previously observed between survey 1 and 2, and clarify the dynamics of the revetment. The sand which accreted up to $x = 8$ m (see red circle in Figure 4.13) could come from seaward transport of eroded sand from the blue location, but also from landward transport of sand eroded from seaward of the original toe (Figure 4.6b). This indicates that the accretion area on the low and mid part of the revetment is partly due to sand accretion, which infiltrated into the revetment. The cobbles deposited in the toe area, as shown by the RFID data on Figure 4.6, also contributed to this accretion. However, the manual measurements of the pure cobble layer thickness do not necessarily detect this

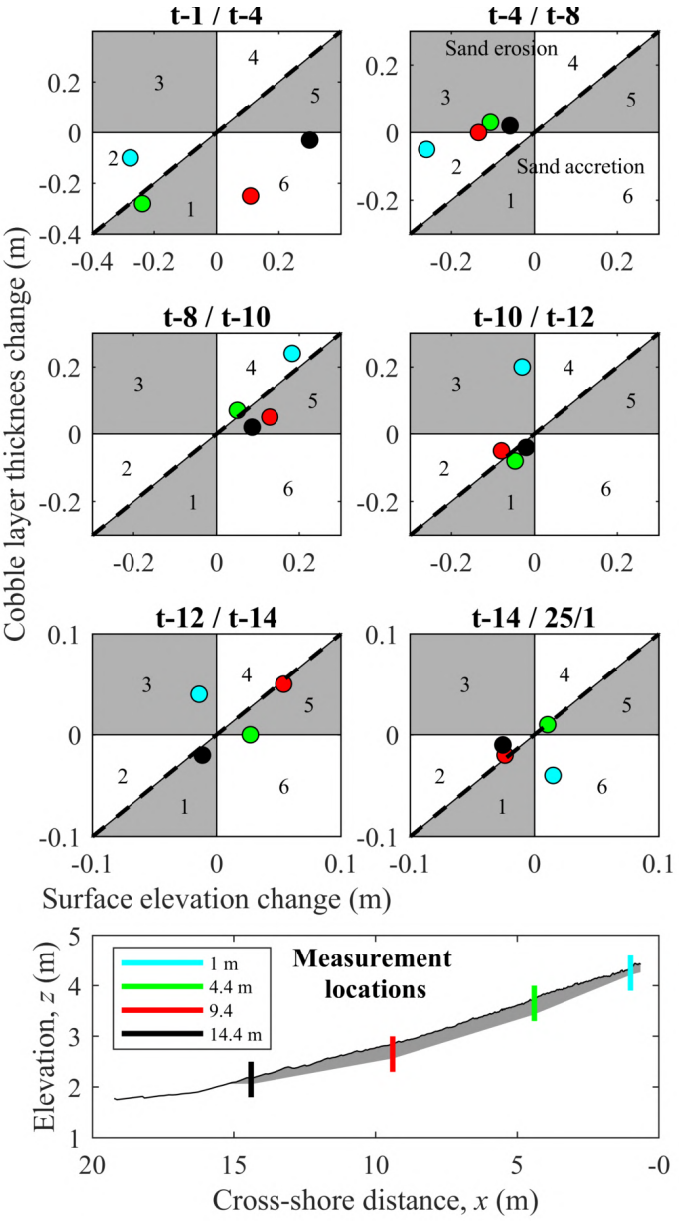

Figure 4.13: Revetment surface elevation change as a function of the pure cobble layer thickness, between each tide where measurements of the cobble layer were obtained (Table 4.2). The dashed black line corresponds to the 1:1 line. The measurement locations were at x = 1 m (blue), x = 4.4 m (green), x = 9.4 m (red) and x = 14.4 m (black), as shown on the bottom panel. The profiles compared refer to the grey shaded pure cobble layer profiles shown in Figure 4.9b and Figure 4.10b. Each plot compares two consecutive cobble layer profiles. Note that there is an extra comparison between the last cobble layer profile, tide 14, and a profile taken the day after, on the 25/1. Also note that "t-1/t-4" represents the comparison of the profiles between survey 1 and 2. The number in each white and grey quadrant refers to the regime discussed in the main text. Note that the 7^{th} regime is represented by the thick black dashed line.

cobble accretion, as the measurement is taken from the surface to the first detected sand elevation. So if cobbles get buried by sand, they are not taken into account in the pure cobble layer thickness. In this context, the area around x = 4.4 m (green circle) seems to gain sand from landward sand fluxes generating accretion at the lower measurement locations, but also from seaward fluxes of sand eroded above (blue circle in Figure 4.13), although it is likely close to a pivot point on the profile. Note this analysis assumes that longshore sediment transport has little net effect on the cross-shore sand movement, as

there is no longshore transport gradient.

4.3.3.2 Bed-level changes at the swash scale

Figure 4.14 shows the continuous bed-level at x = 9.4 m, which experienced sand accretion between tides 1 and 4 (Figure 4.14a), sand erosion between tides 4 and 8 (Figure 4.14b) and sand accretion fron tide 9 and 10 (Figure 4.14c). The right-hand column of Figure 4.14 confirms that the revetment underwent its main shape and slope changes between surveys 1 and 2 and remained in a relatively stable state afterward. Nonetheless Figure 4.14 shows that bed-level changes are a combination of small and medium changes with some rare large events, and that overall, the bed at a single location can oscillate over a 0.3 m vertical range, whether the revetment is significantly reshaped (tide 4, Figure 4.14a) or in a more

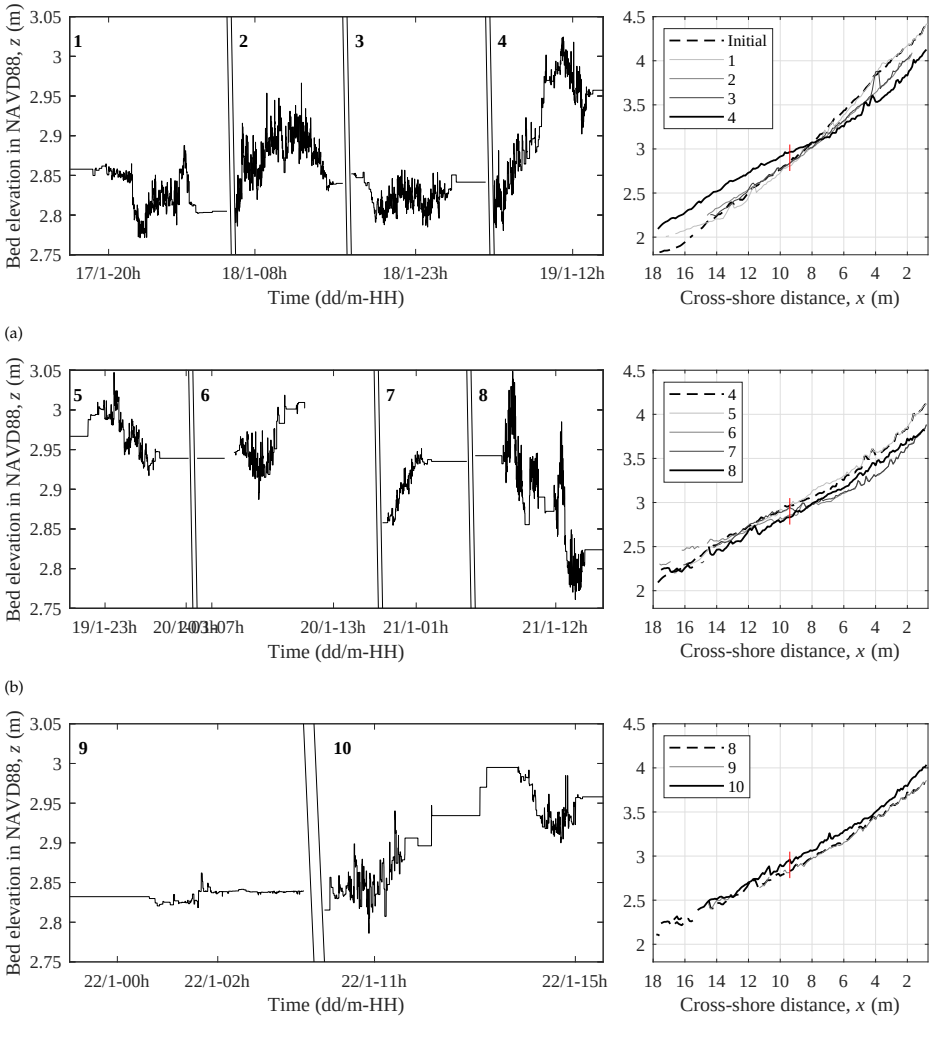

Figure 4.14: *Left panel*: Continuous bed-level at x = 9.4 m, from (a) survey 1 to survey 2, (b) survey 2 to tide 8 and (c) the end of tide 8 to tide 10. Breaks in time where no interaction occurred between swash and cobble is shown by two close parallel lines. *Right panel*: Profile evolution along the lidar measuring transect, from (a) survey 1 to survey 2, (b) survey 2 to tide 8 and (c) the end of tide 8 to tide 10. The dashed line represents the first profile, the thick black line the last profile, and the intermediate profiles are shown from light to dark grey. The vertical red line shows the cross-shore point x = 9.4 m where the revetment bed-level is plotted.

stable state (tide 8 and tide 10, Figure 4.14b). Similar to the revetment surface shape and slope, the sand within the cobble berm appears to reach a more stable state with time. This is observed in Figure 4.13 which indicates that the sand-cobble behaviour gets closer to regime 7 over the course of the experiment. This means that over time, surface changes are driven progressively more by changes in pure cobble layer thickness than by sand accretion and erosion within the cobbles.

Although the sand dynamic within the revetment is likely linked to the sand budget available seaward the revetment – *i.e.*, in the surf zone and breaker bar – the processes involved are more complex and are interdependent, which explains why under the same conditions, sand accretion within the cobbles can occur at the bottom of the revetment while erosion occurs at the top. As a result, sand can be trapped in the revetment and increase the revetment volume while cobbles are transported away. This observation also highlights the capacity of the revetment to retain sand underneath and within the cobbles, even under energetic conditions, and explains the relatively small overall volume loss.

4.3.3.3 Sand surface dynamics

Section 4.3.3.1 showed that the revetment dynamics are not limited to cobble motion, but involves complex internal sand dynamics. If a sufficient volume of sand penetrates the revetment, parts of the cobble ridge can become buried (*i.e.*, saturation of the cobble layer with sand, hereafter refer to as “saturation"), which shifts the visual cross-shore sand–cobble delimitation landward. As a consequence, the sand volume present in the sandy beach seaward of the revetment (equivalent to the sandy part of a composite beach) is also important. Note that although the lidar was removed and no complete GPS and RFID survey were performed after the 24^{th} of January 2019, the revetment was still observed and some individual cobble positions were recorded. Figure 4.15 shows two photos of the revetment taken on two consecutive days, the 27^{th} of January 2019 and the 28^{th} of January 2019. The white circle marks a large cobble which did not move at all between the two observations (checked by GPS). It is clear that while the large cobble has not moved, and the surrounding cobbles have unlikely moved landward under the very calm conditions

Figure 4.15: *Left photo*: photograph of the revetment toe taken on the afternoon on the 27^{th} of January 2019. *Right photo*: photo of the revetment toe taken on the 28^{th} of January 2019. The white circle shows a large cobble which did not move over the two days. *Photo taken by Paul Bayle*.

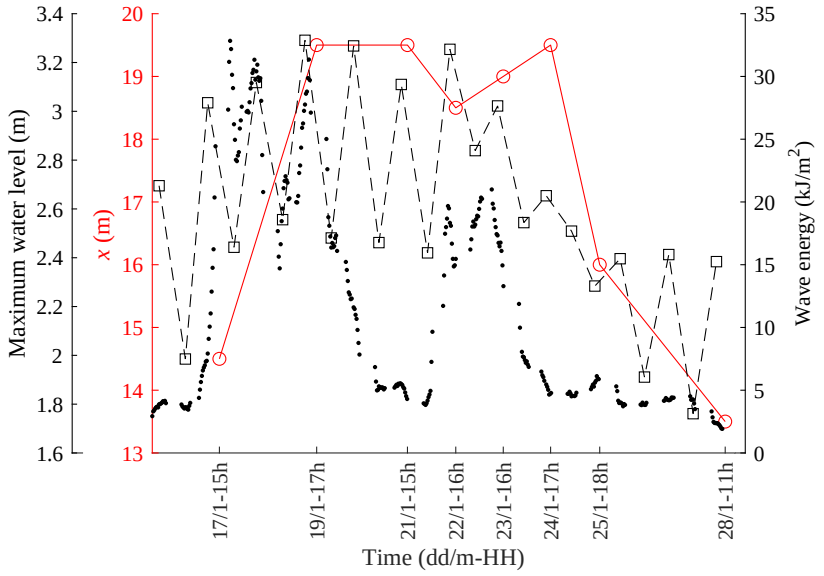

Figure 4.16: *Left axis* (squares): Evolution of the maximum mean water level elevation at each high tide. *Left axis* (circles): Evolution of the cross-shore position of the revetment toe measured during low tide. Note that the direction of the y axis is flipped from all the previous figures, with seaward distance from the lidar increasing upward. *Right axis* (dots): Evolution of the offshore wave energy every 30 minutes during interactions time (zone in grey on Figure 4.5a) and averaged over a 2 hour moving average window. Note that the times shown on the x-axis correspond to the toe location measurements.

occurring during these days, sand accreted on top of them, thus covering the revetment toe and moving the visible toe landward. Sand actually started accumulating on top of the toe on the 25^{th} of January 2019, as shown by Figure 4.16.

Figure 4.16 shows the evolution of the cross-shore sand–cobble limit, the maximum mean water level and the offshore wave energy. From its position at $x = 15$ m measured on 17/1 after a calm period of relatively low water level and wave height, the toe limit advanced seaward to $x = 19.5$ m on 18/1 and 19/1 to remain around this position until the 25/1. This position was associated with high energetic waves, up to $40\,kJ/m^2$, and high water levels, up to 3.26 m, although a small decrease occurred on 20/1 and 21/1. Finally, the toe started moving landward to the position shown by Figure 4.15, at $x = 13.5$ m NAVD88 on 28/1. This is correlated with the weak wave energy, dropping below $5\,kJ/m^2$, and the low water level less than 2.5 m which characterise the end of the spring tidal cycle.

The cross-shore evolution of the sand–cobble limit, hence sand coverage over the revetment, appears to be linked to the offshore wave conditions and water levels, which drive sand accretion and erosion of the sandy beach seaward of the revetment. Indeed, between 18/1 and 24/1, the sandy beach was marked by erosion (Figure 4.6a) while between 24/1 and 28/1, the sand significantly accumulated seaward of the revetment (visual observation). As the wave conditions were very calm between the 24/1 and 28/1, high tide water level relatively low, and because cobbles have unlikely moved landward, the offshore conditions are responsible for the accretion of sand on top of the revetment observed after 25/1. This correlates with the fact that the accretion of sand on the beach is dependent on the available budget directly seaward of the beach (Phillips et al., 2019). As a consequence, the volume of sand able to cover the revetment is a direct function of the offshore sand budget, hence wave conditions and water levels. Note that sand can also generally be transported by

wind, but in this specific case, it did not promote aeolian transport over the revetment. Indeed, although the wind was relatively strong, increasing from 2 to 10 m/s over this period (Figure 4.5), its direction oscillated between 50 and 100 degrees, which corresponds to the offshore direction for this beach. However, the current data does not allow to confidently analyse the exact correlation between wave conditions, water levels and sand budget seaward of the revetment with the sand accretion over the toe (*i.e.*, cross-shore sand-cobble limit) in terms of response time. Future work will investigate long term monitoring of the whole area, and investigate these relationships.

4.4 Discussion

4.4.1 Model of internal sand dynamics

The data revealed that changes in the elevation of the surface of the revetment occurred due to both addition and removal of cobbles from the surface as well as erosion and accretion of sand within. Five of the seven possible regimes were frequently observed in Section 4.3.3.1, and it is assumed that these are the most common for dynamic revetments and natural composite beaches. Note that different regimes were observed at different locations during the same tide as material eroded from one location can be deposited on another. It was also seen that sand accretion and erosion at a particular location is likely dependent on its relative position within the swash zone. The large cobbles accumulated within the toe area (Figure 4.7 and Figure 4.8), which limits cobble transport in this zone and may act as a trap for sand. The combination of cross-shore grading (gradual decrease of cobble size from the bottom to the top) and the relative position of the swash could explain the fact that sand erosion within the cobbles mainly occurred on the upper part of the revetment (sand erosion at $x = 1\,\mathrm{m}$ occurred five times, Figure 4.13). While the internal sand dynamics may be driven by a combination of all these parameters, the sand accretion on top of the revetment toe was related with periods of sand accretion and erosion in the sandy beach seaward of the revetment (Phillips et al., 2019). When enough sand was available seaward of the revetment, sand began saturating the revetment interstices, and accreted on top of the revetment toe (Figure 4.15). Therefore, the water level and wave conditions, which both influence this sediment budget, were found to be related to the position of the sand–cobble limit (Figure 4.16). However, the time response of these processes and the exact relationship will be further investigated with the long term monitoring datasets. In general, as mentioned by Bayle et al. (2020), more investigation of the internal and layer dynamics of revetments and composite beaches is required to fully understand the processes involved. The barriers preventing such measurements are technical, as no accessible tools allow a real-time survey of the thickness of the three different layers found in dynamic revetments or composite beach ridges.

The dynamics of the revetment and the way it rapidly evolves toward a stable state under changing conditions is complex as it involves two types of sediment. Nonetheless, an analysis of the chronology of changes is proposed here. Bayle et al. (2020) found the shape and slope of a dynamic cobble berm revetment is directly correlated to the offshore

wave conditions (wave steepness in their laboratory experiment), with rapid morphological response. This was previously studied for pure gravel beaches by Powell (1990) and van der Meer (1988). Therefore, it is suggested that the reshaping of exposed cobbles happens first until a stable slope is reached, and this triggers the internal sand changes (for example between survey 1 and 2, “t-1/t-4"). The swash motions cause rearrangement of surface particles, which can in turn lead to temporary exposure and movement of underlying gravel and sand. The internal and underlying sand then becomes the most stable part of the revetment, while the pure cobble layer keeps changing under cross and longshore transport (Figure 4.13 and Figure 4.14). Under this constant reshaping, limited sand erosion and accretion occurs. Sand erosion is driven by the backwash water volume which percolates through the cobbles and contributes to the sinking process described in Bayle et al. (2020), while sand accretion and compaction is driven by kinetic sieving (Wright et al., 1982). Kinetic sieving is driven by the vibratory swash mechanism, which acts as a shear force and causes the vertical sorting of particles (small particles at the bottom and large at the top), hence sand compaction within the cobble ridge until saturation. Note that these processes take longer in the upper part of the revetment ($x = 1\,\mathrm{m}$) as it is subject to less swash action.

The previous analysis of sand transport within the revetment coupled with observations led to the schematic model shown in Figure 4.17 describing the revetment states and the associated sand dynamics. Figure 4.17 presents two end states of the dynamic revetment: the Depressed Subsurface Runoff Interface (DSRI) end state and the Elevated Subsurface Runoff Interface (ESRI) end state. These two states presented here are the opposite end states of the dynamic revetment (like the reflective and dissipative are the opposite end state of sandy beaches, Wright and Short, 1984).

The DSRI state (top sketch) has a thick active pure cobble layer in which the subsurface runoff interface is at a low elevation (in red on Figure 4.17) where a tight packing of sand grains reduces further infiltration below this interface. The pure cobble layer above the interface has a high porosity, and extends over a wide active width. The DSRI state occurs after significant sand erosion within the cobbles, which lowers the subsurface runoff interface to a lower elevation within the revetment. Swash water percolating through the permeable layers above and flowing back toward the ocean creates water ponds at the bottom of the revetment as the subsurface runoff interface is lower than the top of the sandy beach at the revetment toe (top left corner photograph in Figure 4.17). Therefore, the cross-shore sand–cobble separation is closer to the sea due to preceding sand erosion at the toe of the revetment.

The ESRI state (bottom sketch) has a thinner and narrower active pure cobble layer due to sand partially filling the pore spaces. This state is observable after a period of sand accretion within the cobbles, which brings the subsurface runoff interface to a higher elevation over the majority of the cross-shore revetment width. Swash volume percolating through the permeable layers and flowing back toward the sea does not create a water

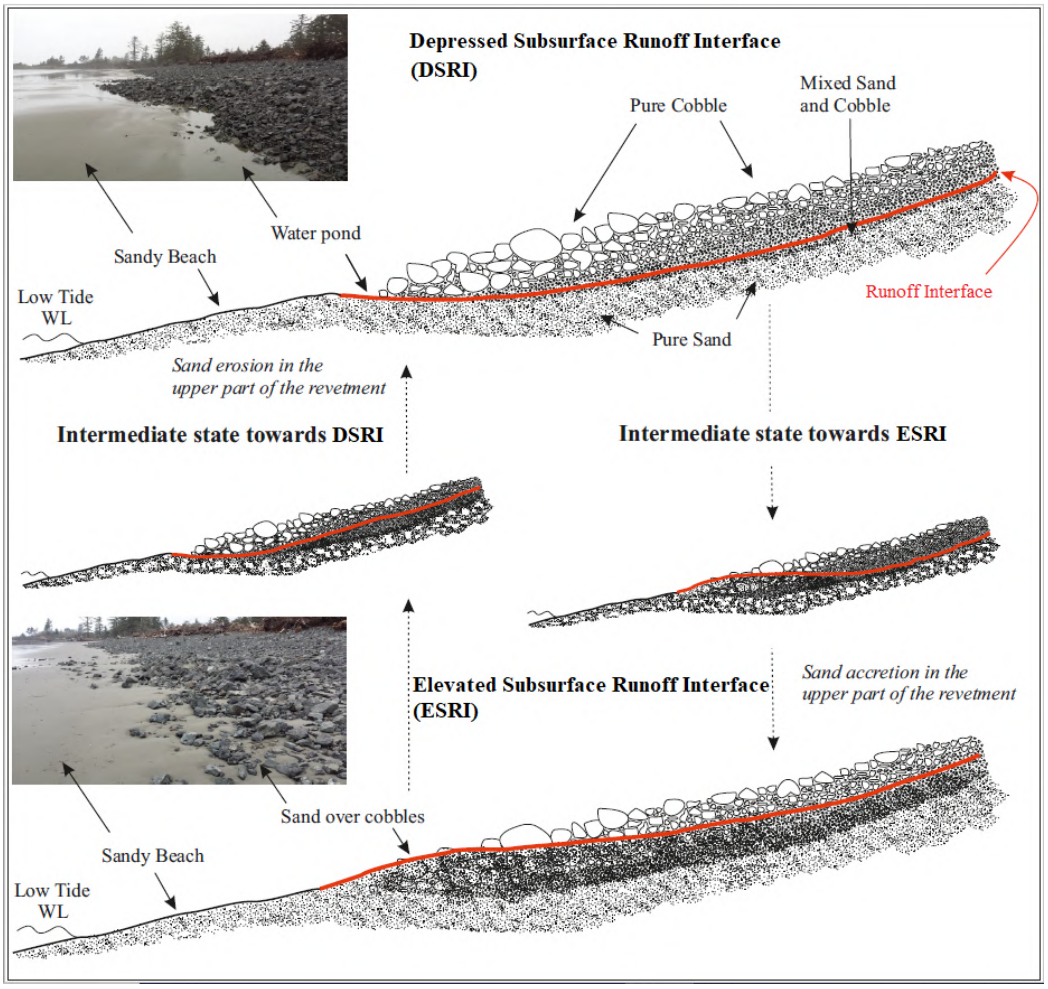

Figure 4.17: Model of the revetment state and the associated internal sand dynamics. The subsurface runoff interface where the swash water volume percolates through the structure is represented by the thick red line. It corresponds to the interface between high and low permeability material and is approximately the interface between the pure cobble and mixed sand and cobble layers. (*Top sketch*): Depressed Subsurface Runoff Interface (DSRI) state. The top photo, taken on the 22^{th} of January 2019, shows the observable revetment features resulting from this state. (*Bottom sketch*): Elevated Subsurface Runoff Interface (ESRI). The bottom photo, taken on the 27^{th} of January 2019, shows the observable revetment features resulting from this state. Note that this model focuses on the internal sand dynamics and so the cobble layer thickness is kept unchanged. *Photos taken by Paul Bayle*.

pond as the elevation of the subsurface runoff interface is higher than the sandy beach level. Therefore, the cross-shore sand–cobble limit is closer to the land due to sand accumulation over the cobbles at the toe of the revetment (bottom left corner photograph in Figure 4.17).

Figure 4.17 also provides insight into the intermediate states. Evolving from the DSRI to the ESRI state (middle right sketch), the subsurface runoff interface elevation firstly increases on the lower part of the revetment due to sand accretion within the cobbles, while maintaining its previous elevation on the upper part (the upper part will rise at a later time to reach the stable ESRI state). During this intermediate state, swashes are globally weaker due to lower water levels and wave energy. This yields to low infiltration and exfiltration flow with less particle rearrangement, leading to less internal and underlying sand erosion and accumulation of sand within the cobbles. In addition, the volume of the revetment increases due to the infiltrated sand volume, which can eventually saturate the interstices

and cover the cobbles.

In contrast, evolving from the ESRI to the DSRI state (middle left sketch), the subsurface runoff interface elevation first decreases on the lower part of the revetment due to sand erosion within the cobbles, while maintaining or increasing its elevation on the upper part (the upper part will drop at a later time to reach the stable DSRI end state). During this state, swash interactions are high, and the combination of high water levels and energetic waves generate energetic swashes leading to significant particle rearrangement. This yields to high infiltration and exfiltration flow within the pure cobble layer. Therefore, assuming that no gravels are lost seaward of the revetment toe as presented in Section 4.3.1.3 and Section 4.3.2.1, the volume of the revetment decreases due to the sand volume washed away from the underlying revetment layers (*i.e.*, winnowing of the internal sand, from the layers referred to 2) and 3) in Section 4.1).

The intermediate state towards DSRI and the DSRI end state is illustrated by plot "t-4/t-8" on Figure 4.13. Between the end of tide 4 and the end of tide 8, sand erosion occurred at each measurement location leading to the DSRI state. Water ponds were visible at the toe of the revetment as shown on the top left corner photograph in Figure 4.17. While the toe of the revetment remained at the same position over this period (between the 19/1 and 21/1 on Figure 4.16) the total revetment volume decreased by $1.48\,m^3/m$. This reduction in total volume due to sand erosion is consistent with the model towards the DSRI end state. In fact it appears that the majority of the volume loss between tides 4 and 8 occurred during the highest energy waves coinciding with the highest tide 6, when $1.66\,m^3/m$ of material was removed from the cobble ridge. Therefore, between tide 6 and tide 8, the revetment had already begun to recover and gained $0.18\,m^3/m$. So the DSRI state was likely attained after tide 6, but because no thickness measurements were taken on that day, tide 8 is used for illustration.

Unfortunately, over the period of lidar measurement, the four measurement locations did not experience sand accretion at the same time, hence there is not a clear example for the Elevated Subsurface Runoff Interface (ESRI) end state. The bottom photo on Figure 4.17 shows the revetment on the 27^{th} of January, which is likely to be at the ESRI state, but this cannot be confirmed since the lidar measurements had ceased. Similarly, it is possible the revetment was in the ESRI state on the first day of measurements, after a period of calm conditions when the toe was further landward..

4.4.2 Performance of the revetment under energetic conditions

This study has shown that the revetment volume can increase and decrease over time due to internal sand accumulation or removal. Between tides 5 and 6, the revetment volume decreased by up to $1.66\,m^3/m$ along the lidar measuring transect. However, over almost the full spring tidal cycle, from 17^{th} of January to 25^{th} of January (so one day after survey 3), the revetment lost only $0.31\,m^3/m$. This highlights the rapid shape and volume changes the revetment can undergo, but also its capacity to rapidly recover after energetic events, demonstrating a dynamic stability. This recovery was related to the internal sand dynamics,

but also to the sand accretion on top of the revetment after saturation. The photos shown in Figure 4.15 prove that the sand accretion continued after 25^{th} of January. Overall, the revetment showed a capacity to store sand on the sub-aerial part of the beach, as shown in the laboratory by Bayle et al. (2020). More generally, although the revetment does not have a large cross-sectional volume of cobble, the vertical rearrangement of the ridge as an active cobble layer with internal sand packing seems to naturally form as a result of the internal sand dynamics, and may do so over time even if a large cross-section of cobble material is initially placed during construction. However, since the revetment was constructed with relatively small volumes of material placed over time, we cannot directly test this theory at North Cove at this point.

In summary, the dynamic cobble berm revetment showed a dynamic stability and remained a coherent structure under the storm conditions during this spring tide cycle. The maximum significant wave height measured was just above 6 m with a peak wave period above 17 s (Figure 4.5). The volume of the dynamic cobble berm revetment was not significantly affected, with minimal net loss due to internal sand loss and local cobble removal by longshore transport, but with almost no material lost offshore. At this study site, the total revetment volume which led to this level of protection for at least an energetic spring tidal cycle was 5196 m^3, corresponding to 16.23 m^3/m (Table 4.1). The total cost for this volume to be placed was $77,591, which corresponds to $242.38 per linear metre. Therefore, although the long-term performance of the revetment is still being monitored, it has already shown robust dynamic behaviour and ability to recover following a spring tide cycle and storm conditions, while protecting the coastline against erosion and overtopping. The overall cost of the structure was around 4 to 10 times lower than an equivalent conventional hard engineering structure, however it is noted that updrift revetment areas may require renourishment over time. With this in mind, ongoing work is monitoring the effectiveness of a “feeder bluff" of cobbles located updrift of the study site.

4.5 Preliminary guidelines for maintenance and nourishment of a dynamic cobble berm revetment

Maintenance of dynamic cobble berm revetment should be expected over time, especially when subject to strong longshore sediment transport as in this study. This short guidance section aims to extend that provided by Bayle et al. (2020), but focusing on the nourishment of the revetment and the sandy beach in front. This guidance is based on the knowledge gained from the North Cove dynamic revetment but is expected to be transferable.

The present analysis showed the revetment is able to store sand underneath the cobbles, and protect most of it during energetic conditions and high water levels. It also showed that during calm conditions, sand naturally accretes over the revetment face – accretion first occurs within the revetment until saturation – moving the visible toe landward. Testing of a “feeder bluff" of cobbles updrift of the study area is currently ongoing, however direct renourishment of the revetment is likely to be required eventually. It is suggested that any revetment renourishment is done during the summer when the revetment may

be expected to be fully or partly covered by sand. Doing so, the sand covered by the imported material is partially protected against aeolian and swash transport and much of this volume can become an integral part of the cobble ridge. The sand and cobbles will then naturally rearrange, through slope reshaping and kinetic sieving, potentially resulting in an enhanced nourishment volume. It is also suggested that a simple and cost effective random placement of the material, as described in Bayle et al., 2020, is sufficient.

4.6 Conclusion

The dynamic cobble berm revetment in North Cove (USA) was intensively monitored over 10 days, during an energetic spring tidal cycle in January 2019. A representative area of the revetment was intensively monitored using lidar, GPS, RFID and visual observations.

The surface elevation of the revetment underwent changes of ±0.5 m over the experiment. These changes were found to be caused by relatively large high tide water level and offshore wave energy. The revetment adapted rapidly to changing wave conditions, reaching a stable shape and slope after four high tides. It also demonstrated a dynamic stability by remaining as a coherent structure despite losing some of its volume. It also showed a capacity to rapidly recover most of its volume after a period of erosion. Overall, the revetment volume decreased on average by $0.67\,m^3/m$. This volume loss was driven by both alongshore cobble transport and seaward sand transport. Longshore sediment transport was shown to have an impact on local and small scale changes, especially in the redistribution of large particles, while cross-shore sediment transport was more important for large scale and overall changes.

The instrumented cobbles illustrated the dominant eastward longshore sediment transport and demonstrated that almost no cobbles were transported seaward of the revetment toe. RFID also allowed a zone of accumulation around the toe of the revetment to be detected. It is not clear whether the cobbles were stuck in this zone or if they were brought there at the end of each tide. Future work will focus on novel techniques to monitor individual cobble in real time to determine where and how they are transported.

The sand dynamics, both within the revetment and seaward of the revetment, appeared to be important in the overall behaviour. The internal sand dynamics were found to be a complex balance of accumulation and removal of sand within the cobbles which varied depending on cross-shore location. The sand within the cobbles was also found to reach a stable state, which likely led to the overall structure stability. Significant internal sand variations were found to be driven by the rearrangement of large particles, mainly during periods of significant revetment shape and slope modification, while smaller variations were attributed to backwash water (erosion) and kinetic sieving (compaction). Future work will focus on novel techniques to monitor the sub-surface runoff interface in real time (or at least more frequently) to assess the runup dissipation and swash absorption relative to active cobble layer dynamics and subsurface permeability.

A model of internal sand dynamics for revetment and composite beaches was developed. The model describes two end states, the Depressed Subsurface Runoff Interface

(DSRI) and the Elevated Subsurface Runoff Interface (ESRI), respectively characterized by a low and high runoff interface elevation. While the end states depend on the amount of sand in the revetment, the intermediate states define how the revetment is changing due to the hydrodynamics, and relative to its previous state. The lower part of the revetment is the most active part in all cases, with rapid saturation and erosion. Note that this model holds for the experiment described here, and further data would be beneficial to robustly validate it.

In conclusion, the dynamic revetment withstood the energetic conditions over the spring tidal cycle, and protected the sand scarp while armouring the underlying sand. It offered low-cost and efficient protection over the 60–metre long study area. However, the reduction of the cobble thickness in some places caused by the unidirectional longshore sediment transport suggests that updrift renourishment may be necessary. Some preliminary guidelines were drawn from this study to extend those presented by Bayle et al. (2020).

Acknowledgements

Funding: Paul Bayle is supported by a PhD scholarship through the Engineering and Physical Sciences Research Council (EPSRC) Centre for Doctoral Training (CDT) in Water Informatics: Science & Engineering (WISE). Traveling and living fees associated with this experiment were partially covered by a Santander Mobility Grant, obtained via the University of Bath.

The authors want to thank the Washington Department of Ecology Coastal Monitoring & Analysis team for their logistical assistance and help in the field. The authors would also like to thank the community of North Cove for their warm welcome and support throughout the experiment. Special thanks to Richard and Dianne Harris for providing a warm and dry place during the experiment, and to Connie Allen for organising the communications and public relations around the experiment. Finally, they want to thank William Bazeley, Neil Price, Robert Dyer and David Surgenor from the University of Bath for their technical support during the experiment preparation.

References

Ahrens, J. P. (1990). Dynamic revetment. *Coastal Engineering* 138, 1837—1850.

Allan, J. C. and Gabel, L. L. (2016). *Monitoring the response and efficacy of a dynamic revetment constructed adjacent to the columbia river south jetty, Clatsop county, Oregon.* Tech. rep. O-16-07. Oregon Department of Geology and Mineral Industries.

Allan, J. C., Geitgey, R., and Hart, R. (2005). Dynamic revetments for coastal erosion stabilization: a feasible analysis for application on the oregon coast. *Oregon Department of Geology and Mineral Industries* Special issue, 37.

Allan, J. C., Harris, E., Stephensen, S., Politano, V., Laboratory, H., Folger, C., and Nelson, W. (2012). *Hatfield Marine Science Center Dynamic Revetment Project*. Tech. rep. Hatfield Marine Science Center, Oregon State University.

Allan, J. C., Hart, R., and Tranquili, J. V. (2006). The use of Passive Integrated Transponder (PIT) tags to trace cobble transport in a mixed sand-and-gravel beach on the high-energy Oregon coast, USA. *Marine Geology* 232.

Allan, J. C. and Komar, P. D. (2002). Extreme storms in the Pacific Northwest coast during the 1997–98 El Niño and 1998–99 La Niña. *Journal of Coastal Research* 18, 175—193.

Almeida, L. P., Masselink, G., Russel, P. E., and Davidson, M. A. (2015). Observations of gravel beach dynamics during high energy wave conditions using a laser scanner. *Geomorphology* 228, 15—27.

Bayle, P. M., Blenkinsopp, C. E., Conley, D., Masselink, G., Beuzen, T., and Almar, R. (2020). Performance Of A Dynamic Cobble Berm Revetment for Coastal Protection, under increasing water level. *Coastal Engineering* 159.

Blenkinsopp, C. E., Mole, M. A., Turner, I. L., and Peirson, W. L. (2010a). Measurements of the time-varying free-surface profile across the swash zone obtained using an industrial LiDAR. *Coastal Engineering* 57, 1059—1065.

Bluck, B. J. (1967). Sedimentation of Beach Gravels: Examples from South Wales. *Journal of Sedimentary Petrology* 37, 128—156.

Carter, R. W. G. and Orford, J. D. (1984). Coarse clastic barrier beaches: a discussion of the distinctive dynamic and morphosedimentary characteristics. *Marine Geology* 60, 377—389.

Church, J. A., Clark, P. U., Cazenave, A., Gregory, J. M., Jevrejeva, S., Levermann, A., Merrifield, M. A., Milne, G. A., Nerem, R. S., Nunn, P. D., Payne, A. J., Pfeffer, W. T., Stammer, D., and Unnikrishnan, A. S. (2013). "Climate Change 2013: The Physical Science Basis. Contribution of Working Group I to the Fifth Assessment Report of the Intergovernmental Panel on Climate Change". Cambridge, United Kingdom and New York, NY, USA: Cambridge University Press. Chap. 13, 1137—1216.

DeConto, R. M. and Pollard, D. (2016). Contribution of Antarctica to past and future sea-level rise. *Nature*, 591—597.

Downie, K. A. and Saaltink, H. (1983). An artificial cobble beach for erosion control. *Coastal Structure '83*. Reston, Va., American Society of Civil Engineers, 846—859.

Kaminsky, G. M., Ruggiero, P., Buijsman, M. C., McCandless, D., and Gelfenbaum, G. (2010). Historical evolution of the Columbia River littoral cell. *Marine Geology* 273, 96—126.

Kirk, R. M. (1992). Experimental beach reconstruction-renourishment on mixed sand and gravel beaches, Washdyke Lagoon, South Canterbury, New Zealand. *Coastal Engineering* 17, 253—277.

Komar, P. and Allan, J. C. (2010). "Design with Nature strategies for shore protection - The construction of a cobble berm and artificial dune in an Oregon State Park". *Puget Sound Shorelines and the Impacts of Armoring—Proceedings of a State of the Science Workshop*. U.S. Geological Survey Scientific Investigations Report 2010-5254, 117—126.

Lesser, G. R. (2009). "An Approach to Medium-term Coastal Morphological Modelling". PhD thesis. University of Canterbury, New Zealand.

Loman, G. J. A., van Gent, M. R. A., and Markvoort, J. W. (2010). Physical model testing of an innovative cobble shore, Part I: Verification of cross-shore profile deformation. *Third International Conference on the Application of Physical Modelling to Port and Coastal Protection*.

Lorang, M. S. (1991). An artificial perch-gravel beach as a shore protection structure. *Coastal Sediments '91*. Vol. 2. Reston, Va., American Society of Civil Engineers, 1916—1925.

Martins, K., Blenkinsopp, C. E., Power, H. E., Bruder, B., Puleo, J. A., and Bergsma, E. W. J. (2017b). High-resolution monitoring of wave transformation in the surf zone using a LiDAR scanner array. *Coastal Engineering* 128, pp. 37 – 43. DOI: 10.1016/j.coastaleng.2017.07.007.

Martins, K., Blenkinsopp, C. E., and Zang, J. (2016). Monitoring Individual Wave Characteristics in the Inner Surf with a 2-Dimensional Laser Scanner (LiDAR). *Journal of Sensors*, pp. 1 – 11. DOI: 10.1155/2016/7965431.

Masselink, G. and Van Heteren, S. (2014). Response of wave-dominated and mixed-energy barriers to storms. *Marine Geology* 352, 321—347.

Michalsen, D. R. (2018). *Feasibility of long-term shoreline stabilisation alternatives between North Cove and Tokeland, WA*. Tech. rep. U.S. Army Corps of Engineers, Seattle District.

Orford, J. D. (1975). Discrimination of particle zonation on a pebble beach. *Sedimentology* 22 (3), 441—463.

Phillips, M. S., Blenkinsopp, C. E., Harley, K. D. S. M. D., and Turner, I. L. (2019). Modes of berm and beachface recoveryfollowing storm reset: observations using a continuously scanning lidar. *Journal of Geophysical Research - Earth Surface* 124 (3), 720—736.

Powell, K. A. (1988). The dynamic response of shingle beaches to random waves. *Coastal Engineering* 130, 1763—1773.

Powell, K. A. (1990). *Predicting Short Term Profile response for shingle beaches.* Tech. rep. SR 219. HR Wallingford, Oxfordshire, UK.

Pye, K. and Blott, S. J. (2018). *Advice on Sustainable Management of Coastal Shingle Resources*. Tech. rep. 273. Natural Resources Wales.

Ruggiero, P., Kaminsky, G. M., Gelfenbaum, G., and Voigt, B. (2005). Seasonal to interannual morphodynamics along a high-energy dissipative littoral cell. *Journal of Coastal Research* 21, 553—578.

Turner, I. L., Russel, P. E., and Butt, T. (2008). Measurement of wave-by-wave bed-levels in the swash zone. *Coastal Engineering* 55, 1237—1242.

Ward, D. L. and Ahrens, J. P. (1992). *Laboratory study of a dynamic berm revetment*. Tech. rep. US Army Corps of Engineers.

Weiner, H. M., Kaminsky, G. M., Hacking, A., and McCandless, D. (2019). *North Cove Dynamic Revetment Monitoring: Winter 2018-2019*. Tech. rep. 19-06-008. Shorelands and Environmental Assistance Program, Washington State Department of Ecology.

Williams, A. T. and Caldwell, N. E. (1988). Particle size and shape in pebble-beach sedimentation. *Marine Geology* 82, 199—215.

Wright, L. D. and Short, A. D. (1984). Morphodynamic variability of surf zones and beaches: a synthesis. *Marine Geology* 56, 93—118.

Wright, L. D., Short, A. D., and Nielsen, P. (1982). *Morphodynamics of high energy beaches and surf zones: A brief synthesis.* Tech. rep. 82/5. Coastal Study Unit, University of Sydney.

van Hijum, E. and Pilarczyk, K. W. (1982). *Equilibrium Profile and Longshore Transport of Coarse Material Under Regular and Irregular Wave Attack*. Publication (Waterloopkundig Laboratorium (Delft, Netherlands)). Delft Hydraulics Laboratory.

van der Meer, J. W. (1988). "Rock slopes and gravel beaches under wave attack." PhD thesis. University of Technology, Delft.

van der Meer, J. W. and Pilarczyk, K. W. (1986). Dynamic Stability of Rock Slopes and Gravel Beaches. *Coastal Engineering* 125, 1713—1726.

Chapter concluding remarks

In this Chapter, the behaviour and performance of the dynamic revetment in North Cove was investigated through a field experiment. Although the diameter and shape of the particles were significantly different, similarities were found with the laboratory results presented in Chapter 3. The revetment shape and slope changed rapidly under swash action while remaining as a coherent structure. As in the laboratory, the revetment was able to recover from periods of erosion, protect the hinterland from erosion by armouring the underlying sand and limit overtopping. However, the important rollover transport observed in the laboratory was not measured in the field. We attribute this difference to the following constraints: 1) due to the size if the RDFI PIT, the instrumented cobbles in North Cove were representative of the larger part of the material. As mentioned in Chapter 4, natural sorting of the revetment in North Cove tends to bring large cobbles at the bottom of the revetment, which are therefore measured by the RFID. 2) The North Cove revetment is different from the revetment tested in the laboratory in a sense that it does not have accommodation space at the back but instead, it is blocked by a woody barrier of drift logs. For this reason, the revetment cannot physically retreat and cobbles cannot rollover the crest, but instead come back down the slope under gravity once they reach the barrier. 3) Strong longshore transport was present in the field, and not in the laboratory. The action of longshore transport on cobbles tends to bring them down-slope, as if a ball was thrown alongshore a slope. Nonetheless, it appeared that longshore transport played a limited role in the overall revetment changes, as it only had a local effect on the overall bed level changes. However, over longer time scale, longshore transport has a significant importance in terms of material losses, and is the main cause of maintenance requirement. The high tide water level and the offshore wave conditions (*i.e.*, energy) were identified as both important in revetment changes, especially when combined. However, it was found that a high water level could generate significant changes even if associated with low energy conditions (Chapter 5 will help us understanding this). The cross-shore grading of the revetment also appeared to be important for particle motion, but technical limitations prevented investigation of the individual particle motion in real-time. Further work using illuminated cobbles tracked using video imagery is currently being developed and may be able to shed light on this.

The sinking process observed in the laboratory was not directly observed, but the importance of the underlying and internal sand dynamics was identified and studied in detail. In the field, both sand accretion and erosion occurred, which suggests that the revetment and underlying sand was closer to a stable state than in the laboratory. Beyond the difference in wave forcing between the two experiments, this different sand dynamics is mainly attributed to the sudden installation of the revetment on a profile which was not in equilibrium with the hydrodynamics forcing, and even in erosion 'demand' under the increased water levels. However, in both experiments, although the pure cobble layer was able to reach a stable state quickly, the overall volume and shape was attained only when the underlying sand was close to a stable state. This observed sand dynamic was

used to develop a model for the behaviour of the different layers of dynamic revetments and composite beach ridges. The further insight gained from this experiment led to the development preliminary design guidelines for dynamic revetment maintenance which complement the guidance presented in Chapter 3.

The overall shape and volume changes of the revetment appeared to be driven by both the cobbles and sand fluxes. To better understand these fluxes, it seems necessary to look at the interaction between the swash and the revetment face. It is therefore important to investigate smaller scale processes, both in time and space, to understand the dynamics of the revetment during a tidal cycle, and this is the topic covered in Chapter 5.

Chapter 5

High-resolution measurements of a dynamic cobble berm revetment during a spring tidal cycle: swash zone morphodynamics

This chapter is based on the research article submitted in Coastal Engineering, and currently under review.

Paul M. Bayle, Chris E. Blenkinsopp, Kévin Martins, George Kaminsky, Heather Weiner and David Cottrell (In review). High-resolution measurements of a dynamic cobble berm revetment during a spring tidal cycle: swash zone morphodynamics. *Coastal Engineering*.

Abstract

Dynamic cobble berm revetments are a promising soft engineering technique capable of protecting sandy coastlines by armouring the sand and dissipating wave energy to protect the hinterland against wave attack. While this type of coastal protection has been studied for the last 30 years, there are few applications, monitoring data is very rare, and their short-term evolution forced by energetic swash motions has never been investigated. To better understand the behaviour of dynamic cobble berm revetments, the revetment at North Cove (WA, USA) was monitored for a 10-day period in January 2019, over a spring tidal cycle. A 2-D lidar was used to survey a cross-shore profile of the revetment, and record all surface changes and interaction with swashes at high spatial (0.1 m) and temporal (swash-by-swash) resolution. Swash events over the revetment mainly generated small fluxes ($\pm 50\, kg/s$), with some rare large events, which showed that revetment changes are caused by a combination of typically small cobble movements as well as sand erosion and accretion within or beneath the cobbles. Onshore and offshore fluxes of sediment balanced out over the duration of a tide, and more generally over the course of the spring tidal cycle, demonstrating the capacity of the revetment to adapt and recover after erosive events. Furthermore, measured net fluxes were 40 times smaller than the gross fluxes, which demonstrated the dynamic stability of the revetment – despite large wave-by-wave transport of material, net changes were typically small. The measured changes in revetment morphology were related to offshore wave conditions, and the revetment was found to rapidly reshape under these conditions, reaching a stable state under the upper swash during the rising tide. The analysis of swash revealed that swashes with a maximum depth comprised between $0.25 - 0.45$ m were characterised by large bed-level change events and negligible mean fluxes. The large events in this range were found to be close to the bore collapse position (within $0 - 1.5$ m landward). Deeper and weaker swashes were identified only in zones inundated more than 40 % of the time. The water level was found to also play a major role in the morphodynamics of the revetment, as the mean shoreline position was always near the location of two morphological features: the pivot zone and the cross-shore limit of bed oscillations. These features were characterised by maximum swashes within the active range $0.25 - 0.45$ m. The results were compared to a similar study on sandy beaches, which provided a better understanding of the dynamic nature and performance of dynamic cobble berm revetments exposed to energetic swash events.

Declaration concerning the article used for this Chapter:

Title	High-resolution measurements of a dynamic cobble berm revetment during a spring tidal cycle: swash zone morphodynamics
Status	Submitted in Coastal Engineering (Elsevier), and currently under review
Details	Paul M. Bayle, Chris E. Blenkinsopp, Kévin Martins, George Kaminsky, Heather Weiner and David Cottrell (In review). High-resolution measurements of a dynamic cobble berm revetment during a spring tidal cycle: swash zone morphodynamics. *Coastal Engineering*.
Contribution from the authors	P.M. Bayle: Planning/Collection/Processing/Analysis of data; Manuscript (70%) C.E. Blenkinsopp: Analysis of the data; Edited drafts of manuscript (12%) K. Martins: Suggestions for analysis; Edited drafts of manuscript (10%) G. Kaminsky: Collection; Edited drafts of manuscript (3%) H. Weiner: Collection; Edited drafts of manuscript (3%) D. Cottrell: Edited drafts of manuscript (2%)
Statement	This paper reports on original research I conducted during the period of my Higher Degree by Research candidature.
Date and Signature	

Preamble

The dynamic revetment studied in North Cove (Chapter 4) showed similarities with the revetment studied in the laboratory (Chapter 3), although they were not made of the same material. They both demonstrated a dynamic stability under energetic conditions and water level changes. Both revetments also reached a stable state, with cobbles attaining this state faster than the underlying sand which was found to play an important role in the morphodynamics of the whole ridge. It seems therefore important to verify if these observations can be identified and explained at a smaller scale, by looking at individual swash events. The following research questions/objectives are raised:

1. Look at swash-induced net mass fluxes spatial and temporal variation, and relate them water level and offshore conditions.
2. Can we identify the development towards a stable state at the swash and tidal scale? Is it similar to the gross and net ratio observed in the laboratory?
3. Can we identify high dynamic swash areas driving the overall morphodynamics changes?

To tackle these research questions, the lidar dataset obtained in North Cove is analysed in detail using a similar approach to that presented in Blenkinsopp et al. (2011), who studied swash fluxes on sandy beaches. The lidar only allows cross-shore changes to be captured with no measurements in the longshore direction consistent with previous field experiments using Lidar and ultrasonic bed sensors(*e.g.*, Turner et al., 2008; Blenkinsopp et al., 2010a; Almeida et al., 2015). As a consequence, profiles changes are assumed to be driven by cross-shore fluxes only. Although the importance of longshore sediment transport in local bed level changes was highlighted in Chapter 4, it is assumed that during storm conditions, cross-shore variations in bed level changes at the swash scale are dominated by cross-shore processes (Masselink and Van Heteren, 2014).

Chapter 5.

5.1 Introduction

Dynamic cobble berm revetments are a type of soft engineering technique intended to protect sandy coastlines against erosion and flooding (Allan et al., 2006; Allan and Gabel, 2016; Bayle et al., 2020). The concept of a dynamic revetment is to create an artificial composite beach, which consists of a lower sandy foreshore and a backshore berm or ridge composed of gravels. The gravel ridge is a highly-dynamic feature that armours the underlying sand (Bayle et al., 2020) and provides overtopping protection to the hinterland (Allan et al., 2006; Komar and Allan, 2010; Loman et al., 2010; Allan et al., 2012, 2015; Allan and Gabel, 2016). Composite beaches have long been recognised as an effective form of natural coastal protection (*e.g.*, see Ahrens, 1990; Allan and Gabel, 2016), showing a great degree of stability and adaptability in response to wave attack (Van Rijn, 2010). Although these coastal landforms are ubiquitous in some regions of the globe, they have received much less attention than purely sand or gravel beaches. In addition, while the concept of dynamic revetments is not new (*e.g.*, van der Meer and Pilarczyk, 1986; Powell, 1988; Lorang, 1991; Ward and Ahrens, 1992; Komar and Allan, 2010; Bayle et al., 2020, and many others), examples of application in the field are scarce and monitoring programs of existing structures are very limited (Bayle et al., 2020). As a consequence, there is an overall lack of understanding of dynamic revetments and composite beaches and their behaviour under the combined effect of varying water levels and wave conditions.

Dynamics revetments (and gravel ridges of composite beaches) are in some aspects similar to that of pure gravel beaches. They are both predominantly influenced by swash processes, both in cross-shore and long-shore direction, which can generate significant changes over a short time scale (Jennings and Schulmeister, 2002). They are also both highly porous features resulting in substantial infiltration/exfiltration of water through the gravel under swash motion (Holland, 2019). While many studies have contributed to a better understanding of swash dynamics and gravel transport on pure gravel beaches (*e.g.*, Carter and Orford, 1984; Williams et al., 2009; Poate et al., 2015; Almeida et al., 2015), equivalent studies on composite beaches or dynamic revetments are rare (Bayle et al., 2020). Yet, such analyses are important as the gravel ridge composing dynamic cobble berm revetments differs in some points from a pure gravel beach as it is founded on sand (Jennings and Shulmeister, 2002). Consequently, research on morphological change of dynamic revetments due to swash motions is needed to better understand the behaviour of dynamic revetments and composite beaches.

Dynamic revetments and composite beach ridges are composed of three layers: 1) A layer of pure gravels, which generally behaves like a pure gravel beach. This layer is dominated by cross-shore transport, which over time, tends to generate a net landward transport (Carter and Orford, 1984). Cross-shore sorting of particles in the pure gravel layer is common, with the direction of sorting depending on the hydrodynamic capacity of the swash to bring the largest particles into motion (Bluck, 1967; Orford, 1975; Williams and Caldwell, 1988). 2) A layer of mixed gravel and sand, composed of coarse sand and small pebbles. This layer is vertically sorted, with particle size decreasing with depth (Pye and

Blott, 2018). 3) A layer of pure sand. The presence of these three layers makes the hydraulic conductivity and water table of a composite beach or beach with a dynamic revetment different from pure gravel beaches, and likely influences the swash dynamics (Holland, 2019). The swash motions cause rearrangement of surface particles, which can in turn lead to temporary exposure and movement of underlying gravel and sand. In addition, sand beneath the gravels can be eroded by the water percolating through the permeable pure gravel layer (Bayle et al., 2020); it can also accumulate and compact under kinetic sieving, which results from the vibratory mechanism of the swash (Wright et al., 1982). The water levels play a key role in the dynamics of composite beaches as hydrodynamic conditions change from dissipative at low and mid tide (shoreline over the mildly sloping beach face) to reflective conditions around high tide, when the swashes interact with the much steeper, gravel berm. Over the sorted gravel layer, however, it remains unclear how the revetment evolves under varying swash conditions and water levels since these determine which region of the revetment is mobilized and most inclined to produce large changes.

The present study aims to improve the understanding of gravel ridge dynamics composing dynamic revetments by analysing swash processes and swash-induced mass fluxes in the field at temporal scales ranging from the minute to the intra-tidal scale. The analysis is performed using high-resolution hydrodynamic and topographic measurements collected with a 2-D lidar scanner along a cross-shore transect of the dynamic revetment in North Cove, Washington State, USA. The field experiments were performed over an energetic spring tidal cycle in January 2019 at a location with a history of extreme erosion. The capacity of 2-D lidar to monitor the swash zone at high temporal and spatial resolution in the field has been demonstrated over the last decade (Blenkinsopp et al., 2010a; Brodie et al., 2012; Almeida et al., 2015; Martins et al., 2016). Here, we employ a method originally designed to extract mass fluxes between individual swash events and study swash-driven cross-shore processes using ultrasonic bed-level sensor data (Turner et al., 2008; Blenkinsopp et al., 2011). The paper is structured as follows: Section 2 presents the methodology including a description of the study area, the lidar setup, the environmental conditions during the experiment, and the data processing techniques. Section 3 presents the swash analysis and quantifies net cross-shore mass fluxes. Section 4 extends the analysis to define two morphodynamic zones on the revetment, and compares the main findings with a similar study on sandy beaches. Finally, Section 5 concludes and discusses potential future work.

5.2 Methodology

5.2.1 Study Site

The dynamic revetment at North Cove, Washington State, USA was used as a case study. The town of North Cove is situated on the U.S. Pacific northwest coast along the northern shore of the Willapa Bay entrance in Washington State (see Figure 5.1a). This open sandy coast faces the Pacific ocean and is therefore exposed to a severe wave climate, particularly in winter with storms producing deep-water significant wave heights greater than 10 m at least once a year (Allan and Komar, 2002; Ruggiero et al., 2005; Michalsen, 2018). Semi-

Figure 5.1: (a) Geographical location of the North Cove dynamic cobble berm revetment. The Grays Harbor waverider buoy is shown as a yellow triangle, and the Toke Point tide station as a green circle, in the bottom left map. (b) Photographs of the dynamic revetment on the 24/01/2019 at low tide; (c) Photographs of the dynamic revetment on the 21/01/2019 at mid-tide (during flood). Note that the top of the revetment is delimited by an artificial drift log barrier. Under very high water levels and energetic conditions, the maximum runup limit reaches this log barrier. *Photos taken by Paul Bayle.*

diurnal tides dominate this part of the coastline, with a tidal range ranging from 2 to 4 m (Kaminsky et al., 2010). Due to its exposure to frequent energetic events, the coastline around North Cove has suffered from serious and continuous erosion, with an average recession estimated at 20 m/yr between 1950 and 1999 (Kaminsky et al., 2010). A maximum rate of recession of 37.3 m/yr was observed between 1963 and 1974. At the beginning of the 21st century, this reduced to approximately 13 m/yr.

Following existing examples of dynamic revetments constructed along the west coast of the USA (Allan and Gabel, 2016; Allan et al., 2012, 2015), the extreme erosion at North Cove motivated the installation of a dynamic cobble berm revetment to protect the coastline from further erosion. Starting in February 2017, an ad-hoc revetment was built using angular and poorly sorted rock from a local quarry. The material has a diameter range varying from a few centimetres to almost one metre (D_{50} = 0.15 m) and is primarily basalt with a bulk density of 1830 kg/m^3, although other mineralogy can be found. The hardness of

the material means that it tends to fracture and abrade into smaller pieces, reducing the D_{50} over time, and adding coarse sand to the material range. For the remainder of this paper, the construction material will be referenced as 'cobbles', as this characterises the predominant material size within the revetment. Cobbles were placed incrementally as needed through multiple treatments, to reach a total volume of 16.23 m^3/m around the monitoring site (Figure 5.1a). At this location, the revetment has a cross-shore width of approximately 20 m in winter (storm season). Wave action has led to cross-shore sorting, with cobble size decreasing landward. Due to the presence of this revetment, the beach is considered to be an artificial composite beach: gravels composing the upper ridge are in direct interaction with waves at mid and high tide (Figure 5.1c); at low tide, the shoreline is well seaward of the cobble toe, and the subearial beach is dominated by sand (Figure 5.1b) with a D_{50} of about 0.18 mm (Kaminsky et al., 2010).

5.2.2 Field experiment

The field experiment was performed over a spring tidal cycle of ten days, from 16/01/2019 to 25/01/2019, which was characterised by large and long-period erosive wave conditions. The principal motivation of the experiment was to collect comprehensive data on the morphological evolution of the dynamic revetment over the study area shown in Figure 5.1a in order to analyse the behaviour and performance of the revetment. The overall revetment topographic evolution was surveyed with Real-Time Kinematic Global Navigation Satellite System (RTK-GNSS) and individual cobbles were tracked with Radio Frequency Identification (RFID, *e.g.* see Bayle et al., 2020). The preliminary analysis of these data revealed that the revetment remained as a coherent structure over the spring tidal cycle, only losing an average of 0.67 m^3/m over the study area. This volume loss was mainly associated with sand erosion from within or beneath the cobbles since no cobbles were transported seaward of the revetment toe and longshore transport was relatively homogeneous across the width of the revetment at the study site. The present contribution focuses on swash-driven cross-shore fluxes studied at the scale of individual swash events using high-resolution hydrodynamic and topographic data from a 2-D lidar deployed along a cross-shore transect of the revetment (Figure 5.1a).

A SICK LMS 511 lidar scanner was deployed for this spring tidal cycle experiment, and was mounted on top of a 6 m-pole strongly attached to a large drift log at the top of the revetment. The pole and lidar were anchored with four guy lines making it nearly immobile even in strong winds (Figure 5.2a). The lidar collected free surface elevation and topographic measurements along a 18.7 m-long cross-shore transect of the cobble revetment (Figure 5.2b) for approximately six hours around each high tide of the spring cycle (three hours before and after) to capture interactions between waves and cobbles. The lidar collected data at 25 Hz with an angular resolution of 0.1667° across a 150° field-of-view. In the remainder of the paper, the cross-shore data are given relative to the lidar position, with the distance x increasing seaward. Elevations z are given relative to the North American Vertical Datum 1988 (NAVD88).

(a)

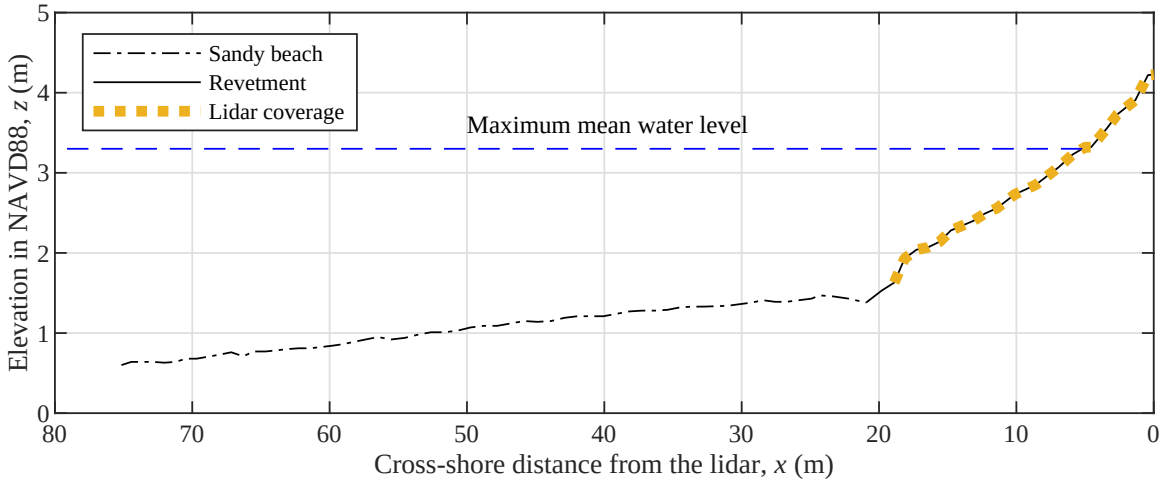

(b)

Figure 5.2: (a) Photographs of the lidar deployment. The image at left was taken at low tide along the lidar transect looking onshore. The image at right shows the mounted lidar when recording during a high tide looking alongshore. The central photograph shows a close-up of the lidar mounting system. (b) Cross-shore profile of the beach along the lidar transect measured with RTK-GNSS. Note that the minimum water level recorded during the experiment was $z = -1$ m referenced to the North American Vertical Datum 1988 (NAVD88), and therefore is not represented on the figure. *Photos taken by George Kaminsky, Heather Weiner, and Paul Bayle*

5.2.3 Environmental Conditions

The weather conditions during the experiment were obtained from publically available continuously operating stations. Water levels were obtained for the Toke Point station (station 9440910; Figure 5.1a) from the NOAA tides and currents open data platform. The validated version of the data is used in this study. Wave height, period, and direction were obtained from the Coastal Data Information Program (CDIP) Grays Harbor waverider buoy (station 46211; Figure 5.1a) from the NOAA National Data Buoy Center open-source platform. Figure 5.3 shows the time series of wave and water-level data for the duration of the field experiment: wave data were available every half hour (Figure 5.3a and b); and water level data every six minutes (Figure 5.3c). The wave conditions were very energetic during the experiment, peaking at $H_s = 6$ m and $T_p = 15$ s on 19/1. During the experiment, incident waves predominantly came from a west/south-west direction, resulting in a near-

normal incidence at the study site.

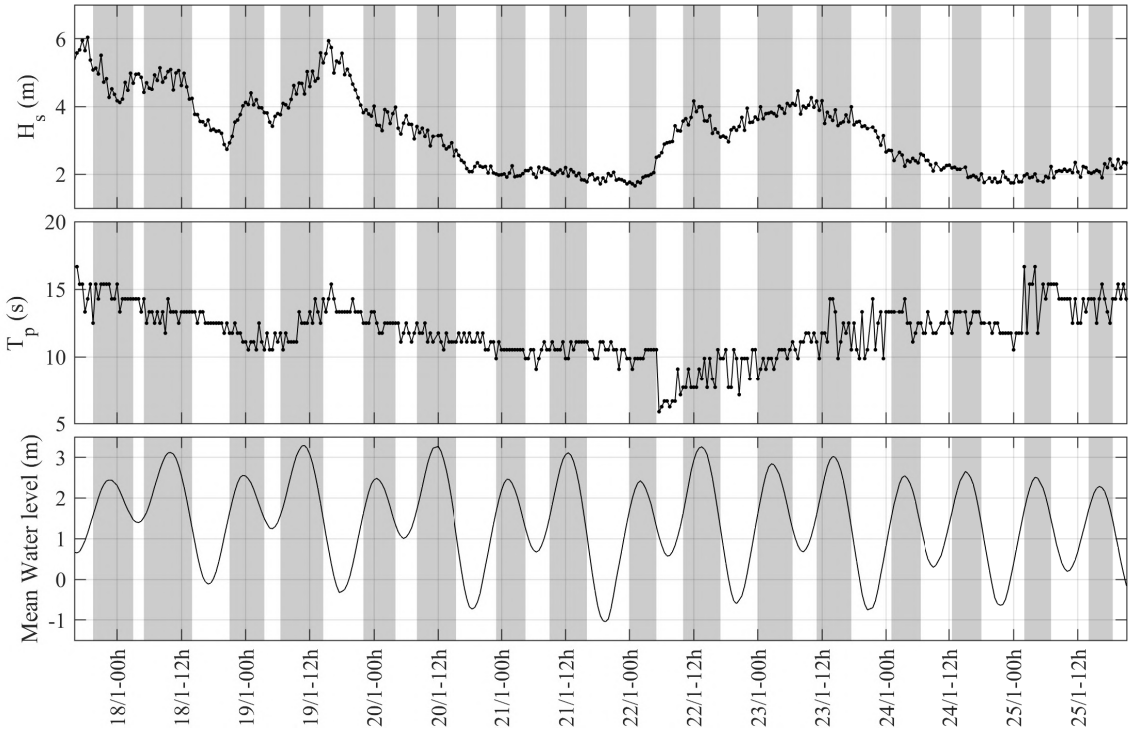

Figure 5.3: Time series of: (a) Significant wave height, H_s (m) ; (b) Peak wave period T_p (s); and (c) Mean water level (m) in the NAVD88. The shaded areas indicate when the Lidar was recording during mid- and high tides, which corresponds to when there was swash interaction with the revetment (from collision regime to overwash regime, Sallenger (2000)). Times are given in Pacific Time (GMT-8).

5.2.4 Lidar data processing

5.2.4.1 Separation of hydrodynamic and topographic measurements

The lidar dataset was first despiked and interpolated onto a 0.1 m horizontal grid (*e.g.*, see Martins et al., 2016; Martins et al., 2017a). Hydrodynamic (broken waves or swashes) and topographic data points were separated following Almeida et al. (2015) and Martins et al. (2016). This methodology, based on the technique proposed by Turner et al. (2008) for ultrasonic bed-level sensors, applies a threshold on the variance computed over a moving 4 s window to extract raw bed points at each cross-shore location. The stationary bed level (referred to as the “bed") is separated from the non–stationary water surface (wave or swash, here referred to as the “swash") to obtain a complete timeseries of bed elevation. Besides providing instantaneous swash depths at a given location, this method also allows the instantaneous shoreline position, which is defined at the most landward wet point, to be tracked in both time and space enabling extraction of the runup and rundown limits. Figure 5.4 shows an example of this separation process over a four–minute window at four cross-shore locations across the revetment. Note that the bed elevation measured with the lidar (see profile in Figure 5.4e) only corresponds to the cobble surface and does not capture the sandy beach seaward of the revetment toe.

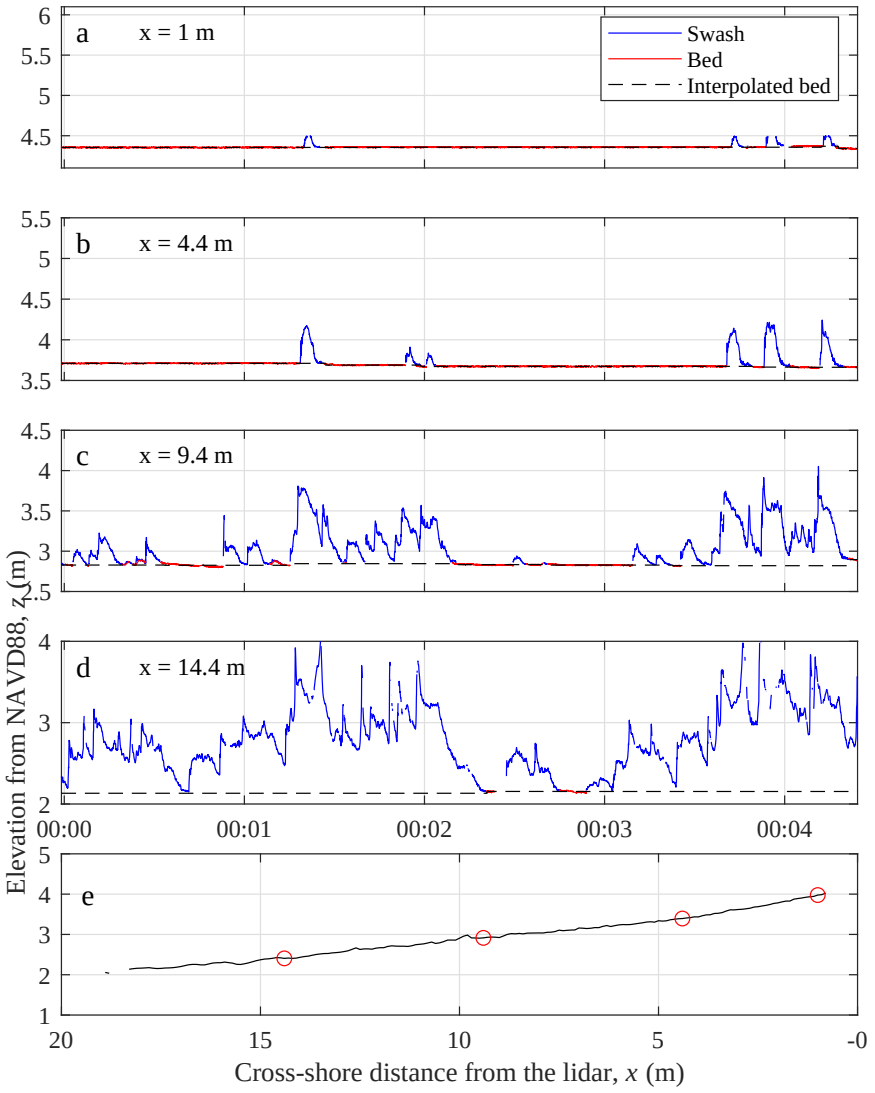

Figure 5.4: Example of “swash" and “bed" extraction over a 4-minute window, for the overnight high tide on 19/01/2019, at (a) x = 1 m, (b) x = 4.4 m, (c) x = 9.4 m and (d) x = 14.4 m. Blue lines represent the “swash" timeseries, red lines the “bed" timeseries and dashed black lines the interpolated and continuous “bed" timeseries. The position of each analysed point presented in (a-d) on the revetment profile is shown by a red circle on panel (e).

5.2.4.2 Definition of individual swash events

The same nomenclature as in Blenkinsopp et al., 2011 is used hereafter to refer to swash terms. Following Hughes and Moseley (2007), individual swash events correspond, at a fixed location in space, to an inundation event between consecutive occurrences of a dry bed. As illustrated in Figure 5.4, each swash event can be composed of several incident waves/bores, defined as local maxima in the swash elevation timeseries. Since at high tide, the most seaward locations in the lidar transect can be continuously submerged, a maximum of 25 bores were allowed per individual swash event. This method and threshold was successfully used in Blenkinsopp et al. (2011) to remove swashes associated with long periods, hence more characteristic of the surf zone dynamics. Therefore, events with more bores detected were considered to be located in the inner surf zone and were disregarded from the present analysis.

5.2.4.3 Net cross-shore mass flux

Using the “bed" timeseries, the net bed-level changes caused by each swash event were computed for each lidar cross-shore position using the bed elevation immediately before and after that event. The net cross-shore mass flux per swash event past any point on the revetment face is directly obtained from these bed-level changes at each discrete point on the revetment surface. This method has previously been applied by Blenkinsopp et al. (2011) in a field experiment investigating swash processes on a sandy beach. It was also illustrated for multiple events in Turner et al. (2009). The volume flux $q(x')$ (positive onshore) past the cross-shore location x' for each swash event is given by:

$$q(x') = \int_{x'}^{x_0} \Delta z(x) dx \tag{5.1}$$

where x_0 is the lidar position (*i.e.*, $q(x_0) = 0$), Δz is the bed-level change at each lidar grid point (m) and dx is the cross-shore spacing between each grid point (0.1 m). The corresponding net cross-shore mass flux per swash $Q(x')$ (positive onshore) is then given by:

$$Q(x') = \rho_b q(x') \tag{5.2}$$

where ρ_b is the bulk mass density ($\rho_b = 1830$ kg/m^3).

The experimental data allow the net cross-shore mass flux to be quantified, which includes both sand and cobble transport for all individual swash events across the revetment. Furthermore, knowing the duration of each swash, the net cross-shore mass flux per second was calculated by simply dividing the net cross-shore mass flux per swash by the duration of the swash.

5.3 Results

The results section is separated into two subsections: the first subsection will present a reference tide to illustrate the typical aspects of revetment behaviour observed in all tides; the second subsection will focus on the bulk analysis of the swash and fluxes of all tides combined.

5.3.1 Cross-shore revetment dynamics for a reference tide

For the following analysis, the data from the overnight high tide on 19/01/2019 are presented and used as a typical high tide to illustrate the main behaviour observed during all tides. During this tide, the wave height, wave period and mean water level reached a maximum of 4.05 m, 13.3 s and 2.48 m respectively (fifth most powerful tide recorded, out of 16). This tide will be referred to as “the reference tide" for the remainder of the paper.

5.3.1.1 Bed-level changes and net cross-shore mass flux

Using the “bed" timeseries (Section 5.2.4.1), net bed-level changes relative to the revetment face morphology at the start of the timeseries were computed at each cross-shore position

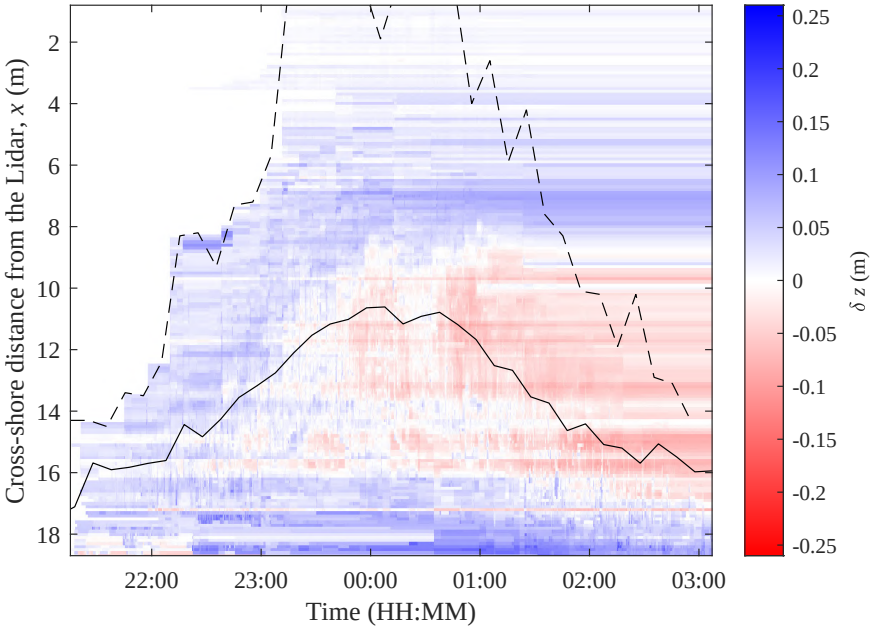

5

Figure 5.5: Change in bed-level through the swash zone during the reference tide, measured using the lidar (the magnitude of x increases in the offshore direction). The dashed and solid lines represent the run-up limit and the mean shoreline position (measured every 10 minutes using the instantaneous shoreline position obtained with the lidar) respectively. The colour scheme represents net bed-level change in metres (measured every second) relative to the revetment face morphology at the start of the timeseries. The net morphological change in the high tide swash zone over the reference tide is characterised by accretion of up to 26 cm. Note that the runup hits the drift log barrier at $x = 0.7$ m and does not progress past this point.

on the 0.1 m grid, for every second. Figure 5.5 shows the morphological evolution of the revetment face through the reference tide over the whole revetment width. During this particular tide, net accretion is observed during the first hour over the entire active part of the revetment. From 23:00 a region of net erosion appears between $x = 9.5$ m and $x = 16$ m.

Figure 5.6a presents percentage occurrence distributions of bed-level changes per individual swash event at four locations across the revetment face. Note that these locations were chosen to cover a large cross-shore area on the revetment face. The majority of swashes induced a net bed-level change smaller than ±3 cm at all four locations, and only a small number of events caused significant changes in bed elevation (< 1 %). In the lower part of the revetment at $x = 14.4$ m and $x = 9.4$ m, around 50 % of swash-induced bed-level changes generate zero-equivalent (±2 mm) net bed-level changes. This percentage increases to 80 % in the upper part of the revetment illustrated here by the distribution at $x = 1$ m and $x = 4.4$ m, which reflects the low capacity of the upper swash to move cobbles. However, some much larger changes did occur, and the maximum swash-induced net bed-level change was +16 cm during the reference tide, and −33 cm over all tides. Note that these changes are well outside the displayed range in Figure 5.6a. Notably, these large single-event bed-level changes are of the same order of magnitude as the total net morphological change at any point on the revetment.

Similar analysis was used to quantify the net cross-shore mass flux caused by individual swash events. Figure 5.6b shows the percentage occurrence of net cross-shore mass fluxes per individual swash event, recorded at the same four cross-shore locations as in Figure 5.6a. The observations made with the net mass flux are similar to the previous ones with bed

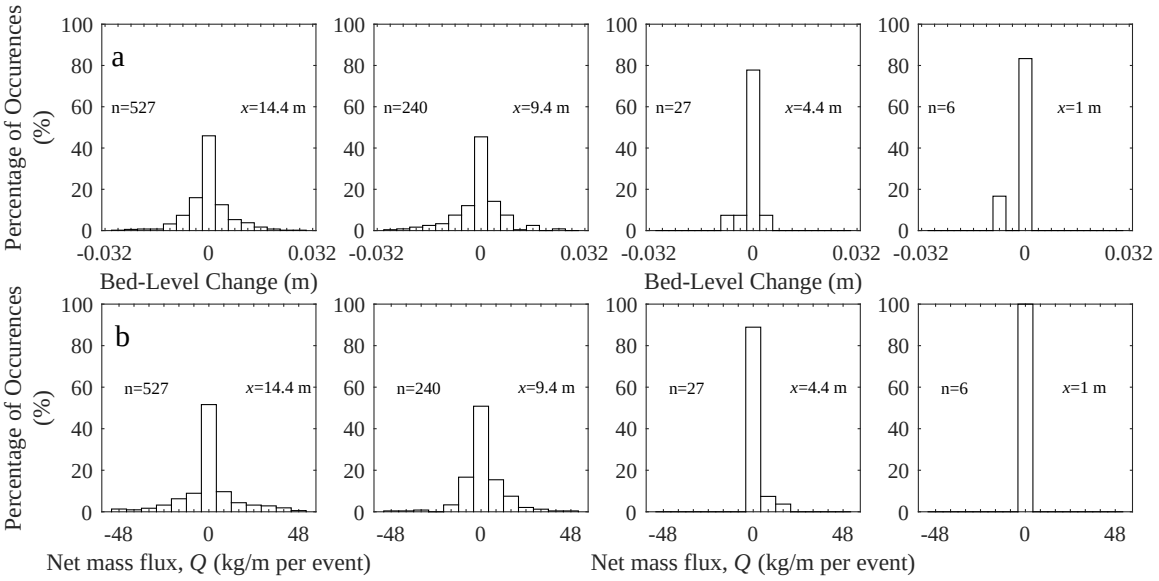

Figure 5.6: (a) Percentage occurrence of bed-level changes caused by swash events at four locations on the beach face during the reference tide, within ±0.04 m range. (b) Percentage occurrence of net cross-shore mass flux caused by swash events at four locations on the beach face during the reference tide, within ±50 kg/m range. In each panel, the number of swash events n and the corresponding cross-shore position are indicated.

level changes. The mid and lower part of the revetment at $x = 14.4$ m and $x = 9.4$ m shows around 50 % of swash-induced bed-level fluxes comprised within ±4 kg/m, whereas the upper part of the revetment illustrated here by the distributions at $x = 1$ m and $x = 4.4$ m have at least 80 % of fluxes are within this range. Furthermore, the standard deviation is smaller on the upper beach face, varying from 0.3 kg/m per swash at $x = 1$ m to 22.6 kg/m per swash at $x = 14.4$ m. Rare events produced large net mass fluxes, with a maximum of +268 kg/m during the reference tide, and −412 kg/m over all recorded tides.

The results shown in Figure 5.6b are essentially symmetrically distributed, and a similar distribution is observed for all tides, whether they experienced net erosion or accretion. Therefore, although the distributions shown in Figure 5.6b are generally slightly positively (accretion) or negatively (erosion) skewed – for instance, at $x = 4.4$ m, the positive skewness represents the general accretion occurring at this position on the revetment (see Figure 5.5) – this suggests that the numerous swash events resulting in variation of revetment volume nearly balance over longer time scales.

5.3.1.2 Net and gross rate of bed volume change

The onshore and offshore balance is further illustrated in Figure 5.7. In this figure, the net and gross rate of bed volume change as defined in Bayle et al. (2020) is used. The net volume change (per metre width) per second represents the rate of absolute volume change over ten minutes, denoted dV_{10}, which represents the mean rate of change over ten minutes. The gross volume change (per metre width) per second, denoted $\overline{dV}$, is quantified by summing the bed level changes measured every 12 s, which is the representative wave period, and then averaged over ten-minute windows.

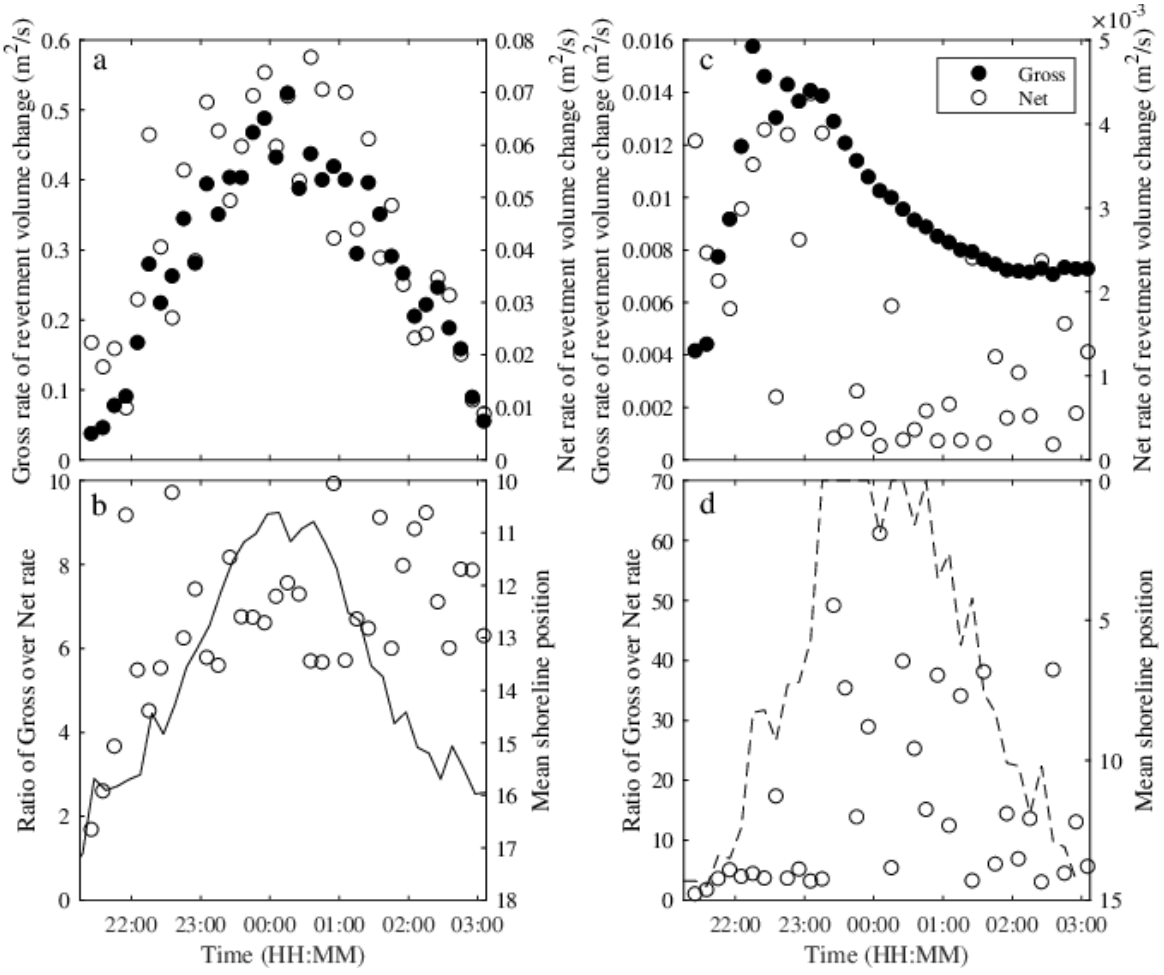

Figure 5.7: (Top panels): Gross (filled circle) and net (empty circle) rate of bed volume change in m^2/s, per 10 minutes windows for the reference tide, (a) calculated over the entire revetment profile length (18.7 m), and (c) calculated every ten minutes from the runup limit (dashed line in Figure 5.5) to a point four meters seaward. Note that two y-axes are used to present both datasets on the same figure. (Bottom panels): Ratio of the gross over the net rate of bed volume change per 10 minute window for the reference tide, (b) calculated over the entire revetment profile length (18.7 m), and (d) calculated every ten minutes from the runup limit (dashed line in Figure 5.5) to a point four meters seaward. The dashed and solid lines represent the runup limit and the intersection of the beach and the mean shoreline position (measured every 10 minutes) respectively.

Figure 5.7a shows the net and gross rate of bed volume change (in m^2/s) over the course of the reference tide. Figure 5.7b shows that the ratio between the gross and net rates varies between 2 and 10. Similar values were observed for all recorded tides, confirming that the reference tide is representative of net and gross mass fluxes observed during all tides. This ratio demonstrates that the revetment elevation is constantly changing over ten minutes, but that the final net change is 2 to 10 times smaller than the magnitude of the changes which cause it. In other words, the cobbles composing the revetment show a highly-dynamic behaviour but remain stable as a whole. This ratio is similar to that measured in the laboratory on a dynamic cobble berm revetment by Bayle et al. (2020). However, in the current experiment, the ratio changes through time due to tidal water level variations: for most of the recorded tide, it first increases with the rising tide (first 30 minutes) but does not decrease with the falling tide. Figure 5.7c examines the gross and net rate of volume change over a four–meter window bounded landward by the ten-minute-averaged runup

limit (dashed black line on Figure 5.5). This method allows only the rates characterising the upper swash to be captured, as it moves up and down the revetment face during the tide. Figure 5.7d shows the ratio between these rates, calculated over the same four–metre window. These two figures show that during the first two hours (rising tide), the ratio is relatively small (around 5), as both the gross and net rates increase. They both reach a peak when the swash limit reaches the top of the revetment (log barrier) around 23:15 (before high tide). The ratio becomes significantly larger after 23:15, up to a peak of 62, as the net rate decreases more than the gross rate – the net rate drops significantly, while the gross rate decreases progressively.

Assuming that the offshore conditions are constant over the duration of the tide, Figure 5.7 shows that net rates are larger during the rising tide than during the falling tide, suggesting that the revetment rapidly reshapes during the rising tide and then remains relatively stable. This is consistent with the study of Bayle et al. (2020) who observed that the front slope of a dynamic cobble berm revetment can significantly reshape and change slope within less than 20 minutes under the action of waves. Therefore, the revetment can undergo rapid and significant net changes under new wave conditions, but then remain relatively stable in elevation and shape for the rest of the tide under the same wave conditions – it reaches a stable state (Bayle et al., 2020). Figure 5.7 also shows that the upper four metres of the swash interacting with the revetment during the rising tide (first 2 hours) generate gross and net changes one order of magnitude smaller than the overall changes driven by the entire swash – hence contributing to approximately a tenth of the overall changes. Their contribution decreases for the rest of the tide, especially during the falling tide (last 2 hours), which means that net and gross changes are mainly driven by deeper swashes in seaward areas.

5.3.2 Bulk analysis of swash characteristics

In this section, all tides are used to analyse swash-induced mass fluxes and swash depth characteristics over the spring tidal cycle. To remove the bias due to varying tidal levels (Figure 5.3c), the percentage of time that the bed is inundated (t_i) is used to indicate relative position within the swash zone (*e.g.*, Blenkinsopp et al., 2011; Masselink et al., 2009, 2005; Aagaard and Hughes, 2006; Masselink and Russell, 2006). The percentage inundation t_i was assessed as a series of ten-minute averages for all tides. Figure 5.8 shows a contour plot illustrating the percentage of bed inundation over the revetment face for the reference tide, where t_i was calculated as a 10-minute average. Note that because the revetment surface is irregular due to the cobble surface, it is possible to have an inundated point landward of a dry point at the same time step. This is particularly the case at the bottom of the revetment, where large cobbles are dominant and can protrude out of the water surface.

5.3.2.1 Swash-induced mass fluxes spatial variations

To investigate the relationship between the inundation-normalised cross-shore position and the net cross-shore mass flux from individual swash events, every measured swash-induced

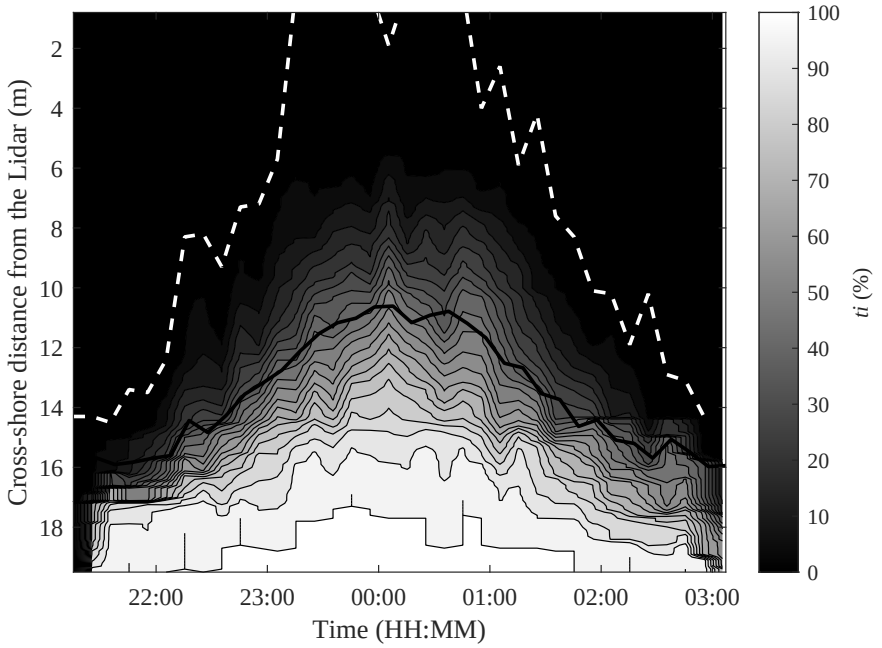

Figure 5.8: Contour plot showing the distribution of the percentage of time that the bed is inundated, t_i as a function of time during the reference tide. Percentage of bed inundation was calculated as a ten–minute average. The dashed white and thick black lines represent the run-up limit and the intersection of the beach and the mean shoreline position respectively.

mass flux was assigned to a window based on the value of t_i at the time of occurrence, with a window size of 10 % bed inundation ranging from $0-10$ % to $90-100$ %. Figure 5.9 shows that while the data in all classes are approximately symmetrically distributed, a distinct spatial variation in the magnitude of net cross-shore fluxes is evident. The variation evolves from a peaked distribution in the upper swash, with more than 60 % of events within the range ±4 kg/m per event, to a very broad distribution in the lower swash zone, with $70-80$ % of fluxes larger than ±4 kg/m. The evolution is progressive through the swash, with the standard deviation increasing from 25 kg/m to 47 kg/m per event with the percentage of inundation window.

Further investigation of the distributions of flux within each percentage window is shown in Figure 5.10a which presents the skewness of net cross-shore mass fluxes within each percentage inundation window, for all tides. Figure 5.10a illustrates that the skewness is negative within the upper swash zone ($0 < ti < 40$); it becomes positive in the mid swash zone ($40 < ti < 90$); and it is close to zero in the lower swash ($t_i > 90$). This analysis suggests that while the distribution is near symmetrical, the upper swash zone is dominated by positive fluxes with negative extreme events whereas the mid and lower swash are dominated by negative fluxes with positive extreme events. This can be explained by the grading of the revetment, as upper swashes are more inclined to generate large underlying sand removal than large cobble deposition. Figure 5.10b presents the mean and standard deviation of net mass flux magnitude per swash as a function of the percentage inundation for all tides. It shows that both the mean and the standard deviation of the net mass flux magnitude increase with percentage inundation t_i, which is consistent with the distributions shown in Figure 5.9. Figure 5.10c shows that when $t_i < 80$ %, the mean of

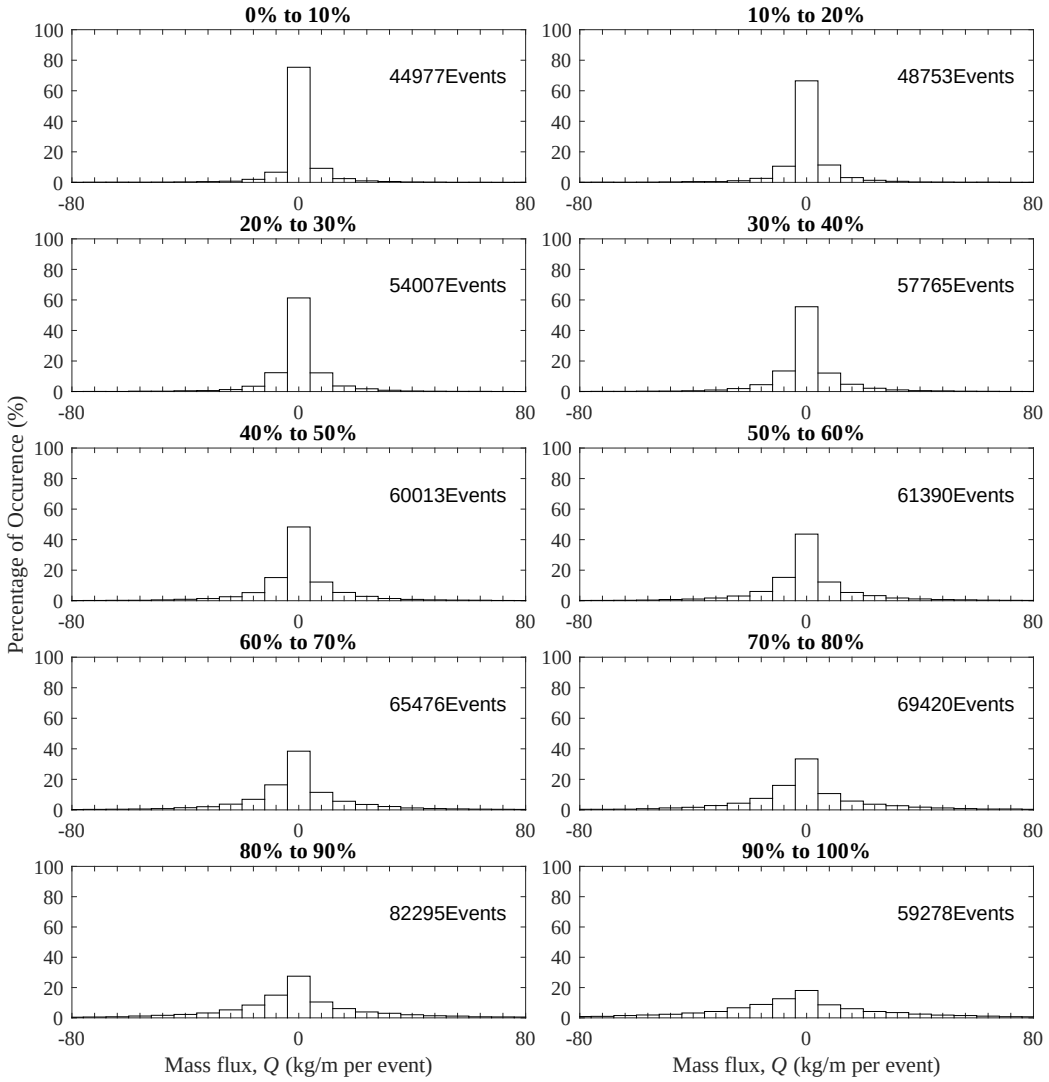

Figure 5.9: Percentage occurrence of net cross-shore mass fluxes grouped in terms of percentage inundation, t_i for all tides recorded by the lidar (Table 5.2). The number of events used for each histogram is included on the plot, and is relatively high due to the spatial coverage of the lidar, which gives one data point every 0.1 m.

net fluxes is very close to zero. This results in net fluxes nearly balancing over the tide, as shown in Section 5.3.1.1 in this region. However, swash areas with $t_i > 80$ % show a high negative mean value, meaning that a large volume of material is transported seaward from this cross-shore location. These fluxes mainly represent cobbles which were transported from the upper to the lower part of the revetment and accumulated at the revetment toe, around $x = 20$ m. It can also represent the underlying erosion of sand, which is transported seaward of the revetment.

5.3.2.2 Depth of swashes

To investigate the role of swashes in the distribution of mass fluxes further, the maximum depth of all swash events were measured and related to the mass flux of the event. In order to remove the effect of splashes, the depth presented is the 95^{th} percentile depth for each swash. Nonetheless, it will be referred to as the “maximum depth" for the rest of the

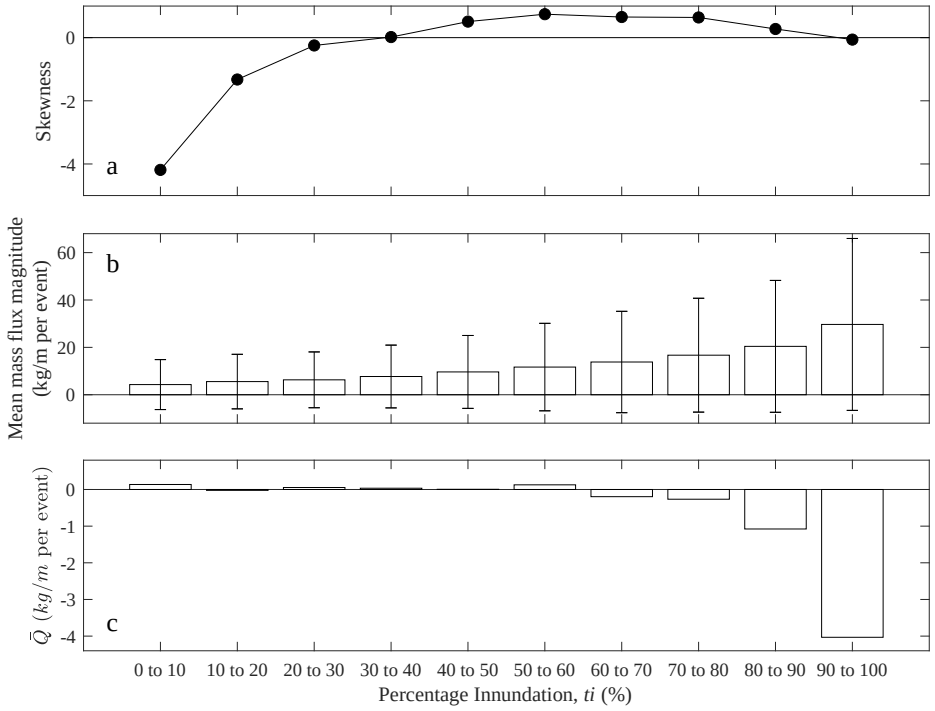

Figure 5.10: (a) Skewness of net cross-shore mass flux distribution, (b) the mean and standard deviation of net cross-shore mass flux magnitude and (c) mean net cross-shore mass flux as a function of percentage inundation, t_i for all tides recorded by the lidar.

paper. The calculation of the maximum depth of a swash measures a depth independently from the duration of the swash – for instance, a maximum depth of 0.40 m can either represent a short swash reaching this depth once, or a longer swash attaining this depth several times. In addition, Figure 5.11 shows that the mean and standard deviation of the net mass fluxes increase as the duration of a swash increases. To eliminate this bias, flux values are presented per second, consistent with Blenkinsopp et al. (2011). The analysis of the bulk distribution of the maximum depth of individual swash events for all points on the revetment and for all tides revealed that 99 % of all swashes have a maximum depth smaller than 70 cm, with 50 % being smaller than 15 cm. Moreover, it showed that 50 % of the depth of swashes which resulted in zero net fluxes are smaller than 3 cm, and 95 % are smaller than 15 cm. For this reason, swashes smaller than 15 cm are referred to as shallow swashes.

Figure 5.12b presents the bulk mean magnitude and standard deviation of the net cross-shore mass fluxes per second (kg/m/s), as a function of the maximum depth of an individual swash, ranging from $0 - 0.05$ m to > 0.70 m. It shows that the net flux per second increases with the maximum depth of swash, with the standard deviation of fluxes varying from 2 kg/m/s in the $0 - 10$ % inundation window to 3.3 kg/m/s in the $90 - 100$ % window. This increase is very similar to that shown in Figure 5.10b per inundation window. The skewness in Figure 5.12a indicates that swashes deeper than 0.45 m are less negatively skewed than shallower swashes, hence are less inclined to produce relatively large offshore transport events (note the presence of a large positive skewness for $0.35 - 0.40$ m which is discussed further below). Furthermore, swashes with a depth > 0.45 m tend to generate

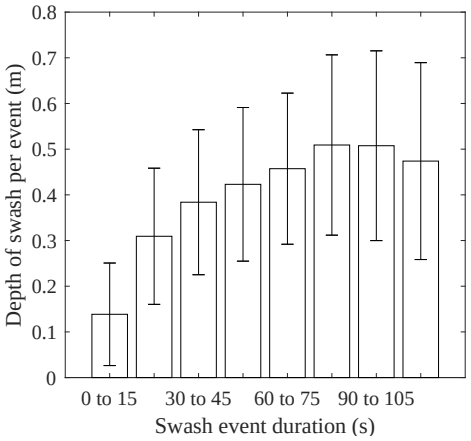

Figure 5.11: Mean and standard deviation (error bar) of the maximum depth of swash measured per 15 s window of swash duration.

smaller extreme fluxes (maximum magnitude of 22 kg/m/s) than shallower events, although they have a larger standard deviation and mean value. This can be explained by the fact that deep swashes are generally long swashes which mainly generate flows which, unlike for pure sandy beaches, are insufficient to mobilise cobbles, hence limit extreme fluxes. Nonetheless, suspended sand leaving the revetment area as well as incoming from the sandy beach contribute to the measured fluxes in these relatively deep swashes. The mean mass fluxes per second in Figure 5.12c shows that shallow swashes tend on average to drive offshore fluxes while deep swashes drive onshore fluxes. Swashes with a depth comprised between 0.25 – 0.45 m are marked by small means (Figure 5.12c), but tend to generate very

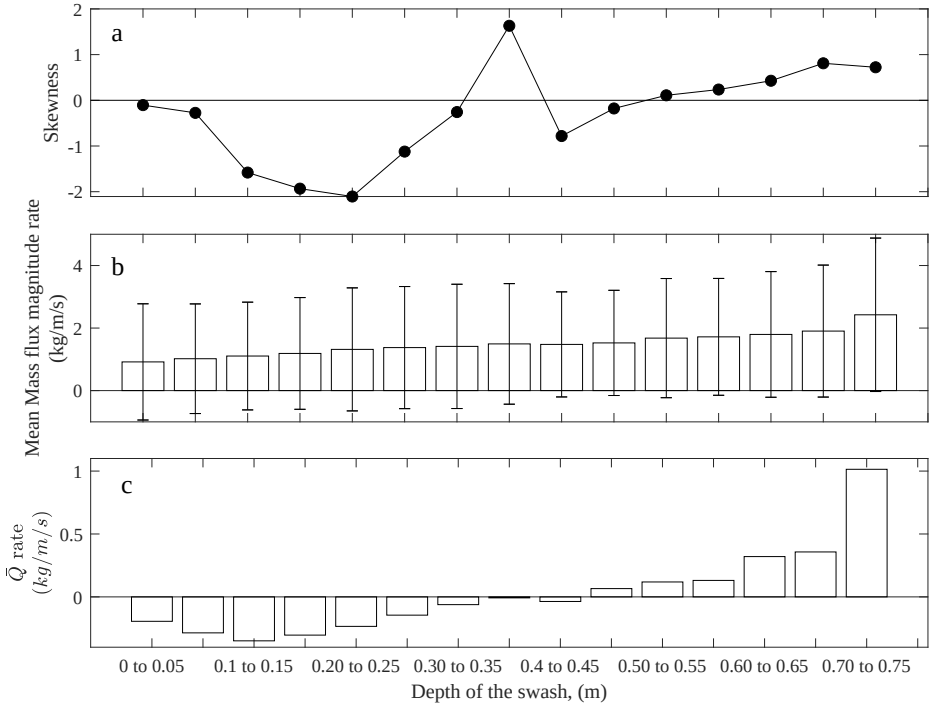

Figure 5.12: (a) Skewness of net cross-shore mass flux per second induced by detected swash events; (b) mean magnitude (histogram) and standard deviation (error bar) of net cross-shore mass flux per second as a function of the maximum depth of individual swash. Note that the bin size increases by 0.05 m and are shown for every other tick; and (c) Mean net cross-shore mass flux per second.

large extreme events (numerous events with a magnitude around 45 kg/m/s). Figure 5.12c shows that between 0.45 – 0.50 m, the mean flux direction over all recorded tides switches from offshore (negative) to onshore (positive).

Based on these analyses, it is clear that swashes within the depth range 0.25 – 0.45 m have important characteristics: they are generally characterised by a near–zero mean of net cross-shore mass fluxes (Figure 5.12c), but also generate large extreme events which appear to balance over time; the range 0.35 – 0.40 m is marked by a large positive skewness in Figure 5.12a, characteristics of large accretive events; the depth 0.45 m marks the point where the direction of mean net fluxes changes (Figure 5.12c). Swashes deeper than 0.45 m are therefore considered as deep swashes, and characterised by small extremes and long swashes.

5.3.2.3 Hydrodynamics of the 0.25 – 0.45 m depth swash events

To further investigate the hydrodynamics of the 0.25 – 0.45 m depth range, the depth of a swash event at a specific point on the revetment is related to the position of the immediately preceding bore collapse. The cross-shore position of the bore collapse is assumed to be at the position of the rundown limit of each swash event evaluated using the shoreline timeseries (Section 5.2.4.1). By subtracting the position of the bore collapse to the measured swash event, the distance between the bore collapse and the event (with a specific depth and flux) is extracted. As a result, by analysing only swashes with depths comprised within 0.25 – 0.45 m, the distribution of event–bore collapse distances is obtained. The analysis of the distribution of the event-bore collapse distances for all fluxes generated by a swash event with a maximum depth in the range 0.25 – 0.45 m shows that most of the events are measured close to the position of the bore collapse which generates them. It shows that in general, the distance to the point where the swash depth is measured to the point of bore collapse is very short (< 2 m). Nonetheless, some swash events within the 0.25 – 0.45 m range can still be located 8 – 9 m landward of the bore collapse position. To assess the hypothesis that large fluxes in 0.25 – 0.45 m depth range are associated with processes

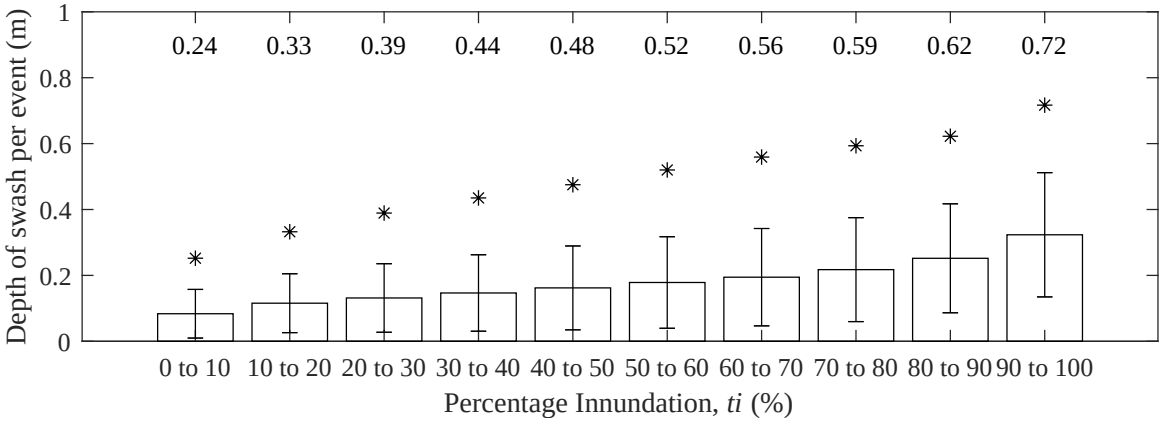

Figure 5.13: Mean, standard deviation (error bar) and "maximum" (stars) of the maximum depths of swash per event as a function of percentage inundation t_i. Note that the "maximum" corresponds to the 95th percentile of the maximum swash depth distribution in each inundation percentage window, and is written above each bar.

happening around the bore collapse, the distribution of event–bore collapse distances is analysed only for fluxes larger 22 kg/m/s. Results showed that large swash–induced fluxes are generally close to the bore collapse, with 99 % of them being within 0 and 1.5 m landward of the preceding bore collapse position.

This analysis of the $0.25 - 0.45$ m range swashes can be expanded by looking at the distribution of maximum depths of swash per inundation window. Figure 5.13 displays the mean, standard deviation and maximum value of the maximum depths of swashes measured in each window, and shows that they all increase with the percentage of inundation. The maximum depth per percentage window – 95^{th} percentile, shown by the upper star and written at the top of each histogram – is an indicator of the maximum swash depth limit per inundation window. Therefore, using this figure for the overall spring tidal cycle, it is possible to determine that swashes with a maximum depth of $0.25 - 0.45$ m can only happen in areas which are inundated more than 10 % of the time.

5.4 Discussion

The discussion is divided into four subsections: the first brings together results from the swash inundation and depth analysis; the second and third identify two morphological features and their swash characteristics; the fourth compares the current results with those obtained for sandy beaches, especially by (Blenkinsopp et al., 2011) who performed a very similar analysis.

5.4.1 Swash inundation and depth characteristics

Using all the tides listed in Table 5.2, the bulk distribution of fluxes across the inundation–normalised swash zone was observed to be almost symmetrically distributed (Figure 5.9), although the skewness suggested that the mid and lower swash are subject to more extreme positive events while the upper swash is subject to more negative ones (Figure 5.10a). Figure 5.10c showed that the mean cross-shore mass flux per swash event is small (±0.24 kg/m per event) for $t_i < 80$ %. However, during individual tides, the absolute value of the mean fluxes per swash was generally larger ($\pm 1.2 - 2.4$ kg/m per event). This implies that the fluxes for each tide balanced over the spring tidal cycle, resulting in a near–zero mean of net mass fluxes over the whole experiment in the region where $t_i < 80$ %. This confirms the capacity of the revetment to behave dynamically under energetic conditions by experiencing large changes, but also the capacity to recover from these changes to end up in an almost unchanged final state. The absolute mean of the net cross-shore mass fluxes significantly increases for the $80-90$ % and $90-100$ % inundation windows indicating a net transport of cobbles toward the revetment toe (around $x = 20$ m). As it was demonstrated that cobbles rarely get transported seaward of the revetment toe (Bayle et al., 2020), these fluxes also partly represent sand removal from within or beneath the cobbles (from the layers described as 2) and 3) in Section 5.1), which contributes to the overall volume loss (*i.e.*, deflation of the cobble surface) over the experiment (Section 5.2.2).

Figure 5.12c showed that fluxes caused by swashes deeper than 0.60 m have a large

positive value of mean flux per event (between 0.4 – 1 kg/m/s), which contrasts with the negative means within the inundation range 80 – 100 % (Figure 5.10). Therefore, this demonstrates that the inundation windows 80 – 100 % are dominated by swashes shallower than 0.60 m, as their overall mean is negative, and that swashes deeper than 0.60 m remain relatively infrequent. The analysis of swash depths revealed that swashes deeper than 0.45 m do not create large fluxes (not larger than 22 kg/m/s), and that overall they can only occur in areas inundated more than 40 % of the time (Figure 5.13). Furthermore, swashes with a maximum depth comprised within 0.25 – 0.45 m are of great importance. While they have a mean value of net mass fluxes close to zero, they generate large fluxes (up to 45 kg/m/s) localised between 0 – 1.5 m from the bore collapse location (Section 5.3.2.3). Over the spring tidal cycle, the switch in flux direction (Figure 5.12c) also occurred within this active range of swash depths.

5.4.2 Pivot zone

The distribution of the mean net mass fluxes per inundation window in Figure 5.10c displays a shift from positive (onshore) to negative (offshore) between $t_i = 50 - 70$ %, when all tides are combined. By completing the same analysis as Figure 5.10c individually for each tide, the percentage inundation value t_i in which this switch occurred was identified for each tide and is shown for the reference tide in Figure 5.14. The green zone on Figure 5.14a represents the percentage range in which the mean net mass flux direction changes from offshore to onshore (or vice versa for other tides). The same region is superimposed on the timeseries of net bed-level change in figure (Figure 5.14b). This region, referred to as the “pivot zone", was identified for each tide and the associated values of t_i are listed in Table 5.1. The position of this zone appears to vary around the mean shoreline position (black line on Figure 5.14) and is never further than 20 % of inundation from it. This also

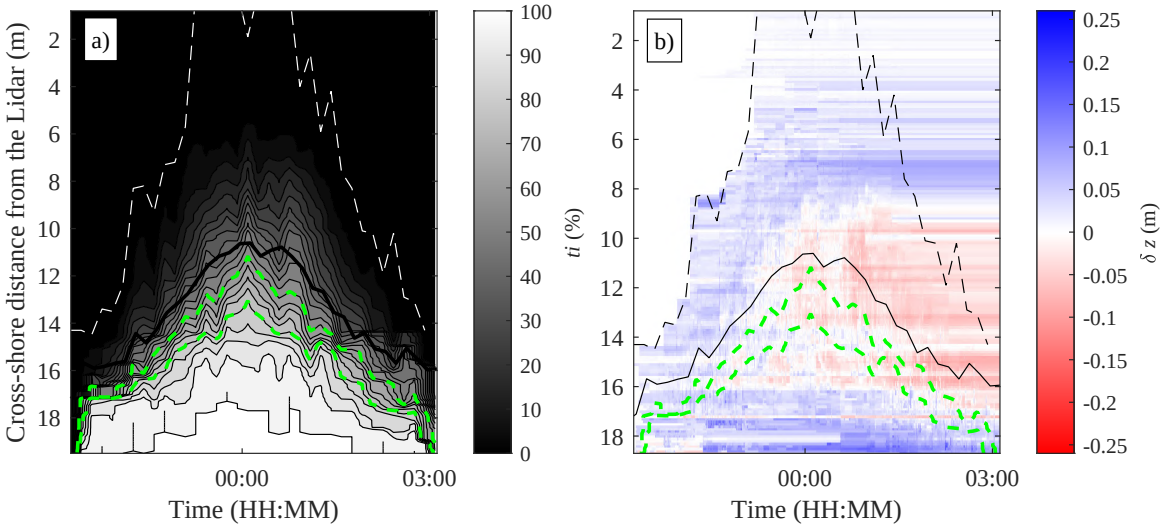

Figure 5.14: (a) Contour plot showing the distribution of the percentage of time that the bed is inundated, t_i as a function of time during the reference tide. (b) Change in bed-level through the swash zone during the reference tide. The green area represents the 60 – 80 % inundation range corresponding to the “pivot zone". The dashed and solid lines represent the run-up limit and the intersection of the beach and mean shoreline position respectively.

Table 5.1: Percentage inundation window and maximum depths of swash associated with the “pivot zone". Note that the first two tides showed only erosive (negative) mean mass fluxes over all the percentage windows and therefore no pivot zone could be identified.

Tide (DD/M-hh)	Pivot zone (%)	Maximum depth (m)
17/1–18h	None	None
18/1–07h	None	None
19/1–21h	60-80	0.46
20/1–08h	10-30	0.44
20/1–23h	70-90	0.37
21/1–08h	70-90	0.44
21/1–23h	30-50	0.35
22/1–10h	70-90	0.53
23/1–01h	30-50	0.36
23/1–10h	40-60	0.45
23/1–23h	70-90	0.53
24/1–12h	20-40	0.31
24/1–23h	70-90	0.41
25/1–12h	10-30	0.31

highlights the importance of the local water level in the morphodynamics of the revetment.

By referring to the equivalent results as shown in Figure 5.13 for each tide (not shown), it was possible to relate the pivot zone to the maximum depth of swash measured in this zone. Table 5.1 lists the percentage inundation range of the pivot zone as well as the maximum depth measured in this region – *i.e.*, no swashes deeper than the maximum value were measured within or landward of the pivot zone – for each recorded tide. Table 5.1 shows that although the inundation range of the pivot zone varies significantly between tides (across almost all percentage inundation windows), the maximum depth of swash within the pivot zone is always (except for the 23/1–23h) within the 0.25 – 0.45 m depth range, and close to the upper bound of this range. This enables the pivot zone to be hydrodynamically described by a zone composed of swashes with a maximum depth close to the seawarAs a consequence, the pivot zone is also related to large extreme events located near the bore collapse point. However, further work is required to take into account fluxes generated by wave breaking on top of swashes.

5.4.3 Cross-shore distribution of bed oscillations

An analysis of spatial and temporal variation of mass fluxes over the reference tide is shown in Figure 5.15. Figure 5.15a presents a timeseries of net cross-shore mass fluxes measured at a single point on the revetment (x = 9.5 m) determined every two minutes and summed over 10–minute intervals. It shows that while the majority of single event fluxes at a point on the revetment causes little or no revetment face volume change (Figure 5.6a), large onshore and offshore mass fluxes occur throughout the tide. This confirms the observation made in Section 5.3.1.1, and shows that revetment changes can be either driven by a small number of swashes causing large fluxes which rearrange the particles or by the accumulation of small

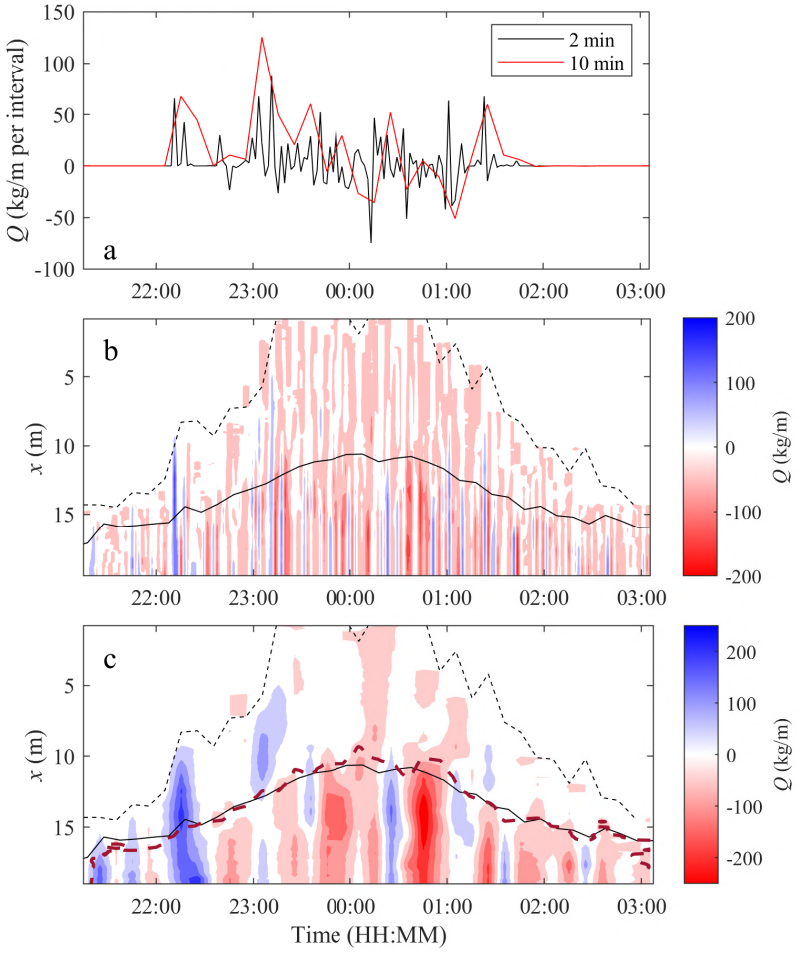

Figure 5.15: (a) Timeseries of net cross-shore mass fluxes for the reference tide at one and ten–minute intervals, at x = 9.5 m. Contour plots of net cross-shore mass flux during the reference tide summed over (b) two minutes and (c) ten–minute time bins. Note that 2 minutes was chosen as it represents the longest swash event recorded. The dashed thick line (violet) marks the cross-shore percentage of inundation limit of the dominant flux oscillations, at 40 % for the reference tide. The dashed and solid lines represent the run-up limit and the intersection of the beach and mean shoreline position respectively. Note that the colour bar scale ranges between ±200 kg/m in (b) and ±250 kg/m in (c).

fluxes, possibly representing the changes in the sand within or underlying the revetment through sand erosion (*i.e.*, winnowing caused by the backwash water) and sand compaction (kinetic sieving). The two lower panels in Figure 5.15 present contour plots of the net cross-shore mass fluxes within two-minute (Figure 5.15b) and ten-minute (Figure 5.15c) intervals. Figure 5.15b shows that at the two minutes sampling interval, there is evidence of oscillating periods of onshore and offshore mass fluxes particularly in the lower parts of the swash zone throughout the entire duration of the tide, although periods of offshore transport are more common. This is confirmed by Figure 5.15c which clearly shows a tendency toward erosive periods when the fluxes are summed over ten minutes.

A feature of Figure 5.15b and Figure 5.15c is that these flux oscillations do not extend all across the revetment during most of the tide except during the first 1 – 2 hours of the rising tide. This again indicates the revetment is more affected by swashes during the rising than the falling tide, suggesting profile stability in the upper part of the swash is rapidly

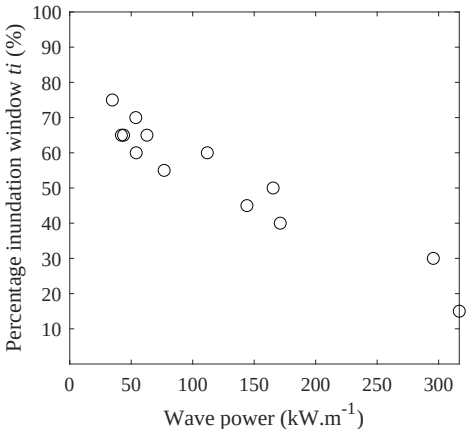

Figure 5.16: Plot of the flux oscillation limit (% of inundation) against the wave power (kW/m). Values of the Pearson r^2 correlation coefficient is 0.92.

reached. The delimitation of these oscillations was extracted for each tide and referred to a corresponding value of inundation percentage t_i. For each tide, this delimitation is located very close to the mean shoreline position (black line in Figure 5.15) – it often coincides with the mean shoreline position, and is never further than 10 % of inundation away from it, while it does not show any correlation with the pivot zone. This highlights once again the importance of the local water level in the morphodynamics of the revetment.

For each recorded tide, the percentage was then plotted against wave power in Figure 5.16. The plot shows a correlation between the relative position of this limit in the swash and the wave power, with a high coefficient of correlation (r^2 = 0.92). It indicates that as the power increases (decreases), the line of delimitation moves landward (seaward) within the normalised swash. By referring to the equivalent figure of Figure 5.13 for each tide, the maximum depth of swash related to this oscillation limit was found to be very similar for all tides, with an average value of 0.34 m. Consequently, as the maximum depth of swash present at this delimitation is globally similar for each tide, the combination of wave power and water levels in a saturated surf zone influences the swash power and the maximum depth of swashes present in percentage inundation windows. Furthermore, locations landward of this limit for the reference tide are only composed of short swashes with a duration of less than 15 seconds (similar range for each recorded tide). Referring to Figure 5.11 shows that swashes shorter than 15 seconds are also relatively shallow. These shallow swashes have a small mean mass flux magnitude per second, with a negative mean net cross-shore mass flux per second (Figure 5.12b,c). For this reason, most of the mass fluxes measured above this limit are negative (Figure 5.15b,c), and are generally weak after the initial rearrangements occurring during the rising tide.

5.4.4 Comparison with sandy beaches

The present results suggest strong similarities with sandy beaches in terms of mass transport in the swash zone. The analysis of the swash-induced bed-level changes (Figure 5.6a) for the reference tide revealed that the majority of elevation changes occurring during the reference tide on the revetment are smaller than ±3 cm, with 50 % to 80 % generating zero

net changes depending on the cross-shore position on the revetment. It also showed that a single swash event can produce large changes of the order of magnitude of the cobble diameter D_{50} = 15 cm, but that in general, these events are rare. These large events are also four to eight times larger than those observed on sandy beaches (Blenkinsopp et al., 2011; Baldock et al., 2006; Turner et al., 2008), although, unlike for sand, these large changes are expected on a dynamic revetment as the movement of a single cobble can significantly change the bed elevation at a point on the surface. The dynamic revetment studied in this paper being composed of a wide material gradation with a D_{50} = 15 cm (Section 5.2.1), bed-level changes within the order of magnitude of the diameter should not be rare and yet, very few events cause a net bed-level change of this order. This observation suggests that bed-level changes are driven by complex particle rearrangements, combining surface cobble transport and underlying sand accretion and erosion. The percentage of inundation distribution of swash-induced fluxes (Figure 5.9) was very similar to that measured on sandy beaches by Blenkinsopp et al. (2011) and suggests that the inundation variability of swash-induced fluxes are independent of the bed-type. Furthermore, the bed oscillation pattern presented in Section 5.4.3 was also observed on a sandy beach by Blenkinsopp et al. (2011), which confirms a degree of independence from the bed-type. However, the skewness variations in Figure 5.10a are opposite to those for sand, which is thought to be due to the difference in cross-shore grading and high infiltration on dynamic revetments.

Table 5.2: Wave energy, power, sediment mass fluxes and ratio between net and gross sediment mass flux for each tide. Q_{net} is the net cross-shore mass flux measured over the entire tide at the maximum mean water level position for each high tide. Q_{abs} is the sum of the absolute value of all fluxes measured at the same position as Q_{net}. Note that two tides (18/1-19h and 19/1-08h) are not used for the bulk analysis, as a few large cobbles were manually placed and removed along the lidar line, and this would have biased the analysis.

Tide (DD/M-hh)	E (kJ/m^2)	P (kW)	Q_{net} **(kg/m)**	Q_{abs} (kg/m)	**Ratio** Q_{net}/Q_{abs}
17/1–18h	27.88	316.8	-773	8906	11.5
18/1–07h	28.81	295.7	-2109	15782	7.5
19/1–21h	17.47	171.1	21	6069	289.0
20/1–08h	11.81	106.3	-1138	5425	4.8
20/1–23h	5.11	42.0	284	6646	23.4
21/1–08h	5.23	43.7	-479	6441	13.4
21/1–23h	4.39	34.6	361	4370	12.1
22/1–10h	16.94	111.9	-547	9475	17.3
23/1–01h	18.83	144.0	-457	7450	16.3
23/1–10h	17.76	144.0	-514	6634	12.9
23/1–23h	7.70	76.7	142	5203	36.6
24/1–12h	5.35	54.0	-73	5430	74.4
24/1–23h	4.66	53.6	-435	3347	7.7
25/1–12h	5.82	62.7	-98	2621	26.7

Net mass fluxes, both for the mean and extreme events, are around 20 % smaller than those observed on sandy beaches (Puleo, 2009; Masselink et al., 2009; Blenkinsopp et al., 2011). The net cross-shore mass fluxes measured at the upper locations, x = 1 m are all comprised between ±1 kg/m (not shown in the figure). This value is one order of magnitude

smaller than that measured on sandy beaches in the upper swash by Blenkinsopp et al. (2011) (±10 kg/m), and therefore suggests that the upper part of the revetment during the reference tide changed less than the upper part of a sandy beach. This is likely due to the lower mobility of the larger particles composing the cobble berm. These small fluxes likely represent the underlying sand dynamics, with sand beneath the cobbles being removed by the percolating water, and compacted by kinetic sieving while the cobbles are slightly rearranged. Generally, smaller fluxes per event were measured on the revetment than on sandy beaches which supports the idea that the revetment is more stable and resistant to wave attack than a sandy beach.

Figure 5.7 showed that while both the gross and net rate of bed volume change over the revetment increase and decrease with the water level over the course of a tide, the ratio between them is not constant and varies from 2 to 10. It also showed that the revetment is able to rapidly reshape and reach a stable shape during the incoming tide, resulting in a decrease in both gross and net changes after the first interaction with the upper swashes. The ratio of 10 matches the value measured in the laboratory by Bayle et al. (2020) on a dynamic cobble berm revetment composed of rounded and well sorted cobble with D_{50} = 6.4 cm. This analysis of stability is further explored by looking at the ratio of the net flux to the sum of fluxes from all individual swashes at a point on the revetment over the course of each tide. This is shown in Table 5.2, where the net cross-shore mass flux (Q_{net}) measured at the maximum mean water level position for each tide is on average

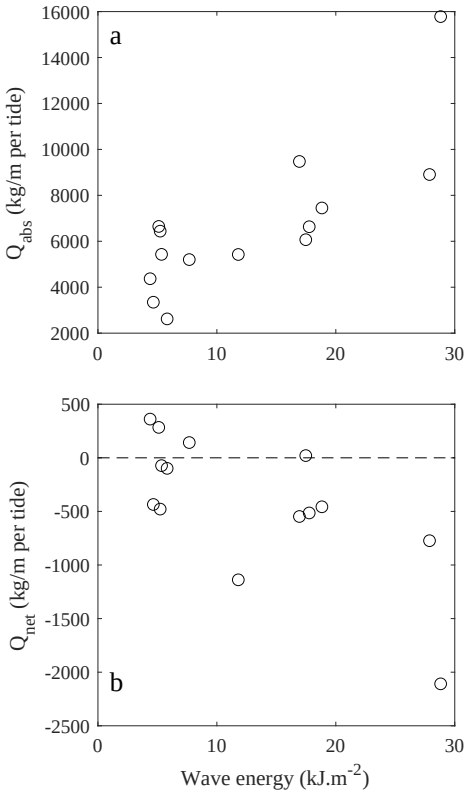

Figure 5.17: Variation in the (a) absolute and (b) net cross-shore mass fluxes measured during all tides at the maximum mean water level for each tide as a function of the offshore wave energy. Values of the Pearson r^2 correlation coefficient are 0.63 and 0.48 for the absolute and net values respectively.

40 times smaller than the absolute cross-shore mass flux (Q_{abs}). Using the same method, Blenkinsopp et al. (2011) measured that the net mass fluxes are on average 63 times smaller than the absolute fluxes for sandy beaches.

Figure 5.17 shows the absolute and net mass fluxes (from Table 5.2) as a function of the offshore wave energy. Figure 5.17 shows that as the wave energy increases, the absolute cross-shore mass fluxes and the magnitude of the net cross-shore mass fluxes both increase (in this case net fluxes are mainly negative). This indicates that more energetic waves generate more absolute cobble motion which translates into smaller, but still important, net fluxes. Figure 5.17 shows that wave climate has an impact on the amount of particle movement during a tide, while previous observations (Figure 5.5, Figure 5.6, Figure 5.7) suggest that the net changes are generally associated with a rapid change in revetment shape during the rising tide. Bayle et al. (2020) demonstrated that the slope of a dynamic revetment changes rapidly as a function of the wave conditions which likely leads to the observed relationship between wave energy and net change. On sandy beaches, changes are slower and the beach slope does not have time to readjust during a high tide. This explains why this relationship between wave conditions and net fluxes was not observed on sandy beaches in Blenkinsopp et al. (2011), although a similar correlation was found with absolute fluxes.

It is important to note that this paper studied bed-level changes and fluxes at the inter-swash event time scale as the lidar cannot measure the intra-swash event fluxes. Studies on sandy beaches at the intra-swash temporal scale from van der Zanden et al. (2015) and Alsina et al. (2018) revealed that bed level changes during a single swash event (uprush and backwash) can be importantly larger than the intra-swash net changes, which are also larger than the inter-swash event changes. Sediment fluxes within a swash are driven by both vertical sediment exchange (such as oscillatory sheet flow) and horizontal advection processes induced by the non-uniformity of the flow (*e.g.*, shear stress larger during the uprush than the backwash). The mechanism can be expected to play a role in the revetment fluxes for the sediment part of the material, but it is likely not important for the gravel part which does not get transported in suspension. Furthermore, the non-uniformity of the flow is further enhanced on the revetment face as most of the backwash infiltrates the cobble layer (Brayne, 2015), which decreases the backwash velocity. Therefore, the intra-swash fluxes are likely different on dynamic revetment than on sandy beaches, but this is yet to be investigated, taking into that the coarse nature of the revetment limits the utilisation of near-bed instrumentation such as conductivity probes.

5.5 Conclusion

The dynamic revetment in North Cove (WA, USA) was monitored over 10 days in January 2019, corresponding to a spring tidal cycle. The swash zone was continuously monitored using a 2-D lidar, and data collected were used to assess the cross-shore mass fluxes of material moved by individual swash events, and analyse the swash–driven morphological changes.

The analysis of bed-level changes and net cross-shore mass fluxes over the revetment demonstrated that revetment changes were mainly driven by very small events (±3 cm and ±50 kg/m), with some rare large bed-level changes of a magnitude similar to the median cobble diameter (D_{50} = 0.15 m). In contrast, some very small fluxes, were also measured in the upper swash zone and attributed to small sand fluxes, suggesting that the dynamics of the sand within or underneath the cobbles also plays a role in the overall elevation change.

For every tide, the distribution of net cross-shore mass fluxes was symmetrical, meaning that positive and negative fluxes tended to balance out over a tide, as the revetment was found to be globally stable. The revetment underwent relatively more net change during the rising tide than the falling tide, by rapidly reaching a stable state driven by the upper swash. Furthermore, it was also shown that over a tide, the sum of all absolute fluxes at the maximum mean water was on average 40 times larger than the magnitude of the net flux at the same point, and that both were correlated to the offshore wave energy.

The analysis of normalised swashes showed that inundation windows < 80 % were characterised by offshore fluxes, and it was inferred that it was associated to both cobble fluxes towards the toe of the revetment, and sand fluxes seaward of the revetment toe which accounted for the total volume loss. The analysis of swash depths revealed that swashes deeper than 0.45 m only occurred in zones inundated more than 40 % of the time, and did not generate large fluxes. In contrast, it was identified that swashes ranging between 0.25 − 0.45 m were important, as they can drive large fluxes per second while keeping a mean flux value close to zero over the tide. The large events occurring in this zone were found to be driven by the bore collapse, which occurs not further than 1.5 m seaward of the position where the flux was measured.

The local water level was found to play a major role in the morphodynamics of the revetment. It was always located near or at the bed oscillation limit and pivot zone, two identified spatial features within the sediment transport distribution. The bed oscillation limit was found to be correlated with the offshore wave power, and were characterised by similar maximum swashes depth (varying around 0.34 m). The pivot zone happened in very different percentage inundation windows across the recorded tides, but was generally characterised by a maximum depth of swash comprised within the 0.25 − 0.45 m range. As a consequence, both zones are partly driven by extreme swashes belonging to the active 0.25 − 0.45 m range of swash depths, themselves generated near the bore collapse.

Future work should focus on a way to monitor the vertical interface between sand cobbles at a high spatial and temporal resolution. Although it was identified that both materials were mobilised by swashes, the event-by-event dynamics of this interface remains unclear.

Acknowledgements

Funding: Paul Bayle is supported by a PhD scholarship through the EPSRC CDT in Water Informatics: Science & Engineering (WISE). Traveling and living fees associated with this experiment were partially covered by a Santander Mobility Grant, obtained via the

University of Bath.

The authors want to thank the entire Washington Department of Ecology CMAP team, for their logistical support in the field. The authors would also like to thank the community of North Cove for their warm welcome and support throughout the experiment. Special thanks to Richard and Dianne Harris for providing a warm and dry place during the experiment, and to Connie Allen for organising the communication and public relations around the experiment. Finally, we thank William Bazeley, Neil Price, Robert Dyer and David Surgenor from the University of Bath for their technical support during the experiment preparation.

References

Aagaard, T. and Hughes, M. G. (2006). Sediment suspension and turbulence in the swash zone of dissipative beaches. *Marine Geology* 228, 117—135.

Ahrens, J. P. (1990). Dynamic revetment. *Coastal Engineering* 138, 1837—1850.

Allan, J. C. and Gabel, L. L. (2016). *Monitoring the response and efficacy of a dynamic revetment constructed adjacent to the columbia river south jetty, Clatsop county, Oregon.* Tech. rep. O-16-07. Oregon Department of Geology and Mineral Industries.

Allan, J. C., Geitgey, R., and Hart, R. (2015). Dynamic revetments for coastal erosion stabilization: a feasible analysis for application on the oregon coast. *Oregon Department of Geology and Mineral Industries* Special issue, 37.

Allan, J. C., Harris, E., Stephensen, S., Politano, V., Laboratory, H., Folger, C., and Nelson, W. (2012). *Hatfield Marine Science Center Dynamic Revetment Project*. Tech. rep. Hatfield Marine Science Center, Oregon State University.

Allan, J. C., Hart, R., and Tranquili, J. V. (2006). The use of Passive Integrated Transponder (PIT) tags to trace cobble transport in a mixed sand-and-gravel beach on the high-energy Oregon coast, USA. *Marine Geology* 232.

Allan, J. C. and Komar, P. D. (2002). Extreme storms in the Pacific Northwest coast during the 1997–98 El Niño and 1998–99 La Niña. *Journal of Coastal Research* 18, 175—193.

Almeida, L. P., Masselink, G., Russel, P. E., and Davidson, M. A. (2015). Observations of gravel beach dynamics during high energy wave conditions using a laser scanner. *Geomorphology* 228, 15—27.

Alsina, J. M., van der Zanden, J., Cáceres, I., and Ribberink, J. S. (2018). The influence of wave groups and wave-swash interactions on sediment transport and bed evolution in the swash zone. *Coastal Engineering* 140, pp. 23 –42.

Baldock, T. E., Barnes, M. P., and Hughes, M. G. (2006). Field observations of instantaneous cross-shore free surface profiles and flow depths in the swash zone. *Coastal Dynamics 2005 : State of the Practice*.

Bayle, P. M., Blenkinsopp, C. E., Conley, D., Masselink, G., Beuzen, T., and Almar, R. (2020). Performance Of A Dynamic Cobble Berm Revetment for Coastal Protection, under increasing water level. *Coastal Engineering* 159.

Blenkinsopp, C. E., Mole, M. A., Turner, I. L., and Peirson, W. L. (2010a). Measurements of the time-varying free-surface profile across the swash zone obtained using an industrial LiDAR. *Coastal Engineering* 57, 1059—1065.

Blenkinsopp, C. E., Turner, I. L., Masselink, G., and Russell, P. E. (2011). Swash zone sediment fluxes: Field observations. *Coastal Engineering* 58, 28—44.

Bluck, B. J. (1967). Sedimentation of Beach Gravels: Examples from South Wales. *Journal of Sedimentary Petrology* 37, 128—156.

Brayne, R. P. (2015). "The Relationship between Nearshore Wave Conditions and Coarse Clastic Beach Dynamics". PhD thesis. University of Exeter.

Brodie, K. L., Slocum, R. K., and McNinch, J. E. (2012). New insights into the physical drivers of wave runup from a continuously operating terrestrial laser scanner. *Oceans, 2012*, pp. 1 – 8. DOI: 10.1109/OCEANS.2012.6404955.

Carter, R. W. G. and Orford, J. D. (1984). Coarse clastic barrier beaches: a discussion of the distinctive dynamic and morphosedimentary characteristics. *Marine Geology* 60, 377—389.

Holland, A. (2019). "Mixed sand and gravel beaches: accurate measurement of active layer depth to develop predictive models of sediment transport". PhD thesis. University of Sussex.

Hughes, M. and Moseley, A. (2007). Hydrokinematic regions within the swash zone. *Coastal Engineering* 27, 2000—2013.

Jennings, R. and Schulmeister, J. (2002). A field based classification scheme for gravel beaches. *Marine Geology* 186, 611—228.

Jennings, R. and Shulmeister, J. (2002). A field based classification scheme for gravel beaches. *Marine Geology* 186, 211—228.

Kaminsky, G. M., Ruggiero, P., Buijsman, M. C., McCandless, D., and Gelfenbaum, G. (2010). Historical evolution of the Columbia River littoral cell. *Marine Geology* 273, 96—126.

Komar, P. and Allan, J. C. (2010). "Design with Nature strategies for shore protection - The construction of a cobble berm and artificial dune in an Oregon State Park". *Puget Sound Shorelines and the Impacts of Armoring—Proceedings of a State of the Science Workshop*. U.S. Geological Survey Scientific Investigations Report 2010-5254, 117—126.

Loman, G. J. A., van Gent, M. R. A., and Markvoort, J. W. (2010). Physical model testing of an innovative cobble shore, Part I: Verification of cross-shore profile deformation. *Third International Conference on the Application of Physical Modelling to Port and Coastal Protection*.

Lorang, M. S. (1991). An artificial perch-gravel beach as a shore protection structure. *Coastal Sediments '91*. Vol. 2. Reston, Va., American Society of Civil Engineers, 1916—1925.

Martins, K., Blenkinsopp, C., Power, H. E., Bruder, B., Puleo, J. A., and Bergsma, E. (2017a). High-resolution monitoring of wave transformation in the surf zone using a LiDAR scanner array. *Coastal Engineering* 128, 37—43.

Martins, K., Blenkinsopp, C. E., and Zang, J. (2016). Monitoring Individual Wave Characteristics in the Inner Surf with a 2-Dimensional Laser Scanner (LiDAR). *Journal of Sensors*, pp. 1 – 11. DOI: 10.1155/2016/7965431.

Masselink, G., Evans, D., Hughes, M. G., and Russell, P. E. (2005). Suspended sediment transport in the swash zone of a dissipative beach. *Marine Geology* 216, 169—189.

Masselink, G. and Russell, P. E. (2006). Flow velocities, sediment transport and morphological change in the swash zone of two contrasting beaches. *Marine Geology* 227, 227—240.

Masselink, G., Russell, P. E., Turner, I. L., and Blenkinsopp, C. E. (2009). Net sediment transport and morphological change in the swash zone of a high-energy sandy beach from swash event to tidal cycle time-scales. *Marine Geology* 267, 18—35.

Michalsen, D. R. (2018). *Feasibility of long-term shoreline stabilisation alternatives between North Cove and Tokeland, WA*. Tech. rep. U.S. Army Corps of Engineers, Seattle District.

Orford, J. D. (1975). Discrimination of particle zonation on a pebble beach. *Sedimentology* 22 (3), 441—463.

Poate, T., Masselink, G., McCall, R., and Russell, P. E. (2015). UK Storms 2014: Gravel Beach Response. *Coastal Sediments 2015*.

Powell, K. A. (1988). The dynamic response of shingle beaches to random waves. *Coastal Engineering* 130, 1763—1773.

Puleo, J. A. (2009). Tidal variability of swash zone sediment suspension and transport. *Journal of Coastal Research* 25, 937—948.

Pye, K. and Blott, S. J. (2018). *Advice on Sustainable Management of Coastal Shingle Resources*. Tech. rep. 273. Natural Resources Wales.

Ruggiero, P., Kaminsky, G. M., Gelfenbaum, G., and Voigt, B. (2005). Seasonal to interannual morphodynamics along a high-energy dissipative littoral cell. *Journal of Coastal Research* 21, 553—578.

Sallenger, A. H. (2000). Storm impact scale for barrier islands. *Journal of Coastal Research* 16, 890—895.

Turner, I. L., Russel, P. E., and Butt, T. (2008). Measurement of wave-by-wave bed-levels in the swash zone. *Coastal Engineering* 55, 1237—1242.

Turner, I. L., Russell, P. E., Butt, T., Blenkinsopp, C. E., and Masselink, G. (2009). In-situ estimates of net sediment flux per swash: Reply to Discussion by T.E. Baldock 'Measurement of wave-by-wave bed-levels in the swash zone'. *Coastal Engineering* 56, 1009—1012.

Van Rijn, L. C. (2010). *Modelling erosion of gravel/shingle beaches and barriers*. Tech. rep. D13b. European Commission, Conscience.

Ward, D. L. and Ahrens, J. P. (1992). *Laboratory study of a dynamic berm revetment*. Tech. rep. US Army Corps of Engineers.

Williams, A. T. and Caldwell, N. E. (1988). Particle size and shape in pebble-beach sedimentation. *Marine Geology* 82, 199—215.

Williams, J., Masseling, G., Buscombe, D., Turner, I., Matias, A., Ferreira, O., Bradbury, A., Metje, N., Coates, L., Chapman, D., Thompson, C., Albers, T., and Pan, S. (2009). BARDEX (Barrier Dynamics Experiment): Taking the beach into the laboratory. *Journal of Coastal Research* 56, 156—162.

Wright, L. D., Short, A. D., and Nielsen, P. (1982). *Morphodynamics of high energy beaches and surf zones: A brief synthesis.* Tech. rep. 82/5. Coastal Study Unit, University of Sydney.

van der Meer, J. W. and Pilarczyk, K. W. (1986). Dynamic Stability of Rock Slopes and Gravel Beaches. *Coastal Engineering* 125, 1713—1726.

van der Zanden, J., Alsina, J. M., Cáceres, I., Buijsrogge, R. H., and Ribberink, J. S. (2015). Bed level motions and sheet flow processes in the swash zone: Observations with a new conductivity-based concentration measuring technique (CCM+). *Coastal Engineering* 105, pp. 47 –65.

Chapter concluding remarks

In this Chapter, the net cross-shore sediment fluxes over the revetment resulting from the interaction between the revetment and swashes were investigated. It was shown that most swash-induced fluxes were very small and almost balanced out over time. A dynamic stability was identified at the swash scale, and the ratio of net and gross rate was found to be similar to that measured in the laboratory. Most of the revetment changes toward a stable state occurred during the rising tide, which confirms the observation made using low frequency measurements in Chapter 4. Furthermore these rapid changes on an incoming tide are consistent with the rapid revetment response to changing wave conditions detailed in Chapter 3. The distribution of individual swash sediment fluxes both in space and time were very similar to those measured on sandy beaches (Blenkinsopp et al., 2011), highlighting the independence of swashes from the type of sediment.

The water level was found to be important for revetment changes as it defines how much of the swash zone interacts with the revetment. In addition, at high tide, the surf zone is generally saturated on dissipative beaches, and the energy reaching the revetment is directly related to the water level at the toe of the revetment. In parallel, offshore wave energy was found to be important as it was correlated with gross and net bed-level changes, hence how much surface cobble moved. Figure 5.7.c,d showed that the first four metres of swash (*i.e.*, the shallowest and least energetic part of the swash) can still generate important net changes, though one order of magnitude smaller than the overall changes driven by the entire swash. This explains why a high water level can generate significant net changes even associated with low energy conditions, as seen in Chapter 4.

In the saturated surf zone studied, the water level and the offshore wave power was found to rule the position of swash-induced morphological variations. These variations were linked to intense swashes which were identified near the bore collapse position. The rearrangement of particles could be partially identified at the swash scale. However, as mentioned in Chapter 4, further analysis will rely on the development of techniques to measure real-time variations in the vertical sand–cobble interface.

Chapter 6

A new approach for scaling beach profile evolution and sediment transport rates in distorted laboratory models

This chapter is based on two research papers: an article accepted (manuscript sent back after addressing the minor corrections) in Coastal Engineering (Elsevier), and an article published in the Special Issue of Journal of Coastal Research. The first article presents a new scaling approach to compare distorted beach profiles from different flume scales. The second article, whose reference is given later, presents more results using the new developed scaling approach presented in the first paper.

Paul M. Bayle, Tomas Beuzen, Chris E. Blenkinsopp, Tom E. Baldock, and Ian L. Turner (In review). A new approach for scaling beach profile evolution and sediment transport rates in distorted laboratory models. *Coastal Engineering*.

Abstract

Laboratory wave flume experiments in coastal engineering and physical oceanography are widely used to provide an improved understanding of morphodynamic processes. Wave flume facilities around the world vary greatly in their physical dimensions and differences in the resulting distortion of the modelled processes are reconciled using scaling laws. However, it is known that perfect model-prototype scaling of all hydro and morphodynamic processes is rarely possible and there is a lack of understanding to what extent distorted models can be used for direct morphological comparison. To address this issue, distorted scale laboratory flume experiments were undertaken in three different facilities, with the aim to measure and compare beach profile evolution under erosive waves and increasing water levels. A novel approach was developed to transform and scale the different experimental geometries into dimensionless coordinates, which enabled a direct quantitative comparison of the beach profile evolution and sediment transport rates between the differing distorted experimental scales. Comparing results from the three experiments revealed that the dimensionless scaled morphological behaviour was similar after the same number of waves – despite very different degrees of model distortion. The distorted profiles appeared to be suitable for comparison as long as a modified version of the Dean number is maintained between them. The new method was then validated with two further published datasets, and showed good agreement for both dimensionless profile shape, dimensionless sediment transport and morphodynamics parameters. The new approach scales the sediment transport by the square of the runup, proportional to HL, rather than H^2, and yields good agreement between the datasets. It is further shown that the new scaling method is also applicable for comparing distorted profile evolution under water level increase, as long as the water level is raised in a similar way between the experiments and by the same total increment relative to the significant wave height ($\Delta h/H_s$).

Declaration concerning the article used for this Chapter:

Title	A new approach for scaling beach profile evolution and sediment transport rates in distorted laboratory models
Status	Accepted with minor corrections (already sent back) in Coastal Engineering (Elsevier)
Details	Paul M. Bayle, Tomas Beuzen, Chris E. Blenkinsopp, Tom E. Baldock, and Ian L. Turner (In review). A new approach for scaling beach profile evolution and sediment transport rates in distorted laboratory models. *Coastal Engineering*.
Contribution from the authors	P.M. Bayle: Planning/Collection/Processing/Analysis of data; Manuscript (65%) T. Beuzen: Collecting/Processing/Analysis of data; Manuscript (10%) C.E. Blenkinsopp: Analysis of the data; Edited drafts of manuscript (10%) T.E. Baldock: Analysis of the data; Edited drafts of manuscript (10%) I.L. Turner: Suggesting data analysis; Edited drafts of manuscript (5%)
Statement	This paper reports on original research I conducted during the period of my Higher Degree by Research candidature.
Date and Signature	

Preamble

The previous Chapters have shown the importance of both laboratory and field experiments in the context of coastal engineering. They have also demonstrated that while field surveys are important and generate datasets under a complete environmental forcing, the simplifications inherent to laboratory experiments are in many aspects very valuable. For instance, the way the degree of protection in term of runup and shoreline retreat was assessed in Chapter 3 could only be achieved in the laboratory, as very few field experiments can give such a reliable comparison of pre- and post-installation. Therefore, laboratories are yet very useful to understand specific aspect and behaviour of coastal protection, and more generally, beach profile evolution under a wide range of waves and water levels conditions.

There are many different flumes around the world, with a wide range of sizes and wave generation capacity. Scientists running a laboratory experiment typically have multiple objectives to fulfil, as was the case for the GWK experiment presented in Chapter 3, and therefore they design their experiment and test conditions primarily with these objectives in and the available facility in mind. Consequently, by optimising experiments for the available facilities there is a typically wide inconsistency in the scales and procedures used by different experimentalists. While a lot of data on beach profile evolution and coastal protection is available from the numerous flume experiments performed in the past, the lack of consistency in scale and procedure means that these are often assumed to not be comparable.

We hypothesise that a lot of distorted flume models exist and could potentially be used together as a dataset to analyse an aspect of beach profile change. This raises the following research questions/objectives:

1. Can a method able to scale distorted profiles be developed and allow a comparison between them?
2. What parameters can be compared with such a method, and how reliable it is?
3. Could a comparison of beach profile measurements under water level increase at different distorted scales be compared, with or without protective structures?

This chapter presents a complete scaling analysis using the GWK profile data, as well as two other medium scale datasets collected by two of the co-authors.

Chapter 6.

6.1 Introduction

Physical models have been widely used in coastal engineering to study complex coastal processes. Such models enable researchers to overcome the inherent obstacles of modeling coastal systems, such as large spatiotemporal timescales and natural variability, and to reproduce conditions in a controlled environment to better understand coastal processes (Hughes, 1993). In coastal engineering and physical oceanography, laboratory wave flumes (hereafter referred to simply as "flumes") have been extensively used to model beach profile evolution under wave forcing. Flumes exist in many laboratories around the world, ranging from prototype scale (100s metres long) to reduced-scale (a few metres long). One of the main challenges when undertaking laboratory experiments is how to correctly relate the observations and results from one experiment to another, and how to relate small-scale experiments to the prototype scale (*i.e.*, nature).

The number of previous studies that are available to perform scaling comparisons between different size flumes is limited. Indeed, every flume experiment has particular objectives and therefore uses specific experimental procedures and test cases to achieve them. For this reason, it is difficult to identify experiments from the literature with similar datasets which allow a complete and unbiased scale comparison. To the authors' knowledge, the only study performing such a comparison was undertaken by van Rijn et al. (2011) in which three similar experiments (with the same wave conditions and procedures) from three different flumes were quantitatively and qualitatively compared. It was shown that the morphodynamics of the different flume experiments at different scales could be compared as long as the scaled models were undistorted relative to each other (*i.e.*, scaling rules respected). However, the undistorted experiments compared in the work reported by van Rijn et al. (2011) were performed in the Hannover, Barcelona and Delft wave flumes, which are relatively large compared to the more common flume sizes that are available to most researchers. As a result, it remains unclear to what extent a comparison can be done between smaller scale flume experiments and prototype, distorted or not.

During the past several decades, many flume-based experiments have been undertaken to investigate beach and dune response to erosive and accretive waves, under monochromatic, bichromatic and random waves (*e.g.*, Vellinga, 1982; Kraus and Larson, 1988). These types of experiments have mainly been undertaken in small and medium flumes due to the relatively small number of large-scale flumes that are available to researchers around the world. More recently, flume experiments have been used to assess the impact of rising water levels on sandy coastline evolution to better understand the potential impacts of sea level rise caused by predicted climate change (IPCC, 2014). In particular, two medium-scale experiments, described in Atkinson et al. (2018) and Beuzen et al. (2018), have investigated beach profile response to erosive waves and a rising water level to study the effect of sea level rise on both engineered and non-engineered coastlines. While these two studies provided new insights into beach profile evolution under rising water levels, the scaled nature of the experiments means that the direct application of these flume-based observations to prototype scale behaviour is unclear.

This paper aims to develop a new scaling methodology for comparing beach profiles of distorted experiments, using three different datasets: a novel prototype-scale laboratory dataset (obtained as a component of the DynaRev experiment Blenkinsopp et al., In review), and two existing medium-scale model datasets (obtained from the experiments described in Atkinson et al., 2018; Beuzen et al., 2018). While each dataset measures beach profile response to erosive waves and increasing water levels, they differ in terms of scale and hydrodynamics. The proposed scaling method is used to analyse the morphological changes and sediment transport pattern of the three experiments under both still and increasing water level, in order to more comprehensively assess the potential and the limitations of the method.

Section 2 provides a summary of the most commonly used physics-based approaches to physical model scaling. Section 3 presents the three experiments used in this study and describe the parameters used in the comparison. Section 4 compares the scale of each experiment and presents a novel approach to scale and compare distorted beach profiles. Section 5 presents the results and the validation of the profile comparison performed with the novel method, under still and increasing water level. Section 6 discusses the constraints associated with the method, and presents a one simple application of the new approach.

6.2 Scaling rules for physical model

The most common approach to scale a physical experiment is to use scaling laws in which the ratio of a parameter in the prototype and scaled model (Vellinga, 1982; van Rijn et al., 2011) is expressed as follows:

$$n = \frac{p_p}{p_m} \tag{6.1}$$

where p_p represents the parameter in the prototype and p_m the same parameter in the scaled model (this is not limited to prototype, as two models can be compared to each other). This ratio is used in scaling laws, which are generally well established even though they often differ slightly from one author to another (Noda, 1972; Kamphuisk, 1972; Vellinga, 1986; van Rijn et al., 2011). For free surface flows dominated by gravity effects, hydrodynamic parameters are most commonly scaled using the Froude scaling law which assumes that the Froude number at model and prototype-scale is conserved. This law is represented by:

$$n_H = n_L = n_T^2 = n_h = n_u^2 \tag{6.2}$$

where H is the wave height, L the wavelength, T the wave period, h the water depth (if finite depth wave conditions are used) and u is the wave orbital velocity. This relationship ensures that the hydrodynamics of the scaled model are physically consistent with the prototype, and if Froude scaling is respected then the model hydrodynamics can be considered to be undistorted.

To verify the physical (geometrical) relationship between model and prototype, the

distortion scale ratio is used (Noda, 1972; Kamphuisk, 1972; van Rijn et al., 2011), and defined as:

$$n_g = \frac{n_l}{n_h} \tag{6.3}$$

where n_g is the distortion scale ratio for physical geometry, n_l is the ratio of length and n_h the ratio of height between model and prototype. In the present context, these parameters usually represent the length and the height of the beach profile being analysed. If the result of Eq. 6.3 is unity, then the physical geometry of the model is undistorted (*i.e.*, same beach slope), otherwise, it is distorted.

While Froude scaling (Eq. 6.2) must be respected in a model to scale hydrodynamic parameters correctly, the distortion scale ratio Eq. 6.3 is often considered to be a more flexible parameter. Noda (1972) and Vellinga (1982) defined different accepted ranges of distortion for this parameter as $n_l/n_h = (n_h)^{0.32}$ and $n_l/n_h = (n_h)^{0.28}(n_{ws})^{-0.56}$ respectively (w_s being the sediment settling velocity) – the range being bounded by this value and 1. These two methods give the same order of magnitude for the accepted range of distortion, in which models are assumed to be qualitatively and quantitatively comparable to the prototype, as long as the Froude scaling is respected. van Rijn et al. (2011) also defined an accepted distortion range for both dune and beach erosion experiments. It has been argued that distorted models can be used if the qualitative behaviour of the beach profile is the most important feature, and not the precise quantitative reproduction of hydro and morphodynamics (Vellinga, 1982; van Rijn et al., 2011; Baldock et al., 2011; Atkinson et al., 2018).

Other parameters have been identified (Hughes, 1993; Alsina et al., 2015; Baldock et al., 2010; van Rijn et al., 2011) as important for model scaling, and they are presented in Table 6.1, along with their generally accepted thresholds. Following the aforementioned scaling laws, two experiments which are undistorted regarding the Froude and geometry scaling automatically have the same surf similarity (ξ_0) and wave steepness (H/L) parameters. However, these laws do not consider the sediment size and type, which are two important parameters incorporated into the dimensionless fall velocity (also referred to as the "Dean number", (Gourlay, 1968; Dean, 1973), the Shields's number and the Reynolds number (see Table 6.1). As a result, an additional scaling parameter $n_{D_{50}}$ has been taken into consideration in many studies (Noda, 1972; Kamphuisk, 1972; van Rijn et al., 2011). According to these studies, various authors have suggested acceptable ranges within which results can be considered comparable to prototype and have defined some rules to scale it – $n_{D_{50}} = (n_h)^{0.83}$ for $n_h < 2.2$ and $n_{D_{50}} = 1.7(n_h)^{0.2}$ for $n_h > 2.2$ (van Rijn et al., 2011). Generally, the sediment diameter is scaled so that the excess of bed shear stress or friction velocity are the same in all experiments – *i.e.*, the difference between the actual bed shear stress at a given depth and the critical value required to initiate motion is the same for all experiments. As a result, if Froude scaling (Eq. 6.2) is respected and the sand is correctly scaled, then the Shields's and Dean number are maintained between prototype and model, but the grain Reynolds number is not. This physical inconsistency is inherent to model

Table 6.1: Important parameters to consider for scaling of coastal engineering models. H_0 is the deepwater significant wave height (m), T_p the wave peak period (s), L_0 is the associated deepwater wavelength (m), Δ is the beach slope angle, w_s is the sediment settling fall velocity (m/s), $\tau_0(d)$ is the bed shear stress (N/m^2) at the depth d (m), ρ_ss and ρ are respectively the sediment and water density (kg/m^3), g is the acceleration due to gravity (m/s^2), D_{50} is the median sediment diameter (m), u_* is the friction velocity (m/s) and ν is the kinematic viscosity (m^2/s). The lower case "0" indicates deepwater wave condition for the rest of the paper. The lower case 'crit' indicates the critical value of the parameter.

Parameter name	**Parameter symbol**	**Parameter equation**	**Threshold**
Surf similarity or Iribarren number (Battjes, 1974)	ξ_0	$\tan\beta/\sqrt{H_0/L_0}$	$\xi_0 < 0.3$, Dissipative; $0.3 < \xi_0 < 1$, Intermediate; $\xi_0 > 1$, Reflective
Dimensionless fall velocity (Gourlay, 1968; Nayak, 1970; Dean, 1973)	Ω_0	$H_0/(w_s T_p)$	$\Omega_0 < 1$, Dissipative; $1 < \Omega_0 < 6$, Intermediate; $\Omega_0 > 6$, Reflective
Modified dimensionless fall velocity (Hattori and Kawamata, 1980)	Ω_β	$H_0 \tan\beta/(w_s T_p)$	$\Omega_\beta < 0.08$, Onshore transport dominates; $\Omega_\beta > 0.08$, Offshore transport dominates
Shields's number (Shields, 1936)	θ_0	$\tau_0(d)/(\rho_s - \rho)gD_{50}$	$\theta_0(d) > \theta_{crit,susp}$, Suspension transport expected at depth d; $\theta_0(d) > \theta_{crit,bedload}$, Bedload transport expected at depth d.
Wave steepness	W_{st}	H_0/L_0	–
Grain Reynolds number	$R_{e*}(d)$	$u_* D_{50}/\nu$	$R_{e*}(d) > R_{e_{crit}}$, Inertia force is strong enough at depth d; $R_{e*}(d) < R_{e_{crit}}$, Inertia force is not strong enough at depth d, which limits bedload transport.

scaling and means that the sand grain size always introduces scaling error, whether via the Shields's and Dean number or the Reynolds number. Furthermore, the modified version of the Dean number, including the slope, is only conserved if the compared experiments have the same initial slope. Therefore, using similar sand size in model and prototype and matching the modified version of the Dean number would automatically lead to a distorted model regarding the Froude scaling law.

Besides this paradox, sand scaling is not performed in many laboratory experiments for two primary reasons: firstly, for practicality and reduced operational costs, flumes tend to have a permanent type of sand regardless of the experiment; and, secondly, for small scale models, the theoretical scaled sand diameter would be so small that it would have cohesive properties which would significantly influence sediment transport behaviour. Indeed, according to the Shields entrainment function (Shields, 1936), the critical Shields's number required to initiate motion significantly increases for sediment characterised by a critical Reynolds number smaller than 2. Moreover, according to the initiation of suspended sediment transport curve (van Rijn, 1993, 2012; Soulsby, 1997), sediment with a dimensionless grain number smaller than 3 do not undergo bedload transport but instead, switches directly from immobile to suspended. For these reasons, lightweight (often artificial) sediment has been used in many experiments in the past.

Based on existing scaling rules, a model can be undistorted in one aspect (*e.g.*, hydrodynamics) but distorted in another (*e.g.*, geometric scale). Previous laboratory studies have mainly focused on models which are distorted with respect to sediment size only (van Rijn et al., 2011) — not respecting the sediment scaling rules, but respecting the geometric and/or Froude scaling — but little attention has been given to models distorted with re-

spect to hydrodynamics (Froude scaling) or physical geometry (distortion scale ratio), or both. As a result, the suitability of such models to be used for qualitative and quantitative comparisons has not been thoroughly assessed.

To relate the morphological changes observed in a model to the prototype, it is important to compare the data at the same relative time using existing scaling rules (*e.g.*, $n_{TM} = (n_h)^{0.5}$, van Rijn et al., 2011; Vellinga, 1986). However, these rules are only applicable if the compared experiments have the same distortion scale ratio n_g (or at least within the accepted range of distortion) and if the hydraulic Froude scaling is respected. In consequence, it is complicated to scale time for models which are distorted regarding these latter rules. To overcome this issue, a common approach is to compare profiles after the same number of waves. This does not remove completely the time component from the analysis, as it is equivalent to a hydrodynamic time instead, but it is generally accepted as a good approximation (Kamphuisk, 1972; Vellinga, 1986).

In addition to considering scale effects in laboratory models, it is crucial to have a reliable methodology to compare a modelled profile with the prototype. One approach is to convert the local coordinate of each profile in the laboratory setting into dimensionless coordinates shared by both scales. van Rijn et al. (2011) attempted this by multiplying the local profile coordinate by the square of the local offshore significant wave height (H_{m0}), which is appropriate if the model is not distorted with respect to geometry (*e.g.*, same beach slope). Here we propose that for distorted models, a similar approach can be employed using the method adopted by Peregrine and Williams (2001) for swash flows. Peregrine and Williams (2001) used parameters shown in Eq. 6.4 and Eq. 6.5 to remove beach gradient and non-dimensionalise the non-linear shallow water equation for swash flows:

$$x^* = \frac{(sin\beta)x}{A} \tag{6.4}$$

$$z^* = \frac{(cos\beta)z}{A} \tag{6.5}$$

where β is the angle of the beach slope, x and z are the local coordinate system, x^* and z^* are the new dimensionless coordinate system, and A is half of the length of the vertical excursion of the undisturbed swash, measured from the lower boundary of the swash to the maximum height of run-up. These two equations (Eq. 6.4 and Eq. 6.5) appear more suitable for the analysis of distorted profiles as they rotate all profiles onto the same 45° gradient (*e.g.*, Guard and Baldock, 2007). This scaling does not however relate the coordinate system to the offshore wave conditions of each experiment and this paper also provides the method to address this.

6.3 Methodology

6.3.1 Wave flume and instrumentation

The methodology presented in this paper for comparing distorted datasets was developed from two scaled model datasets and a prototype-scale dataset obtained in three differ-

ent laboratories. The details of each wave flume are presented here and summarised in Table 6.1.

The prototype-scale dataset was obtained from the DynaRev experiment, which was undertaken in the Groβer WellenKanal (GWK) large wave flume laboratory, during August and September 2017. The flume is located at the Forschungszentrum Kuste (FZK Coastal Research Centre), which is a joint institution between the University of Hannover and the Technical University Braunschweig located in Hannover, Germany. A complete experimental description can be found in Blenkinsopp et al. (In review) and further details of the experiment are presented in Bayle et al. (2020). The flume is 309 m long, 7 m deep and 5 m wide and equipped with a combined piston-flap-type wave paddle. Reflected waves and low-frequency resonance (*e.g.*, seiche) are damped at the paddle using Automatic Reflection Compensation (ARC). A mechanical profiler was used to measure the beach profile after each test. The profiler consists of a mechanical roller attached to a mobile trolley which runs along the flume sidewalls. It measures the bed coordinates, within 1-2 cm of vertical and horizontal accuracy. The coordinate system is defined as follows: the cross-shore position, x has its origin at the wave paddle and is positive toward the beach; the vertical elevation, z is positive upward the concrete bottom of the flume.

The first scaled model dataset was obtained from an experiment performed in the University of New South Wales (UNSW) flume located at the Water Research Laboratory (WRL), Sydney, Australia. The complete experimental description and results can be found in Beuzen et al. (2018). This flume is 44 m long, 1.6 m deep and 1.2 m wide. It uses a piston-type wave paddle backed with specialised foam blocks to damp wave reflections. Beach profiles were measured using a laser measurement system, as described in Atkinson and Baldock (2016). This system consists of an array of five SICK DT50-P111 class 2 laser distance sensors mounted above the flume on a trolley rolling on the flume sidewall. The final measured profile is an average of the five cross-shore profiles obtained and is measured within 2 mm of vertical and horizontal accuracy. The coordinate system is defined as follows: the cross-shore position, x has its origin at the bottom of the beach profile and is positive toward the beach; the vertical elevation, z is positive upward the bottom of the flume.

The second scaled model dataset was obtained from an experiment undertaken in the University of Queensland (UQ) flume at the School of Civil Engineering, Brisbane, Australia. The flume is 22 m long, 1 m deep and 1 m wide, a complete description is given in Baldock et al. (2017). The flume has a piston-type wavemaker with active wave absorption. Beach profiles were obtained using the original laser measuring system developed by Atkinson and Baldock (2016). It measures the bed coordinates within 2 mm of vertical and horizontal accuracy. The coordinate system is defined as follows: the cross-shore position, x has its origin at the wave paddle and is positive toward the beach; the vertical elevation, z is positive upward the bottom of the flume.

Table 6.2: Size of the three physical laboratory flumes used in this paper, along with the general test conditions and characteristics for each experiment.

	Length (m)	Width (m)	Height (m)	H_s (m)	T_p (s)	Slope	Sand D_{50} (mm)	Water Level (m)	Time at each water level (h)
GWK	309	5	7	0.8	6	1:15	0.33	4.5 4.6 4.7 4.8 4.9	20 7 7 7 14
UNSW	44	1.2	1.6	0.15	1.25	1:10	0.35	1 1.015 1.030 1.045 1.060 1.075	7.67 4.67 3 3 3 12.67
UQ	22	1	1	0.16	1.18	1:15	0.30	0.6 0.65	24 25

6.3.2 General test conditions

The details of the test conditions for the three experiments are presented and summarised in Table 6.2. The three experiments used in this paper had different purposes:

- GWK experiment: the primary aim was to test the coastal protection performance of a dynamic cobble berm revetment installed on a sandy beach under erosive waves and water level changes. The performance of the revetment was assessed by comparing beach profiles, shoreline retreat and runup with and without the structure under the same hydrodynamic forcing (Blenkinsopp et al., In review; Bayle et al., 2020). The current paper primarily focusses on test cases with a sand-only beach (SB0 in Bayle et al., 2020) except for the example in the Appendix.
- UNSW experiment: this study compared beach profile evolution of an unprotected sandy beach and a sandy beach protected by a seawall or a revetment, under erosive waves and rising water level (Beuzen et al., 2018). The current paper primarily focuses on the test case with a sand-only beach exposed to erosive waves and changing water level (E1 in Beuzen et al., 2018) except for the example in the Appendix.
- UQ experiment: this experiment investigated the response of beach profiles under erosive and accretive waves and water level changes to investigate the accuracy of the Bruun rule and derivatives (Atkinson et al., 2018). The sandy beach tested was not protected. The results used here correspond to test E5 from Atkinson (2018).

All three experiments investigated the response of a sandy beach profile under erosive wave conditions and with a rising water level. All started with a planar sandy beach profile, and the sand in each experiment was relatively similar in size and was non-cohesive in all cases. Based on the specified significant wave height and peak wave period, time series of irregular waves were generated using a JONSWAP spectrum, with a peak enhancement coefficient of 3.3. First-order wave generation was chosen for all experiments and each flume had a system to absorb the reflection. The different profiling systems do not affect the profile comparison as the measurement error associated with them is too small relative to the observed changes in bed elevation.

Beyond the scale of each flume experiment, there were a few other notable differences. GWK and UQ had the same initial beach slope (1:15) whereas UNSW had a steeper profile (1:10). Under a fixed water level, the beach profiles were exposed to 20 hours, 7.67 hours and 24 hours of waves for GWK, UNSW and UQ respectively. Regarding water level changes, GWK and UNSW used a series of incremental water level rises (four steps for GWK and five steps for UNSW) for a total rise of 0.4 m and 0.075 m respectively, while UQ used a single step water level rise of 0.05 m. These two approaches for raising the water level were shown to give the same final beach profile, as long as enough time was allowed for the profile to reach a quasi-equilibrium (Beuzen et al., 2018). As a result, intermediate profiles may not be comparable, but the end profiles should be. Finally, the profile evolution was surveyed at irregular and different time steps for each experiment.

6.3.3 Morphological parameters

The definitions of the beach profile morphological features used in the comparison of the three experiments are presented in Figure 6.1. The evolved beach profile is represented by a double bar system as this is the type of profile obtained in all the experiments used in this study. The offshore bar is referred to as the 'outer bar' and the onshore bar as the 'inner bar'. The distance between the crests of these two bars is used to define the size of the trough. The elevation of the bar and berm crest relative to the still water level is defined as z_{bar} and z_{berm} respectively. The elevation of the bar and berm crest above the initial profile is defined as h_{bar} and h_{berm} (not shown) respectively. The cross-shore position of the outer bar is defined relatively to the shoreline as x_{bar}. The most landward point on the beach where zero bed-level changed is measured over time is defined as x_0.

The main parameter used in this study to assess similarities and differences between experiments is the cross-shore sediment transport pattern. The local total sediment transport volume (bedload and suspended load) per unit width at a given cross-shore position x', $q(x')$ (m^3/m), was defined at each time interval as the sum of the beach volume change relative to the initial planar profile, from the most landward point of the profile (x_0) to the point of interest (x'):

$$q(x') = \int_{x'}^{x_0} \Delta z(x) dx \tag{6.6}$$

where x_0 is the landward location of no profile change (*i.e.*, $q(x_0) = 0$), Δz is the observed

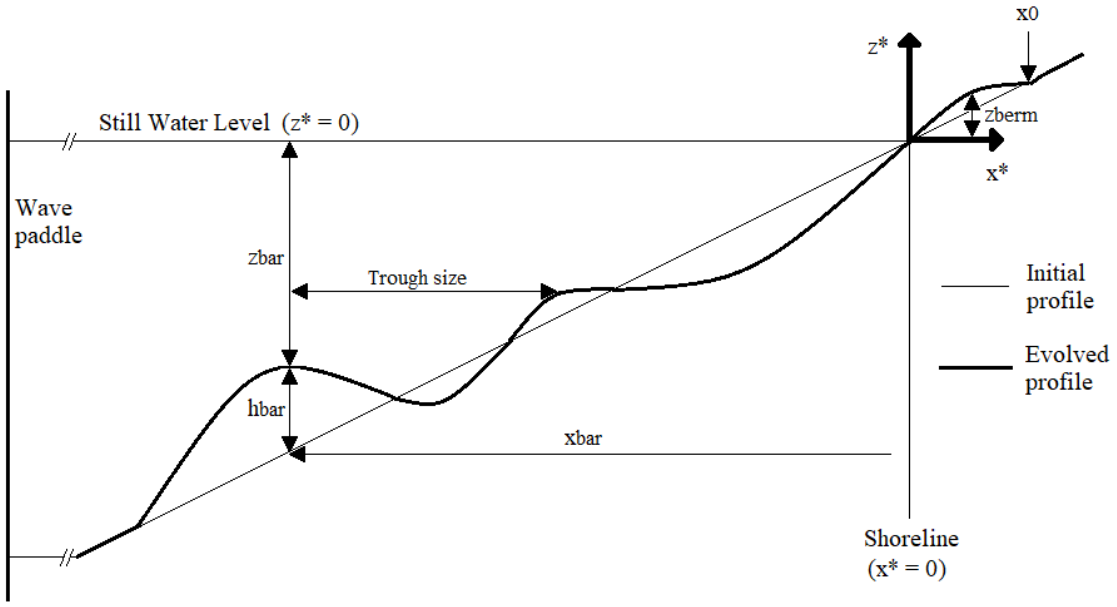

Figure 6.1: Definition of the morphological parameters used in this study. Note that the '*' refer to the dimensionless coordinate system (see Section 6.4.2).

change in bed elevation (m) between the profile and the initial planar profile at location x and dx is the cross-shore increment (m). The bulk cross-shore sediment transport volume is defined as the integral of $q(x')$ over the same cross-shore limits (Baldock et al., 2011; Atkinson and Baldock, 2014). Closure errors in the integration ($q(x_{end}) \neq 0$, where x_{end} is the offshore limit of the active profile and the integration commences from the seaward limit (x_0)) can still occur due to unaccounted volume missed by the profile measurements, as well as variable sediment porosity and compaction. Closure errors were accounted for here following the methodology of (Baldock et al., 2011) by uniformly distributing any residual error through the active profile between x_0 and x_{end}. The offshore limit of the active profile, x_{end}, was extracted from the profile data as the offshore point where no significant change occurred over time. Extracted values were validated with the theoretical value of the depth of closure for each experiment.

6.4 Scale analysis

6.4.1 Distortion analysis

The GWK experiment is considered to be at prototype scale, while the two other experiments are considered to be medium-scale. Although in the comparative analysis presented below, particular attention is given to the comparison of the medium-scale experiments with the prototype, the comparison of the two medium-scale models is also of interest. The parameters used to perform the scale analysis are shown in Table 6.3.

The horizontal length of the model, l corresponds to the cross-shore extent of the sand profile used in each flume (Vellinga, 1982; van Rijn et al., 2011). It represents the horizontal distance between the toe of the initial planar profile and the shoreline position at the initial

Table 6.3: Parameters used for the scale analysis. The names associated with the symbols are in Table 6.2.

	l (m)	h (m)	H_0 (m)	L_0 (m)	W_{st}	ξ_0	Ω_0	Ω_β	θ_0(d)	R_{e*}(d)	$\Delta h/H_s$
GWK	60	4	0.838	56.20	0.015	0.55	3.38	0.24	0.269	12.52	0.5
UNSW	10	1	0.153	2.44	0.063	0.40	2.78	0.28	0.060	6.42	0.5
UQ	9	0.6	0.170	2.17	0.078	0.24	3.87	0.26	0.097	6.52	0.31

water level. As the initial profile was planar for the three experiments, this directly relates to the gradient of the slope. The vertical height of the model, h corresponds to the still water level elevation above the toe of the initial planar profile. For UNSW and UQ, the planar slope ends directly on the bottom of the flume, such that the value of h is equal to the original water depth. However, for GWK where a 0.5 m high flat layer of sand was placed offshore of the planar profile, the value of h is smaller than the water depth. These parameters are used to calculate the distortion scale ratio n_g (Table 6.4) between the three experiments. GWK and UNSW have a distortion scale of $n_g = 1.5$ whereas GWK and UQ have a value of $n_g = 1$, so are not geometrically distorted. UNSW and UQ are distorted with a ratio of $n_g = 0.67$.

The offshore significant wave height, H_0 (Table 6.3) is obtained by deshoaling the significant wave height at the wave paddle to deep water using the linear wave theory. The corresponding offshore wavelength, L_0 (Table 6.3) is calculated using the peak wave period T_p (Table 6.2). The maximum wave orbital velocity U_{max} (not shown) at the offshore point of no change x_{end} (corresponding to water depths of 2.32 m, 0.4 m and 0.33 m deep for GWK, UNSW and UQ respectively) is obtained using the linear wave theory. These parameters along with h are used to assess the Froude scaling law for hydraulic comparison (Table 6.4). Froude scaling is not maintained between any of the experiments (see Eq. 6.2). As a result, the offshore wave steepness differs for each experiment (Table 6.3), with UQ having the steepest waves and GWK the least steep.

As suggested by Vellinga (1986), Baldock et al. (2010) and van Rijn et al. (2011), the surf similarity parameter or Iribarren number, ξ_0 was calculated (Table 6.3). The Iribarren number for the GWK experiment characterises an intermediate beach state with plunging waves (Battjes, 1974; Wright and Short, 1984). For UNSW, it characterises an intermediate beach state with spilling waves and for UQ, it characterises a dissipative beach state with spilling waves.

The settling fall velocity of sand used in the calculation of the Dean number and its modified version (see Table 6.1) was 0.041, 0.044 and 0.037 m/s for GWK, UNSW and UQ respectively. Although the Dean numbers (Ω_0) differ between each experiment, they all fall within a range which is characteristic of an intermediate beach profile. The modified version (Ω_β) is more interesting when dealing with scale comparison as it also takes into

Table 6.4: Froude scaling parameters (n_{H_0}, n_{L_0}, n_l, $n^2_{T_p}$, n^2_u and n_h), and distortion scale n_g.

	n_{H_0}	n_{L_0}	$n^2_{T_p}$	n_h	n_l	n^2_u	n_g
GWK-UNSW	5.46	23.04	23.04	4	6	11.63	1.5
GWK-UQ	4.93	25.85	25.85	6.67	6.67	7.13	1
UNSW-UQ	0.90	1.12	1.12	1.67	1.12	0.61	0.67

account the initial beach slope. Therefore, as explained in Baldock et al. (2010), this allows the slope to be linked directly to the grain size, with a steep slope and coarse grain size being comparable to a gentle slope and fine grain size. In the current study, UNSW has the largest value of Ω_β while UQ and GWK have slightly smaller values (see Table 6.3). Note that UNSW has a steeper slope, but also the coarser sand.

The Shields and Reynolds number are both calculated at $x = x_{end}$, which is near the back of the bar. The UNSW and UQ Shields's number are significantly smaller than for the GWK (Table 6.3), however all are above the critical value for initiation of motion ($\theta_{crit,bedload}$ is equal to 0.038, 0.0375 and 0.0403 for GWK, UNSW and UQ respectively). Note however that only GWK is significantly above the critical value for suspended transport, with $\theta_{crit,susp} \approx 0.08$ for the three experiments. As a result, morphological changes and sediment transport behaviour seaward of the bar crest are expected to be different for UNSW and UQ, as sediment transport in this area will mostly consist of bedload. The grain Reynolds number at x_{end} is twice as large for GWK than for the two medium-scale models. The critical Reynolds numbers for GWK, UNSW and UQ are 4.7, 5.1 and 4.2 respectively. This indicates a lack of transport potential at the x_{end} cross-shore locations (depths) for UNSW and UQ.

As explained in Section 6.3.2, the sequence of water level increases was different for each experiment. The water level for UQ was increased in a single large step, while in the other two experiments the water level was increased in small incremental steps. Although the sudden increase in depth at UQ affects the wave orbital velocity at x_{end}, the U_{max} ($0.1693\,m/s$) remains larger than the critical orbital velocity required to initiate motion U_{crit} ($0.1267\,m/s$), hence the Shields's number at the higher water level (0.0773) is still higher than the critical threshold for bedload transport (0.0403). The incremental steps in GWK and UNSW have a smaller impact on the orbital velocity and Shields's number at x_{end}. The total water level increase is noted Δh and, divided by the significant wave height H_s, gives the water level increase relative to the wave height for each experiment (Table 6.3). For GWK and UNSW, the total water level rise corresponds to 50 % of the wave height whereas it is only 31 % for UQ.

In summary, GWK and UNSW are distorted with respect to physical geometry (n_g = 1.5) and Froude scaling law, and thus have different wave steepness. They do not have the same Iribarren number and to a minor extent Dean number. They do not have the same Shields and Reynolds number, implying no suspended sediment transport at the back of the bar for UNSW. They are entirely distorted in scale, however their relative water level rise is identical. On the other hand, GWK and UQ are undistorted with respect to physical geometry scale (n_g = 1), but are distorted with respect to the Froude scaling law, and thus have different wave steepness. They also differ in terms of the Iribarren number, and to a minor extent Dean number. They do not have the same Shields's and Reynolds number, with minimal suspended sediment transport at the back of the bar for UQ. Additionally, the relative water level rises do not match, with GWK being larger than UQ and the UQ water level rise occurring in a single step. The two medium-scale experiments (UQ and

UNSW) are fully distorted with respect to each other in terms of all criteria discussed above, except for the Reynolds number. This implies that similar sediment transport and bedform formation is likely to occur on the seaward side of the bar, with a small amount suspended sediment transport for UQ but none for UNSW. UNSW also used a larger relative water level rise than UQ. The value of the Iribarren and Dean numbers are characteristic of erosive conditions for all the experiments, hence an erosive profile is expected to develop. They also have very similar values of the modified version of the Dean number, Ω_β. Given that the experiments are significantly distorted to each other as highlighted by the discussion above, it is not possible to apply any time scaling laws. Instead, the number of waves is used as a relative time.

6.4.2 Dimensionless profile comparison

It is important to use a suitable method to compare the different profiles from the three distorted experiments. To align experimental profiles along the same slope in dimensionless space, it is necessary to rotate them and plot them relative to a common physical parameter. For this study, this was chosen to be the runup limit, R, defined as the vertical elevation not exceeded by any wave run-up measured from the still water line, which is taken as the point at which no changes occur on the sub-aerial beach between consecutive profiles.

Using this parameter instead of A in Eq. 6.4 and Eq. 6.5 taken from Peregrine and Williams (2001), the local coordinates are converted into dimensionless coordinates as:

$$x^* = \frac{x(sin\beta)}{R} \tag{6.7}$$

$$z^* = \frac{z(cos\beta)}{R} \tag{6.8}$$

with β the angle of the initial beach slope, x and z the local coordinates and x^* and z^* the new dimensionless coordinates. Note that in Peregrine and Williams (2001), $R = 2A$, so there is a factor two difference in the method presented here compared to the scale presented in Peregrine and Williams (2001). Other starred symbols used later are also dimensionless.

Before applying these transformations, the coordinate systems of each dataset were set to a common datum, using their respective initial still water shoreline position, such that the initial shoreline position becomes the origin in the new dimensionless space (see Figure 6.1). Therefore, the three profiles have the same origin for the initial planar slope, with positive values in x^* and z^* indicating landward and above the original shoreline respectively. In addition, the maximum berm elevation should be slightly below $z^* = 1$ for each experiment as the berm is usually built close to the level of the largest run-up events. Eq. 6.7 and Eq. 6.8 were developed to enable comparison of profiles of different scales, with minimum disruption to profile shape and conservation of profile perturbations and features.

6.5 Results

6.5.1 Beach profile comparison for a fixed water level

6.5.1.1 Beach profile evolution

Figure 6.2 demonstrates that despite the differences in experimental procedure described in Section 6.3.1, the beach profile in each experiment developed a double bar system that moved offshore through time. This is a commonly observed feature in laboratory tests (Larson and Kraus, 1989; Baldock et al., 2011; Masselink et al., 2016; Eichentopf et al., 2018) and often on natural coastlines (Ruessink et al., 2007a,b; Thornton et al., 2007; Turner et al., 2006). The profiles are characterised by a dominant outer bar corresponding to the main breakpoint bar for the wave conditions used. The inner bar is smaller, located landward of the outer bar and has a higher crest elevation than the outer bar for all cases. This feature has sometimes been associated with the splash-jet motion of plunging waves pushing material onshore (Dette et al., 2002). The trough present between the two bars has a different size and shape for each experiment.

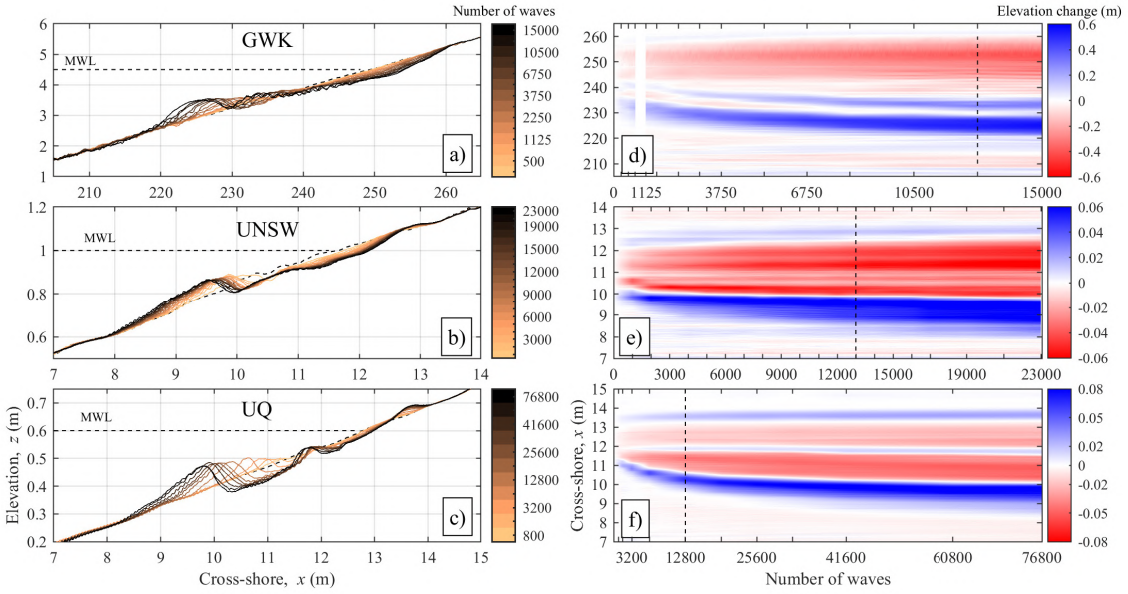

Figure 6.2: a), b) and c): Beach profile evolution from the initial planar slope to the final profile for GWK (top panels), UNSW (middle panels) and UQ (bottom panels), at their respective initial water level (see Table 6.3 for more details). The dashed black profile represents the initial planar slope. Each measured profile at the end of each run is associated with a number of waves and is represented from light copper to black. d), e) and f): Beach profile elevation change relative to the initial profile, as a function of the number of waves. Accretion is shown in blue and erosion in red. The vertical black dashed lines indicate the relative moment at which the profile is taken for the comparison, which corresponds to the profile after 12750, 13000 and 12800 waves for GWK, UNSW and UQ respectively. Note that the profiles are shown in their original and respective coordinates system.

All profiles display an accretive berm, but of different size, h_{berm}. The berm developed in the UQ experiment is larger than for the other two experiments. In addition, the inner surf zone for GWK and UNSW features a Low Tide Terrace (Wright and Short, 1984) type profile, with multiple ripples present in the GWK profiles, with a typical ripple length of approximately 1.4 m. This part of the profile is much smaller in cross-shore extent for

UQ. For UQ and UNSW, the outer bar does not have a clearly defined edge. Instead, the bar stretches along the offshore slope with ripples on top. As observed in Baldock et al. (2017), this may be related to the orbital sheet flow which is not strong enough to flatten the bed at this depth in a medium-scale experiment (small Shields and Reynolds number, see Section 6.4.1). The sediment at this depth is assumed to mainly move under bedload transport, with no or limited suspended transport for UNSW and UQ because the Shields number is very close to the threshold for suspension. The bar at GWK is less elongated and displays a more abrupt offshore edge, characteristic of sheet flow with both bedload and suspended sediment transport. Nevertheless, it seems that the depth of closure for all experiments lies at the seaward limit of the bar, in agreement with the observations of Baldock et al. (2017).

6.5.1.2 Dimensionless comparison

The scale parameters and the method presented in Section 6.4.2 (Eq. 6.7 and Eq. 6.8) were applied for each experiment. The non-dimensional profiles measured after approximately the same number of waves are shown in Figure 6.3a, where the value of R (the vertical elevation at x_0, where zero bed-level change was measured) for each experiment was measured at $z = 1.020\,\text{m}$ for GWK, $z = 0.137\,\text{m}$ for UNSW and $z = 0.095\,\text{m}$ for UQ. Note that the ratios of the distance between the bar and the shoreline and the distance between the shoreline and the berm are conserved through this transformation (and relative distances are conserved in general).

Figure 6.3a shows that beyond the general qualitative similarity (double bar system and berm) presented in Section 6.5.1.1, the relative lengths of the profiles are consistent. The GWK and UNSW profile are very similar with respects to the bar and berm location (although the shape is different), beach face erosion and shoreline position while for the UQ profile, these features are further seaward. The berm is located below $z^* = 1$ for each profile (below the measured R) and the berm formed is larger for the two medium-scale experiments than for the prototype. The beach face steepens with erosion for all the experiments.

The values of the modified version of the Dean number are very similar between experiments, as discussed and shown in Table 6.3. Therefore, although there was no attempt to follow any hydrodynamic scaling rules between these experiments (Section 6.4.1), they are expected to reach the same beach profile state in the Wright and Short (1984) classification. As a consequence, the development of the bar follows the same trend for the three experiments, as shown in Figure 6.4. This figure uses the approach from Eichentopf et al. (2018) which consists of plotting the bar height, h_{bar} as a function of the bar location, x^*_{bar} with both values normalised by their final position. Note that this normalisation was performed with the profiles scaled in the dimensionless space. Figure 6.4 displays three lines with the same gradient, suggesting that the seaward movement of the bar and its height during the profile formation are consistent between experiments. A similar trend was also observed in Eichentopf et al. (2018), with profiles obtained from experiments with a value of Ω_β similar

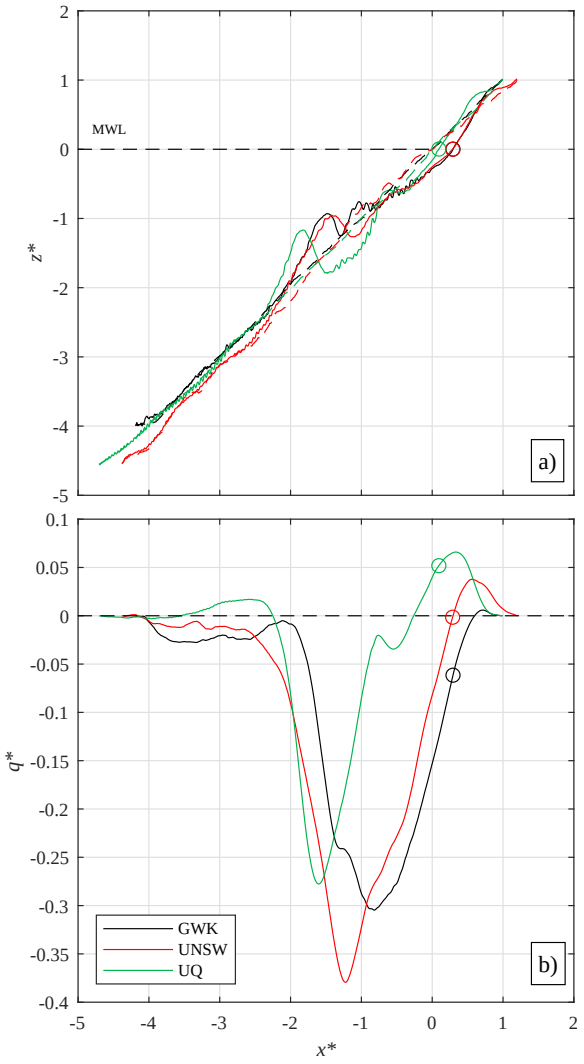

Figure 6.3: a) Beach profiles in dimensionless space using Eq. 6.7 and Eq. 6.7. The dashed line represents the initial planar beach slope. The solid lines represent the profile measure after 12750, 13000 and 12800 waves for GWK, UNSW and UQ respectively, for the initial water level. The origin corresponds to the shoreline position for the three initial profiles. b) Dimensionless sediment transport over the active profile. Positive values represent onshore transport and negative values represent offshore transport. For both figures, GWK is in black, UNSW is in red and UQ is in green. The circles mark the shoreline position in each experiment, following the same colour pattern.

to the current experiments ($\Omega_\beta = 0.24$). The main differences between these profiles are the cross-shore position and elevation of the inner bar, as well as the size of the trough which is deeper and wider for UQ and UNSW than for GWK.

Figure 6.3b shows the dimensionless sediment transport $q*$, calculated between the profiles shown in Figure 6.3a, using Eq. 6.6. The transport was calculated from $x = x_0$, where no profile change was measured on the sub-aerial beach between consecutive profiles (corresponding to R), to the seaward end of the active profile x_{end}. The closure errors were corrected as explained in Section 6.3.3. Positive values correspond to onshore sediment transport and negative values to offshore sediment transport. This parameter is considered as the key parameter to assess the degree of comparability between experiments, as similarities in the pattern and magnitude of sediment transport largely contribute to the overall qualitative comparability of the profiles. Figure 6.3b globally shows very similar

dimensionless cross-shore sediment transport curves in all three cases. The scaled and prototype models have a peak transport rate within a factor of 1.4. However, minor differences persist as onshore sediment transport is larger for the two medium-scale experiments than for the prototype, which explains the larger berm in these cases. Furthermore, the position of the shoreline relative to the berm differs for each experiment. For the UQ experiment the shoreline is situated in a region of onshore transport near the top of the berm, whereas it is located in a region of offshore sediment transport in the GWK; and at the beach pivot point for UNSW. Note that because of closure errors, there are some uncertainties in the direction of the sediment transport and magnitude seaward of $x^* = -3$. The other qualitative difference is in the respective location of the maximum offshore transport. This peak occurs at $x^* = -0.9$ for GWK, which corresponds to the trough of the inner bar. For UNSW and UQ, it is observed at $x^* = -1.2$ and $x^* = -1.6$ respectively, corresponding to the trough of the outer bar. This is likely due to the larger value wave steepness in the medium-scale models, resulting in waves breaking relatively further offshore for UNSW and UQ than for GWK.

The application of the new scaling approach allowed the three distorted experiments to be compared. The general profile shape, bar behaviour and most importantly, the sediment transport pattern have shown good agreement between the experiments. However, while these distorted models are qualitatively comparable, it is clear that an erosive condition cannot be compared with an accretive condition. Therefore, only experiments expected to develop a similar profile shape under a comparable sediment transport pattern can be quantitatively compared together, using this scaling method. By looking at the morphological parameters presented in Table 6.3, it then appears that the modified version of the Dean number (Ω_β) should closely match between the experiments (distorted or not) to be selected.

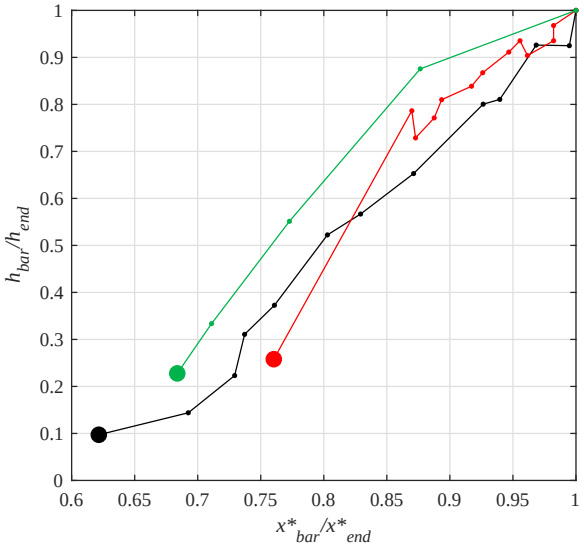

Figure 6.4: Bar height, hbar evolution as a function of the dimensionless cross-shore bar position, x^*_{bar}. Both values are normalised by their position after 12750, 13000 and 12800 waves for GWK (black), UNSW (red) and UQ (green) respectively, for the initial water level. The large dots mark the initial value. Note that the lines are going to the right, which indicates offshore movement.

6.5.2 Analysis of the method and additional datasets

6.5.2.1 Validation of the scaling method with additional datasets

The methodology presented in this paper was developed using the three distorted experiments presented above. However, this method would ideally be applicable for all laboratory datasets with similar overall profile forcing and response (*i.e.*, erosive or accretive), thus enabling the scientific community to quantitatively compare distorted models. For this purpose, it is important that all experiments have comparable values of the modified version of the Dean number (Ω_β). In this section, two additional flume datasets with similar values of Ω_β are analysed and compared:

- SANDS Data CIEM, obtained at the Canal d'Investigació i Experimentació Marítima (CIEM) of the Universitat Politecnica de Catalunya (UPC) in Barcelona, Spain (Alsina and Caceres, 2011);
- CRIEPI Data (L5), obtained in the Large Wave Flume (LWF) of the Central Research Institute of Electric Power Industry, Japan, in 1996 (Shimizu and Ikeno, 1996).

Table 6.5 shows the main characteristics and parameters for the two additional experiments. The objective here was to use the newly developed scaling method on datasets not used to develop the method, in order to validate it and assess its functionality. There were no attempts to analyse the differences between the experiments further than the profile shape and sediment transport. For this reason, the detailed scale analysis of these two extra datasets is not presented here. It is suggested that one should be able to assess if datasets are comparable using the modified version of the Dean number (Ω_β), and then perform a scaling analysis of the wanted parameters to be compared.

The two extra experiments used random waves, with a JONSWAP spectrum They extend the previous analysis by introducing two intermediate model scales to those already presented, as well as two different sediment grain diameters. They both While the beach slopes are the same as those analysed previously, these experiments have a smaller (SANDS) and a coarser (L5) sand diameter. For the SANDS experiment, the value of parameters in the three rightmost columns in Table 6.5 lie between those for GWK and UNSW with the exception of a smaller sediment size. L5 has the largest wave steepness (W_{st}), modified Dean number (Ω_β), and sediment size (D_{50}), but has the smallest Iribarren number (ξ_0). Figure 6.5a and Figure 6.5b show the dimensionless profiles after approximately the same number of waves (GWK: 12750, UNSW: 13000, UQ: 12800, SANDS: 12500, and L5: 12600).

The SANDS profile closely matches the GWK profile, with very similar bar locations and elevations, trough size, berm height and elevation and beach face slope. The offshore sediment transport peak is located at the same relative position as for GWK (Figure 6.5b)

Table 6.5: Flume size, wave conditions and main parameters for the two extra datasets used in this section.

	Length (m)	Width (m)	Height (m)	$H_s - H_0$ (m)	T_p (s)	Slope	Sand D_{50} (mm)	W_{st}	ξ_0	Ω_β
SANDS	100	3	4.5	0.53 – 0.56	4.14	1:15	0.25	0.021	0.46	0.30
CRIEPI (L5)	205	3.4	6	1.20 – 1.27	3	1:10	0.97	0.091	0.22	0.32

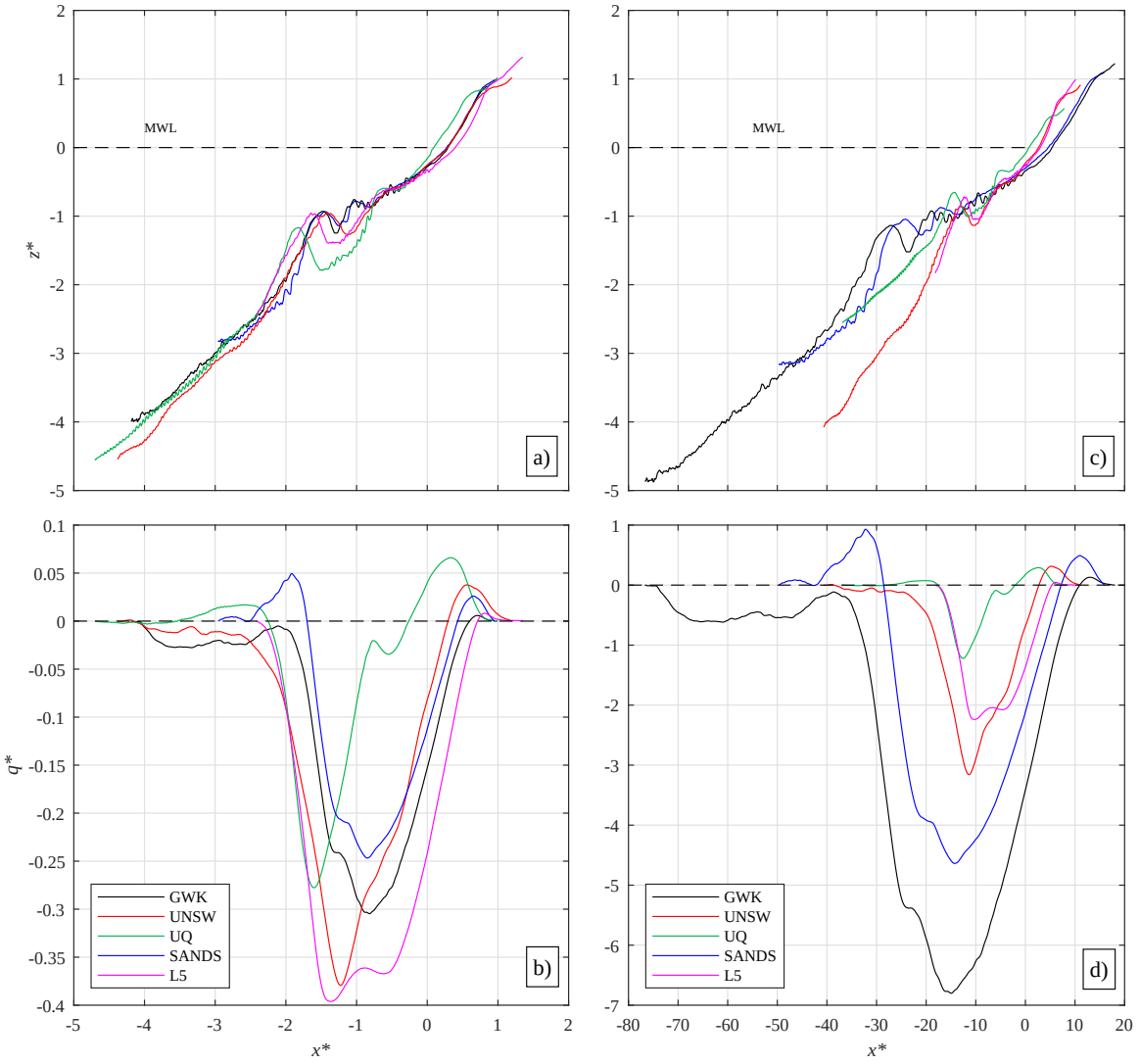

Figure 6.5: a) Beach profiles in dimensionless space using Eq. 6.7 and Eq. 6.8 and c) beach profiles in dimensionless space normalised by H_{m0}, from van Rijn et al. (2011). The solid lines represent the profile after 12750 (GWK), 13000 (UNSW), 12800 (UQ), 12500 (SANDS) and 12600 (L5), for still water level. Note that for better clarity, the initial planar profiles are not shown. The origin corresponds to the shoreline location for the three initial profiles. b) dimensionless sediment transport over the active profile scaled using Eq. 6.7 and Eq. 6.8 and d) dimensionless sediment transport over the active profile scaled using Hm02, from van Rijn et al. (2011). Positive values represent onshore transport and negative values represent offshore transport. For all figures, GWK is in black, UNSW is in red, UQ is in green, SANDS is in blue and L5 is in magenta.

— at the inner bar trough — which can here also be related to the relatively small wave steepness W_{st}. In contrast, the onshore sediment transport around the berm is closer to that for the UNSW dataset.

The L5 profile is similar in shape to that for UQ, with a large trough and a small value of ξ_0. However, although the sand is relatively coarse, the berm height is among the smallest. This is confirmed by the weak onshore sediment transport around the berm area (Figure 6.5b). The offshore sediment transport peak is located at the same relative position as for UNSW and UQ — at the outer bar trough — which is also related to a high wave steepness.

6.5.2.2 Analysis of the new scaling method

In this section, the scaling method is analysed using only the three original datasets. By scaling the coordinate system with R in Eq. 6.7 and Eq. 6.7, the sediment transport per unit width (*i.e.*, x^* times z^*) scales with $cos\beta sin\beta/R^2$. As a result, sediment transport is scaled by a factor of 0.0638, 5.1050 and 7.8743 for GWK, UNSW and UQ respectively. This gives a factor of 123 for the sediment transport rate between GWK-UQ, 80 between GWK-UNSW and 1.5 between UNSW-UQ. For future use of Eq. 6.7 and Eq. 6.8 when the elevation of zero beach change is not availabel for each profile, a predicted value of $R_{2\,\%}$ can be used instead. In this study, similar results to those presented in Figure 6.3 and Figure 6.5 were obtained by estimating $R_{2\,\%}$ using the run-up equation developed by Blenkinsopp et al. (2016) (Eq. 6.9). Therefore, it is suggested that predicted $R_{2\,\%}$ can be used as a substitute for R, using the best run-up equation availabel for each study site, in order to align the berm position near $z^* = 1$.

The approach of Ibrahim and Baldock (2020) is used to relate the scaling based on R to the offshore wave conditions. This involves rewriting the Peregrine and Williams (2001) solution for swash overtopping in terms of H, L_0 and $tan\beta$. Taking the most widely applicable runup scaling as that due to Hunt (1959), R is typically proportional to $(H_0L_0)^{1/2}tan\beta$. Therefore, from Eq. 6.4 and Eq. 6.5, the sediment transport per unit width scales with $(H_0L_0)tan\beta$ (ignoring a factor $cos^2\beta$ which is almost equal to 1 for all realistic beach slopes). This gives a factor of 128 for the sediment transport rate between GWK-UQ, 84 between GWK-UNSW and 1.5 between UNSW-UQ, which are close to those obtained with measured values of R. While the two medium-scale models have almost identical values of H_0L_0 (≈ 0.37), the different beach slopes introduce a scale factor of 1.5 on the dimensionless transport. This is consistent with the additional factor of $tan\beta$ introduced into the Dean parameter by Hattori and Kawamata (1980) (Table 6.1).

van Rijn et al. (2011) performed a similar comparison of profiles and volumes of sediment transport between three undistorted large-scale laboratory experiments. They used the factor H_{m0} to non-dimensionalise the profile, and H_{m0}^2 to non-dimensionalise the volume of sediment transport. Figure 6.5c shows the same profiles as in Figure 6.5a but non-dimensionalised using H_{m0} as per van Rijn et al. (2011). Using this scaling method, the similarity between profiles is less than that observed in Figure 6.5a. The shape of the profiles and the relative positions of the main morphological features are quite different for all experiments (see Table 6.6) with dissimilarity in terms of slope, beach profile length and height, and therefore bar and berm elevation and position. According to the van Rijn et al. (2011)approach, the volume of sediment transport per unit width scales with H_{m0}^2, hence by a factor of 0.7022, 0.0234 and 0.0289 for GWK, UNSW and UQ respectively, which gives a ratio of only 24 between GWK-UQ, 30 between GWK-UNSW and 1.2 between UNSW and UQ. Figure 6.5d shows this result, demonstrating very different non-dimensional offshore transport rates between models and prototype experiments. In addition, the onshore sediment transport component is also distorted and does not relate to the size of the observed berm. For distorted models, it is therefore suggested that scaling with the runup (which

Table 6.6: Comparison of four parameters – bar height (h_{bar}) (see Figure 6.1), depth of the bar crest (z_{bar}) (see Figure 6.1), horizontal distance between the bar crest and the berm crest and vertical elevation of the berm crest above the mean water level (z_{berm}) – after 12750 (GWK), 13000 (UNSW), 12800 (UQ), 12500 (SANDS) and 12600 waves (L5). The values are given, from left to right, as: original coordinate / scaled coordinate using the method presented in this paper / scaled coordinate using van Rijn et al. (2011) scaling.

	Bar height (h_{bar})	Bar depth (z_{bar})	Horizontal Distance Bar - Berm	Berm elevation (z_{berm})
GWK	0.55m / 0.52 / 0.64	0.95m / 0.93 / 1.14	36.4m / 2.29 / 42.07	0.90m / 0.88 / 1.06
UNSW	0.07m / 0.49 / 0.42	0.13m / 0.95 / 0.86	3.46m / 2.29 / 21.17	0.09m / 0.87 / 0.78
UQ	0.06m / 0.67 / 0.38	0.11m / 1.17 / 0.65	3.40m / 2.45 / 19.32	0.07m / 0.82 / 0.45
SANDS	0.33m / 0.51 / 0.56	0.59m / 0.94 / 1.05	21.48m / 2.29 / 38.33	0.56m / 0.91 / 1.00
L5	0.63m / 0.71 / 0.49	0.94m / 0.98 / 0.74	24.00m / 2.51 / 19.13	0.88m / 0.92 / 0.70

incorporates H, L and β, and hence Iribarren number) is more appropriate than using just the wave height. Interestingly, Pujara et al. (2020) show that swash backwash flows also scale with HL, and backwash flows could be expected to have a significant influence on sediment transport rates and erosion on the upper beach.

6.5.2.3 Analysis of the scaled profiles and parameters

The scaling method developed here enables the original coordinates – which significantly differ from one experiment to another due to the wide range of flume sizes – to be scaled in the same dimensionless space. Table 6.6 presents four measurements in original coordinates, in dimensionless space using the method presented in this paper (Figure 6.5a), and using the van Rijn et al. (2011) scaling (Figure 6.5b) for the five datasets presented in Figure 6.5. Measurements in the original coordinates vary depending on the size of the flume, however when the new scaling method is used, these measurements scale to comparable values. For the present data, in the new dimensionless coordinates, the bar depth is approximately equal to 1 (*i.e.*, similar to the run-up elevation), the berm elevation (z_{berm} on Figure 6.1) is around 0.9 (*i.e.*, near the vertical runup limit) and the horizontal distance between the bar crest and the berm crest only varies from 2.29 to 2.51. This confirms that experiments with a similar modified Dean number can be scaled and compared using the scaling method presented, regardless of the original size of the flume or sediment diameter. By contrast, the same analysis performed with van Rijn et al. (2011) scaling gives a larger range of non-dimensional values for the same features, as it does not correct for the slope and uses the wave height H for the horizontal and the vertical scaling. Table 6.6 suggests that scaling on the runup (*i.e.*, on $tan\beta$ and $(HL)^{1/2}$) is more appropriate, particularly for distorted models.

As can be seen in Figure 6.5, for the five experimental datasets analysed, the scaling method presented in this paper produces peak negative values of the sediment transport within a factor of 1.6 (SANDS having the smallest value with $q* = -0.25$ and CRIEPI the largest with $q* = -0.40$). In contrast, the scaling from van Rijn et al. (2011) gives peak values within a factor of 7. Further, the total bulk sediment transport volume (Baldock et al., 2017), as defined in Section 6.3.3, is also well scaled with the current method. Figure 6.6 shows the values of the bulk sediment transport for the five datasets, obtained using the

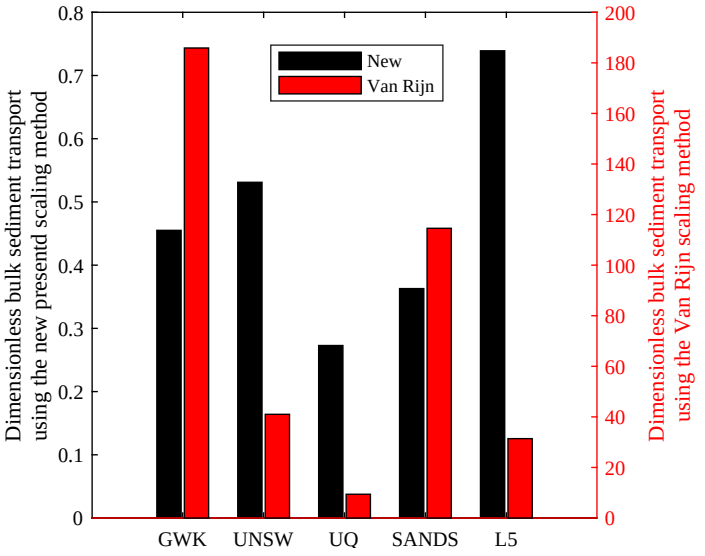

Figure 6.6: Bar chart showing the bulk sediment transport volume in dimensionless space, using the new scaling method (left-hand side axis) and the van Rijn et al. (2011) scaling method (right-hand side axis), measured after 12750 (GWK), 13000 (UNSW), 12800 (UQ), 12500 (SANDS) and 12600 waves (L5). Note the difference in range between the left and right-hand side axes.

current scaling (black bar, left-hand side axis) and the van Rijn et al. (2011) scaling (red bar, right-hand side axis). The range of the bulk sediment transport is smaller using the proposed scaling method, with values varying from 0.27 (UQ) to 0.74 (CRIEPI) (*i.e.*, within a factor 3), while for the van Rijn et al. (2011) scaling, the bulk transport ranges over a factor of 20. However, while the total bulk sediment transport is more uniformly scaled with the presented method, values still differ between the five experiments. This is expected, as the modified Dean numbers are not exactly the same and the number of waves is not exactly the same for each experiment, however without more data on the detailed hydrodynamics (wave velocity and instantaneous sediment transport) of each experiment, it is hard to attribute the quantitative differences to specific parameters. Nonetheless, and as stated throughout the paper, the sediment transport patterns are very similar, and thus a qualitative comparison is considered valid, without comparing absolute values (see the Appendix).

The parameters used in the scaling analysis (see Table 6.3) of each experiment are also scaled and brought into dimensionless space. As a result, the wave steepness is scaled by $tan\beta^{-1}$, the Iribarren number by $tan\beta^{1/2}$ and H_0 by $cos\beta/R$. By contrast, by scaling with H_{m0}, the van Rijn et al. (2011) method keeps the values of the Iribarren number and wave steepness unchanged, while it squares the wave height. To confirm that the scaled profiles and hydrodynamics are still representative and do not generate artificial features, it is important to compare them with known observations. Figure 6.7a shows the bar depth (z_{bar}) as a function of H_0*, and shows that the bar depth increases with wave height when using the current scaling. Assuming that the bar depth corresponds to the average depth of wave breaking, this relationship is in line with the characteristics of wave breaking (Robertson et al., 2013). However, this relationship is not captured when using van Rijn et al. (2011) scaling. Furthermore, Figure 6.7b shows that the ratio $\gamma* = H_0 * /z_{bar}*$

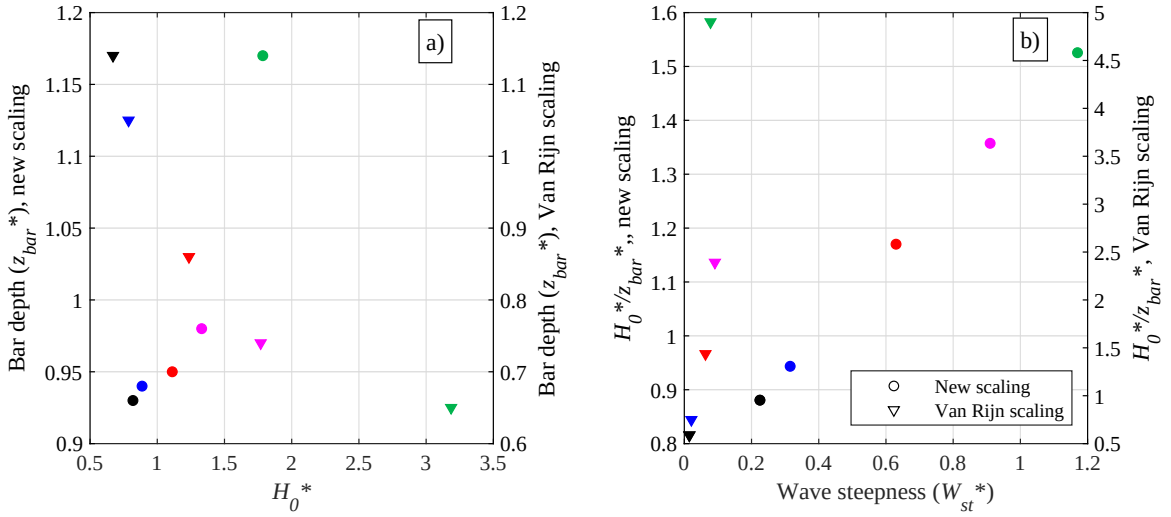

Figure 6.7: (a) Bar depth (z_{bar}*) as a function of the deep water significant wave height (H_0*), in dimensionless space. (b) Deep water significant wave height over bar depth (H_0 * /z_{bar}) as a function of the wave steepness (W_{st}*) in dimensionless space. On both figures, left axis and circles show the values using the new scaling method while the right axis and the triangles show the values using van Rijn et al. (2011). Values were measured after 12750 (GWK, in black), 13000 (UNSW, in red), 12800 (UQ, in green), 12500 (SANDS, in blue) and 12600 waves (L5, in magenta).

is proportional to the wave steepness when using the presented scaling, while it is not with van Rijn et al. (2011) scaling. As H_0 is proportional to H_b, and assuming that z_{bar} corresponds to the average depth of wave breaking, the ratio H_0 * /z_{bar}* is related to the breaker index and therefore, as presented in Robertson et al. (2013), proportional to the wave steepness. The scaled profiles and hydrodynamics respect the general relationships of coastal engineering and are therefore, assumed to be valid for further analysis. It is worth noting again that z_{bar} * (z_{bar}/R) has a smaller range than γ* = H_0 * /z_{bar}*, which is consistent with the wavelength being relevant, and possibly a useful predictor with further testing.

6.5.3 Beach profile comparison with increasing water level

6.5.3.1 Beach profile evolution

In this section, the new scaling method is extended for profile comparison under increasing water level using the three original datasets. Figure 6.8a-c show the beach profile at the end of each water level increment for each of the three experiments. As explained in Section 6.3.2, the water level was increased in 4 and 5 incremental steps for GWK and UNSW respectively, while for UQ the water level was raised by one large step. Figure 6.8d-f show the bed-level changes relative to the initial planar slope (blue marks accretion and red erosion), as a function of the number of waves.

UQ does not behave similarly to the other two experiments. Indeed, it can be seen on Figure 6.8f that while the initial outer bar fades away, the initial inner bar moves offshore and becomes a secondary outer bar. Meanwhile, a secondary inner bar is formed. In contrast, GWK and UNSW retain their initial bar which becomes wider and attaches to the inner bar. As observed by Swart (1974) and Atkinson et al. (2018), the cyclic behaviour of the bars observed at UQ can be common in laboratory flume experiments when a very

large number of waves is run, highlighting the fact that equilibrium is likely impossible to reach. Furthermore, this behaviour may also represent another aspect of the morphological hysteresis presented in Baldock et al. (2017), who showed that the morphological response of a profile is directly linked to the active beach state for the new hydrodynamic conditions. In the current study, this behaviour is mainly observed in the UQ dataset where the large single step water level rise suddenly increases the water level above the initial outer bar, stranding the outer bar, and thus reduces the wave orbital velocity at the bar and makes the inner surf zone more reflective. In addition, the ratio of total water level increase to significant wave height ($\Delta h/H_s$) for UQ (0.3) differs from GWK and UNSW (0.5). This introduces an additional geometrical distortion and further distorts the Froude scaling. For these reasons, the profile obtained at UQ is considered to be too different from the others, and therefore it is not used in the following comparison for an increasing water level.

The profile evolution for GWK and UNSW initially appear quite different, especially around the outer bar area. The UNSW bar seems to decay and becomes relatively larger than the GWK bar. This is mainly due to the weak orbital velocity on the seaward side of the bar for UNSW, which decreases further with water level rise. The area between $x = 8$ m and $x = 9$ m is assumed to be dominated by bedload transport (see Section 6.4.1) for the initial water level. As the water level is raised, the bed shear stress at this location likely decreases and approaches the critical shear stress value, and therefore, a large part of the outer bar volume cannot be transported onshore. This weak transport is also enhanced by the larger sediment used at UNSW. However, to a lesser degree, the widening of the outer bar is also observed at GWK.

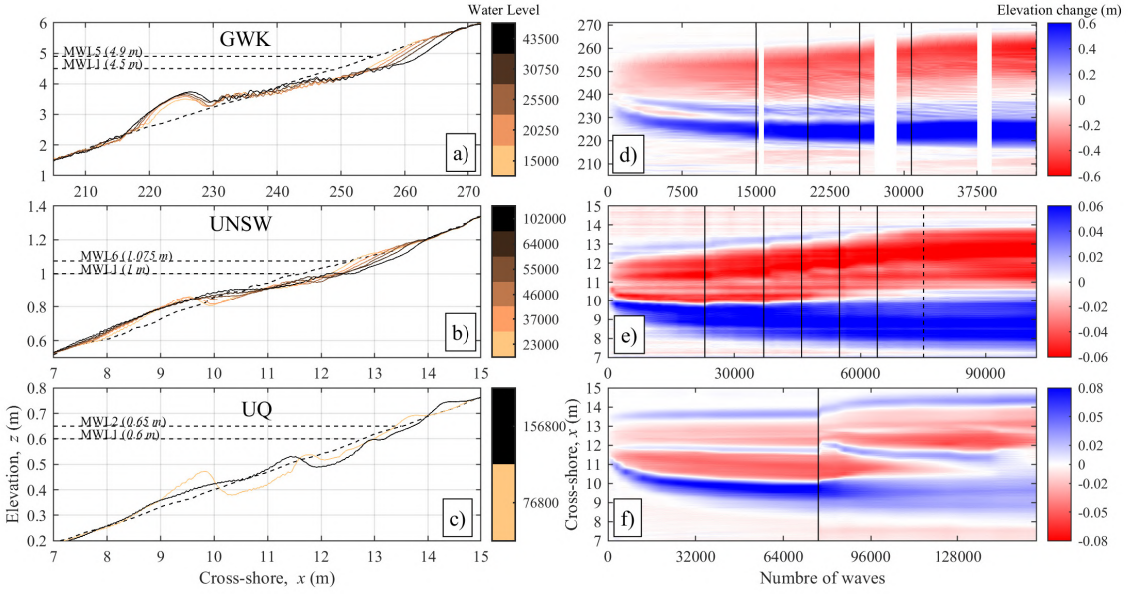

Figure 6.8: a), b) and c): Beach profile evolution under water level rise. The final profile for each water level increment is shown for GWK (top panels), UNSW (middle panels) and UQ (bottom panels) (see Table 6.3 for more details). The dashed black profile represents the initial planar slope. Then each measured profile at the end of each water level (and the corresponding number of waves) is represented by a colour, from light copper to black. d), e) and f): Beach profile elevation change relative to the initial planar profile, in function of the number of waves. Accretion is shown in blue and erosion in red. The times at which the water level was increased are shown using a vertical black line. The vertical black dashed line on e) marks the UNSW profile used for the dimensionless comparison.

Further investigation suggests that similar and comparable qualitative behaviours are observed in both experiments under water level increase. First of all, the shoreline was eroded as the berm retreated, and the bar moved landward and upward as the water level was increased. In both cases, the length of the profile, calculated from the bar crest to the berm crest, increases with the water level rise. From the end of the initial water level to the profile measured after the same number of waves at the final water level, the profile length increases by 48 cm (from 3.41 m to 3.89 m) for UNSW and by 5.54 m (from 36.30 m to 41.84 m) for GWK, which corresponds to an increase of 14.2 % and 15.2 % in length for UNSW and GWK respectively. Therefore, it appears that the profiles became more dissipative as the water level was raised, with the shoreline retreating faster than the bar. This behaviour was also observed in Atkinson et al. (2018). The berm elevation, z_{berm} also increases in both experiments, by 2 cm and 4. cm for GWK and UNSW respectively. On the other hand, the berm height, h_{berm} remains constant throughout both experiments, suggesting it is approximately self-similar at each water level. Figure 6.8d and Figure 6.8e show a less distinct inner bar as the outer bar moves landward and attaches to it, making the trough less pronounced. However, Figure 6.5a and Figure 6.5b still show the presence of an inner bar at $x = 245$ m for GWK, and $x = 12$ m for UNSW at the final water level, located upward and landward of their initial position.

6.5.3.2 Dimensionless comparison

Figure 6.9a confirms the observations made in Section 6.5.3.1, showing that the dimensionless width of the surf zone, from the bar to the berm, increases with a very similar gradient for both experiments. To ensure a valid comparison at each water level, the values were taken from profiles measured after approximately the same number of waves at that water level. In Figure 6.9, it is observed that while the surf zone lengthens at the same rate (Figure 6.9a), the pace of the bar and berm retreat differs between the two experiments

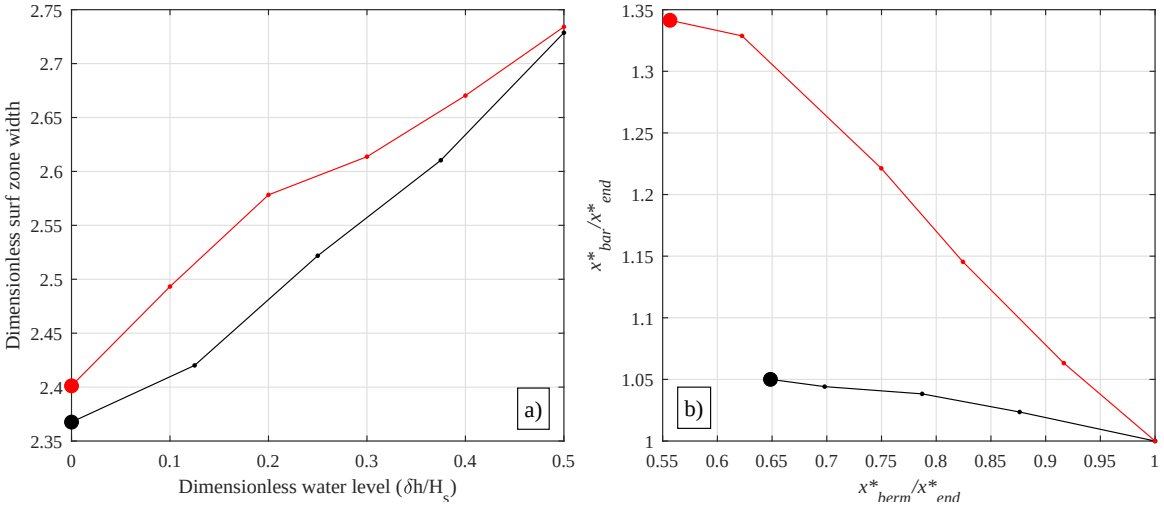

Figure 6.9: a) Evolution of the dimensionless surf zone width against the dimensionless water level ($\Delta h/H_s$). Note that UNSW (red) had 5 steps while GWK (black) had 4. b) Cross-shore position of the bar as a function of the cross-shore position of the berm, both normalised by their final value. The large dots mark the initial value.

(Figure 6.9b). Except for the first water level increment, where the berm and bar retreat are very similar between UNSW and GWK, UNSW is characterised by a larger retreat of the bar and berm than GWK. This is likely to be, in part, a consequence of the large number of waves run at each intermediate water level at UNSW. This pattern is also visible on the dimensionless profile comparison plotted in Figure 6.10a. Note that the final water level in each experiment is not shown in Figure 6.10a as it would be at different elevations in the dimensionless space. As such, the elevations of the various profile perturbations cannot be compared directly as they are relative to a different water level and wave conditions for each experiment, hence only the trend is compared. In addition to the previous observations, it is noted that the trough length for UNSW is consistently longer than that for GWK.

Overall, although the beach profile shape is very different, the behaviour of the profile

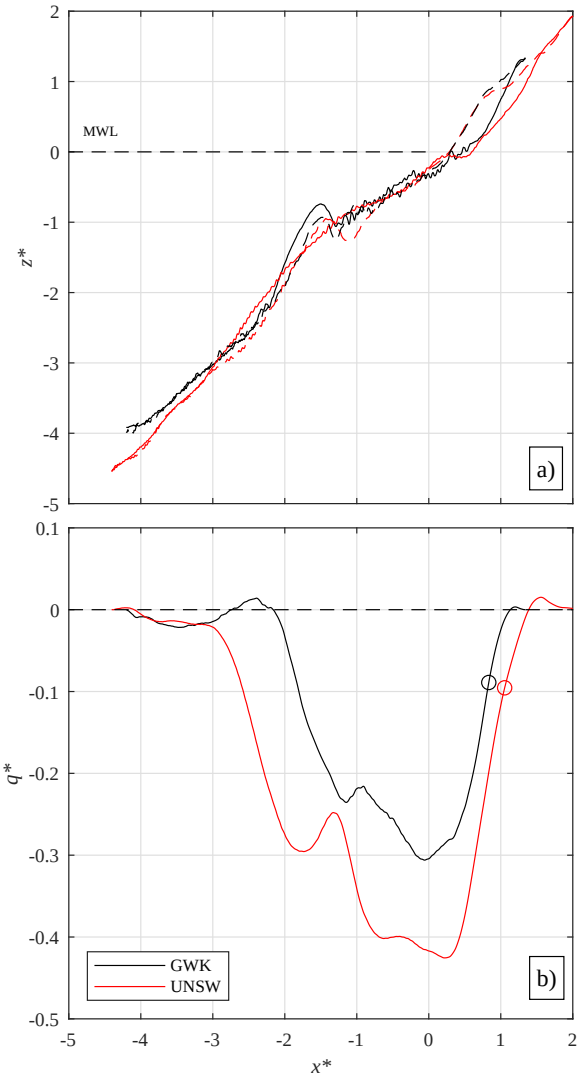

Figure 6.10: a) Beach profiles in dimensionless space. The dashed lines represent the profiles at the end of the initial water level. The solid lines represent the profiles measured after 10700 waves at z_{wl} = 4.9 m (final water level, GWK) and after 11000 waves at z_{wl} = 1.075 m (final water level, UNSW). The origin corresponds to the shoreline location of the three planar profiles. b) dimensionless sediment transport over the active profile. Positive values represent onshore transport and negative values represent offshore transport. For both figures, GWK is in black and UNSW is in red. The circle marks the final shoreline position in each experiment.

under water level increase is similar for GWK and UNSW, with the profile lengthening while moving upward and landward, and the berm height being maintained. Although more waves were run at UNSW, the scaled sediment transport curves of the two experiments are very similar (Figure 6.10b). As in Figure 6.3, Figure 6.3b shows that the onshore transport around the berm is smaller for the prototype than for the medium-scale model. However, the shoreline is located in a region of offshore sediment transport in both cases. The inner surf zone is still dominated by offshore sediment transport for all experiments. The maximum offshore transport occurs between $x^* = 0.5$ and $x^* = -0.7$ for UNSW, and $x^* = 0.3$ and $x^* = -0.1$ for GWK, which corresponds to the area of inner bar trough on the dashed profiles for both experiments. Overall, the UNSW and GWK transport rates show a similar pattern with peaks in transport rate occurring at similar cross-shore locations. The sediment transport magnitude is within a factor of 1.4, as for the fixed water level case. The total dimensionless bulk sediment transport values are 0.64 (GWK) and 0.82 (UNSW), which are similar but confirms that they cannot be directly compared. The very similar trends are considered comparable, however, as demonstrated in the Appendix.

6.6 Discussion

6.6.1 Constraints associated with the new scaling method

The approach developed in this paper allows distorted experimental profiles with similar modified Dean number (Ω_β) to be compared. This parameter indicates evolution to a similar beach state and to a certain extent, a comparable dimensionless bulk sediment transport (Baldock et al., 2011). From the extended comparison shown in Figure 6.5, and using the dataset from van Rijn et al. (2011), it is suggested that the new scaling approach is appropriate for Ω_β values ranging between 0.24 and 0.35 and for intermediate beach states and erosive conditions (random waves). As shown in Figure 6.5, the new method is able to scale profiles with different initial planar slopes and with a large range of grain sizes, such that the profile shape and local sediment transport pattern can be quantitatively compared. To summarise, the newly developed approach is associated with the following four constraints:

- Random waves: the methodology is only valid for profiles developed under random waves.
- Similar modified Dean number: the comparisons presented in this paper focus on profiles developed under similar erosive condition, in order to show the similarities between distorted experiments in terms of profile development and sediment transport. It is assumed that this technique would work for accretive conditions with similar modified Dean number, but this is yet to be experimented and confirmed.
- Initially planar beach: the datasets compared in this paper all develop from an initially planar slope after approximately the same number of waves. The method works for different initial slopes, such as the Dean profile, as long as the experiments compared have the same type of initial slope.
- Data available after the same number of waves: for the purpose of the comparison,

it was required to have measured profiles available after approximately the same number of waves.

While constraint 1 is fixed, constraint 2 and 3 can vary depending on the dataset compared, and constraint 4 is more a practical constraint for the comparison – *i.e.*, the number of waves represents equivalent dimensionless time. Existing and future datasets can therefore be compared together, as long as they are consistent with these constraints.

While profiles formed under water level increase in each experiment have a very different shape and did not well matched with this scaling (Figure 6.10a), the method still showed good performance in comparing beach profiles behaviour (Figure 6.9 and Figure 6.10b) of distorted flume experiments under water level increase (*e.g.*, profile length increase, sediment transport). In addition to the four constraints above, the additional conditions that need to be respected for the method to be applicable in the case of water level increase are: 1) a similar procedure for the increase of the water level; and, 2) a comparable ratio of the total water level increase over the significant wave height ($\Delta h/H_s$). Note that in this paper, only the progressive incremental steps could be fully assessed and compared. Therefore, further work is required to identify if other matching water level increase procedures are compatible with this method. As for a fixed water level, the method enables a comparison of the profile evolution and sediment transport pattern.

6.6.2 Application of the new scaling method for a fixed water level

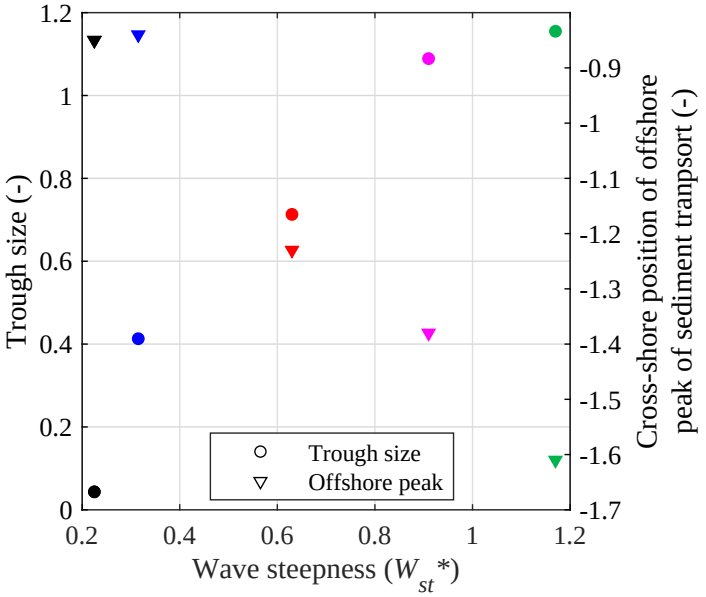

Figure 6.11: Cross-shore position of the offshore peak of sediment transport as a function of the offshore wave steepness (W_{st}^*), in dimensionless space using the new scaling method. Values were measured after 12750 (GWK), 13000 (UNSW), 12800 (UQ), 12500 (SANDS) and 12600 waves (L5). Note that the value is given relative to the initial shoreline for the planar slope in dimensionless space.

As discussed in Section 6.5.2.3, the new scaling method proposed in this paper was used to effectively compare beach profiles, sediment transport curves and morphodynamic behaviour from distorted experiments. During this analysis it was observed that the location of the peak offshore sediment transport could be related to the offshore wave steepness

(Section 6.5.1.2 and Section 6.5.1.1). As an example application of the new scaling method, this relationship is further analysed in Figure 6.11. Figure 6.11 shows that the offshore sediment transport peak location moves further offshore with steeper waves. This can be explained by the fact that steeper waves generate sediment transport further offshore than less steep waves, as for a given depth, the shear stress associated with the orbital velocity is stronger for a steeper wave. Furthermore, less steep waves tend to break over the trough, as mentioned in Strauss (2009), which explains why the peak of offshore sediment transport is located in the inner bar trough area for GWK and SANDS, but located in the outer bar trough for UNSW, UQ and CRIEPI.

6.7 Conclusions

Three laboratory flume experiments at different and distorted scales (one prototype (GWK) and two medium-scale (UNSW and UQ)) are reported and compared. These experiments all investigated beach profile evolution under erosive wave conditions and water level rise, with some coastal protection tests under similar conditions performed in the GWK and UNSW experiments. A scale analysis of the hydrodynamics, physical geometry and other key parameters was performed between each experiment. The experiments are distorted with respect to those parameters and also in terms of Froude scaling, Shields's number and Reynolds number. However, they had a very similar modified Dean number.

A novel approach based on the scaling proposed for swash flows by Peregrine and Williams (2001) was applied to transform local coordinates into dimensionless coordinates free of the beach slope, allowing direct comparison of distorted profiles. The comparison of these distorted experiments focused on the analysis of profile shape and development, and mainly on the sediment transport pattern. It demonstrated that as long as the modified Dean number is similar, distorted experiments can be compared using the developed method.

The approach was then validated with two additional datasets which confirmed that the profile shape and sediment transport were suitable for comparison as the peak of erosion occurred around the same relative position, and with the scaled magnitude within a factor of 1.6. The dimensionless coordinates are related to the offshore wave conditions following Ibrahim and Baldock (2020) and with this scaling, the sediment transport scales with $H_0 L_0$, which brings the data into good agreement for profiles exposed to the same number of waves. There is a significant difference between the dimensionless transport rates, profiles shape and morphodynamics parameters when scaled using this new approach and the conventional approach applicable for the scaling of undistorted profiles (*e.g.*, van Rijn et al., 2011).

The new scaling method was also applied to tests with increasing water levels. In this case, it was shown that in addition to the modified version of the Dean number, the same procedure for the water level increase and the same relative water level rise are required for a match between the distorted profiles and for the method to be applicable.

Appendix: Application of the new scaling method under increasing water level

The following analysis presents an example application of the scaling approach developed in this paper for water level increase, using the UNSW and GWK data. As presented in Section 6.3.2, the GWK and UNSW experiments investigated beach response with a rising sea level on "natural" beaches and beaches with a seawall installed on the upper beach. The DynaRev experiment at GWK investigated the performance of a dynamic cobble berm revetment (Blenkinsopp et al., In review; Bayle et al., 2020). The UNSW experiment (Beuzen et al., 2018) investigated the influence of a rubble mound and vertical seawall on fronting beach morphology in a rising sea. In both cases, results with a seawall were compared with the case of an equivalent non-engineered sand beach. In this section, erosion volumes are compared for the engineered and non-engineered beaches at two scales by applying Eq. 6.7 and Eq. 6.8. However, as the value of R is hard to obtain on an engineered beach, the equation developed by Blenkinsopp et al. (2016) is used to calculate runup and is defined as:

$$R_{2\,\%} = 1.165 H_0 \xi_0^{0.77} \tag{6.9}$$

with H_0 the offshore significant wave height and ξ_0 the offshore Iribarren number.

Figure 6.A1 shows the dimensionless volume of sand which was eroded when a seawall structure was present compared to the volume of sand eroded when no structure was placed. The scaling approach allows the volume of erosion in different and distorted scale experiments to be compared, and shows that in all cases the volume of beach erosion with the presence of the protection is close to but smaller than the volume of erosion without the protection for the same wave and water level forcing. To explicitly quantify this effect, a dimensionless "interaction parameter" (IP) is defined to quantify the relative interaction between wave run-up and the structure. The IP defines the elevation buffer between $R_{2\%}$ and the structure toe, ranging from 0 ($R_{2\%}$ does not reach the structure toe) to 2 (MWL is $R_{2\%}$ above the structure toe) and is defined simply as:

$$IP = \frac{R_{2\,\%} - (z_{structure} - z_{mwl}}{)} R_{2\,\%} \tag{6.10}$$

where, $R_{2\,\%}$ is calculated using Eq. 6.9, $z_{structure}$ is the elevation of the structure toe, and z_{mwl} is the elevation of the mean water level. When the shoreline is far from the structure (low IP), wave runup is mostly over sand, therefore, the erosion occurs almost as for a beach with no coastal structure present. This is shown by the navy blue points close to the 1:1 line. As the water level increases (higher IP), the structure increasingly limits wave runup, hence reducing the area over which sand can be eroded. This is represented by IP values in the range 0.7 to 1.8 which lie further below the 1:1 line. Note that the IP for GWK dynamic cobble berm revetment is not exceeding 1.2.

The above analysis provides an application of the new scaling method and demon-

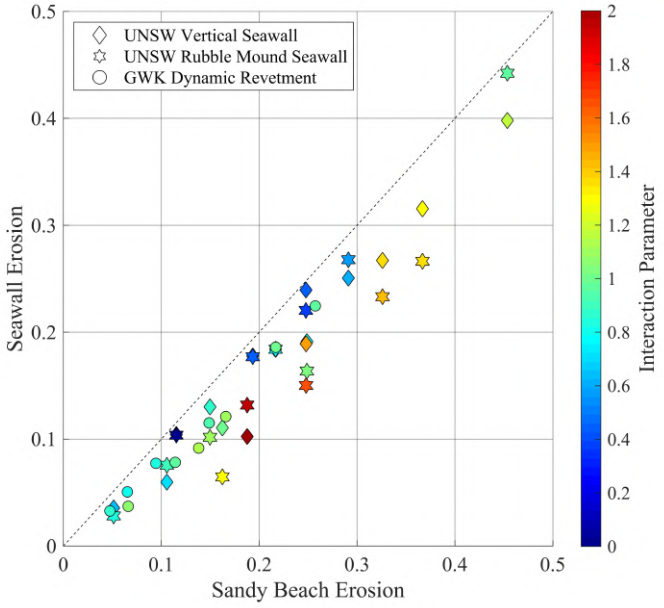

Figure 6.A1: Dimensionless volume of sand eroded on protected beach versus volume of sand eroded for non-protected beach. The dash black line represents the 1:1 line. Each type of structure is represented by a symbol: Diamonds for UNSW rubble mound seawall; Stars for UNSW vertical seawall; Circles for GWK dynamic cobble berm revetment. A dimensionless interaction parameter (IP) was created to account for the relative interaction between wave run-up and the structure.

strates that it can be successfully used to quantify the response of a sand beach in the presence of coastal engineering structures on distorted profiles under water level rise, which increases the potential use of existing datasets.

Acknowledgements

Funding: The DynaRev project has received funding from the European Union's Horizon 2020 research and innovation programme under grant agreement No 654110, HYDRALAB. The two medium-scale experiments were funded by an Australian Research Council Discovery Grant, DP140101302. Paul Bayle is supported by a PhD scholarship through the EPSRC CDT in Water Informatics: Science & Engineering (WISE).

The authors gratefully thank Matthias Kudella, Stefan Schimmels, and all staff and technicians from the Groβer WellenKanal (GWK) flume for their support before, during and after the DynaRev experiment. They also thanks Iv'an C'aceres and Sonja Eichentopf for the precious help in the selection of extra dataset for the analysis.

References

Alsina, J. M. and Caceres, I. (2011). Sediment suspension events in the inner surf and swash zone: Measurements in large-scale and high-energy wave conditions. *Coastal Engineering* 58 (8), pp. 657–670.

Alsina, J. M., Sanchez-Arcilla, A., Gironella, X., and Baldock, T. E. (2015). Design of scaled movable bed experiments using numerical models. *Journal of Coastal Research* SI 50, pp. 379 – 383.

Atkinson, A. L., Baldock, T. E., Birrien, F., Callaghan, D. P., Nielsen, P., Beuzen, T., Turner, I. L., Blenkinsopp, C. E., and Ranasinghe, R. (2018). Laboratory investigation of the Bruun Rule and beach response to sea level rise. *Coastal Engineering* 136, 183—202.

Atkinson, A. (2018). "Laboratory Beach Profile Dynamics and Responses to Changing Water Levels with and without Nourishment". PhD thesis. University of Queensland.

Atkinson, A. and Baldock, T. E. (2014). Formation and development of a breaker bar under regular waves. Part 2: Sediment transport and morphology. *Coastal Engineering* 88, pp. 55–68.

Atkinson, A. and Baldock, T. E. (2016). A high-resolution sub-aerial and sub-aqueous laser based laboratory beach profile measurement system. *Coastal Engineering* 107, pp. 28–33.

Baldock, T. E., Alsina, J. A., Caceres, I., Vicinanza, D., Contestabile, P., Power, H., and Sanchez-Arcilla, A. (2011). Large-scale experiments on beach profile evolution and surf and swash zone sediment transport induced by long waves, wave groups and random waves. *Coastal Engineering* 58 (2), pp. 214–227.

Baldock, T. E., Birrien, F., Atkinson, A., Shinamoto, T., Wu, S., Callaghan, D. P., and Nielsen, P. (2017). Morphological hysteresis in the evolution of beach profiles under sequences of wave climates - Part 1; observations. *Coastal Engineering* 128, 92—105.

Baldock, T. E., Manoonvoravong, P., and Pham, K. S. (2010). Sediment transport and beach morphodynamics induced by free long waves, bound long waves and wave groups. *Coastal Engineering* 57 (10), 898—916.

Battjes, J. A. (1974). Surf similarity. *14th International Conference of Coastal Engineering*, pp. 466–480.

Bayle, P. M., Blenkinsopp, C. E., Conley, D., Masselink, G., Beuzen, T., and Almar, R. (2020). Performance Of A Dynamic Cobble Berm Revetment for Coastal Protection, under increasing water level. *Coastal Engineering* 159.

Beuzen, T., Turner, I. L., Blenkinsopp, C. E., Atkinson, A., Flocard, F., and Baldock, T. E. (2018). Physical model study of beach profile evolution by sea level rise in the presence of seawalls. *Coastal Engineering* 136, 172—182.

Blenkinsopp, C. E., Bayle, P. M., Conley, D., Masselink, G., Gulson, E., Kelly, I., Ganderton, P., Almar, R., Turner, I. L., Baldock, T. E., Beuzen, T., McCall, R. T., Renier, A., Troch, P., Sanchez, D. G., Hunter, A., Bryan, O., Hennessey, G., McCarroll, J., Barrett, A., Schimmels, S., and Kudella, M. (In review). High-resolution, prototype-scale laboratory measurements of nearshore wave processes and morphological evolution of a sandy beach and dynamic cobble berm revetment. *Scientific Data*.

Blenkinsopp, C. E., Matias, A., Hiwe, D., Castelle, B., Marieu, V., and Turner, I. L. (2016). Wave runup and overwash on a prototype-scale sand barrier. *Coastal Engineering* 113, pp. 88–103.

Dean, R. G. (1973). Heuristic model of sand transport in the surf zone. *Proceedings of engineering dynamics in the surf zone, Institute of Engineers, Australia*.

Dette, H. H., Larson, M., Murphy, J., Newe, J., Peters, K., Reniers, A., and Steetzel, H. (2002). Application of prototype flume tests for beach nourishment assessment. *Coastal Engineering* 47, pp. 137–177.

Eichentopf, S., Cáceres, I., and Alsina, J. M. (2018). Breaker bar morphodynamics under erosive and accretive wave conditions in large-scale experiments. *Coastal Engineering* 138, 36—48.

Gourlay, M. R. (1968). *Beach and Dune Erosion Tests*. Tech. rep. M935/M936. Delft Hydraulic Laboratory, the Netherlands.

Guard, P. A. and Baldock, T. E. (2007). The influence of seaward boundary conditions on swash zone hydrodynamics. *Coastal Engineering* 54, pp. 321–331.

Hattori, M. and Kawamata, R. (1980). Onshore–offshore transport and beach profile change. *Proceedings of the* 17^{th} *International Conference on Coastal Engineering*, pp. 1175–1193.

Hughes, M. (1993). *Physical models and laboratory techniques in coastal engineering*. London: World Scientific.

Hunt, I. A. (1959). Design of Seawalls and Breakwaters. *Journal of Waterways and Harbors Division* 85.

IPCC (2014). *Climate Change 2013 – The Physical Science Basis: Working Group I Contribution to the Fifth Assessment Report of the Intergovernmental Panel on Climate Change*. Cambridge: Cambridge University Press.

Ibrahim, M. S. I. and Baldock, T. E. (2020). Swash overtopping on plane beaches – reconciling empirical and theoretical scaling laws using the volume flux. *Coastal Engineering* 157.

Kamphuisk, J. W. (1972). Scale selection for mobile bed wave models. *Proceedings of the* 13^th *International Conference on Coastal Engineering*, pp. 1173–1195.

Kraus, N. C. and Larson, M. (1988). *Beach profile change measured in the tank for large waves 1956-1957 and 1962*. Tech. rep. CERC-88-6. Coastal Engineering Research Centre Vicksburg MS.

Larson, M. and Kraus, N. C. (1989). *SBEACH: Numerical model for simulating storm-induced beach change*. Tech. rep. CERC-89-9. Coastal Engineering Research Centre, US Army Corps of Engineers.

Masselink, G., Ruju, A., Conley, D., Turner, I., Ruessink, G., Matias, A., Thompson, C., Castelle, B., Puleo, J., Citerone, V., and Wolters, G. (2016). Large-scale Barrier Dynamics Experiment II (BARDEX II): Experimental design, instrumentation, test program, and data set. *Coastal Engineering* 113, pp. 3–18.

Nayak, J. V. (1970). "Equilibrium Profile of Model Beaches". PhD thesis. University of California.

Noda, E. K. (1972). Equilibrium beach profile scale–model relationship. *Journal of Waterways, Harbors and Coastal Division*, pp. 511–528.

Peregrine, D. H. and Williams, S. M. (2001). Swash overtopping a truncated plane beach. *Journal of Fluid Mechanics* 440, pp. 391–399.

Pujara, N., Miller, D., Park, Y. S., Baldock, T. E., and Liu, P. L. F. (2020). The influence of wave acceleration and volume on the swash flow driven by breaking waves of elevation. *Coastal Engineering* 158.

Robertson, B., Hall, K., Zytner, R., and Nistor, I. (2013). Breaking waves: review of characteristic relationship. *Coastal Engineering* 55 (1).

Ruessink, B. G., Coco, G., Ranasinghe, R., and Turner, I. L. (2007a). Coupled and non-coupled behavior of three-dimensional morphological patterns in a double sandbar system. *Journal of Geophysical Research* 112.

Ruessink, B. G., Coco, G., Ranasinghe, R., and Turner, I. L. (2007b). Double bar beach dynamics on the high-energy meso-macrotidal French Aquitanian Coast: A review. *Marine Geology* 245, pp. 141–159.

Shields, A. (1936). "Anwendung der Ähnlichkeitsmechanik und der Turbulenz Forschung auf die Geschiebebewegung". PhD thesis. Mitt. der Preuss. Versuchsamst für Wasserbau und Schiffbau, Deutschland.

Shimizu, J. and Ikeno, M. (1996). Experimental study on sediment transport in surf and swash zones using large wave flume. *Proceedings of the* 25^{th} *International Conference on Coastal Engineering*, pp. 3076–3089.

Soulsby, R. (1997). "Dynamics of marine sands". PhD thesis. Thomas Telford, UK.

Strauss, D. R. (2009). "Morphological modeling of intermediate beach state transitions". PhD thesis. Griffith School of Environment Science, Environment, Griffith University.

Swart, D. (1974). "Offshore Sediment Transport and Equilibrium Beach Profiles". PhD thesis. University of Technology, Delft.

Thornton, E., MacMahan, J., and Sallenger, J. A. (2007). Rip currents, mega-cusps,and eroding dunes. *Marine Geology* 240, pp. 151–167.

Turner, I. L., Aarninkhof, S. G. J., and Holman, R. A. (2006). Coastal imaging applications and research in Australia. *Journal of Coastal Research* 22, pp. 37–48.

Vellinga, P. (1982). Beach and Dune erosion during storm surge. *Coastal Engineering* 6 (4), pp. 361–387.

Vellinga, P. (1986). "Beach and dune erosion during storm surges". PhD thesis. Delft University of Technology, Delft, the Netherlands.

Wright, L. D. and Short, A. D. (1984). Morphodynamic variability of surf zones and beaches: a synthesis. *Marine Geology* 56, 93—118.

van Rijn, L. C. (1993, 2012). *Principles of sediment transport in rivers, estuaries and coastal seas*. Aqua Publications, Amsterdam, The Netherlands.

van Rijn, L. C., Tonnon, P. K., Sánchez-Arcilla, A., Cáceres, I., and Grüne, J. (2011). Scaling laws for beach and dune erosion processes. *Coastal Engineering* 58 (7), pp. 623–636.

Concluding remarks

This paper developed a new scaling method for distorted experiments, to compare beach profile, sediment transport and morphological parameters under erosive conditions and water level increase. The method was used and validated for a range of modified Dean number, and two applications were presented. The method showed good results for fixed water level, with a large range of parameters that can be compared, including local and bulk sediment transport. The method was successfully used to compare beach profile behaviour and sediment transport under increasing water level, but was not able to satisfactorily match the shape of the profiles. We hope that this scaling approach will allow existing and future datasets to be used together to study morphological changes.

The method was successfully used to compare sediment transport patterns on beaches protected by different types of coastal defence. Furthermore, at the moment of writing this thesis, our collaborators at the University of Queensland, Australia, are running a small scale model of the DynaRev experiment presented in Chapter 3. Therefore, this scaling method will be very useful to enable comparison of the results. Indeed, the sand in the UQ flume is still similar to that used in the GWK and therefore as demonstrated, the model is automatically distorted in one aspect. It is expected therefore, that this method will enable future work on dynamic revetments using smaller scale experimental facilities to be undertaken and compared with lab and even field results, providing further evidence for the development of comprehensive design guidance.

It is expected that the number of laboratory datasets investigating sea level rise effects will increase in the future, and therefore this method will help the community by increasing our ability to compare datasets collected in different laboratories. In the second part of the chapter, we use the method to compare two distorted datasets to analyse the beach profile evolution under sea level rise, and compare the results with an empirical model of long term sea level rise.

Chapter 6.

Paul M. Bayle, Tomas Beuzen, Chris E. Blenkinsopp, Tom E. Baldock, and Ian L. Turner (2020). Beach Profile Changes under Sea Level Rise in Laboratory Flume Experiments at Different Scale. *Journal of Coastal Research 95(sp1)*, 192-196.
DOI: 10.2112/SI95-038.1

Abstract

Laboratory wave flume experiments have been used to provide improved understanding of beach profile evolution under different wave and water level conditions. However, the understanding of the processes involved in the evolution of beach profile under Sea Level Rise (SLR) toward equilibrium is unclear. Two similar, but distorted experiments were performed at large and medium scale in order to study the qualitative morphological changes involved in beach profile evolution under SLR. Both experiments showed similar beach profile evolution. The profile change predicted by the Profile Translation Model (PTM) and the Bruun Rule underestimated the observed reatreat in both experiments. The length of the active beach profile increased under SLR. For the large scale experiment, the reflection coefficient of the beach decreased while the vertical runup increased significantly. The beachface changed faster than the outer surf zone, making the beach more dissipative.

Declaration concerning the second article used for this Chapter:

Title	A new approach for scaling beach profile evolution and sediment transport rates in distorted laboratory models
Status	Published in the Special Issue of Journal Of Coastal Research
Details	Paul M. Bayle, Tomas Beuzen, Chris E. Blenkinsopp, Tom E. Baldock, and Ian L. Turner (2020). Beach Profile Changes under Sea Level Rise in Laboratory Flume Experiments at Different Scale. *Journal of Coastal Research 95(sp1)*, 192-196. DOI: 10.2112/SI95-038.1.
Contribution from the authors	P.M. Bayle: Planning/Collection/Processing/Analysis of data; Manuscript (65%) T. Beuzen: Collecting/Processing/Analysis of data; Manuscript (10%) C.E. Blenkinsopp: Analysis of the data; Edited drafts of manuscript (10%) T.E. Baldock: Analysis of the data; Edited drafts of manuscript (10%) I.L. Turner: Suggesting data analysis; Edited drafts of manuscript (5%)
Statement	This paper reports on original research I conducted during the period of my Higher Degree by Research candidature.
Date and Signature	

Preamble to the second part

The concept of beach profile evolution under sea level rise has been studied by many authors (SCOR Working Group, 1991), and is dominated by the Bruun rule (Bruun, 1954). The concept of the Bruun rule is based on the following assumptions:

- Zero net longshore sediment transport (2-D model).
- A concave equilibrium profile is retained as the sea level rises.
- Sediment moves only offshore.
- The volume eroded is immediately transported offshore and deposited: no response time parameter.
- The rise in the bed elevation in the offshore part of the surf zone as a result of this deposition equals the rise in sea level: therefore water depth stays constant in the offshore part of this region.
- The whole profile must be made of sand, and easily erodible.
- The sea level rise must be much smaller than the berm height ($S <<<< B$; Figure 6.P1).

The Bruun rule concept states that: a) there is a shoreward displacement of the beach profile as the upper beach is eroded; b) the material eroded from the upper beach is equal in volume to the material deposited on the nearshore bottom; and c) the rise of the nearshore bottom as a result of this deposition is equal to the rise in sea level, thus maintaining a constant water depth in that area. This concept is applicable for long term sea level rise, considering that the beach profile evolves from one equilibrium state to another. However, this concept is used in many short term sea level rise (*e.g.*, storm surge) studies in coastal engineering and management (Pye and Blott, 2018). The concept and assumptions applied to the short term sea level rise are assessed and plotted in Figure 6.P1.

Figure 6.P1a shows an initial beach profile at equilibrium, where L represents the length of the profile from the shore to the depth of closure d_c. When the sea level rises by S (Figure 6.P1b), the Bruun rule concept says that the material eroded from the shore will be deposited in the outer surf zone with a thickness S' equal to the rise S. Therefore, the depth of closure and its cross-shore location does not change because the transfer is instantaneous. However, because the shoreline retreats, the value of L of the new active profile changes and becomes longer. When the next sea level rise happens, the same processes occur (Figure 6.P1c). So again, the value and actual location of d_c does not change, while the shoreline retreats and the factor L increases. It is important to note that the berm height B decreases, as it is supposed that there is no onshore sediment transport. However, if B is really large (and it must be large compared to S according to the underlying hypothesis), this change might be negligible at least for the first SLR step shown on Figure 6.P1b. It becomes an important change after a few iterations of rising if the back-shore beach slope is flat. So, following the rule and its assumption, we should end up with a different equilibrium beach profile (Figure 6.P1d). There is an upward and landward translation of the profile as stated by the rule, but the profile is not conserved and becomes longer (Figure 6.P1d). It tends to go toward an infinite abrasive platform as described in Johnson (1919) if no other processes are

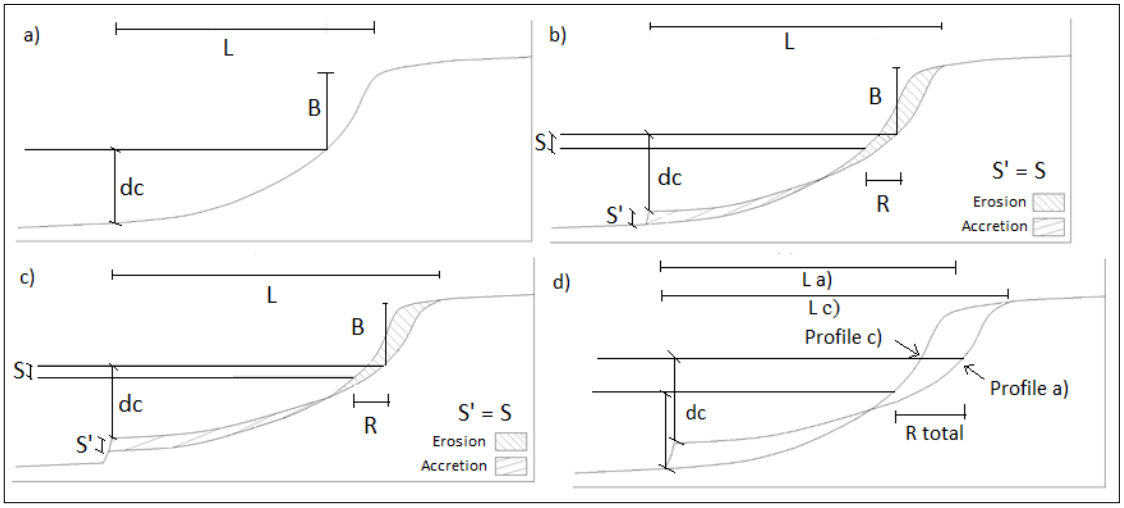

Figure 6.P1: (a) Schematic beach profile to illustrate the Bruun rule concept; (b) Schematic of the first sea level rise and resulting profile dimensions; (c) Schematic of the second sea level rise; (d) Comparison of the beach profile after two SLR (comparison between subplots a and c). S is the SLR (m), S' is the thickness of the deposited material (m), d_c is the depth of closure (m), R the shoreline retreat (m), B is the berm height (m) and L is the length of the active profile. Note that a progressive increase could be considered as an infinity of small discrete increments.

acting. These processes, such as longshore sediment transport gradient, onshore transport etc. . . , are usually effective in the long term but not in the short term.

It appears that if we follow the Bruun rule concept, the profile should become longer and more dissipative. The objective of this paper is therefore to use the GWK and UNSW dataset to analyse the profile evolution under rapid water level increase, and see if the Bruun rule concept stand even outside equilibrium.

6.8 Background

6.8.1 Beach profile equilibrium

The concept of beach profile equilibrium was first presented in Johnson (1919), as the profile that would naturally develop to a stable state under given forcing – *i.e.*, no significant change in the profile evolution with time. Bruun (1954) extended this concept to define an equilibrium beach profile shape with the equation:

$$h = Ax^{2/3} \tag{6.11}$$

where h is the water depth, x is the cross-shore location and A is a scaling parameter controlled by the sedimentology and wave climate (Bruun, 1954; Dean, 1977). Eq. 6.11 and the concept of beach profile equilibrium form the basis of the well-known Bruun rule (Bruun, 1962) for predicting beach recession with Sea Level Rise (SLR):

$$R = \frac{L}{B + h}S \tag{6.12}$$

where R is the shoreline recession (m), L is the length of the active profile (m), B is the berm height taken from the still water level to the top of the berm (m), h is the depth of closure (m) and S is the total sea level rise. This equation is based on a number of assumptions, including that the profile before and after SLR is at equilibrium. Although Eq. 6.11 is a simple and intuitive way to represent a beach profile at equilibrium, it has been argued that the shape it defines is not representative of natural beach profiles as it does not include any of the perturbations observed in nature, such as a bar, trough and berm, and was rarely observed in the field (Bruun, 1983; Dean, 1991; Rosati et al., 2013). Furthermore, beach profile equilibrium is unlikely to ever be attained in nature due to constant changes in hydrodynamics and sediment availability. Therefore, the Bruun rule Eq. 6.12 cannot be expected to work perfectly, and is unlikely to be representative of all morphodynamic processes which drive coastal retreat.

Atkinson et al. (2018) performed a comparison of the existing methods to predict shoreline retreat and the evolution of beach profiles at quasi-equilibrium under rising water levels, including the Bruun Rule (Eq. 6.12) and the (Rosati et al., 2013) modified version of the Bruun Rule, including onshore sediment transport. A Profile Translation Model (PTM) was also developed to predict the evolution of beach profiles of arbitrary shape under water level rise. This method uses an actual measured profile and assumes it is near equilibrium, and then translates it upward by the value of water level rise, and landward until the erosion and deposition volumes match. As a result, onshore sediment transport and deposition over beach berms is taken into account automatically, in contrast to the modified version of (Rosati et al., 2013) where this has to be estimated or based on measurement. The PTM provided similar predictions to those of the other methods tested, with the predicted shoreline retreat being within 30 % of the observed retreat, but with the additional advantage that profile perturbations like bars and berms could be maintained

through the evolution process.

None of the approaches discussed above have been tested using results from a large-scale laboratory experiment. In general, previous work has focused on understanding the profile evolution caused by water level changes, from one quasi-equilibrium beach profile to another. As discussed above, the maintenance of a constant beach profile shape is one of the crucial assumptions of the Bruun Rule and its derivatives. Beach profiles do typically have seasonal characteristics and shapes around which they fluctuate, which could be considered as a longterm quasi-equilibrium state. However, at shorter time scales, rapid water level fluctuations (*e.g.*, storm surge) typically allow insufficient time for a new equilibrium beach profile to develop. Therefore, the Bruun rule and its derivatives may not apply in this context, and the processes involved in the evolution of a beach profile under water level changes before reaching a complete new equilibrium may differ significantly from these rules.

6.8.2 Assessment of Equilibrium

Laboratory studies have demonstrated that complete, stable equilibrium cannot be achieved in a wave flume for sandy beaches forced by erosive random waves (*e.g.*, Moore, 1982; Rector, 1954). However, the rate of morphological change can be observed to decrease over time. When this rate is small and reaches a certain threshold of change, the profile state is defined as 'quasi-equilibrium' (*e.g.*, Baldock et al., 2017; Beuzen et al., 2018; Atkinson et al., 2018).

Following the approach of Beuzen et al. (2018), equilibrium was assessed based on the evolution of three morphological indicators: shoreline position; the sediment transport rate; and the bar crest position. The shoreline position was defined as the intersection of the still water level with the beach profile. The bar crest position was determined as the location of maximum elevation of the offshore bar. The bar height was calculated by subtracting the initial planar bed elevation at the crest position from the bar crest elevation. The sediment flux (q, m^3/m) was defined as in Eq. 6.6.

The rate of change of these morphological parameters is expected to reduce through time for both experiments toward quasi-equilibrium conditions. The degree to which equilibrium was attained is expressed as the ratio of the rate of change during the final run and the initial rate of change (first run, 20 minute duration) for each parameter expressed as a percentage.

6.9 Results

The results section only uses the GWK and UNSW datasets, as it was previously shown that UQ was not suitable for beach beach profile comparison under SLR. The profiles are compared after the same number of waves, and in both the original and dimensionless space.

6.9.1 Observed beach profile evolution

Figure 6.12 shows the profiles at the end of testing at each water level for the GWK and UNSW experiments, in their original coordinates. As mentioned before, similar and comparable qualitative behaviour was observed in both experiments. The shoreline was eroded as the berm retreated and increased in volume, and the bar moved landward and upward as the water level was increased. In both cases, the length of the profile, calculated from the bar crest to the shoreline, increases with the water level rise. From the end of the initial water level to the profile measured after the same number of waves at the final water level, the profile length increases by 0.44 m (from 2.66 m to 3.10 m) for UNSW (16.5 % longer), and by 6.85 m (from 28.81 m to 35.66 m) for GWK (23.8 % longer). Therefore, it appears that the profiles became more dissipative as the water level was raised, with the shoreline retreating faster than the bar. This behaviour was also observed in Atkinson et al. (2018). The berm height (from the still water level to the top of the berm, as defined in the Brunn rule) also increases in both experiments, by 2 cm and 4.5 cm for GWK and UNSW respectively. On the other hand, the berm height calculated by subtracting the initial planar bed elevation at the berm position from the berm crest elevation remains constant throughout both experiments, suggesting it is approximately self-similar at each water level. As a consequence, the inner surf zone becomes wider, and wave energy is dissipated over a larger area.

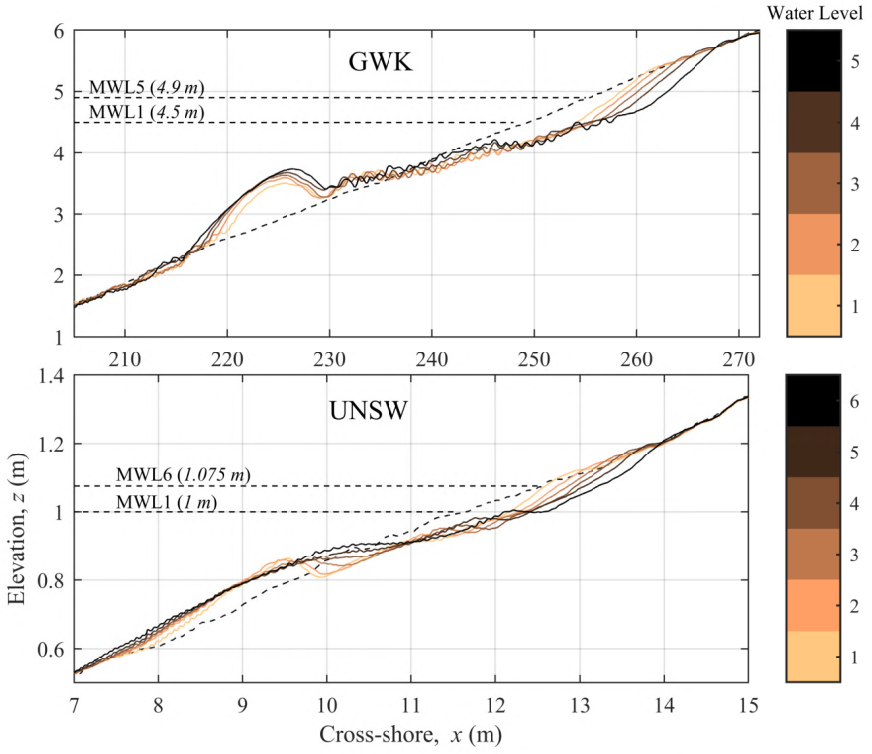

Figure 6.12: Beach profile evolution under water level rise for GWK (top panel) and UNSW (bottom panel). The dashed black profile represents the initial planar slope. The final profile for each water level is represented by a colour, from light copper to black. The horizontal dashed lines represent the initial and final water level (see Table 6.1 for more details). Note that this figure is extracted from Figure 6.8, but that the water level increment is indicated instead of the number of waves.

6.9.2 Beach profile equilibrium

The rate of change of each of the parameters presented in the Section 6.8.2 section was calculated for the last runs and compared to the rate of change during the first run (first 20 minutes), at the initial and final water levels for both experiments in the original coordinates. The last profile in each experiment was measured after the same number of waves – 10700 waves at z_{wl} = 4.9 m (final water level, GWK) and after 11000 waves at z_{wl} = 1.075 m (final water level, UNSW). The rate of change reduced with time for all parameters in both experiments (Table 6.7). They were both closer to equilibrium at the end of the initial water level. For both cases, GWK appears to be further from equilibrium than UNSW. It is evident that the bulk sediment transport rate reduces at a slower rate than the other indicators examined here. This may be expected since it is an integrated indicator of change across the entire profile, and even at a state of equilibrium, significant sediment transport will occur under energetic wave action. However, the time-averaged net rate would be expected to approach zero given sufficient time (theoretical equilibrium beach profile).

Table 6.7: Ratio of the rate of change during the final run and the initial rate of change (first run, first 20 minutes) expressed as a percentage for the shoreline position, sediment transport rate and bar crest position: final rate of change*100 / initial rate of change. Values are shown for both the initial and final water levels.

	Initial water level			Final water level		
	Shoreline (%)	q (%)	Bar (%)	Shoreline (%)	q (%)	Bar (%)
GWK	15	17	11	11	42	33
UNSW	8	12.2	4	3.4	21.1	11.6

6.9.3 Profile translation model predictions

Figure 6.13 shows the application of the Profile Translation Model developed by Atkinson et al. (2018) to the GWK and UNSW profiles in dimensionless coordinates (Eq. 6.7 and Eq. 6.8). For both experiments, the observed shoreline retreat (0.53 for GWK and 0.77 for UNSW) was greater than predicted by the PTM (0.39 for GWK and 0.55 for UNSW), and also more than the Brunn rule (0.38 for GWK and 0.53 for UNSW) and the Rosati et al. (2013) modified version of the Bruun rule (0.38 for GWK and 0.53 for UNSW). This represents a shoreline retreat 36 % (GWK) and 40 % (UNSW) larger than the retreat predicted by the Bruun rule. On the other hand, the bar retreated less than predicted by the PTM in both experiments. This observation can be at least partly explained by the increase in the profile length with water level rise discussed in the Section 6.9.1.

6.10 Discussion

The shoreline retreat observed in the two distorted experiments under water level increase (Figure 6.13) differed significantly from the predictions of the PTM, Bruun rule and the Rosati rule, with both receeding more than predicted. Referring to Eq. 6.12, the length of the profile L is increasing at a greater rate than the berm height B and hence a larger recession is observed. It is also observed that the theoretical end profile given by the PTM did not represent the shape of the entire length of the final active profile. This can be explained by a combination of factors. Firstly, the profile at the end of the first water

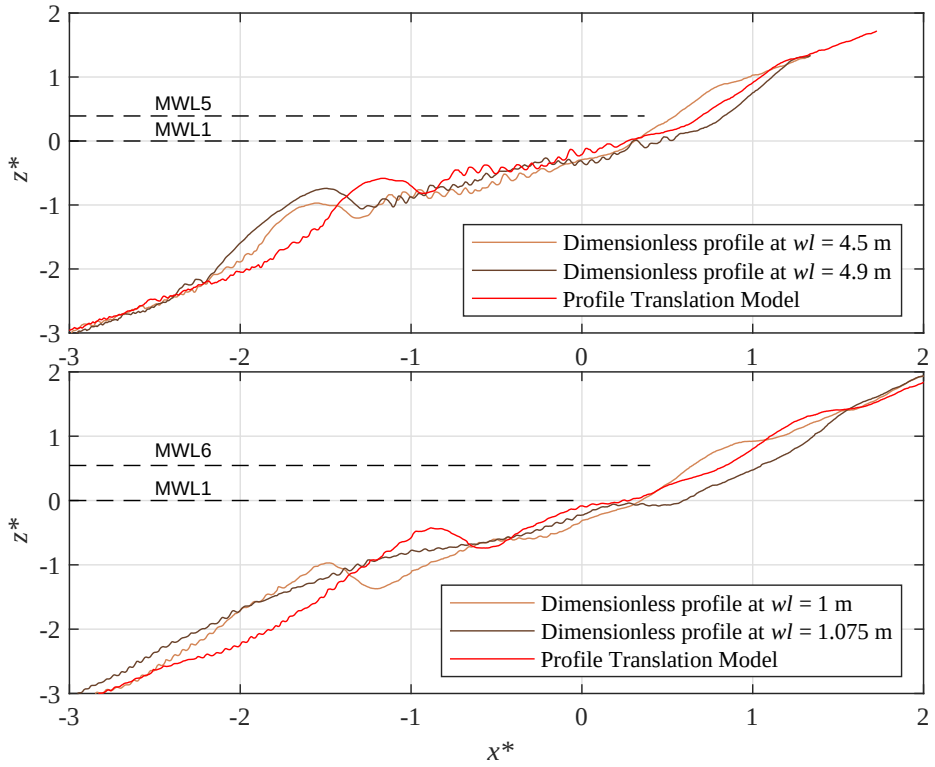

Figure 6.13: Comparison of the real beach profile evolution and profiles predicted by the Profile Translation Model (PTM), for GWK (top panel) and UNSW (bottom panel) in the dimensionless space. Profile at the end of the initial water level is shown in light copper and profile after 10700 waves at zwl = 4.9 m (final water level, GWK) and after 11000 waves at zwl = 1.075 m (final water level, UNSW) in black. The red line represents the theoretical final profile under water level increase obtained by translating the profile at the end of the initial water level (light copper) using the Profile Translation Model (PTM).

level was not at equilibrium in both experiments, though the UNSW profile was closer to equilibrium. Therefore, the bar would be expected to move further offshore (mainly for GWK, Table 6.7) and the shoreline to retreat further (for both GWK and UNSW, Table 6.7) if sufficient run time was possible. The profile would have then been longer before raising the water level, and the translated profile could be expected to better match the PTM prediction. The second factor is that Table 6.7 suggests that the shoreline was closer to equilibrium at the end of testing at the final water level than for the initial, whereas the bar was further from equilibrium (different state of equilibrium for the different indicators). The bar clearly showed a landward and upward movement from its previous position. Therefore the bar may be expected to move landward given additional time, while the shoreline was likely to remain stable. This process would eventually shorten the profile length as equilibrium was approached. This may be explained by the fact that it is easier and faster to erode the beach face than it is to fully redistribute the sand in the surf zone, thus landward and upward movement of the bar is slower than shoreline erosion. However, as previously noted, equilibrium is difficult if not impossible to attain in both the laboratory and nature, and therefore, a beach profile will likely respond to a rise in water level, both on short (storm surge) and long (SLR) timescales in an out of equilibrium state.

Figure 6.14 shows that as the length of GWK beach profile increased under SLR, the coefficient of reflection decreased. The profile was therefore less reflective, and so by

definition, more dissipative. On the other hand, the wave runup increased significantly with SLR. Note that the experiment was designed so that the incident significant wave height at the wave paddle remained constant at all water levels. Therefore, the beach received more incident energy as the coefficient of reflection reduced with rising water level, and this can at least partly explain the increase in runup height. The runup increase can also be caused by the fact that the SLR is increasing relatively faster than the bar crest elevation. Thus, the depth above the bar increases and so the energy dissipated above the bar is likely lower. Under relatively rapid SLR (*e.g.*, storm surge), beach profile is likely to reshape in a similar manner to the profiles in GWK and UNSW, leading to more dissipative profile shape and increased runup height, hence potential coastal erosion threat.

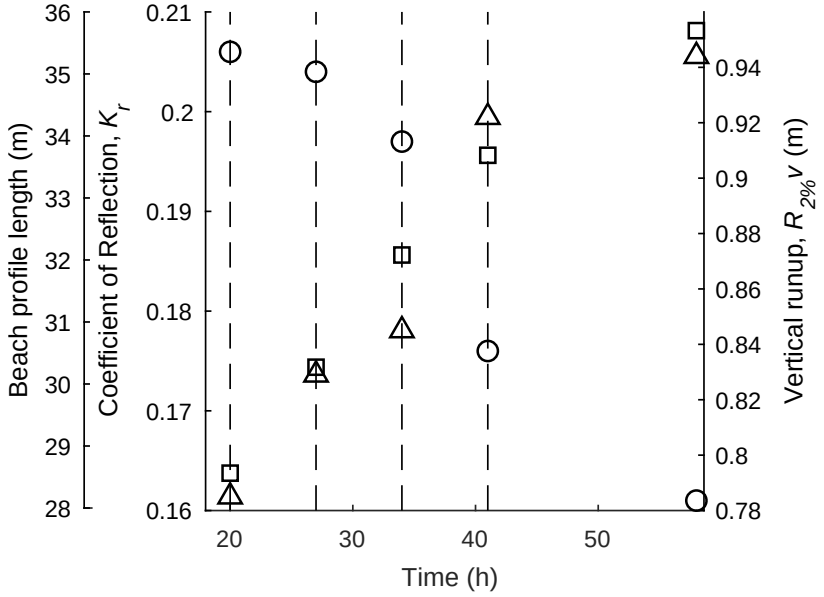

Figure 6.14: Coefficient of reflection K_r (circles), vertical runup $R_{2\,\%v}$ (triangles) and length of the beach profile (squares) at the end of each water level test for GWK only (see Table 6.1) in original coordinates. The vertical dashed lines show the times at which sea level was raised. The first 20 hours corresponding to beach profile development from the initial planar slope are not shown, meaning the time starts at 20 hours. The reflection coefficient and runup were calculated over the last 2 hours of waves at each water level. The length of the profile was calculated from the bar crest to the shoreline.

6.11 Conclusions

Two distorted laboratory flume experiments at different scale were used to study beach morphological changes under water level rise. They showed similar beach profile evolution and shoreline retreat which exceeded the predictions of the PTM and the Bruun rule. The length of the active beach profile increased over the course of water level rise for both GWK and UNSW, causing the profile to become more dissipative. This is explained by the fact that the experiments may not have allowed sufficient time for equilibrium to be attained. Nevertheless, this behavior is likely to regularly occur during short term SLR (*e.g.*, storm surge).

The observed morphology changes meant that for GWK, the reflection coefficient of the beach decreased while the vertical runup and the length of the profile increased significantly as the water level was increased. The beachface changes faster than the outer surf zone,

and this leads to increasing wave runup with water level rise, hence coastal threat.

Acknowledgements

The DynaRev project (GWK) has received funding from the European Union's Horizon 2020 research and innovation programme under grant agreement No 654110, HYDRALAB. The medium scale experiment (UNSW) was funded by an Australian Research Council Discovery Grant, DP140101302. Paul Bayle is supported by a PhD scholarship through the EPSRC CDT in Water Informatics: Science & Engineering (WISE).

References

Atkinson, A. L., Baldock, T. E., Birrien, F., Callaghan, D. P., Nielsen, P., Beuzen, T., Turner, I. L., Blenkinsopp, C. E., and Ranasinghe, R. (2018). Laboratory investigation of the Bruun Rule and beach response to sea level rise. *Coastal Engineering* 136, 183—202.

Baldock, T. E., Birrien, F., Atkinson, A., Shinamoto, T., Wu, S., Callaghan, D. P., and Nielsen, P. (2017). Morphological hysteresis in the evolution of beach profiles under sequences of wave climates - Part 1; observations. *Coastal Engineering* 128, 92—105.

Beuzen, T., Turner, I. L., Blenkinsopp, C. E., Atkinson, A., Flocard, F., and Baldock, T. E. (2018). Physical model study of beach profile evolution by sea level rise in the presence of seawalls. *Coastal Engineering* 136, 172—182.

Bruun, P. (1954). *Coast erosion and the development of beach profiles*. Tech. rep. 82. Technical Memorandum, Beach Erosion Board, Corps of Engineers.

Bruun, P. (1962). Sea-level rise as a cause of shore erosion. *Journal of the Waterways and Harbours Division* 88, 117—130.

Bruun, P. (1983). Review of conditions for uses of the Bruun rule of erosion. *Coastal Engineering* 7 (1), 77—89.

Dean, R. G. (1977). *Equilibrium beach profiles: U.S. Atlantic and Gulf coasts*. Tech. rep. 12. Department of Civil Engineering, University of Delaware.

Dean, R. G. (1991). Equilibrium beach profiles: characteristics and applications. *Journal of Coastal Research* 7 (1).

Johnson, D. W. (1919). *Shore processes and shore-line development*. New York, John Wiley & Sons.

Moore, B. (1982). "Beach profile evolution in response to changes in water level and wave height". MA thesis. University of Delaware, Newark, DE.

Rector, R. L. (1954). *Laboratory Study of Equilibrium Profiles of Beaches*. Tech. rep. 41. Technical Memorandum, U.S. Army Corps of Engineers.

Rosati, J. D., Dean, R. G., and Walton, T. L. (2013). The modified Bruun Rule extended for landward transport. *Marine Geology* 340, 71—81.

SCOR Working Group (1991). The response of beaches to sea-level changes: a review of predictive models. *Journal of Coastal Research* 7 (3), 895—921.

Chapter concluding remarks

The method developed in the first part of the paper was successfully used to investigate a research question, showing the potential of the method. The Bruun rule concept, and related empirical models of beach profile evolution and shoreline retreat under SLR were compared to two sets of laboratory data, including a prototype scale dataset. The analysis of the Bruun rule concept in Figure 6.P1 was observed. It was found that over a short time scale, the beach profile length increases, with the profile becoming more dissipative and the shoreline retreating further than predicted by commonly used sea level rise models.

While it is recognised that the time independency of the Bruun rule makes it unrealistic, this rule has sometimes given an accurate prediction of shoreline retreat under long term sea level rise SCOR Working Group, 1991. However, the inherent paradox of the assumptions makes it incorrect for application at a shorter time scale, such as for storm surge or over spring tidal cycles, and reveals that the equilibrium assumption is a key rule of the Bruun rule. Therefore, it is believe that the observed profile lengthening and large shoreline retreat are real processes which will need to be taken into account to develop reliable short term coastal management plans.

Chapter 7

Conclusions and further work

7.1 Conclusions

In this thesis, the behaviour and performance of a dynamic cobble berm revetment as a coastal protection was investigated under energetic wave conditions and water level changes. For the first time, a dynamic revetment was tested in a prototype scale laboratory flume (Chapter 3). A comprehensive set of lidar and ground-based topography data were also obtained in the field, providing a unique dataset at high temporal and spatial resolution (Chapter 4 and 5). A new scaling method was developed to compare distorted beach profile experiments under both a fixed and increased water level (Chapter 6, first part). This method was used to investigate beach profile evolution under sea level rise, and results were assessed against empirical prediction models (Chapter 6, second part). In this Conclusions Chapter, the findings are summarized and discussed with respect to the initial objectives, with one paragraph addressing one bullet point for each objective. Finally, the results of this study are placed in a wider context and some future investigations and work are suggested.

7.1.1 Dynamic cobble berm revetment as a coastal defence

Dynamic cobble berm revetments provide efficient protection to the hinterland against wave attack. They were shown to significantly reduce the horizontal and vertical wave runup and shoreline retreat. The mechanisms involved in this level of protection are: 1) the energy dissipation due to cobble movement and water infiltration; and 2) the rollover transport which increases the crest height allowing the material to be mainly transported landward. The reduction of the runup and shoreline retreat by the revetment is likely the reason why composite beaches have been recognised as natural coastal defences (Allan et al., 2015). However, the level of protection had never previously been studied or quantified, and this study brings the qualitative and quantitative evidence of this.

Dynamic cobble berm revetments also protect the beach on which it is placed, by armouring the underlying sand. Under energetic conditions and water level increase, the revetment retains some sand on the sub-aerial part of beach leading to a larger volume of sand than without the presence of the revetment under the same forcing. The mechanisms involved in this protection are linked to the sand stability, and the internal sand dynamic

with accretion and erosion of the protected sand.

The dynamic cobble berm revetment showed, both in the laboratory and field, that it can withstand very energetic wave conditions and water level changes. The revetment can maintain its global shape and structural coherence while actively protecting the beach and hinterland. However, the revetment slope is very dependent on incident waves, and can change very rapidly. Furthermore, the volume of the ridge, which includes both gravels and sand, can also change over the course of a tide. But in all observed cases, the revetment is able to recover by adapting its shape and slope to the wave forcing and by recovering its volume during calmer and more accretive conditions.

Some preliminary design and maintenance guidelines could be defined. Generally, dynamic cobble berm revetments can be easily installed without high-level engineering skills or complex machinery. The installation and nourishment of the revetment can be as simple as dumping the material on top of the high tide berm and allowing waves to reshape it to a stable state. Partly because of this simple installation, the revetment is a very cost effective structure. It is significantly cheaper than common hard engineering solutions, and can be considered to integrate better into the environment. Although installation of a revetment brings a significant amount of gravel onto a sandy beach, which may be problematic in many touristy area, a large part of the sandy beach remain exposed at low tide, hence retaining much of its aesthetic and leisure value and it can be seen on the natural composite beach in Chapter 2, Figure 2.6.c. This type of protection allows a large range of material sizes and grades (rounded to angular) to be used, which promotes local sourcing.

7.1.2 Dynamic cobble berm revetment behaviour

Under energetic conditions and water level increase, dynamic cobble berm revetment undergo constant bed-level changes but overall shape and volume is maintained through time. Indeed, the gross changes measured are at least one order of magnitude larger than the net changes. Under sea level rise, the revetment tested in the laboratory retreated and moved upward, but at a slower pace than the rate of water level increase. This was not observed in the field as the woody barrier of drift logs creates a physical constraint, preventing the revetment from retreating. However in both cases, the revetment changes did not affect significantly the shape of the structure or the core body of material. The adaptation of the revetment involve rearrangement of the cobble layer, but also changes in the underlying sand profile.

Dynamic cobble berm revetments are dynamically stable. The ratio of gross over net change can be space-dependent when the revetment grading is high and large particles tend to be transported to the bottom of the revetment, interacting with swashes and other particles in a different way than smaller material. The stability of the revetment is also time-dependent, as the revetment is able to rapidly reach a stable state at the intra-tidal time scale under incident wave forcing. It also can reach a stable state at the inter-tidal time scale, rapidly reaching it after a few high water levels with energetic waves.

The morphodynamics of the revetment are very much influenced by the high tide

water level, at both the long term and swash scale. Taking into account the dissipative nature of composite beaches, the surf zone tends to saturate during storm conditions, and therefore the water level becomes an important parameter influencing the swash energy. In parallel, the revetment morphodynamics is also very much dependent on the offshore wave conditions which drive both slope and rates of change, hence global cobble motion and net morphological changes. Revetment volume changes and shape is mainly caused by cross-shore processes on the short and medium time scale. However, longshore transport remains important especially for the overall revetment volume, as it progressively depletes updrift locations and nourishes areas downdrift.

The revetment completely ingrates with the underlying sand. The underlying sand plays an important role in the overall stability of the revetment, and since almost no cobbles are transported seaward of the revetment toe, sand movement is also mostly responsible for overall volume changes. Thus, revetment state is mainly dependent on the internal sand content and dynamics and is defined as a function of this parameter in the model presented in Chapter 4. The inter-tidal stable state of the revetment is attained only when the underlying sand reaches a stable state, and therefore the underlying sand dynamic is the driver of the overall stability.

7.1.3 New scaling method for beach profile comparison

A new scaling method was developed to enable distorted model experiments to be compared.

The method allows beach profiles with a similar modified Dean number to be confidently compared. The scaling method enables qualitative and some quantitative comparisons of beach profile features, local and bulk sediment transport and morphodynamic parameters. Under water level increase, the method is applicable (with limitation in comparing the beach profile shape) only if similar water level change procedure and relative water level increases are applied between the models. The method can also be used for engineered beach cases, and was used to perform a distorted comparison of beach protected by a seawall and a dynamic cobble berm revetment.

With the help of the scaling method, it was identified that the profile becomes longer and more dissipative under rapid sea level rise, and the shoreline undergoes a larger retreat than given empirical models. This behaviour does not follow the Bruun rule and associated empirical models of shoreline and profile retreat, showing that the assumption of equilibrium is crucial.

7.2 Implications and perspectives for the future

7.2.1 Improving dynamic cobble berm revetment knowledge

The dynamic cobble berm revetment tested in the laboratory was composed of rounded and well sorted cobbles (low grading), while the revetment in North Cove was composed of angular and poorly sorted material (high grading). Although both showed many similarities in their behaviour and capacity to protect the beach, the cross-shore grading appeared

to be an important parameter. Therefore, understanding the differences inherent to these materials would be a valuable contribution to assess the pros and cons of each particle type, and improve the design guidelines for future users. At the moment of writing this thesis, the analysis of the DynaRev2 experiment, which repeated DynaRev but using poorly sorted angular material (similar to the North Cove revetment), is being undertaken.

Other design variations and a wider range of test conditions could be assessed in the laboratory, to test different material and structure geometries, but also to investigate the internal sand processes. This would significantly improve the range of application of dynamic revetments, and provide a crucial understanding of sand-cobble interface dynamic which is critical for numerical modelling (McCall et al., 2019). This type of test could be performed simultaneously across different flumes, and compared together using the scaling method presented in Chapter 6.

While dynamic revetments demonstrated a satisfying performance at protecting the beach and shore while maintaining its global shape, both in the lab and in the field, both experiments were relatively short. It would be very valuable for the coastal engineering community to have long term analysis of revetment behaviour and performance, to assess whether it is consistent with the current results. At the time of writing this thesis, our collaborators at the Washington State Department of Ecology are analysing 2 years of seasonal datasets to investigate the long term dynamics of the revetment in North Cove.

7.2.2 Application

While a few applications already exist (see Chapter 2 and 3), the number of dynamic cobble berm revetments implemented to protect a sandy beach is limited. Following this study, it is hoped that the coastal engineering community will pay more attention to such structures, and gain confidence in their capacity to protect the coast efficiently. The preliminary design guidelines provided in Chapter 3 and 4 should give the basic knowledge to implement such structures, but ongoing studies will likely strengthen these guidelines. Moreover, in the context of climate change, many national environmental agencies are starting to prioritise solutions which "work with nature" to manage coastal retreat (Pye and Blott, 2018).

Dynamic revetment are low-cost structures that can be easily implemented without advanced engineering skills or equipment. The material used can also be locally supplied, and the possibility to use angular and poorly sorted material make this solution affordable. As a consequence, this type of solution appears to be a good alternative for many developing countries under the threat of coastal erosion.

7.3 Recommendation for further work

During this study, some important results were obtained which our understanding of dynamic cobble berm revetments, composite beaches and beach profile evolution. As always, many of these results either brought new research questions or relied on hypotheses that could not be verified. In this section, the principal research directions that emerged from the present work are addressed.

7.3.1 New technical tools

The understanding of dynamic revetments and composite beaches are interlinked, and this is an under-researched area with multiple open research questions. Some of these research questions are nowadays limited by the absence of the measurement tools to address them. Two main required developments are highlighted here:

- Real-time cobble tracking system: the RFID technique used in this study provides discrete measurements of the position of instrumented cobbles. It is therefore impossible to assess the real-time movement, as only the initial and final position are given, and therefore their transport pattern is mostly unknown. There is therefore the need to develop engineered cobbles that could be tracked in real time. At the best, this technique would require limited equipment and could be used both in the field and laboratory.
- Real-time sand-cobble interface location: the sand and cobble interface, hence pure cobble layer thickness, measured in this study relied on discrete measurements and linear interpolations between them. To better understand the internal sand and cobble dynamics, and eventually validate and complete the model presented in Chapter 4, real-time (or at least more frequent) measurement techniques should be developed. The technique should be independent of the amount of water above the measurement zone, to be able to analyse the internal dynamics of the ridge at a swash-by-swash timescale.

7.3.2 Beach profile evolution under rapid sea level rise

The 2-D evolution of the beach profile under water level increase revealed that the profile lengthens and the shoreline erodes further than predicted by the existing empirical models. However, the next profile evolution steps are not clear and need to be tested in the lab to answer the following questions:

- Does the bar move landward until the profile again reaches its initial length? Does a new bar appear as observed in the UQ dataset presented in Chapter 6?
- Since the shoreline retreats further than the prediction, does onshore transport drive shoreline advancement, which could then be explained by the concept of morphological hysteresis (Baldock et al., 2017), or does the shoreline remain more eroded than the prediction?

7.3.3 Laboratory tests and numerical modelling to develop a design guidance

As mentioned before, flumes of different scale can be used together to improve our understanding of dynamic revetment, but also to test some design and responses to different forcing in order to developed a recognised design guidance. In addition, this can be easier and more feasible since a new scaling method for distorted profile was developed in Chapter 6. Three suggestions are listed below:

- Cobble diameter to ensure dynamic stability. Dynamic revetments are expected to reshape, but remain stable under storm wave attack without significant loss of material.
- Crest height to protect from wave overtopping.
- Total volume, which should be sufficient to ensure that the function of the structure is not diminished if material is moved seaward, alongshore or buried.

The results showing that the internal and underlying sand dynamics drive the overall state and stability of the revetment is assumed to be one of the key thing to model and explore for improving numerical models.

Bibliography

Ahrens, J. P. (1990). Dynamic revetment. *Coastal Engineering* 138, 1837—1850.

Allan, J. C. and Gabel, L. L. (2016). *Monitoring the response and efficacy of a dynamic revetment constructed adjacent to the columbia river south jetty, Clatsop county, Oregon.* Tech. rep. O-16-07. Oregon Department of Geology and Mineral Industries.

Allan, J. C., Geitgey, R., and Hart, R. (2015). Dynamic revetments for coastal erosion stabilization: a feasible analysis for application on the oregon coast. *Oregon Department of Geology and Mineral Industries* Special issue, 37.

Allan, J. C., Harris, E., Stephensen, S., Politano, V., Laboratory, H., Folger, C., and Nelson, W. (2012). *Hatfield Marine Science Center Dynamic Revetment Project*. Tech. rep. Hatfield Marine Science Center, Oregon State University.

Allan, J. C. and Komar, P. (2004). Environmentally compatible berm and artificial dune for shore protection. *Shore and Beach* 721, 9—16.

Almeida, L. P., Masselink, G., Russel, P. E., and Davidson, M. A. (2015). Observations of gravel beach dynamics during high energy wave conditions using a laser scanner. *Geomorphology* 228, 15—27.

Antonov, J. L. (2005). Thermosteric sea level rise, 1955-2003. *Geophysical Research Letters* 32 (12).

Atkinson, A. L., Baldock, T. E., Birrien, F., Callaghan, D. P., Nielsen, P., Beuzen, T., Turner, I. L., Blenkinsopp, C. E., and Ranasinghe, R. (2018). Laboratory investigation of the Bruun Rule and beach response to sea level rise. *Coastal Engineering* 136, 183—202.

Baldock, T. E., Birrien, F., Atkinson, A., Shinamoto, T., Wu, S., Callaghan, D. P., and Nielsen, P. (2017). Morphological hysteresis in the evolution of beach profiles under sequences of wave climates - Part 1; observations. *Coastal Engineering* 128, 92—105.

Baldock, T. E., Manoonvoravong, P., and Pham, K. S. (2010). Sediment transport and beach morphodynamics induced by free long waves, bound long waves and wave groups. *Coastal Engineering* 57 (10), 898—916.

Battjes, J. A. (1974). Surf similarity. *14th International Conference of Coastal Engineering*, pp. 466–480.

Bergsma, E. W. J., Blenkinsopp, C. E., Martins, K., Almar, R., and Almeida, L. P. M. de (2019). Bore collapse and wave run-up on a sandy beach. *Continental Shelf Research* 174, 132—139.

Beuzen, T., Turner, I. L., Blenkinsopp, C. E., Atkinson, A., Flocard, F., and Baldock, T. E. (2018). Physical model study of beach profile evolution by sea level rise in the presence of seawalls. *Coastal Engineering* 136, 172—182.

Bindoff, N. L., Stott, P. A., AchutaRao, K. M., Allen, M. R., Gillett, N., Gutzler, D., K.Hansingo, Hegerl, G., Hu, Y., Jain, S., Mokhov, I. I., Overland, J., Perlwitz, J., Sebbari, R., and Zhang, X. (2013). "Climate Change 2013: The Physical Science Basis. Contribution of Working Group I to the Fifth Assessment Report of the Intergovernmental Panel on Climate Change". Cambridge, United Kingdom and New York, NY, USA: Cambridge University Press. Chap. 10, 867—952.

Blenkinsopp, C. E., Bayle, P. M., Conley, D., Masselink, G., Gulson, E., Kelly, I., Ganderton, P., Almar, R., Turner, I. L., Baldock, T. E., Beuzen, T., McCall, R. T., Renier, A., Troch, P., Sanchez, D. G., Hunter, A., Bryan, O., Hennessey, G., McCarroll, J., Barrett, A., Schimmels, S., and Kudella, M. (In review). High-resolution, prototype-scale laboratory measurements of nearshore wave processes and morphological evolution of a sandy beach and dynamic cobble berm revetment. *Scientific Data*.

Blenkinsopp, C. E., Matias, A., Hiwe, D., Castelle, B., Marieu, V., and Turner, I. L. (2016). Wave runup and overwash on a prototype-scale sand barrier. *Coastal Engineering* 113, pp. 88–103.

Blenkinsopp, C. E., Mole, M. A., Turner, I. L., and Peirson, W. L. (2010a). Measurements of the time-varying free-surface profile across the swash zone obtained using an industrial LiDAR. *Coastal Engineering* 57, 1059—1065.

Blenkinsopp, C. E., Turner, I. L., Masselink, G., and Russell, P. E. (2011). Swash zone sediment fluxes: Field observations. *Coastal Engineering* 58, 28—44.

Bluck, B. J. (1967). Sedimentation of Beach Gravels: Examples from South Wales. *Journal of Sedimentary Petrology* 37, 128—156.

Bonneton, P., Michallet, H., Martins, K., and Lannes, D. (2018). A nonlinear weakly dispersive method for recovering the elevation of irrotational surface waves from pressure measurements. *Coastal Engineering* 138, 1—8.

Boorman, L. A., Goss-Custard, J., and McGorty, S. (1989). *Climate Change, Rising Sea Level and British Coast*. Tech. rep. NERC Institution of Terrestrial Ecology Research Publication No. 1. HMSO, London.

Brown, A., Corbett, B., and Strauss, D. (2011). *GCSMP Implementation Plan Activities 2011/2012 - Summary of Narrowneck Reef Monitoring to June 2011*. Tech. rep. 123.2. Griffith Centre for Coastal Management.

Bruun, P. (1954). *Coast erosion and the development of beach profiles*. Tech. rep. 82. Technical Memorandum, Beach Erosion Board, Corps of Engineers.

Bruun, P. (1962). Sea-level rise as a cause of shore erosion. *Journal of the Waterways and Harbours Division* 88, 117—130.

Bruun, P. (1983). Review of conditions for uses of the Bruun rule of erosion. *Coastal Engineering* 7 (1), 77—89.

Cailleux, A. (1945). Distinction des galets marins et fluviatiles. *Societe Geologique de France Bulletin* 15, pp. 375–404.

Bibliography

Carter, R. W. G. and Orford, J. D. (1984). Coarse clastic barrier beaches: a discussion of the distinctive dynamic and morphosedimentary characteristics. *Marine Geology* 60, 377—389.

Cartwright, A., Brundrit, G., and Fairhurst, L. (2008). *Global Climate Change and Adaptation – A Sea-Level Rise Risk Assessment*. Tech. rep. Cape Town, South Africa: LaquaR Consultant CC.

Church, J. A., Clark, P. U., Cazenave, A., Gregory, J. M., Jevrejeva, S., Levermann, A., Merrifield, M. A., Milne, G. A., Nerem, R. S., Nunn, P. D., Payne, A. J., Pfeffer, W. T., Stammer, D., and Unnikrishnan, A. S. (2013). "Climate Change 2013: The Physical Science Basis. Contribution of Working Group I to the Fifth Assessment Report of the Intergovernmental Panel on Climate Change". Cambridge, United Kingdom and New York, NY, USA: Cambridge University Press. Chap. 13, 1137—1216.

Cooper, J. A. G. and Pilkey, O. H. (2004). Sea-level rise and shoreline retreat: time to abandon the Bruun rule. *Global and planetary change* 43, 157—171.

Council, N. C. (2007). *The Dynamics of Mixed Sand-and-Gravel Beaches and the Hawke's Bay Monitoring Programme*. Tech. rep. Napier City Council.

DeConto, R. M. and Pollard, D. (2016). Contribution of Antarctica to past and future sea-level rise. *Nature*, 591—597.

Dean, R. G. (1973). Heuristic model of sand transport in the surf zone. *Proceedings of engineering dynamics in the surf zone, Institute of Engineers, Australia*.

Dean, R. G. and Dalrymple, R. A. (2002). "Coastal Processes with Engineering Applications". Cambridge University Press. Chap. 3, 35—65.

Dornbusch, U. (2017). Design requirement for mixed sand and gravel beach defences under scenarios of sea level rise. *Coastal Engineering* 124, pp. 12–24.

Downie, K. A. and Saaltink, H. (1983). An artificial cobble beach for erosion control. *Coastal Structure '83*. Reston, Va., American Society of Civil Engineers, 846—859.

Dyer, K. R. (1989). Sediment processes in estuaries: Future research requirements. *Journal of Geophysical Research* 94 (C10), 14327—14339.

ESA (2016). *Surfer's point shore enhancement project - 2015-2016 Monitoring Report*. Tech. rep. ESA.

Eichentopf, S., Cáceres, I., and Alsina, J. M. (2018). Breaker bar morphodynamics under erosive and accretive wave conditions in large-scale experiments. *Coastal Engineering* 138, 36—48.

Everts, C. H., Eldon, C. D., and Moore, J. (2002). Performance of cobble berm in Southern California. *Shore and Beach* 704, 4—14.

Large Scale Experimental Storm Impact on Nourished Beach Using Cobble-Gravel-Sand Mix (May 2015). Vol. Volume 7: Ocean Engineering. International Conference on Offshore Mechanics and Arctic Engineering.

French, P. W. (2001). *Coastal defences : processes, problems and solutions*. London: London : Routledge.

Gallach-Sanchez, D. (2018). "Experimental study of wave overtopping performance of steep low-crested structures". PhD thesis. Ghent University, p. 215.

Gourlay, M. R. (1968). *Beach and Dune Erosion Tests*. Tech. rep. M935/M936. Delft Hydraulic Laboratory, the Netherlands.

Grasso, F., Michallet, H., Barthelemy, E., and Certain, R. (2009). Physical modeling of intermediate cross-shore beach morphology: transients and equilibrium states. *Geophysical Research Oceans* 114.

Guza, R. T. and E, B. T. (1982). Swash oscillations on a natural beach. *Journal of Geophysical Research* 87 (1), pp. 483–491.

Hedges, T. S. and Mase, H. (2004). Modified Hunt's equation incorporating wave setup. *Journal of Waterways, Port, Coastal, Ocean Engineering* 130, pp. 109–113.

Holman, R. A. (1986). Extreme value statistics for wave run-up on a natural beach. *Coastal Engineering* 9 (6), pp. 527–544.

Hudson, T., Keating, K., and Pettit, A. (2008). *Delivering benefits through evidence. Coast estimation for coastal protection - summary of evidence*. Tech. rep. SC080039/R7. Environment Agency, Bristol: Environmental agency.

Hughes, S. A. (2004). Estimation of wave run-up on smooth, impermeable slopes using the wave momentum flux parameter. *Coastal Engineering* 51, pp. 1085–1104.

Hunt, I. A. (1959). Design of Seawalls and Breakwaters. *Journal of Waterways and Harbors Division* 85.

Jennings, R. and Shulmeister, J. (2002). A field based classification scheme for gravel beaches. *Marine Geology* 186, 211—228.

Johnson, C. N. (1987). Rubble beaches versus revetments. *Coastal Sediments '87*. Reston, Va., American Society of Civil Engineers, 1217—1231.

Johnson, D. W. (1919). *Shore processes and shore-line development*. New York, John Wiley & Sons.

Kirk, R. M. (1992). Experimental beach reconstruction-renourishment on mixed sand and gravel beaches, Washdyke Lagoon, South Canterbury, New Zealand. *Coastal Engineering* 17, 253—277.

Komar, P. and Allan, J. C. (2010). "Design with Nature strategies for shore protection - The construction of a cobble berm and artificial dune in an Oregon State Park". *Puget Sound Shorelines and the Impacts of Armoring—Proceedings of a State of the Science Workshop*. U.S. Geological Survey Scientific Investigations Report 2010-5254, 117—126.

Kraus, N. C., Larson, M., and Wise, R. (1998). Depth of closure in beach fill design. *Proceedings 12th National Conference on Beach Preservation Technology, Florida Shore and Beach Preservation Association*.

Kraus, N. C. and McDougal, W. G. (1996). The Effects of Seawalls on the Beach: Part I, An Updated Literature Review. *Journal of Coastal Research* 12 (3), pp. 691–701.

Krebs, J., Fankhauser, S., Hall, J., Johnson, D. A., Parry, M., and Wynne, G. (2013b). "Managing the land in a changing climate: Adaptation sub-committee Progress". Adaptation sub-committee. Chap. 5, 93—107.

Bibliography

Krebs, J., Fankhauser, S., Hall, J., Johnson, D. A., Parry, M., and Wynne, G. (2013a). *Managing the land in a changing climate.* Tech. rep. Progress Report 2013. Adaptation Sub-Committee.

Kriebel, D. L. and Dean, R. G. (1985). Numerical simulation of time-dependent beach and dune erosion. *Coastal Engineering* 9, pp. 221–245.

Krumbein, W. C. (1940). Flood gravels of San Gabriel Canyon, California. *Geological Society of America Bulletin* 51, pp. 639–676.

Lippmann, T. C. and Holman, R. A. (1990). The spatial and temporal variability of sand bar morphology. *Journal of Geophysical Research* 95 (C7), 11575—11590.

Loman, G. J. A., van Gent, M. R. A., and Markvoort, J. W. (2010). Physical model testing of an innovative cobble shore, Part I: Verification of cross-shore profile deformation. *Third International Conference on the Application of Physical Modelling to Port and Coastal Protection*.

Longuet-Higgins, M. S. and Stewart, R. W. (1964). Radiation stresses in water waves; a physical discussion, with applications. *Deep Sea Research and Oceanographic Abstracts* 11 (4), 529—562.

Longuet-Higgins, M. S. and Stewart, R. W. (1988). The effects of seawalls on the beach: an extended literature review. *Journal of Coastal Research* (SI) 4, 1—28.

Lorang, M. S. (1991). An artificial perch-gravel beach as a shore protection structure. *Coastal Sediments '91*. Vol. 2. Reston, Va., American Society of Civil Engineers, 1916—1925.

Martins, K., Bonneton, P., Mouraghes, A., and Castelle, B. (2020). Non-hydrostatic, Non-linear Processes in the Surf Zone. *Journal of Geophysical Research: Oceans* 125 (2).

Mase, H. (1989). Random wave runup height on gentle slope. *Journal of Waterways, Port, Coastal, Ocean Engineering* 115, pp. 649–661.

Masselink, G. and Hughes, M. (1998). Field investigation of sediment transport in the swash zone. *Continental Shelf Research* 18 (10), pp. 1179–1199.

Masselink, G. and Van Heteren, S. (2014). Response of wave-dominated and mixed-energy barriers to storms. *Marine Geology* 352, 321—347.

Matsumoto, H. and Young, A. P. (2018). Automated Cobble Mapping of a Mixed Sand-Cobble Beach Using a Mobile LiDAR System. *Remote Sensing* 10.

McCall, R., Rijper, H., and Blenkinsopp, C. (2019). Towards the development of a morphological model for composite sand-gravel beaches. *Coastal Sediment 2019*, pp. 1889–1900.

McDougal, W. G., Kraus, N. C., and Ajiwibowo, H. (1996). The Effects of Seawalls on the Beach: Part II, Numerical Modeling of SUPERTANK Seawall Tests. *Journal of Coastal Research* 12 (3), pp. 702–713.

Miller, I. M., Warrick, J. A., and Morgan, C. (2011). Observations of coarse sediment movements on the mixed beach of the Elwha Delta, Washington. *Marine Geology* 282 (3), pp. 201–214.

Moore, B. (1982). "Beach profile evolution in response to changes in water level and wave height". MA thesis. University of Delaware, Newark, DE.

Mouraghes, A., Bonneton, P., Lannes, D., Castelle, B., and Marieu, V. (2019). Field data-based evaluation of methods for recovering surface wave elevation from pressure measurements. *Coastal Engineering* 150, 147—159.

Nayak, J. V. (1970). "Equilibrium Profile of Model Beaches". PhD thesis. University of California.

Nielsen, P. and Hanslow, D. J. (1986). Wave Runup Distributions on Natural Beaches. *Journal of Coastal Research* 7, pp. 1139–1152.

Orford, J. D. (1975). Discrimination of particle zonation on a pebble beach. *Sedimentology* 22 (3), 441—463.

Orford, J. D., Jennings, S. C., and Pethick, J. (2003). Extreme storm effect on gravel-dominated barriers. *Proceedings of the International Conference on Coastal Sediments '03*.

Pettijohn, F. J. (1975). *Sedimentary Rocks*. 2nd Edition, Harper and Row Publishers, New York.

Phillips, M. S., Blenkinsopp, C. E., Harley, K. D. S. M. D., and Turner, I. L. (2019). Modes of berm and beachface recoveryfollowing storm reset: observations using a continuously scanning lidar. *Journal of Geophysical Research - Earth Surface* 124 (3), 720—736.

Pilarczyk, K. W. and Boer, K. D. (1983). *Stability and profile development of coarse material and their application in coastal engineering*. Tech. rep. Delft Hydraulics.

Poate, T. G., McCall, R. T., and Masselink, G. (2016). A new parameterisation for runup on gravel beaches. *Coastal Engineering* 117, 176—190.

Policy Research Corporation (2004). *The economics of climate change adaptation in EU coastal areas*. Tech. rep. European Commission.

Polidoro, A., Pullen, T., and Dornbusch, U. (2014). *Wave run-up on shingle beach - a new method*. Tech. rep. HR Wallingford for Environment Agency.

Powell, K. A. (1988). The dynamic response of shingle beaches to random waves. *Coastal Engineering* 130, 1763—1773.

Powell, K. A. (1990). *Predicting Short Term Profile response for shingle beaches.* Tech. rep. SR 219. HR Wallingford, Oxfordshire, UK.

Power, H. E., Atkinson, A. L., Hammond, T., and Baldock, T. E. (2013). Accuracy of Wave Runup Formula on Contrasting Southeast Australian Beaches. *Proceedings of the 21st Australasian Coastal & Ocean Engineering Conference, (Sydney, Australia)*, pp. 618–623.

Powers, M. C. (1953). A new roundness scale for sedimentary particles. *Journal of Sedimentary Petrology* 23, pp. 117–119.

Pye, K. and Blott, S. J. (2018). *Advice on Sustainable Management of Coastal Shingle Resources*. Tech. rep. 273. Natural Resources Wales.

Ranasinghe, R., Larson, M., and Savioli, J. (2010). Shoreline response to a single shore-parallel submerged breakwater. *Coastal Engineering* 57, pp. 1006–1017.

Ranasinghe, R., Symonds, G., Black, K., and Holman, R. A. (2004). Morphodynamics ofintermediate beaches: a video imaging and numerical modelling study. *Coastal Engineering* 51, 629—655.

Ranasinghe, R. and Turner, I. (2006). Shoreline response to submerged structures: A review. *Coastal Engineering* 53, pp. 65–79.

Rector, R. L. (1954). *Laboratory Study of Equilibrium Profiles of Beaches*. Tech. rep. 41. Technical Memorandum, U.S. Army Corps of Engineers.

Rhein, M., Rintoul, S. R., Aoki, S., Campos, E., Chambers, D., Feely, R. A., Gulev, S., Johnson, G. C., Josey, S. A., Kostianoy, A., Mauritzen, C., Roemmich, D., Talley, L. D., and Wang, F. (2013). "Climate Change 2013: The Physical Science Basis. Contribution of Working Group I to the Fifth Assessment Report of the Intergovernmental Panel on Climate Change". Cambridge, United Kingdom and New York, NY, USA: Cambridge University Press. Chap. 3, 867—952.

Roman-Blanco, B. L. D. S., Coates, T. T., Holmes, P., Chadwick, A. J., Bradbury, A., Baldock, T. E., Pedrozo-Acuna, A., Lawrence, J., and Grüne, J. (2006). Large scale experiments on gravel and mixed beaches: experimental procedure, data documentation and initial results. *Coastal Engineering* 53, 349—362.

Rosati, J. D., Dean, R. G., and Walton, T. L. (2013). The modified Bruun Rule extended for landward transport. *Marine Geology* 340, 71—81.

Ruggiero, P., Holman, R. A., and Beach, R. A. (2004). Wave run-up on a high-energy dissipative beach. *Journal of Geophysical Research* 109.

Ruol, P., Zanuttigh, B., Martinelli, L., Kofoed, J. P., and Frigaard, P. (2011). Near-Shore Floating Wave Energy Converters: applications for coastal protection. *In J. M. Smith, & P. Lynett (Eds.), Coastal Engineering 2010: Proceedings of the 32nd International Conference on Coastal Engineering. Coastal Engineering Research Council*.

SCOR Working Group (1991). The response of beaches to sea-level changes: a review of predictive models. *Journal of Coastal Research* 7 (3), 895—921.

Sallenger, A. H. (2000). Storm impact scale for barrier islands. *Journal of Coastal Research* 16, 890—895.

Scott, T., Masselink, G., O'Hare, T., Davidson, M., and Russell, P. (2015). Multi-annual sand and gravel beach response to storms in the southwest of England. *Coastal Sediments 2015*.

Seymour, R. J., Bockstael, N. E., Campbell, T. J., Dean, R. G., Komar, P. D., Pilkey, O. H., Pratt, A. P., Snow, M. R., van Dolah, R. F., Weggel, J. R., and Wiegel, R. L. (1995). "Beach Nourishment and Protection". Washington, DC: The National Academies Press. Chap. 5, 107—126.

Short, A. D. (1979). Three dimensional beach stage model. *Journal of Geophysical Research* 87, 553—571.

Short, A. D. and Masselink, G. (1999). *Handbook of beach and shoreface morphodynamics*. Wiley.

Sneed, E. D. and Folk, R. L. (1958). Pebbles in the lower Colorado River, Texas, a study in particle morphogenesis. *Journal of Geology* 66, pp. 114–150.

Sorensen, J. (1997). National and international efforts at integrated coastal management: definitions, achievement, and lessons. *Coastal Management* 25, 3—41.

Stark, N. and Hay, A. E. (2016). Pebble and cobble transport on a steep, mega-tidal, mixed sand and gravel beach. *Marine Geology* 382, pp. 210–22.

Stockdon, H. F., Holman, R. A., Howd, P. A., and Sallenger, A. H. (2006). Empirical parameterization of setup, swash, and runup. *Coastal Engineering* 53, 573—588.

Storms, J. E. A., Weltje, G. J., Terra, G. J., Cattaneo, A., and Trincardi, F. (2008). Coastal dynamics under conditions of rapid sea-level rise: Late Pleistocene to Early Holocene evolution of barrier–lagoon systems on the northern Adriatic shelf (Italy). *Quaternary Science Reviews* 27 (11–12), pp. 1107–1123.

Swart, D. (1974). "Offshore Sediment Transport and Equilibrium Beach Profiles". PhD thesis. University of Technology, Delft.

Tomasicchio, G. R., D'Alessandro, F., and Musci, E. (2010). A multi-layer capping of a coastal area contaminated with materials dangerous to health. *Chemistry and Ecology* 26, 155—168.

Trueba, J. L. and Andrew, A. D. (2014). Rollover, drowning, and discontinuous retreat: Distinct modes of barrier response to sea-level rise arising from a simple morphodynamic model. *Journal of Geophysical Research: Earth Surface* 119 (4), pp. 779–801.

Turner, I. L., Russel, P. E., and Butt, T. (2008). Measurement of wave-by-wave bed-levels in the swash zone. *Coastal Engineering* 55, 1237—1242.

Van Rijn, L. C. (2010). *Modelling erosion of gravel/shingle beaches and barriers*. Tech. rep. D13b. European Commission, Conscience.

Van der Meer, J. W., Allsop, N. W. H., Bruce, T., Rouck, J. D., Kortenhaus, A., Pullen, T., Schüttrumpf, H., Troch, P., and Zanuttigh, B. (2018). *Eurotp 2018. Manual on wave overtopping of sea defences and related structures. An overtopping manual largely based on European research, but for worldwide applicatio*.

Voudoukas, M. I., Wziatek, D., and Almeida, L. P. (2012). Coastal vulnerability assessment based on video wave run-up observations at a mesotidal, steep-sloped beach. *Ocean Dynamics* 62, pp. 123–137.

Vousdoukas, M. I., Ranasinghe, R., and Mentaschi, L. (2020). Sandy coastlines under threat of erosion. *Nature Climate Change* 10, pp. 260–263.

Wadell, H. A. (1922). Volume, Shape and Roundness of Rock Particles. *The Journal of Geology* 40, pp. 443–451.

Wang, P. and Kraus, N. C. (2005). Beach profile equilibrium and patterns of wave decay and energy dissipation across the surf zone elucidated in a large-scale laboratory experiment. *Coastal Research* 21, 522—534.

Ward, D. L. and Ahrens, J. P. (1992). *Laboratory study of a dynamic berm revetment*. Tech. rep. US Army Corps of Engineers.

Watt, T. (2006). *Modelling the behaviour of shingle beaches: a review*. Tech. rep. University of Sussex.

Weiner, H. M., Kaminsky, G. M., Hacking, A., and McCandless, D. (2019). *North Cove Dynamic Revetment Monitoring: Winter 2018-2019*. Tech. rep. 19-06-008. Shorelands and Environmental Assistance Program, Washington State Department of Ecology.

Wentworth, C. K. (1919). A laboratory and field study of cobble abrasion. *The Journal of Geology* 27, pp. 507–521.

Wentworth, C. K. (1922). A scale of grade class terms for clastic sediments. *The Journal of Geology* 30, pp. 377–392.

Williams, A. T. and Caldwell, N. E. (1988). Particle size and shape in pebble-beach sedimentation. *Marine Geology* 82, 199—215.

Wright, L. D., Chappell, J., Thom, B. G., Bradshaw, M. P., and P.Cowell (1979). Morphodynamics of reflective and dissipative beach and inshore systems: Southeastern Australia. *Marine Geology* 32 (1), pp. 105–140.

Wright, L. D. and Short, A. D. (1984). Morphodynamic variability of surf zones and beaches: a synthesis. *Marine Geology* 56, 93—118.

Wright, L. D., Short, A. D., and Nielsen, P. (1982). *Morphodynamics of high energy beaches and surf zones: A brief synthesis.* Tech. rep. 82/5. Coastal Study Unit, University of Sydney.

Zanuttigh, B., Martinelli, L., Castagnetti, M., Ruol, P., Kofoed, J. P., and Frigaard, P. (2010). Integration of wave energy converters into coastal protection schemes. *3rd International Conference on Ocean Energy, Bilbao*.

Zingg, T. (1935). Beiträge zur Schotteranalyse. *Min. Petrog. Mitt. Schweiz.* 15, pp. 39–140.

van Enckevort, I. M. J. and Ruessink, B. G. (2003). Video observations of nearshore bar behaviour. Part 1: alongshore uniform variability. *Continental Shelf Research* 23 (5), 501—512.

van Gent, M. R. A. (2010). Dynamic cobble beaches as sea defence. *Proceedings of the Third International Conference on the Application of Physical Modelling to Port and Coastal Protection, Barcelona.*

van Hijum, E. and Pilarczyk, K. W. (1982). *Equilibrium Profile and Longshore Transport of Coarse Material Under Regular and Irregular Wave Attack*. Publication (Waterloopkundig Laboratorium (Delft, Netherlands)). Delft Hydraulics Laboratory.

van der Meer, J. W. (1988). "Rock slopes and gravel beaches under wave attack." PhD thesis. University of Technology, Delft.

van der Meer, J. W. and Janssen, J. P. F. M. (1994). *Wave run-up and wave overtopping at dikes and revetments*. Tech. rep. 485. Delft hydraulics.

van der Meer, J. W. and Pilarczyk, K. W. (1986). Dynamic Stability of Rock Slopes and Gravel Beaches. *Coastal Engineering* 125, 1713—1726.

van der Meer, J. W. and Stam, C. M. (1992). Wave runup on smooth and rock slopes of coastal structures. *Journal of Waterways, Port, Coastal, Ocean Engineering* 118, pp. 534–550.

Appendix A

Full description of the DynaRev experiment: "High-resolution, prototype-scale laboratory measurements of nearshore wave processes and morphological evolution of a sandy beach with and without a dynamic cobble berm revetment"

Appendix A.

This research article has been submitted to Scientific Data.

Chris E. Blenkinsopp, Paul M. Bayle, Daniel Conley, Gerd Masselink, Emily Gulson, Isabel Kelly, Rafael Almar, Ian L Turner, Tom E. Baldock, Tomas Beuzen, Robert McCall, Huub Rijper, Ad Reniers, Peter Troch, David Gallach-Sanchez, Oscar Bryan, Alan Hunter, Gwyn Hennessey, Peter Ganderton, Matthias Kudella, Stefan Schimmels (In review). High-resolution, prototype-scale laboratory measurements of nearshore wave processes and morphological evolution of a sandy beach with and without a dynamic cobble berm revetment. Scientific Data.

Abstract

High quality laboratory measurements of nearshore waves and morphology change at prototype-scale are essential to support new understanding of coastal processes and enable the development and validation of predictive models. The DynaRev experiment was completed at the GWK large wave flume over 8 weeks during 2017 to investigate the response of a sandy beach to water level rise and varying wave conditions with and without a dynamic cobble berm revetment. A large array of instrumentation was used throughout the experiment to capture: (1) wave transformation from intermediate water depths to the runup limit at high spatio-temporal resolution, (2) beach profile change including wave-by-wave changes in the swash zone, (3) detailed hydro and morphodynamic measurements around a developing and a translating sandbar.

Declaration concerning the article used for this Chapter:

Title	High-resolution, prototype-scale laboratory measurements of nearshore wave processes and morphological evolution of a sandy beach with and without a dynamic cobble berm revetment
Status	Submitted to Scientific Data
Details	Chris E. Blenkinsopp, Paul M. Bayle, Daniel Conley, Gerd Masselink, Emily Gulson, Isabel Kelly, Rafael Almar, Ian L Turner, Tom E. Baldock, Tomas Beuzen, Robert McCall, Huub Rijper, Ad Reniers, Peter Troch, David Gallach-Sanchez, Oscar Bryan, Alan Hunter, Gwyn Hennessey, Peter Ganderton, Matthias Kudella, Stefan Schimmels (In review). High-resolution, prototype-scale laboratory measurements of nearshore wave processes and morphological evolution of a sandy beach with and without a dynamic cobble berm revetment. Scientific Data.
Contribution from the authors	Chris E. Blenkinsopp: Design of the experiments/Collection/Processing/Analysis; Manuscript (45%) Paul M. Bayle: Design of the experiments/Collection/Processing; Help with the analysis; Edited drafts of manuscript (35%) Daniel Conley: Design of the experiments/Collection; Edited drafts of manuscript (10%) Gerd Masselink: Design of the experiments/Collection; Edited drafts of manuscript (5%) Emily Gulson, Isabel Kelly, , Rafael Almar, Ian L Turner, Tom E. Baldock, Tomas Beuzen, Robert McCall, Huub Rijper, Ad Reniers, Peter Troch, David Gallach-Sanchez, Oscar Bryan, Alan Hunter, Gwyn Hennessey, Peter Ganderton, Matthias Kudella, Stefan Schimmels: Collection (5%)
Statement	This paper reports on original research I conducted during the period of my Higher Degree by Research candidature.
Date and Signature	

Appendix A.

Preamble

This paper, written by Chris Blenkinsopp, reports on the complete DynaRev experiment. This experiment was prepared in collaboration with the University of Plymouth, but I was responsible for the complete design and procedure, coordination, management during the experiment and data processing. This is not included in the main thesis as it was not written by myself, and many aspect of the experiment are not related to the topic of this thesis.

A.1 Background and Summary

High quality field and numerical investigations are providing new insights into a wide variety of coastal processes and coastal protection solutions (*e.g.* Almeida et al., 2017; Briganti et al., 2018). However numerical modelling approaches are not yet capable of accurately reproducing all coastal hydro and morphodynamic phenomenon, and the difficulties involved in capturing field data in the desired wave, tide and wind conditions mean that laboratory wave flume experiments, where conditions and data collection can be closely controlled, remain extremely valuable. Large-scale experiments (*e.g.* Masselink et al., 2016; Eichentopf et al., 2020) are particularly valuable as they mostly avoid scaling issues, and improvements in the instrumentation and measurement techniques available mean that the quality and resolution of data continues to improve and provide new insights.

The DynaRev experiment was designed to investigate the response of a sand beach and the resilience of a dynamic cobble berm revetment to constant wave forcing and a rising water level at near prototype-scale in a controlled laboratory environment through high spatio-temporal resolution morphology measurements. A dynamic revetment is a nature-based coastal protection approach which consists of a cobble ridge constructed around the high tide runup limit to artificially mimic composite beaches (Allan and Komar, 2004). This commonly occurring beach type consists of a lower foreshore of sand and a backshore ridge constructed of gravel or cobbles that stabilises the upper beach and provides overtopping protection. Dynamic revetment structures contrast with static coastal defence structures as they are specifically designed to reshape under wave attack. In addition to the morphology data, high-resolution measurements of nearshore hydrodynamic processes were also collected.

DynaRev took place over a 2-month period from August to September 2017 in the Large Wave Flume (Groβer Wellenkanal, GWK), Hannover, Germany. A total of 141.6 hours of testing under wave action was completed. This testing comprised two "phases", with each phase being split into a series of "runs" varying from 20 minutes to 3 hours in duration.

Phase SB – Unmodified sand beach response to a rising water level: Starting with a plane slope, the evolution of the beach profile was measured under constant wave forcing (H_s = 0.8 m, T_p = 6.0 s). The mean water level in the flume was then raised by a total of 0.4 m in incremental steps of 0.1 m. Following the completion of the water level rise increments, the short-term response of the beach was measured for a range of different wave conditions expected to produce both erosion and accretion.

Phase DR – Dynamic cobble berm revetment response to a rising water level: Again starting with a plane slope, a sand beach was measured as it evolved under the same constant wave conditions as used in Phase SB for 20 hours to provide a natural beach profile on which to construct the dynamic revetment. The cobble revetment was installed at the location of the sand beach berm which developed prior to the first water level increment and was designed such that its crest height was at the elevation of the $R_{2\,\%}$ runup level for the second water level increment to ensure significant overtopping as the water level increased. The sand foreshore and dynamic revetment were then allowed to

Appendix A.

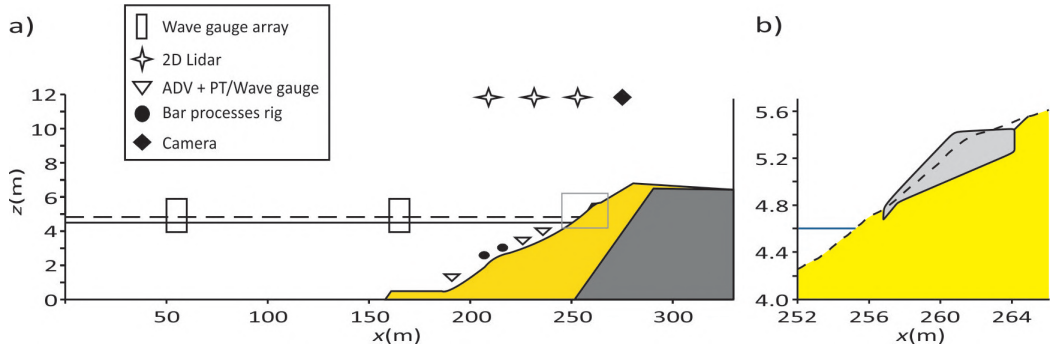

Figure A.1: (a) Schematic of flume setup showing primary locations (see Table 1). The yellow shaded area represents the sand volume and the dark grey shaded area is the permanent 1:6 impermeable slope. The black solid and dashed horizontal lines indicate the minimum (z_{wl} = 4.5 m) and maximum (z_{wl} = 4.9 m) water levels. (b) Close up of the dynamic cobble berm revetment geometry after construction corresponding to the grey box in (a). The light grey region indicates the dynamic revetment and the dashed line shows the beach profile prior to revetment construction.

reshape under constant wave conditions over the remaining water level increments, with the test durations at each water level mirroring those in Phase SB. Finally, higher energy storm waves were used at the end of the final water level increment to investigate revetment resilience to higher energy conditions.

The availability to researchers of prototype-scale measurements of nearshore hydro and morphodynamics at the spatio-temporal resolution achieved during DynaRev is very limited. Potential uses for the datasets obtained during the DynaRev test program are wide-ranging and include: the assessment of dynamic cobble berm revetment performance (Bayle et al., 2020), the investigation of nearshore processes such as the formation and dynamics of nearshore sandbars, the response of sandy coasts to a rising sea level, morphology change in the swash zone, wave-by-wave sediment transport rates, air entrainment in breaking waves (see Appendix B) and the development of numerical models (McCall et al., 2019).

A.2 Methods

A.2.1 Experimental Setup

The GWK large wave flume is 309 m long, 7 m deep and 5 m wide with a combined piston-flap type wavemaker. A schematic of the experimental setup is shown in Figure A.1. All coordinates are given as the distance from the wave paddle rest position (x = 0 m), elevation above the horizontal flume bed (z = 0 m) and across-flume distance from the centreline (y = 0 m). Both phases of the experiment used an initially planar sand beach with a gradient of 1:15 which was placed on top of a permanent 1:6 asphalt slope with a minimum sand depth of 3.1 m on the active part of the profile. The beach was constructed using 1660 m^3 of sand from the GWK facility's material store with characteristics D_{50} = 330 µm, D_{90} = 650 µm and D_{10} = 200 µm. A 25 m long layer of sand with a thickness of 0.5 m was installed in front of the slope in order to provide an additional supply of sediment. The toe of this layer was located at x = 161 m, the toe of the beach slope at x = 188.5 m and the top of the slope was at x = 283 m, z = 6.8 m.

After the first water level rise of Phase DR, a dynamic revetment structure was constructed on the modified sand beach profile. The revetment was composed of 9.375 m^3 (15 tonnes) of well sorted rounded granite cobbles with characteristics D_{max} = 90 mm, D_{min} = 50 mm, D_{50} = 63 mm, D_{85}/D_{15} = 1.32, bulk density = 1600 kg/m^3 and porosity = 0.41. The toe of the revetment was located at x = 256.8 m, z = 4.77 m, with a 1:6 slope leading to the crest at x = 260.7 m, z = 5.42 m. The revetment slope was selected based on the guidance of Powell (1993) for recharge of shingle beaches.

The top of the revetment extended horizontally from the crest until it intersected with the sand beach at x = 264.1 m, z = 5.4 m. Note that due to the slope of the modified sand profile approaching that of the designed revetment at the installation location, it was necessary to dig out 7.2 m^3 of sand to enable the designed cobble volume to be placed (see Figure A.1). A large suite of instruments was deployed during the experiment. All instruments were logged by PCs connected to a local area network with a shared timeserver to ensure time-synchronisation. Table 1 lists all instruments and their locations within the flume, and the primary instrument positions are shown in Figure A.1 (noting that some instruments were moved in response to water level increases and/or evolving beach morphology).

A.2.2 Wave measurements

The incident and reflected wave fields were measured offshore of the beach using a pair of combined resistance-capacitance wave gauge arrays, each comprising four gauges. The seaward gauges in each array were located at x = 50 m and x = 160 m, with spacings of 1.9 m, 3.3 m and 4.8 m between consecutive gauges. A further wave gauge was located at x = 180 m and was co-located with a Nortek Vector acoustic Doppler velocimeter (ADV) which was positioned to measure wave conditions at the toe of the sand beach slope.

Measurements of the time-varying water surface elevation throughout the surf and swash zones were obtained using an array of three SICK LMS511 2D Lidar instruments mounted in the flume roof at an elevation, z = 11.8 m and at cross-shore positions x = 230, 242 and 255 m. The sampling rate of all three scanners was 25 Hz with an angular resolution of 0.166°. The dense spacing of the Lidars in the array ensured complete coverage of the surf and swash zones (x = 221.4 m to x = 275.8 m) throughout the experiment, with at least 12 m of overlap between the scanning regions of adjacent instruments. The use of Lidar arrays to obtain wave data throughout the surf and swash zone was demonstrated by Martins et al. (2017a). Typically, Lidar requires bubbles to be present on the water surface to ensure that the incident laser light is scattered sufficiently to obtain a valid detection. During the experiment described here, it was found that the instruments performed better than during previous field deployments, with valid return signals even when levels of aeration were very low or in some cases, non-existent. It is thought that this was due to the presence of fine sediment in the water column whichcaused light to be scattered from the water surface. Example wave data obtained using the Lidar array is shown in Figure A.2.

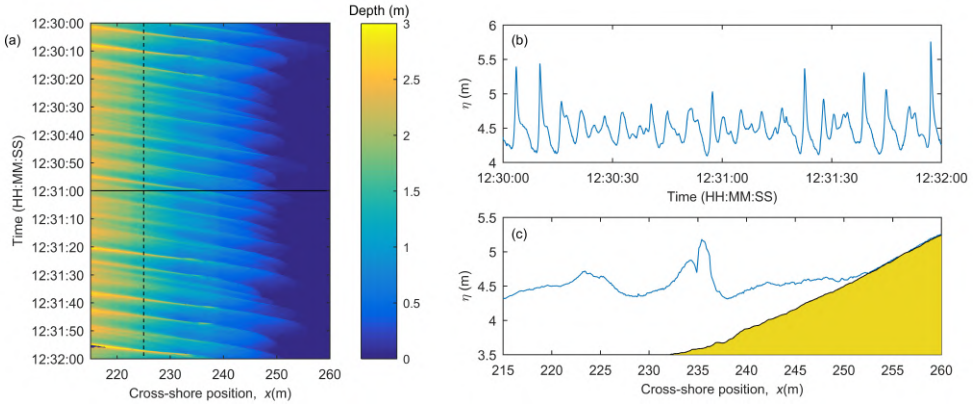

Figure A.2: Example wave measurements. (a) Timestack of depth measured by the Lidar throughout the surf and swash zones. (b) Timeseries of water surface elevation at $x = 225\,\text{m}$ as indicated by the vertical dashed line in (a). (c) Measured free- surface profile through the surf and swash zone at the time indicated by the horizontal solid line in (a). Note that the measurements capture the splash-up generated by a breaking wave at $x = 235.5\,\text{m}$.

A.2.3 Morphodynamic measurements

The emergent and submerged beach profile, between $x = 183\,\text{m}$ and $x = 270\,\text{m}$ was measured at the end of each run using a mechanical roller attached to the overhead trolley which ran along the centre of the flume. Figure A.3a shows an example profile measurement.

Additional measurements of the submerged beach profile were obtained using a Reson SeaBat 7125 multibeam echo-sounder. The echo-sounder was mounted on a vertical arm fixed to the overhead trolley of the mechanical profiler The receiver was oriented in the vertical plane and aligned centrally along the length of the flume. A range of different cross-shore locations, depths and angles were tested to optimise data collection leading to a primary deployment position of $x = 223.71\,\text{m}$, $z = 3.8\,\text{m}$ and an angle of 30 above the horizontal. The instrument has a 128° opening angle 0.54 beam divergence angle, operates at a frequency of $400\,kHz$ and was sampled at 1 ping per second. Note that the shallow depths and presence of bubble clouds during wave sequences make real-time detection of the changing bed difficult using conventional processing methods, however new algorithms which make use of the double acoustic reflection from the water surface to the bed and back to the receiver are being developed and will be reported in future works. The multibeam setup is described in greater detail in Appendix B.

Wave-by-wave measurements of the changing beach face profile were obtained using the landward-most Lidar located at $x = 255\,\text{m}$. Lidar detects the uppermost surface at each scan position within the swash zone – either swash surface (when submerged) or the emergent bed (between swash events) (Blenkinsopp et al., 2010b). By separating the "swash" and "bed" signals within the Lidar dataset using the variance-based approach of Almeida et al. (2015) (see Figure A.3b) it is possible to obtain the beach profile landward of the swash rundown position between every swash event (Figure A.3c).

Measurements of the entire three-dimensional bathymetry were obtained at irregular intervals when the flume was drained using a FARO Focus 3D terrestrial laser scanner. A total of 11 surveys of this type were completed throughout the duration of the experiment.

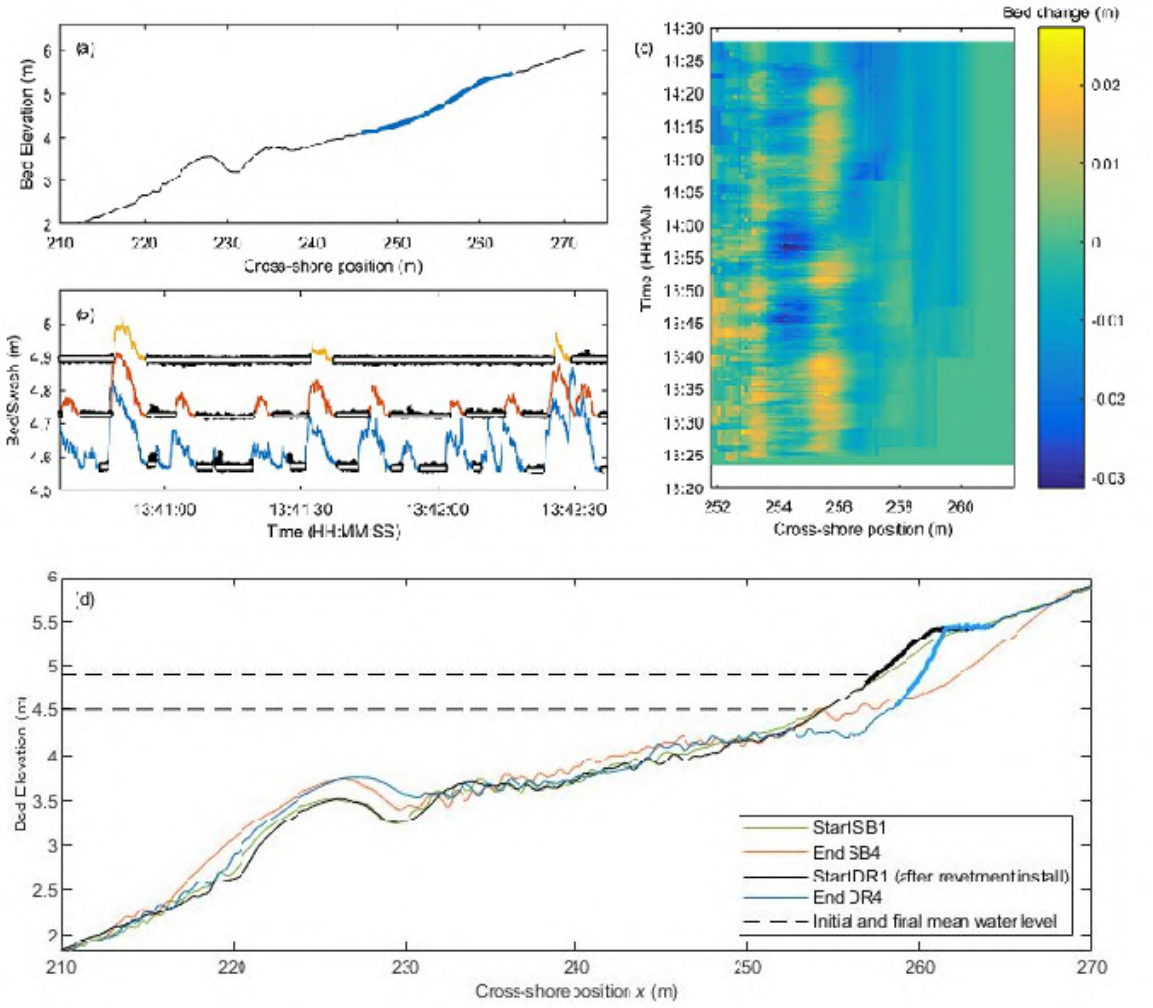

Figure A.3: Example morphology data. (a) An example beach profile as measured by the mechanical profiler (black) and the swash zone profile obtained from the Lidar data (blue). (b) Separation of bed (black dots) and swash data at x = 253.8 m (blue), x = 255.3 m (red) and x = 256.8 m (orange) for an example section of data. The mean bed elevation between each swash event is shown in white. (c) Bed elevation change relative to the initial profile in the swash zone at the wave-by-wave timescale. (d) Beach profile data showing the evolution of the sand beach and dynamic revetment modifed from (Bayle et al., 2020). The revetment surface is marked with a thicker line.

A.2.4 Surf Zone / Sandbar Measurements

Two measurement rigs were installed immediately landward and seaward of the predicted sandbar location and each housed an array of instrumentation designed to measure hydrodynamics, sediment transport and morphological change during bar formation and migration. The main instrument mounting bars for these rigs were located at x = 226.5 m and 233.5 m. Each of the measurement rigs was fixed to the walls on a mechanism such that they could be lifted and lowered manually to the bed after each run to ensure that all instruments remained a constant height above the evolving bed (see Table 1).

Each rig was equipped with the following instruments which were sampled at 25 Hz: 2 optical backscatter sensors (OBS) mounted at 5 and 10 cm from the bed, two electromagnetic current meters at elevations of 5 and 10 cm above the bed and a pressure transducer (PT) mounted 45 cm above the bed. Finally, a ripple profile scanner (RPS) was mounted 75 cm

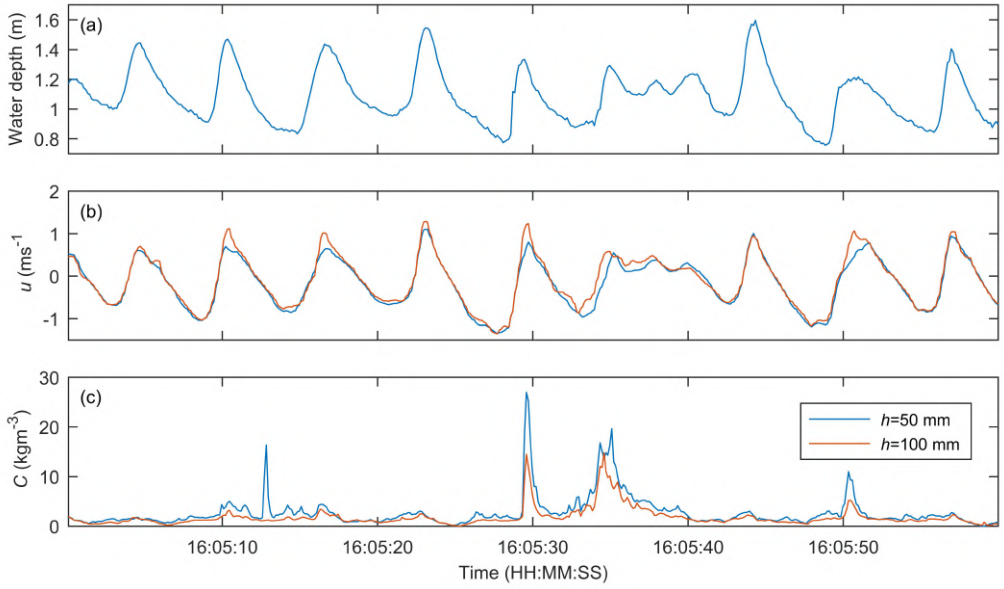

Figure A.4: Timeseries data from surf zone rig 1, $x = 226.5$ m. (a) Water depth derived from pressure transducer data, (b) cross-shore flow velocity measured 50 mm (blue) and 100 mm (red) above the bed using EMCMs, and (c) suspended sediment concentrations 50 mm (blue) and 100 mm (red) above the bed measured using OBS.

above the bed to obtain local bed profile measurements along a 0.9 m transect. The RPS on each rig was sampled alternately for one minute to avoid cross talk between instruments. In addition to the two rigs, two Nortek ADVs were located at $x = 235$ m and 242 m and maintained at a height 150 mm above the bed. Each ADV was co-located with a pressure transducer and an additional stand alone pressure transducer was installed at $x = 231.7$ m, $z = 4.13$ m.

Note that the two surf zone rigs described here were present for the entirety of Phase SB and the first 20 hours of the Phase DR testing. The instruments and scaffold rigs were removed during installation of the dynamic cobble berm revetment to avoid the risk of damage due to impact from stray cobbles from the revetment. Example post-processed data from the seaward surf zone rig is presented in Figure A.4.

A.2.5 Swash zone measurements

The swash zone was monitored by a high definition IP camera (Vivotek IB9381-HT) which was mounted in the flume roof at $z = 11.8$ m landward of the runup limit, facing the wave paddle. The cross-shore position of the camera varied with the water level. A series of ground control points (GCPs) were positioned within the camera field of view to enable generation of rectified timestack images. The position of these GCPs was surveyed using the FARO Focus 3D terrestrial laser scanner.]

The timestack images of swash flow are complimented by the data from the most landward Lidar which monitored flow depths and bed elevations within the swash zone. Separation of the "bed" and "swash" using the method of Almeida et al. (2015) as described above enables not only extraction of wave-by-wave bed elevations, but also estimates

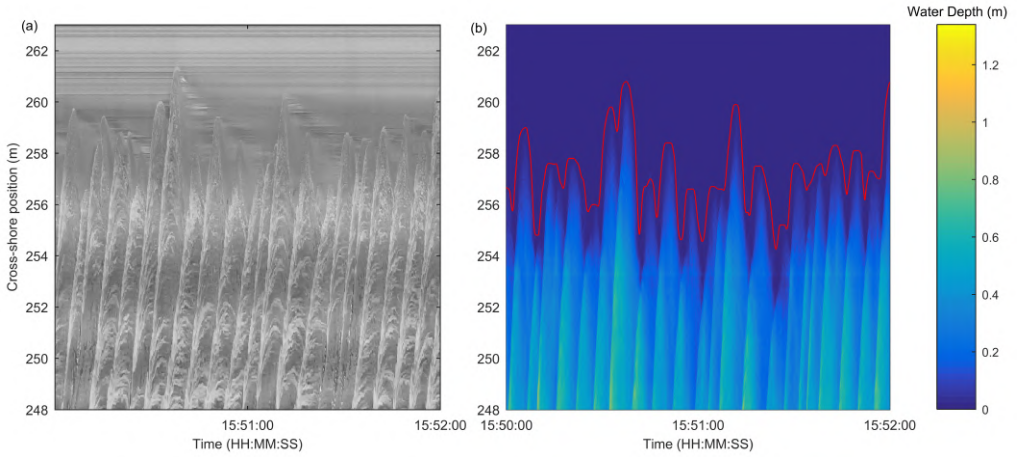

Figure A.5: Example swash data. (a) Video timestack extracted from the high definition video. (b) Timestack of water depth extracted from the Lidar data with the timeseries of shoreline position added in red

of the shoreline timeseries and depth-averaged flow velocity (Blenkinsopp et al., 2010b) and capture of the bore collapse process (Bergsma et al., 2019). Example swash zone measurements are presented in Figure A.5.

A.2.6 Instrumented Cobbles

The movement of individual cobbles within the dynamic revetment was monitored using an RFID tracking system similar to that used by Allan et al. (2006). The RFID system consists of three components: Passive Integrated Transponder (PIT) tags, the module reader and the antenna.

Texas Instruments TRPGR30ATGA PIT tags with a unique identification number and a detection range of 0.6 m were installed in 97 cobbles. The tags were placed inside holes drilled into the short axis of the cobbles and sealed using epoxy glue. Following PIT installation, the cobbles were washed, dried and painted in 3 different colours: 20 cobbles were painted pink and placed on the bottom layer of the revetment (at the sand interface) during its construction; 30 cobbles were painted orange and placed 20 cm above the bottom of the revetment (mid layer); 47 cobbles were painted green and placed at the toe and on the top layer of the revetment. All cobbles were placed along the centre line of the revetment in groups of 3 cobbles at 0.4 m cross-shore intervals. An additional 7 cobbles were initially placed at the revetment toe. Finally, the crest line of the revetment was painted yellow to enable modification of the crest by waves to be easily observed.

The RFID reader used here was a Texas Instrument Series 2000 RI-STU-251B which transmits a radio frequency of 130.2 kHz and was connected to a logging computer via an RS232 serial connection. A 120 dB beeper was used to provide an audible beep when a PIT was detected. A Texas Instrument Ri-ANT-G02E antenna was connected to the module reader. The antenna measured 20 cm by 20 cm and was attached to a telescopic pole (up to 5 m long) to allow cobble detection from the side of the flume, avoiding the need for the operator to walk on, and potentially damage the revetment. Instrumented cobble surveys were completed at the end of each water level increment and day of testing during

Phase DR by passing the antenna over the revetment surface in a systematic manner. The identification number and cross-shore position of each detected cobble was recorded for each survey.

A.2.7 Test Program

As noted above, the experiment was divided into two phases corresponding to sand beach (Phase SB) and dynamic revetment (Phase DR) testing. Within each phase, the profile was monitored as it evolved under wave forcing and increasing water level. Testing within each phase was undertaken at 5 different water levels (0.1 m increments), and at each water level the experiment was divided into "runs" of increasing duration as the rate of morphological change reduced (133 runs in total). An overview of the test program is provided in Table 2 and the details of all runs are listed in the dataset associated with this paper. The initial case for both phases was a 1:15 planar sand beach with a water level z_{wl} = 4.5 m.

A.2.7.1 Phase SB – Unmodified sand beach response

Starting with an initially planar slope, the beach was first allowed to evolve naturally under constant wave forcing (H_s = 0.8 m, T_p = 6.0 s). The mean water level in the flume was raised by a total of 0.4 m in steps of 0.1 m. Measurements were undertaken for a period of 20 and 17 hours for the first (z_{wl} = 4.5 m) and final (z_{wl} = 4.9 m) water levels, and for 7 hours at the intermediate levels. In total this testing was divided into 63 runs with durations ranging from 20 minutes to 3 hours. Run names for this phase are given as SB<WL increment>_<Run No.>, where water level (WL) increments are numbered 0 for the initial water level of 4.5 m to 4 for z_{wl} = 4.9 m and run numbering is started from 1 for each WL increment. Following the completion of the WL increments, "resilience testing" was completed to investigate the short-term response of the beach to a range of different wave conditions ("tests") expected to produce both erosion and accretion. This testing was undertaken at the highest water level (z_{wl} = 4.9 m). Each test was divided into 3 to 7 runs with durations ranging from 20 to 60 minutes. These runs were labelled SBE for erosive cases and SBA for cases expected to cause accretion, numbered according to test number and then run number, e.g. SBE1_3 for erosive test 1, run 3. Note that the beach profiles at the start of test SB1 and end of SB4 are shown in Figure A.3d.

A.2.7.2 Phase DR – Dynamic cobble berm response

Initially a 1:15 planar sand beach was reshaped naturally under constant wave conditions (H_s = 0.8 m, T_p = 6.0 m) for 20 hours, repeating the first WL increment of Phase SB (z_{WL} = 4.5 m) to provide a natural beach profile on which to construct the dynamic cobble berm revetment. The cobble revetment was installed at the location of the sand beach berm according to the configuration given in section 2.1. The revetment was designed such that it would be overtopped significantly as the water-level rose. The sand foreshore and dynamic revetment were then reshaped under constant wave conditions over the remaining water level increments with the test durations at each water level mirroring those in Phase SB. Run

Table 1: Primary instrument positions.

Abbrev.	Instrument	Purpose (measurement units)	*x* (m)	*z* (m)
WG1	Wave gauge	Water surface elevation in the deep flume section (m)	50	-
WG2	Wave gauge		51.9	-
WG3	Wave gauge		55.2	-
WG4	Wave gauge		60	-
WG5	Wave gauge	Water surface elevation in the deep flume section (m)	160	-
WG6	Wave gauge		161.9	-
WG7	Wave gauge		165.2	-
WG8	Wave gauge		170	-
ADV1	Nortek Vector	Flow velocity (ms^{-1}) – shoaling waves	180	2.5
ADV2	Nortek Vector	Flow velocity (ms^{-1}) – surf zone	235	3.67
ADV3	Nortek Vector		242	4.22
WGADV1	Wave gauge	Water surface elevation at ADV1 location (m)	180	2.5
PTADV2	Pressure transducer	Pressure at ADV2 location (kPa)	235	3.67
PTADV3	Pressure transducer	Pressure at ADV3 location (kPa)	242	4.05
PT3	Pressure transducer	Pressure (kPa) between the surf zone/ bar processes instrument rigs	231.7	*z* = 4.13 m
LID1	SICK LMS511 2D Lidar	High resolution water surface elevation (m) – surf zone	230.04	11.76
LID2	SICK LMS511 2D Lidar		242.02	11.85
LID3	SICK LMS511 2D Lidar	Swash surface elevation, Beach/revetment profile (m)	254.99	11.82
CAM	Vivotek IB9381-HT high resolution camera	Surf, Swash	272	11.8
MB	Reson 7125 Multibeam	Bubble cloud (dB)	Adjustable	Adjustable
FARO	FARO Focus 3D (Lidar)	3D topography (m)	Adjustable	Adjustable
RFID	Instrumented cobbles	Cobble movement	97 cobbles placed at 3 depths along the revetment centreline	
Surf Zone Instrumentation Rigs were reset to maintain constant instrument elevations above the bed at the start of every test, thus all elevations are presented in mm relative to the local bed and given the notation *h*.				
Abbrev.	**Instrument**	**Purpose (measurement units)**	***x* (m)**	***h* (mm)**
PT1	Pressure transducer	Pressure (kPa)	226.5	450 mm
OBS1	Optical backscatter sensor	Suspended sediment concentration (kg/m^3)		100 mm
OBS2	Optical backscatter sensor			50 mm
RPR1	Ripple Profiler	Bed profile (m)		760 mm
EM1	Valeport Electromagnetic Current Meter	Flow velocity (ms^{-1})		50 mm
EM2	Valeport Electromagnetic Current Meter			100 mm
PT2	Pressure transducer	Pressure (kPa)	233.5	450 mm
OBS3	Optical backscatter sensor	Suspended sediment concentration (kg/m^3)		100 mm
OBS4	Optical backscatter sensor			50 mm
RPR2	Ripple Profiler	Bed profile (m)		750 mm
EM3	Valeport Electromagnetic Current Meter	Flow velocity (ms^{-1})		110 mm
EM4	Valeport Electromagnetic Current Meter			55 mm

names for this phase are given as DR<WL increment>_<Run No.>, where WL increments and run numbers follow those for Phase SB. Note that the beach profiles immediately after revetment construction (start of DR1) and the end of test DR4 are shown in Figure A.3d.

Appendix A.

Table 2: Overview of the test program.

WL increment/Test	Duration (hr)	H_s (m)	T_p (s)	Water level z_{wl} (m)	Number of Runs	Run Durations (minutes)
Phase SB - Morphological response of a sandy beach with a rising water level						
SB0	20	0.8	6	4.5	14	20,20,20,30,30,60,60,60,120,120,120,180,180,180
SB1	7	0.8	6	4.6	9	20,20,20,30,30,60,60,60,60,60
SB2	7	0.8	6	4.7	7	20,40,60,60,60,60,120
SB3	7	0.8	6	4.8	7	20,40,60,60,60,60,120
SB4	17	0.8	6	4.9	11	20,40,60,60,60,60,120,120,120,180,180
Phase SB – Resilience testing at the maximum water level z_{wl} = 4.9 m						
SBE1	2	1	7	4.9	3	20,40,60
SBE2	4	1.2	8	4.9	5	20,40,60,60,60,60
SBA1	6	0.6	12	4.9	7	20,40,60,60,60,60,60
Phase DR – Morphological response of a sandy beach with a dynamic revetment to a rising water level						
DR0	20	0.8	6	4.5	14	20,20,20,30,30,60,60,60,120,120,120,180,180,180
Dynamic revetment installation						
DR1	7	0.8	6	4.6	9	20,20,20,30,30,60,60,60,120
DR2	7	0.8	6	4.7	7	20,40,60,60,60,60,120
DR3	7	0.8	6	4.8	7	20,40,60,60,60,60,120
DR4	17	0.8	6	4.9	11	20,40,60,60,60,60,120,120,120,180,180
Phase DR – Resilience testing at the maximum water level z_{wl} = 4.9 m						
DRE1	2	0.9	6	4.9	3	20,40,60
DRE2	2	1	7	4.9	4	20,20,20,60
DRE3	1	1	8	4.9	3	20,20,20
DRA1	2	0.8	6	4.9	2	60,60
Phase DR – Resilience testing with recharged revetment at the maximum water level z_{wl} = 4.9 m						
DRN1	2	0.8	6	4.9	2	60,60
DRN2	0.66	1.0	8	4.9	2	20,20
DRN3	2	0.8	6	4.9	2	60,60
DRN4	0.66	1.0	9	4.9	2	20,20
DRN5	0.33	1.2	8	4.9	1	20
DRN6	1	0.8	6	4.9	1	60

After completion of the WL increments, "resilience testing" of the revetment under varying wave conditions was undertaken at the highest water level, z_{wl} = 4.9 m. Each test was divided into 2 to 4 runs with durations ranging from 20 to 60 minutes. These runs were labelled DRE for erosive cases and DRA for cases expected to cause accretion, and numbered as per the Phase SB resilience tests.

Finally, to investigate the effect of recharging the revetment, 2.5 m^3 of additional cobbles, corresponding to a 0.2 m thick layer were placed on the front face of the revetment. Following this recharge, the response of the revetment to a range of different high energy, erosive wave cases was measured. These runs were labelled DRN and numbered using the same notation as the resilience tests.

A.2.8 Wave Conditions

Wave paddle steering signals were generated according to the JONSWAP spectrum (using a peak enhancement coefficient of 3.3) specified using significant wave height, H_s and peak wave period T_p. For Phases SB and DR constant wave forcing was applied, $H_s = 0\,\text{m}$ and $T_p = 6\,\text{s}$. This wave condition was chosen to be mildly erosive based on experience at the BARDEX2 experiment, which had a similar setup (Masselink et al., 2016) and according to the criteria of Hattori and Kawamata (1980) based on dimensionless fall velocity. For each of the five water levels used, a two-hour long wave paddle signal was generated to produce an identical timeseries of waves at the wave paddle, taking water depth into account. These two-hour signals were segmented to account for the durations of the runs (20, 30, 40, 60, 120 and 180 minutes) to allow the same two-hour signal to be repeated multiple times at each WL increment with interruptions for beach profiling. Reflected waves as well as low frequency resonance were damped at the paddle using an automatic reflection compensation.

For the resilience testing, erosive and accretionary wave conditions were specified primarily based on the dimensionless fall velocity according to the criteria of Hattori and Kawamata (1980), Dean (1973), and Dalrymple and Thompson (1976). The erosive cases were ordered such that the wave energy and wave runup increased with each consecutive run.

A.3 Data Records

The data detailed in this paper is available for download from DOI 10.5281/zenodo.3889796. Additional metadata is provided within each $*.mat$ file detailing how the data from each instrument is stored. Note also that all raw, unprocessed data is available at DOI 10.5281/zenodo.3855650.

A.4 Technical Validation

All data was collected using well-established coastal field and/or laboratory techniques using commercially available instrumentation. Post-processing has been undertaken to remove outliers and convert spatial data to the x, y, z coordinate system defined above.

All wave gauges were calibrated at regular intervals throughout the experiment using a standard procedure. For each calibration, the water level was lowered from 5 m to 0.5 m in increments of 0.3 m and the voltage from all wave gauges at each water level was recorded for 180 s to create a calibration function relating water level to voltage.

The exact location and orientation of the Lidar array was confirmed through comparison with the mechanical beach profiler data when no waves were running (see Table 3). A RMSE smaller than 0.014 m was obtained. The time-varying free surface elevations obtained from the Lidar data were compared with point measurements from pressure transducers PT1, PT2 and PT3 and wave gauge WGADV1. For all runs the signals matched closely with zero lag. All optical backscatter sensors were calibrated after the experiment by applying the method of Betteridge et al. (2007) using sand from DynaRev in a specially

Table 3: Data files associated with the DynaRev experiment available from DOI 10.5281/zenodo.3889796.

Filename	Data description	Instruments (ref. Table 1)
DynaRev_TestProgram.xlsx	Complete list of test cases	-
DynaRev_Profiles.mat	Beach profiles measured after each run	Mechanical profiler
DynaRev_Paddle_Files.zip	Wave paddle driver files in ascii format	Wave paddle
DynaRev_DAQ.mat	Timeseries data collected by the central data acquisition system	WG1 to 8, WGADV1 ADV1, ADV2, ADV3 PTADV2, PTADV3 Measured wave paddle stroke
DynaRev_SurfZone.mat	Timeseries data from the surf zone rigs	PT1, PT2, PT3 OBS1 to OBS 4 EM1 to EM4
DynaRev_Lidar_<Phase><WL increment>-<Run No.>.mat	Timeseries x, z data from the combined Lidar array in .mat format. The data for each run is stored in a separate file, e.g. "DynaRev_Lidar_SB1-5.mat" contains the data for Phase SB, WL 1 (z_w = 4.6 m), Run 1.	LID1, LID2, LID3
DynaRev_TimeStack.mat	Image timestack of swash zone	CAM
DynaRev_RFID.xlsx	Table containing instrumented cobble positions	RFID
DynaRev_3Dscans.zip	Point cloud data from 11 3D Lidar scans of the morphology in ".xyz" format	FARO
DynaRev_Lib	Scripts for post-processing raw instrument data	

constructed sediment tower at the University of Plymouth.

A.5 Code Availability

All code provided in DynaRev_Lib is written in MATLAB (R2019b). This folder contains the scripts used to process the raw data in order to obtain the post-processed data provided within the repository.

The 3D Lidar point clouds described in Table 3 are provided in ".xyz" format which can be opened using the open source CloudCompare software package. The filename for each scan includes the date collected and the run after which the scan was completed, *e.g.*, 20170918_DR2_7.xyz was completed after Run DR2-7 on 18^{th} September, 2017. A table providing the timings and notes about each scan is included within the DynaRev_3Dscans data record.

References

Allan, J. C., Hart, R., and Tranquili, J. V. (2006). The use of Passive Integrated Transponder (PIT) tags to trace cobble transport in a mixed sand-and-gravel beach on the high-energy Oregon coast, USA. *Marine Geology* 232.

Allan, J. C. and Komar, P. (2004). Environmentally compatible berm and artificial dune for shore protection. *Shore and Beach* 721, 9—16.

Almeida, L. P., Masselink, G., McCall, R., and Russell, P. E. (2017). Storm overwash of a gravel barrier: Field measurements and XBeach-G modelling. *Coastal Engineering* 120.

Almeida, L. P., Masselink, G., Russel, P. E., and Davidson, M. A. (2015). Observations of gravel beach dynamics during high energy wave conditions using a laser scanner. *Geomorphology* 228, 15—27.

Bayle, P. M., Blenkinsopp, C. E., Conley, D., Masselink, G., Beuzen, T., and Almar, R. (2020). Performance Of A Dynamic Cobble Berm Revetment for Coastal Protection, under increasing water level. *Coastal Engineering* 159.

Bergsma, E. W. J., Blenkinsopp, C. E., Martins, K., Almar, R., and Almeida, L. P. M. de (2019). Bore collapse and wave run-up on a sandy beach. *Continental Shelf Research* 174, 132—139.

Betteridge, K. E. F., Thorne, P. D., and Cooke, R. D. (2007). Calibrating multi-frequency acoustic backscatter systems for studying near-bed suspended sediment transport processes. *Continental Shelf Resources* 28, pp. 227–235.

Blenkinsopp, C. E., Turner, I. L., Masselink, G., and Russell, P. E. (2010b). Validation of volume continuity method for estimation of cross-shore swash flow velocity. *Coastal Engineering* 57, pp. 953–958.

Briganti, R., Dodd, N., Incelli, G., and Kikkert, G. (2018). Numerical modelling of the flow and bed evolution of a single bore-driven swash event on a coarse sand beach. *Coastal Engineering* 142.

Dalrymple, R. A. and Thompson, W. (1976). Study of equilibrium beach profiles. *Proceedings of the* 15^{th} *International Conference on Coastal Engineering*, pp. 1277–1296.

Dean, R. G. (1973). Heuristic model of sand transport in the surf zone. *Proceedings of engineering dynamics in the surf zone, Institute of Engineers, Australia*.

Eichentopf, S., van der Zanden, J., Caceres, I., and Baldock, T. E. (2020). Influence of storm sequencing on breaker bar and shoreline evolution in large-scale experiments. *Coastal Engineering* 157.

Hattori, M. and Kawamata, R. (1980). Onshore–offshore transport and beach profile change. *Proceedings of the* 17^{th} *International Conference on Coastal Engineering*, pp. 1175–1193.

Martins, K., Blenkinsopp, C., Power, H. E., Bruder, B., Puleo, J. A., and Bergsma, E. (2017a). High-resolution monitoring of wave transformation in the surf zone using a LiDAR scanner array. *Coastal Engineering* 128, 37—43.

Masselink, G., Ruju, A., Conley, D., Turner, I., Ruessink, G., Matias, A., Thompson, C., Castelle, B., Puleo, J., Citerone, V., and Wolters, G. (2016). Large-scale Barrier Dynamics

Experiment II (BARDEX II): Experimental design, instrumentation, test program, and data set. *Coastal Engineering* 113, pp. 3–18.

McCall, R., Rijper, H., and Blenkinsopp, C. (2019). Towards the development of a morphological model for composite sand-gravel beaches. *Coastal Sediment 2019*, pp. 1889–1900.

Powell, K. A. (1993). *Dissimilar Sediments: Model tests of replenished beaches using widely graded sediments*. Tech. rep. SR 250. HR Wallingford.

Appendix B

Published material not used for the thesis: "Breaking Wave Imaging using Lidar and Sonar"

Appendix B.

This research article has been published in IEEE Journal of Oceanic Engineering, and the accepted pre-print manuscript is used here.

Oscar Bryan, Paul M. Bayle, Christopher E. Blenkinsopp, and Alan J. Hunter (2019). Breaking Wave Imaging using Lidar and Sonar, IEEE Journal of Oceanic Engineering.
doi: 10.1109/JOE.2019.2900967.

Abstract

The two-phase flow generated from breaking ocean waves plays a crucial role in various geophysical processes, including dissipation of wave energy and atmospheric gas exchange.This paper presents a technique to measure the two-phase flow generated by breaking waves at prototype scale. We have demonstrated the validity and potential of this technique in the Large Wave Flume (Grosser Wellenkanal, GWK) facility in Hanover, Germany. Actively breaking, depth-limited waves were measured using an array of three downward-looking lidars mounted above the water surface and an upward-looking multibeam sonar below. This novel setup enabled the characterisation of the complete upper boundary (free water surface and splash-up) and seaward lower boundary (entrained cavity and bubble plume) of the breaking wave. We have quantified the migration of the lower boundary as the cavity and plume are entrained in the water column – penetrating towards the seabed, moving onshore with the passage of the wave crest, and then rising as it is slowly advected offshore. We have also estimated the overall composition of the splash, cavity, and plume as the breaking wave evolves over time. Our observations are consistent with results from previous small-scale laboratory experiments and the suitability of the technique for experimentation at prototype scale has been demonstrated.

Declaration concerning the article used for this Chapter:

Title	Breaking Wave Imaging using Lidar and Sonar
Status	Published in IEEE Journal of Oceanic Engineering
Details	Oscar Bryan, Paul M. Bayle, Christopher E. Blenkinsopp, and Alan J. Hunter (2019). Breaking Wave Imaging using Lidar and Sonar, IEEE Journal of Oceanic Engineering. doi: 10.1109/JOE.2019.2900967
Contribution from the authors	O. Bryan: Collection/Processing/Analysis of the data (30%) P. M. Bayle: Design of the experiments; Collection/Processing/Analysis of data; Edited drafts of manuscript (30%) C. E. Blenkinsopp: Analysis of the data; Manuscript (20%) A. J. Hunter: Analysis of the data; Manuscript (20%)
Statement	This paper reports on original research I conducted during the period of my Higher Degree by Research candidature.
Date and Signature	

Appendix B.

Preamble

The data presented in this paper were collected during the DynaRev large scale experiment, presented in Appendix A. The analysis uses the Lidar and bathymetry (profiler) datasets from the DynaRev experiment. In addition, but not presented in the Scientific Data paper, a series of multibeam sonar data are used. This dataset was also collected during the DynaRev experiment, however, due the the complexity and specificity of this dataset, it was decided not to include it in the general data report/paper.

I was responsible for the design of the DynaRev experiment, therefore I planned the sonar measurement and conducted the survey. The data extraction was mainly done by Oscar Bryan, but I then took the lead for the data processing during the second year of my PhD.

The paper aims at measuring a breaking using a lidar and a sonar, in order to get an underwater and free surface measurement to better understand the envelop and shape of a breaking wave and associated bubble plume.

B.1 Introduction

Breaking in shallow water is a phenomenon that has long been a subject of fascination within both the scientific and non-scientific communities. Wave breaking on beaches leads to dissipation of incident wave energy and is a driver for a range of nearshore processes including sediment suspension and transport, nearshore circulation, bar formation and wave runup (textite.g., Aagaard and Greenwood, 1995; Bonneton et al., 2010; Hoefel and Elgar, 2003; Stockdon et al., 2006). Upon breaking, the wave overturns generating a splash-up and entraining a plume of air bubbles. Thus, after wave breaking there exists a continuum of time-dependent void fractions α, bounded by the upper surface of the splash where $\alpha \to 1$ and the lower boundary of the evolving bubble plume where $\alpha \to 0$.

In plunging breaking waves, which are common on intermediate to dissipative beaches (Battjes, 1974), a jet is formed as the wave overturns and encloses a cavity of air (commonly called a breaking wave vortex, *e.g.*, Mead and Black, 2001; Blenkinsopp and Chaplin, 2008; Robertson, 2013) between the underside of the jet and the front face of the wave. After the overturning jet strikes the surface water ahead of the wave at the "plunge point" (*e.g.*, Longuet-Higgins and Cokelet, 1976), air is entrained into the water column beneath the surface water due to two primary mechanisms (Deane and Stokes, 2002): 1) formation of larger bubbles (diameter $D > 2\,\text{mm}$) by the fragmentation of the air cavity or "vortex" (Deane and Stokes, 2002); and 2) entrainment of smaller bubbles by the impact and subsequent splashing of the overturning jet and in the shear layer between the jet and the water in the preceding trough (Deane and Stokes, 1999). Once entrained, the bubbles form a plume which is driven rapidly down into the water column after which it disperses as bubbles are advected by turbulence and wave-generated currents, and rise back to the surface (de Leeuw and Leifer, 2002).

Entrainment of air by breaking waves has been shown to influence physical processes, including air-sea transfer of gases (Melville, 1996), generation of sea-surface sound (Deane, 1997) , and the production of the sea-salt aerosol Blanchard, 1963. As a consequence, many researchers have investigated the aerated regions generated by breaking waves in both the laboratory and the field. In the field, the majority of quantitative measurements have been confined to bubble clouds in the open ocean which were defined by Deane (2016) as the remnants of the high air fraction plumes that are generated during active wave breaking. These field measurements have primarily focussed on the measurement of bubble size distributions (*e.g.*, Medwin, 1970; Deane, 1997; Czerski et al., 2011) or void fractions (*e.g.*, Vagle and Farmer, 1998; Al-Lashi et al., 2016) using acoustic or optical methods. Investigation of active bubble plumes during and directly after breaking waves is less common as such plumes are acoustically and optically opaque, and the location of breaking waves in the field is highly variable, making it difficult to locate an instrument to adequately capture the entrainment and subsequent evolution of the bubble plume.

Obtaining high-quality measurements of the production and evolution of the bubble plumes beneath actively breaking waves is important for our understanding of the wave breaking process and the process of air entrainment (Kiger and Duncan, 2012). Bubble

plume entrainment has been shown to contribute significantly to the energy dissipated during wave breaking (Lamarre and Melville, 1991), active bubble plumes are thought to contribute to air-sea gas transfer (Melville, 1996) and such data is needed for the validation of multiphase models of wave breaking (*e.g.*, "A polydisperse two-fluid model for surf zone bubble simulation").

Smith (2005, 2014) used an upward-looking multibeam system in deep water breaking waves and found that it was possible to acoustically image the underside of the bubble plumes generated by actively breaking wave crests. In the nearshore, Deane and Stokes (1999) and Stokes and Deane (1999) took a specially designed optical system into the surf zone of a natural beach to examine bubble formation mechanisms and measure bubble size distributions during the early moments of breaker generated plumes. As with breaking wave geometry, the majority of investigations of breaker generated plume measurements have been undertaken in the laboratory using conductivity-based sensors (*e.g.*, Lamarre and Melville, 1991; Cox and Shin, 2003), optical methods (*e.g.*, Leifer et al., 2003) and optical fibre probes (*e.g.*, Serdula and Loewen, 1998; Blenkinsopp and Chaplin, 2007, 2010). In particular Lamarre and Melville (1991) and Blenkinsopp and Chaplin (2007) investigated bulk characteristics of breaker generated bubble plumes in small-scale laboratory wave flumes including the time-variation of bubble plume depth, horizontal position and volume.

Due to the short duration of the breaking process and the highly variable location of the break point on natural beaches, quantitative measurements of the water surface during breaking have been obtained almost exclusively at small-scale in laboratory wave flumes using video imagery obtained through the flume wall. These studies have primarily investigated the nature of wave breaking (*e.g.*, Galvin, 1968), the breaking wave vortex geometry (*e.g.*, Blenkinsopp and Chaplin, 2008; Robertson, 2013) or other geometrical properties of breaking waves such as the plunge and splash distances (*e.g.*, Galvin, 1969; Smith and Kraus, 1991). In additional to video-based studies, recent work by Smith and Kraus (2016) has examined the potential for X-ray methods to capture the evolving shape of very small-scale overturning waves and wave breaking has also been studied using numerical methods (*e.g.*, Landrini et al., 2007; Zheng et al., 2009). While multiple researchers have investigated the potential to determine wave heights in the field from oblique, shore-based video imagery, quantitative measurements of the water surface in the field at a resolution suitable for investigating the changing shape of waves during the breaking process have only recently been made possible thanks to the development of LiDAR (Light Detection And Ranging) technology for the measurement of water surface elevation. Martins et al. (2017a) deployed an array of three lidars along a shore-perpendicular pier and obtained measurements of the water surface elevation as it varied in time at a spatial resolution of centimetres from the break point to the runup limit at a sandy beach in North East England. It should be highlighted that while this approach provides detailed measurements of the changing wave geometry, the lidars are only able to capture the upper surface of the overturning jet and subsequent splashes generated by breaking waves.

The splash generated by a breaking wave is perhaps the most impressive visual aspect

Figure B.1: Waves breaking in the GWK flume.

of waves breaking on our coastlines, often reaching heights greater than that of the incident wave. These splashes contribute to energy dissipation (Blenkinsopp and Chaplin, 2007) and bubble entrainment (Jansen, 1986), and are a significant feature of breaking waves that must be reproduced in computational models of the breaking process. Despite this, there have been few investigations and even fewer measurements of the splash process to date meaning that current understanding is limited. Peregrine (1981) presented a simple one-dimensional model of the splash-up process. Several laboratory experiments (*e.g.*, Miller, 1976; Jansen, 1986; Nadaoka, 1986; Nadaoka et al., 1989; Bonmarin, 1989; Tallent et al., 1990) have used video imagery to capture the splash generated by small-scale breaking waves and demonstrated that upon falling back to the water surface, the initial splash-up generated by the overturning motion pushes up a smaller secondary splash-up. This secondary splash-up is projected forward before falling back to the water surface where it creates strong vortex-like motions and generates another, smaller jet-splash cycle. This process has also been observed in the results of numerical models of the wave breaking process (*e.g.*, Landrini et al., 2007), and Jansen (1986) showed that as many as eight of these jet-splash cycles may occur before the organised motion completely breaks down. In their study of void fractions both above and below the water surface of small-scale depth-limited breakers, Blenkinsopp and Chaplin (2007) measured the temporal evolution of breaker generated splash-up characteristics including splash volume and found that the splash process accounted for at least 2.5 to 5 % of the energy dissipated during breaking in their test cases. To the authors' knowledge, quantitative data on breaker generated splashes at field scale is currently lacking.

This study presents a novel technique that allows measurements of the upper and lower envelope of the rapidly evolving two-phase flow generated by actively breaking depth-limited waves obtained in prototype-scale breaking waves in a large-scale laboratory wave flume. Novel data are obtained via a combined approach to image the upper surface of the splash using an array of downward-looking LiDAR (Light Detection And Ranging)

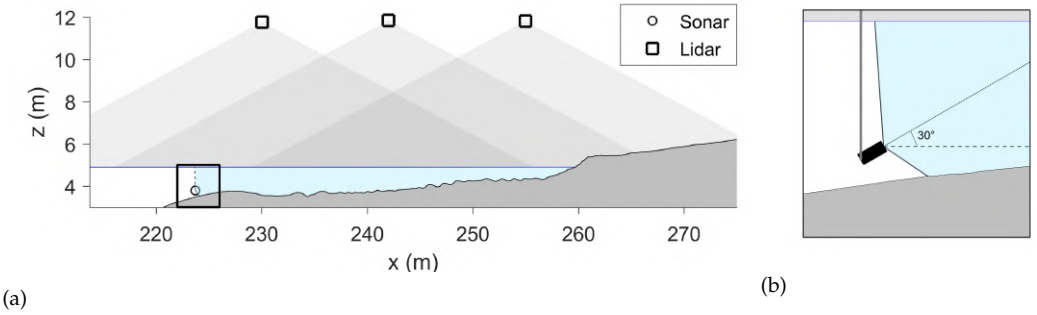

Figure B.2: Laboratory and equipment setup, showing: (a) sonar and lidar positions within the flume; and (b) a close-up of the sonar configuration.

instruments suspended above the water surface synchronised with measurements of the lower/seaward surface of the evolving bubble plume obtained using an upward-looking multibeam SoNAR (Sound Navigation And Ranging) instrument.

B.2 Methodology

B.2.1 Experimental Facility and Instrumentation

B.2.1.1 Wave Flume

The data presented in this paper was collected as part of the larger DynaRev experiment which was completed to investigate natural and engineered coastlines in a rising sea-level. The experiment took place in the Large Wave Flume (Groβer Wellenkanal, GWK) in Hannover, Germany, during August and September 2017. The flume measures 309 m long, 5 m wide and 7 m deep Lopez De San Roman-Blanco et al., 2006 and is shown in Figure B.1. A sandy beach with a median grain size of diameter $D_{50} = 0.33\,mm$ was installed with an initial plane slope of 1:15. This initially planar slope was reshaped by wave action to form a barred profile. The coordinate system was defined as follows: the vertical elevation, z is defined positive upwards from the base of the flume; the cross-shore coordinate system has its origin at the wave paddle and is positive in the direction of the beach. A combined piston-flap-type wave paddle was used to generate irregular waves with a significant wave height $H_s = 0.8$ m at the wave paddle and peak period, $T_p = 6$ s. The water depth was 4.9 m. The individual wave analysed in Section III corresponds to the first wave of a test run and thus propagated and broke in unaerated water. The breaker height, H_b was approximately 1.1 m and it is assumed that the waves measured in the flume are homogeneous in the cross-flume direction. It is noted that a small wave caused by the ramping up of the wave paddle breaks prior to the arrival of the wave of interest and generates a small bubble plume with its seaward boundary at $x = 234$ m. However this plume is landward of the seaward boundary of the bubble plume analysed below and is not expected to influence the results presented.

(a)

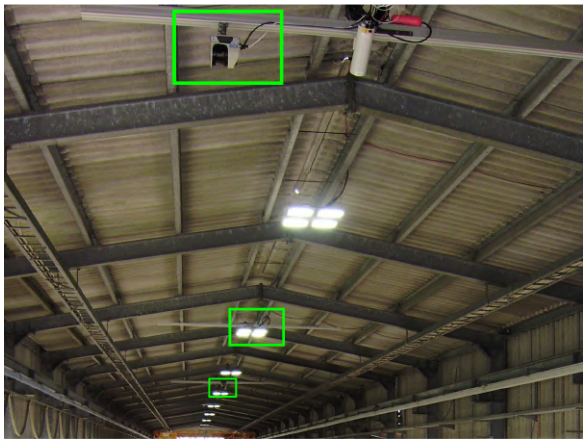

(b)

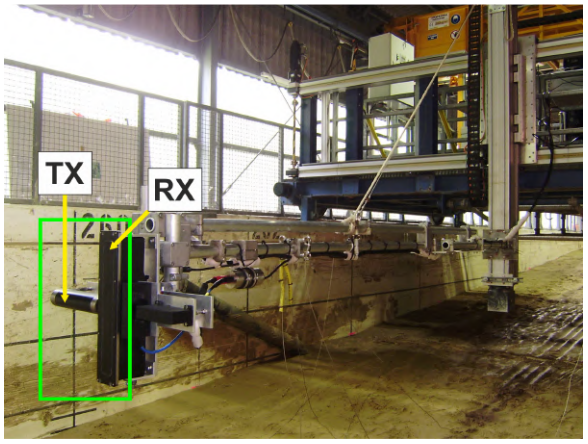

(c)

Figure B.3: Instrumentation: (a) trolley and mechanical profiler; (b) fixed roof deployment of the three SICK lidars; and (c) adjustable pole mounting of the Reson Seabat 7125 multibeam sonar from the trolley, with the transmitter (TX) and receiver array (RX) indicated. Note that the pole is shown in its horizontal position for mounting / adjusting the sonar and was lowered to its vertical position for the measurements.

B.2.1.2 Mechanical Profiler

A mechanical profiler was used to measure the sandy beach profile. The profiler consists of a mechanical roller attached to an overhead trolley which runs along a gantry on the flume

side walls, as shown in Figure B.3a. The system enables measurements of the complete bed profile to approximately $1-2$ cm vertical accuracy.

B.2.1.3 Lidars

An array of three SICK LMS 511 lidar scanners was used to measure the time-varying water surface elevation along an 80 m transect on the flume centreline. All three lidars were sampled by a single computer at a scan rate of 25 Hz and angular resolution of 0.166 deg. However, the data from the lidars were downsampled to 10 Hz to match the sonar scan rate. Each lidar is capable of obtaining measurements within a 190 degree field of view, though here we consider only the central 150 degrees within which valid water surface measurements were obtained. The lidars were mounted to the flume roof at $z = 11.80$ m, (6.9 m above the still water line) at cross-shore locations $x = 230$ m, $x = 242$ m and $x = 255$ m and looked vertically down. The installed lidar array is shown in Figure B.3b and illustrated in Figure B.2a. Note that when used to measure breaking and broken waves in the setup described here, the lidar instruments detect the upper boundary of the water/splash/air-water mixture.

B.2.1.4 Sonar

A Reson SeaBat 7125 multibeam echo-sounder was used to image the underwater bubble plumes generated by the breaking waves. This instrument operates at a frequency of 400 *mathrmkHz*. It has an opening angle of 128° and a 0.54° beam divergence angle. Operating parameters were tuned in baseline still water conditions (*c.f.*, Figure B.4) to maximise data quality; this lead to a transmitter power of 195 dB, receiver gain of 44 dB, a frame rate of 10 pings/s, and a corresponding maximum range of 25 m. The frame rate was selected by qualitatively optimizing the trade-off between reverberation noise and temporal resolution. The acoustic intensity levels were not calibrated for this device and, therefore, only the relative measurements are considered in this work. The instrument was mounted on a vertical arm fixed to the overhead trolley of the mechanical profiler. The receiver was oriented in the vertical plane and aligned centrally along the length of the flume (the instruments are shown in Figure B.3c). The cross-shore location was adjusted by moving the trolley along the flume walls and the deployment depth and orientation angle were also adjustable. A range of different cross-shore locations, depths, and angles were tested to optimise observability of the plume. A final deployment angle of 30 deg above horizontal looking towards the beach was selected so that the opening angle would cover the seaward edge of the breaker generated plumes (Figure B.2b). For the data presented in this paper, the instrument was positioned at $x = 223.7$ m across-shore, $y = 0$ m along-shore (on the flume centreline), and $z = 3.8$ m in elevation, as illustrated in Figure B.2a. Note that when used to measure breaking and broken waves in the setup described here, the sonar detects the pre-breaking water surface and the lower-seaward boundary of the evolving bubble plume.

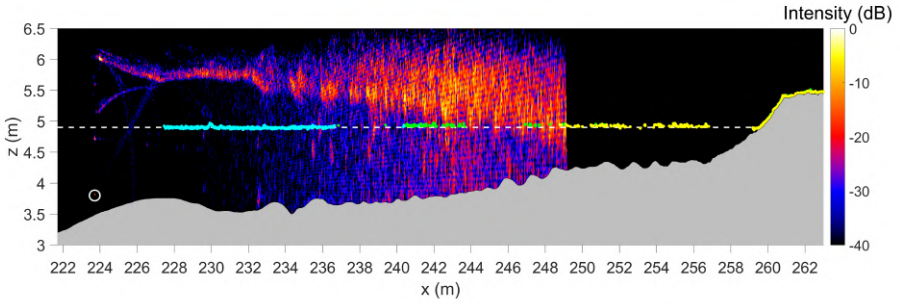

Figure B.4: Baseline lidar and sonar measurements during still water conditions. The water surface measurements from each lidar are shown in green, cyan and yellow for the seaward, middle and landward lidars respectively. Sonar backscatter intensity is plotted on a 1 cm grid and is represented by the colourmap. The still water level (z = 4.9 m) is represented by the dashed white line. The sonar position is shown by the white circle. The sand bottom measured by the mechanical profiler is represented by the grey region.

B.2.2 Data Processing

B.2.2.1 Synchronisation and co-registration

During the experiment, all data collection computers were time-synchronised over a local area network to a common time server. In order to correctly align the lidar data from all three instruments, the exact position and orientation of each lidar was established by measuring fixed targets at known locations within the flume. The position and orientation of the sonar was established by measuring the horizontal and vertical offset from the known gantry position. The temporal and spatial synchronisation of data from the lidar array and sonar was confirmed visually by observing animations of the data from multiple waves passing through the measurement region. The maximum synchronisation error is expected to be half a time-step at the sonar scan rate, *i.e.*, $\leq 50\,mathrmms$. Sonar data corresponding to the region above the water surface were removed based on measurements from the lidar array. These data represent secondary reflections which are not straightforward to interpret and they have, therefore, been masked. The synchonised and co-registered data are shown in Figure B.5. The data from the three different lidars are indicated in different colours and the acoustic back-scatter intensity measured by the sonar has been expressed in dB relative to the maximum recorded value over all of the frames.

B.2.2.2 Measurement of Cavity/Plume Boundary

The sonar data were processed semi-automatically to detect and track the seaward boundary of the combined cavity / plume region. This enabled measurement of the boundary's spatiotemporal migration and the variation of its acoustic backscatter intensity. For each frame, the procedure was initiated using a manual selection of two points on the observed boundary – one at the top near the water surface and another at the bottom towards the bed. A straight line fit was made through the two selected points and rectangular windows were distributed uniformly in depth along its length between the water surface and the bed.

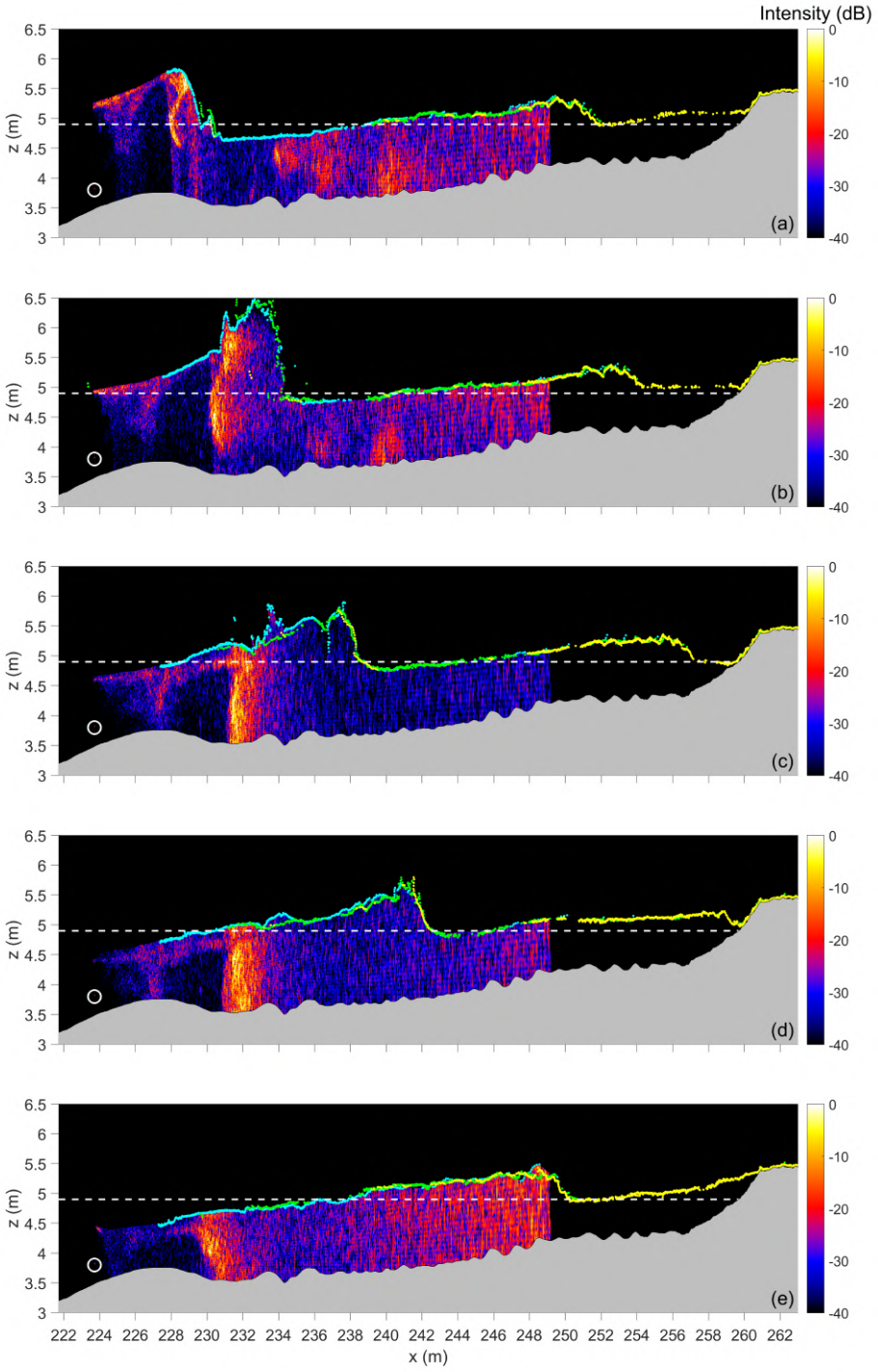

Figure B.5: Sonar and lidar measurements at key times during a breaking wave event: (a) initial overturning; (b) primary splash-up; (c) plume reaching the bed; (d) plume intensity peak raising from mid depth to the near surface; (e) plume fading and moving offshore before the next wave. The sonar measurements above the water surface are caused by multipath reflections and do not represent meaningful measurements in this region. Therefore, this region has been coloured black to aid readability of the figure. The complete data set can be viewed in the accompanying animation available on IEEE Xplore.

For the results in this paper, one hundred windows of width 2 m were used. Histograms of the acoustic intensity were formed within each of the windows and a minimum intensity threshold was used to check whether the backscatter level exceeded the noise floor. For

the windows where this condition was met, a percentile threshold relative to the window's maximum intensity was used to demark the plume boundary. The other windows were excluded and used to delimit the vertical bounds. In this work, a minimum intensity threshold of −26 dB and a percentile threshold of 95 % were selected based on a qualitative assessment of performance. These parameters were tuned to provide robust detection for the current data set and will need to be retuned for alternative data. This procedure is illustrated in Figure B.6

B.2.2.3 Segmentation of Two-Phase Flow Regions

The two-phase flow that is generated during a wave breaking event can be segmented into three distinct regions: 1) the *cavity* of air beneath the overturning wave; 2) the *plume* of aerated water caused by the penetrating jet; and 3) the *splash* above the water surface (see Figure B.7). We have taken steps to make an approximate segmentation of these three regions from the synchronised lidar and sonar data. The seaward boundary of the combined cavity/plume region is estimated using the method presented in Section B.2.2.2 and the water surface elevations of the breaking wave surface and splash are obtained directly from the lidar measurements. The area between these two boundaries is not measured. However, by making simple assumptions for their expected geometry based on images from the work of Blenkinsopp and Chaplin (2007) (Figure 4; hereafter BC4) and taking the simplest approach of projecting straight lines between well-defined regions of the flow, the approximate areas of the cavity, plume, and splash regions can be estimated.

To this end, we have taken the following steps. The upper boundary of the splash region is measured directly by the lidar array, while the underlying water surface is assumed to define the lower boundary. This lower boundary is occluded by the splash. As a first-order approximation, the boundary is defined here by a straight line between defined features in the data: the seaward turning point in the lidar data between the overturning jet and the splash; and the point where the splash meets the undisturbed water surface in front of the wave. The underwater boundary estimated from the sonar measurements is assumed to be caused initially by the formation of the cavity and is consistently curved in shape. The occluded part of the cavity boundary can be approximated as two straight lines that connect to the aforementioned turning point in the lidar measurements between the overturning jet and the splash. This is illustrated in Figure B.7a. Transition from the cavity to plume is assumed to occur when the curved underwater boundary is observed to straighten and the acoustic intensity changes from a sharp reflection to diffuse scattering. We assume that the cavity transitions quickly into the plume and there is only a short period of time when a partial cavity and partial plume co-exist. The occluded part of the plume boundary is approximated by connecting straight lines from the observed boundary edges to the features previously defined to delineate the seaward and landward boundaries of the splash region. This is illustrated in Figure B.7b. We acknowledge that this is a crude approach as it is limited by the fact that we are unable to observe the landward boundary of the plume, or the boundary between cavity / plume and splash. Nonetheless it provides

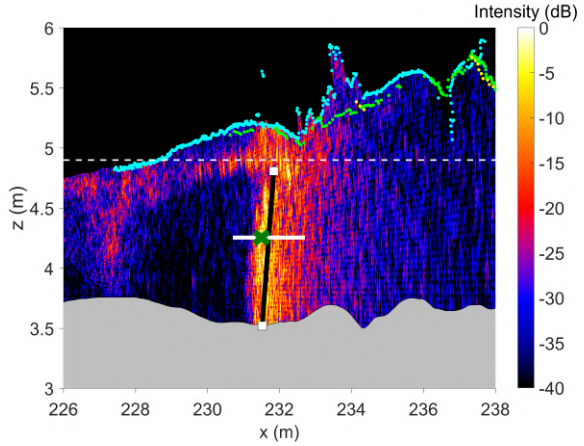

(a)

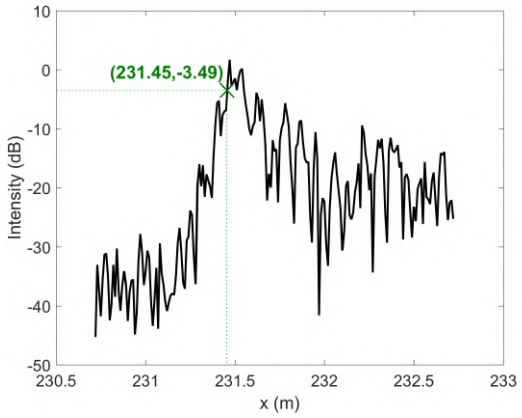

(b)

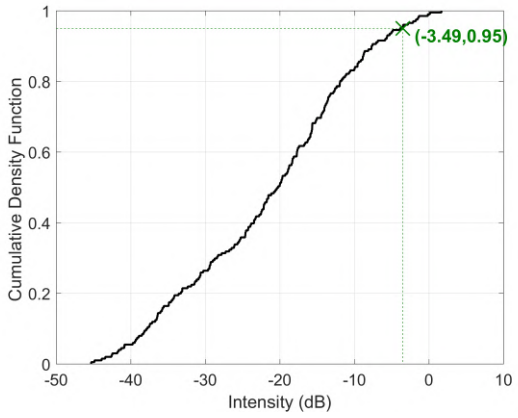

(c)

Figure B.6: Illustration of the detection procedure for the underwater boundary: (a) manually defined line approximation and 1 of 100 2 m-wide windows distributed along its length; (b) measured acoustic backscatter intensity within the window; and (c) associated cumulative density function. The 95^{th} percentile is used to define the boundary and is indicated by the green crosses.

an indication of the evolution of the main structures observed within the two-phase flow and is expected to capture trends in the evolving areas of these features.

B.3 Results

B.3.1 Breaking Wave Visualisation

Synchronised and co-registered data from the profiler, lidars, and sonar are plotted during still water conditions in Figure B.4 and at several key times during a breaking wave in Figure B.5, illustrating the measurements obtained from above and below water. The complete data set can be viewed in the animation that accompanies this paper, which is available on IEEE Xplore.

As previously observed in the field by Martins et al. (2017a) it is evident that the lidar array provides the capability to measure the evolving water surface at a spatial resolution of the order of cm. This is sufficient to capture complex features of the breaking process, including the upper surface of the flow as the wave overturns and produces subsequent splash-up cycles. The water surface measurements from the lidar array are complemented by the sonar data which also captures the changing water surface from below and matches well with the lidar. In addition, the sonar is able to detect the boundary of the evolving

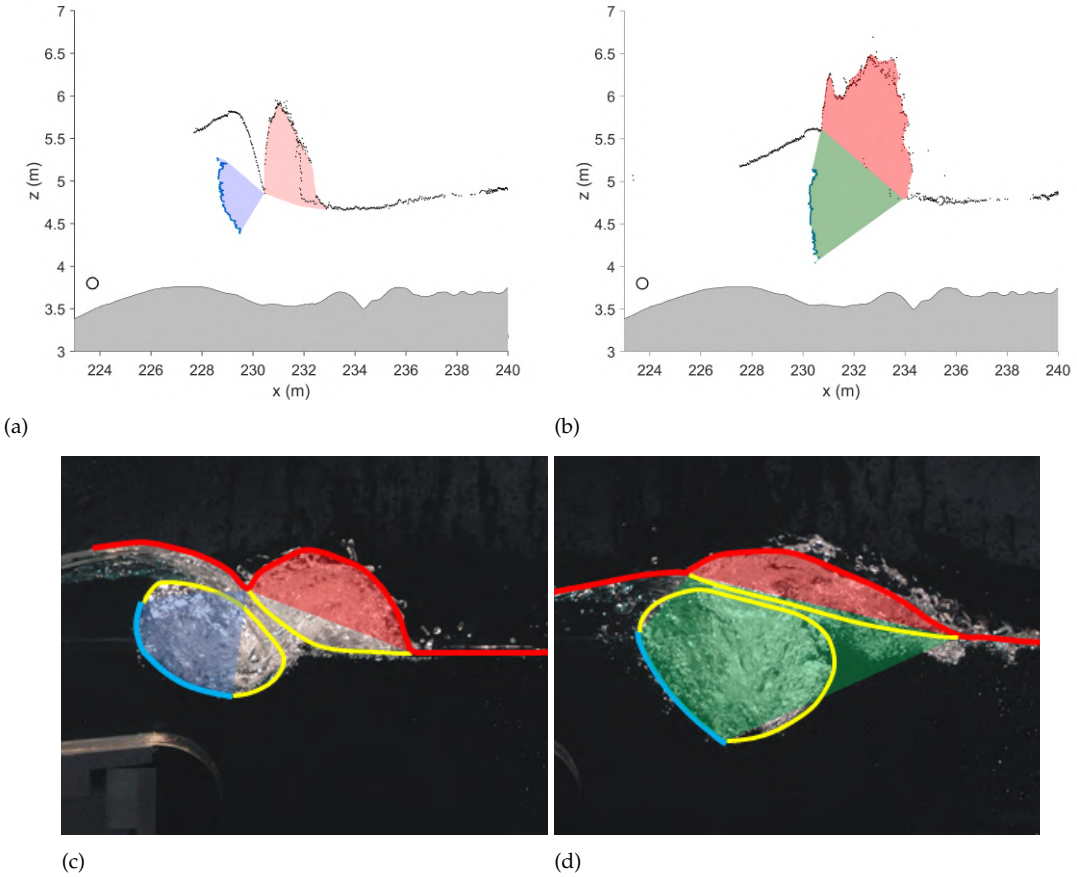

Figure B.7: Illustration of the approximate cavity / plume / splash segmentation procedure on: (a,b) the current work, where the black and blue dots show the lidar and sonar measurements, respectively; and (c,d) photographs of small scale breaking waves from BC4, where the yellow curves show the observed boundaries and the red and blue curves show the expected equivalent boundaries that would be measured by lidar and sonar. In each case, the red, blue, and green areas are the approximate segmentation of splash, cavity, and plume regions.

aerated regions generated during the breaking process, including the cavity and plume. In this case, the relative position of the sonar meant that only the seaward boundary of these regions was observed. Thus, the combination of lidar and sonar measurements enable the above and below-surface features of the two-phase flow generated by an actively breaking wave (including cavity, plume, and splash) to be measured at prototype scale for the first time.

The sequence of breaking wave measurements is described below and compared to the laboratory visualisations presented in BC4. It should be noted that the waves presented there broke over a truncated reef structure into deep water (approximately $7H_b$) which meant that generated bubble plumes were unaffected by the bed. In the current experiment, the penetration of the bubble plume is restricted by the presence of the bed. Additionally, the waves shown in BC4 were observed to be more strongly plunging than that analysed in the current paper, though it is noted that the values of the surf similarity parameter are comparable ($\xi_{b,\text{current}} = 0.38$ vs $\xi_{b,\text{BC4}} = 0.48$) and indicate weakly plunging waves in both cases (Battjes, 1974). Further validation could be made against the theoretical models for plunging waves (*e.g.*, Longuet-Higgins and Cokelet, 1976).

Figure B.5a shows the wave as it initially overturns at $x = 228$ m. It is evident that the curved feature observed in the sonar image between $x = 228$ m and 229 m and $z = 4.5$ m and 5.7 m is the smoothly curving underside of the water surface as the wave overturns (also observed in BC4(a)), while the lidar detects the upper surface of the overturning jet. The region between these two surfaces enables an estimate of the cavity volume per unit width as discussed in Section B.3.3. It is noted that the overturning jet has impacted with the wave trough and there is evidence of the initial stages of splash generation around the water surface between $x = 230$ m and 231 m. In Figure B.5b, the primary splash is fully developed (compare to BC4(c)) and can be observed to extend from the wave crest at $z = 5.6$ m to a peak elevation of 6.5 m, which is almost twice the breaking wave height. The curved shape of the initially entrained cavity is still evident but observed to be driven deeper in the water column and we speculate that the less defined cavity boundary suggests that the initial cavity has begun to break up into smaller air pockets and bubbles to form a plume. Figure B.5c can be compared to BC4(g)). A secondary splash-up is evident between $x = 237$ m and 239 m, formed by the impact of the primary splash as it falls back to the water surface. The plume has now formed and been driven further into the water column, reaching the flume bed. In Figure B.5d, the base of the plume remains at the flume bed. In Figure B.5e, it is evident that the seaward plume boundary has moved back towards the wave paddle, advected by seaward flow velocities associated with the passage of the wave trough. The acoustic back-scatter intensity is reduced throughout the plume suggesting rising and dispersion of the plume bubbles as the next wave approaches. It is noted however that while the acoustic backscatter of the plume is decreasing, we might expect significant number of bubbles and suspended sediment to remain in the water column and these obscure the acoustic detection of the following waves.

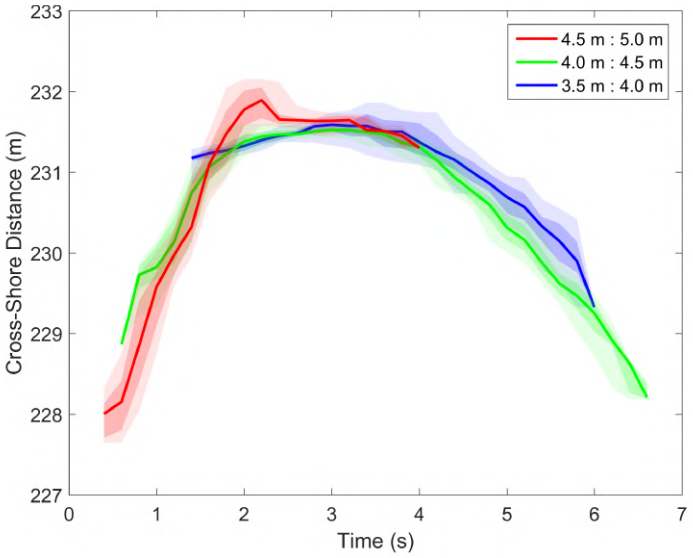

Figure B.8: Cross-shore migration of the bubble plume's offshore boundary for depths in the ranges 4.5 – 5 m (red), 4 – 4.5 m (green), and 3.5 – 4 m (blue); the solid lines are the median positions and the shaded regions show the 50 and 90-percentiles.

B.3.2 Evolution of the Cavity / Plume Boundary

By estimating the boundary as described in Section B.2.2.3, the horizontal movement of the seaward boundary of the cavity / plume during the breaking event can be tracked. Furthermore, the acoustic backscatter intensity along this boundary can be measured. In the present work, uncalibrated intensity measurements were made at a single frequency. However, further development using calibrated measurements at multiple frequencies, will provide an opportunity to characterise small-scale properties of the plume, such as the bubble size distribution and density (Vagle and Farmer, 1992, 1998).

Figure B.8 presents the mean horizontal position of the cavity / plume seaward boundary relative to the wave paddle within three different vertical bands: z = 5.0 m to 4.5 m, 4.5 m to 4.0 m and 4.0 m to 3.5 m. Also plotted are the 50^{th} and 90^{th} percentiles of the cross-shore distance which indicate that the uncertainty in the mean boundary position; these remain approximately constant and are smaller than 0.5 m throughout. When initially entrained, bubbles are only present in the upper depth band (z = 5.0 m-4.5 m). As the depth of the plume increases, the plume boundary is detected in the lower bands. From t = 4 s only the lower bands are present as the wave trough passes above the seaward boundary of the plume and the upper band lies above the water surface. For the first 2 seconds, the boundary moves onshore at an approximately constant speed of 2.3 m/s. This is slightly slower than the wave celerity of 2.8 m/s predicted by linear wave theory for a water depth (wave trough to bar crest) of 0.8 m. Similar behaviour was observed by Blenkinsopp and Chaplin (2007) (Fig 7) who found that the centroid of bubble plumes generated by small-scale laboratory breakers moved at or slightly below the velocity predicted by linear theory during the entrainment phase. Between t = 1.7 s and 2.7 s, it is observed that the bubbles in the upper layer move more rapidly landward than those in the lower bands consistent with higher wave generated landward flow velocities at the surface (*e.g.*, Govender et al.,

2002). The majority of air entrainment occurs during passage of the wave crest. Once the crest has passed beyond the seaward boundary of the bubble plume around $t = 4$ s, the entrained bubble plume is advected offshore by the predominantly seaward directed flow velocities as associated with the wave trough. The peak offshore flow velocity is measured just before the next breaking wave arrives and is estimated to be approximately $1.8\,m/s$. This is comparable to the peak horizontal flow velocity at mid-depth predicted by linear theory of $1.89\,m/s$ and of the same order of magnitude as the peak offshore velocity of $0.9\,m/s$ measured 10 cm above the bed at $x = 233.5$ m (3 m to 5 m landward of the plume boundary position) by an electromagnetic current meter. Figure B.8 presents the mean horizontal position of the cavity / plume seaward boundary relative to the wave paddle within three different vertical bands: $z = 5.0$ m to 4.5 m, 4.5 m to 4.0 m and 4.0 m to 3.5 m. Also plotted are the 50^{th} and 90^{th} percentiles which indicate that the uncertainty in the mean boundary position; these remain approximately constant and are smaller than 0.5 m throughout. When initially entrained, bubbles are only present in the upper depth band ($z = 5.0\,m - 4.5$ m). As the depth of the plume increases, the plume boundary is detected in the lower bands. From $t = 4$ s only the lower bands are present as the wave trough passes above the seaward boundary of the plume and the upper band lies above the water surface. For the first 2 seconds, the boundary moves onshore at an approximately constant speed of $2.3\,m/s$. This is slightly slower than the wave celerity of $2.8\,m/s$ predicted by linear wave theory for a water depth (wave trough to bar crest) of 0.8 m. Similar behaviour was observed by Blenkinsopp and Chaplin (2007) (Fig 7) who found that the centroid of bubble plumes generated by small-scale laboratory breakers moved at or slightly below the velocity predicted by linear theory during the entrainment phase. Between $t = 1.7$ s and 2.7 s, it is observed that the bubbles in the upper layer move more rapidly landward than those in the lower bands consistent with higher wave generated landward flow velocities at the surface (*e.g.*, Govender et al., 2002). The majority of air entrainment occurs during passage of the wave crest. Once the crest has passed beyond the seaward boundary of the bubble plume around $t = 4$ s, the entrained bubble plume is advected offshore by the predominantly seaward directed flow velocities as associated with the wave trough. The peak offshore flow velocity is measured just before the next breaking wave arrives and is estimated to be approximately $1.8\,m/s$. This is comparable to the peak horizontal flow velocity at mid-depth predicted by linear theory of $1.89\,m/s$ and of the same order of magnitude as the peak offshore velocity of $0.9\,m/s$ measured 10 cm above the bed at $x = 233.5$ m (3 m to 5 m landward of the plume boundary position) by an electromagnetic current meter.

Acoustic backscatter intensity measured along the estimated cavity / plume boundary is presented in Figure B.9 in a Lagrangian frame of reference as a function of depth and time. This figure shows the injection and subsequent rise of the cavity and plume with key times labelled (a) to (e).

Strong acoustic backscatter that is not associated with the water surface is initially detected as the cavity captured by the overturning jet forms at (a) and is subsequently driven rapidly down through the water column over approximately 1 second between (a)

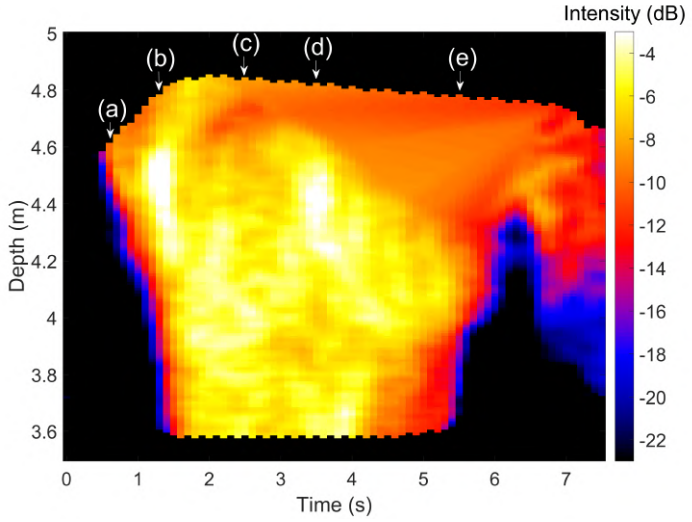

Figure B.9: Acoustic backscatter intensity along the detected cavity / plume boundary in a Lagrangian frame of reference as a function of depth and time. The labelled white arrows correspond to the associated frame in Figure B.5.

and (b) when it reaches the bed. Previous observations in the laboratory by (Blenkinsopp and Chaplin, 2007) and (Lamarre and Melville, 1991) would suggest that the initial large air volumes that form the cavity are broken up into smaller bubbles to form a plume as the aerated region penetrates through the water column, though this cannot be observed directly in the present measurements. During the following period from (b) to (e), lasting approximately 4 seconds, bubbles are detected throughout the water column as the plume evolves due to bubble breakup, advection by currents, bubble rise and dispersion. Following point (e), the base of the remaining plume is observed to rise from the bed at a rate of approximately 0.5 to 0.75 m/s before the arrival of the aerated flow from the next wave. The aerated flow generated by the subsequent (second) wave is less clear due to masking by the remaining bubbles from the first wave. By the third wave, the level of ambient bubbles in the water column makes acoustic imaging of the bubble plumes almost impossible.

Strong peaks in intensity are observed between (b) and (d). It is unlikely that these are caused by bubble resonance because the expected bubble diameters are distributed in the range $50 - 2500$ um (*e.g.*, Blenkinsopp and Chaplin, 2010) corresponding to resonance frequencies in the range 3 kHz to 140 kHz (Szczuka, 1989) and the sonar is operating at 400 kHz, well outside this range.

B.3.3 Evolution of the Two-Phase Flow Regions

Figure B.10 presents the temporal variation of the volume per unit width of the cavity, plume and splash features as defined in Section B.2.2.3. Because the current method only detects the seaward side of the cavity and plume and the transition between cavity and plume is ill-defined, it is acknowledged that these estimates are crude but are useful to provide an indication of the temporal evolution of these features.

The cavity is a shortlived feature as the large air volumes initially entrained beneath the overturning jet rapidly break-up into smaller bubbles leading to a more disperse plume

feature. The measurements presented here indicate that once formed, its volume remained approximately constant for 0.25 s, followed by a sudden decrease as the plume became dominant. The volume per unit width of the plume increases approximately linearly, consistent with the observations of Blenkinsopp and Chaplin (2007) and Lamarre and Melville (1991) in small-scale laboratory waves. The observed increasing volume is consistent with an initially high void fraction and low volume plume which increases in cross-sectional area as the base of the plume moves down through the water column, and the horizontal extent increases as bubbles are advected landward. It was not possible to estimate the decay of the plume volume in the current measurements due to the break down of the assumptions used to estimate plume volume from the landward-facing sonar. However, Blenkinsopp and Chaplin (2007) observed an exponential decay. Future work could deploy a second, seaward-looking sonar to enable these measurements and indeed improve on the other volume measurements presented here.

While Blenkinsopp and Chaplin (2007) and Lamarre and Melville (1991) observed a linear increase in plume volume per unit width with time, their measurements indicated that the peak volume, normalised by the initial cavity volume enclosed beneath the over-

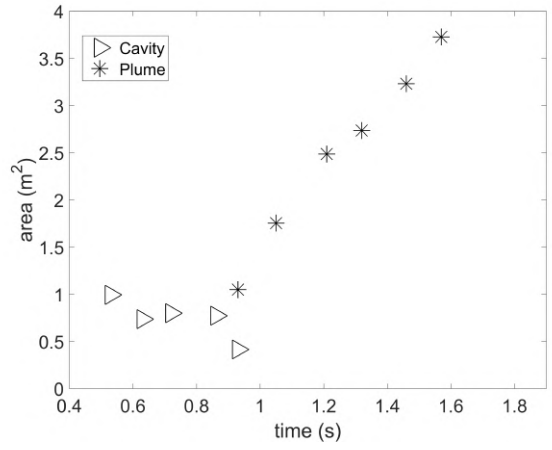

(a)

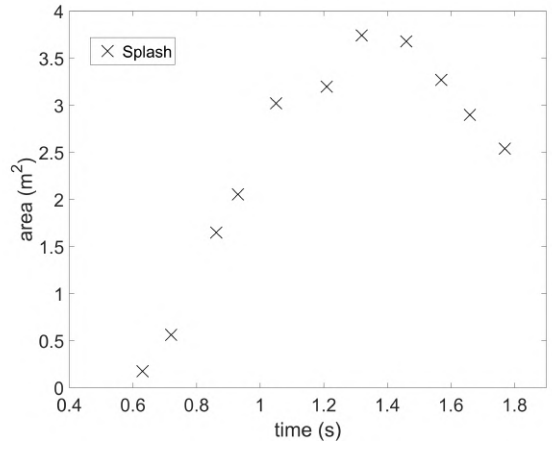

(b)

Figure B.10: Temporal evolution of the estimated areas of the cavity, plume, and splash.

turning jet obtained from images was between 1.0 (Lamarre and Melville, 1991) and 1.6 (Blenkinsopp and Chaplin, 2007). It is not clear whether the peak plume volume is measured in the current measurements as it was not possible to detect the subsequent plume decay, nonetheless the current measurements indicate a normalised peak volume of at least 3.75. This much larger plume volume in the current experiment is expected to be mainly due to differences in the nature of wave breaking (less intensely plunging waves) leading to a smaller peak cavity volume, greater uncertainty in the estimate of the peak cavity volume and potentially scale effects. The volume of splash per unit width is observed to increase as the primary splash-up is generated and is projected vertically up and landwards, followed by a decrease as it falls under the influence of gravity. This evolution is similar to that observed by Blenkinsopp and Chaplin (2007). However they estimated peak splash volume normalised by the initial cavity volume enclosed beneath the overturning jet to be between 1.25 and 1.6 whereas this value is 3.85 in the current measurements. It is noted that the peak splash and plume volumes measured in the current experiment are very similar, and this was also observed by Blenkinsopp and Chaplin (2007).

B.4 Conclusions and Future Work

In this paper, synchronised laboratory measurements of the time-varying water surface and bubble plume boundary in actively breaking, depth-limited waves were obtained at prototype-scale. An array of downward-looking lidar scanners were able to measure the rapidly varying surface profiles during wave shoaling, overturning and subsequent splashing. The lower, seaward boundary of the bubble plume generated by the breaking process was imaged acoustically by an upward-looking sonar. While further validation is needed, these measurements have demonstrated the potential to use this approach to obtain new information about the behaviour of the bubble plume and splashes generated by actively breaking waves at prototype-scale. The strength of our method is that we can observe the combined above water and underwater boundaries of the two-phase flow at high temporal resolution. A limitation is that only the boundaries that are within line of sight to the sonar can be observed. However, this can be addressed in future work by using multiple sonar sensors.

Based on some simple assumptions, it was possible to segment and investigate the bulk movements of the air cavity, plume and splash regions of the flow. It was observed that the overall evolution of the bubble plume and splash was comparable to that observed in previous small-scale laboratory measurements by Blenkinsopp and Chaplin (2007, 2010). In common with these measurements, it was observed that the bubble plume boundary moves landward after breaking at a speed slightly lower than the wave celerity predicted by linear theory. The volume per unit width of the plume increased approximately linearly as the plume was driven down to the bed and dispersed and the approximate rise speed of the bubble plume was consistent with that predicted by Leifer et al. (2000).

The experiment described here clearly demonstrates the potential of the combined lidar/ sonar methodology to obtain measurements in a highly complex and difficult to mea-

sure flow and has demonstrated that the bulk behaviour of bubble plumes and splashes generated in prototype-scale breaking is comparable to that at small-scale. Future work will use the method to investigate a wider range of wave conditions and breaker types using an optimised instrument configuration and more advanced data analysis method in a wave flume. An array of landward and seaward-looking sonar devices should be deployed to ensure adequate coverage of the entire bubble plume boundary and a wider frequency bandwidth to capture the bubble scattering characteristics. Calibrated backscatter intensity measurements at multiple frequencies should be used to estimate useful properties of the bubble plume, including bubble size distribution and density. The ability to image the complete bubble plume and splash boundaries opens up the potential to relate the bubble plume and splash properties to the wave parameters, potentially enabling bubble plume / splash characteristics to be inferred based purely on wave measurements. Controlled lab testing provides the opportunity to overcome real world issues associated with instrument deployment and contamination of the acoustic data due to remnants of precious and subsequent waves. Leading on from a successful detailed lab study and overcoming these issues, the methodology developed here has the potential to obtain valuable measurements of active breaking waves in the field.

Acknowledgments:

This work was supported financially by the European Union's Horizon 2020 Research and Innovation Programme under grant no. 654110, HYDRALAB+. Oscar Bryan and Alan Hunter were further supported by a University of Bath Alumni Fund grant. Paul Bayle's PhD research is supported through a studentship from the EPSRC Water Informatics, Science and Engineering (WISE) Centre for Doctoral Training. We would like to thank staff at the Large Wave Flume (Grosser Wellenkanal, GWK), in particular Matthias Kudella and Stefan Schimmels for making the experiment a success. We also thank members of the DynaRev project team who provided assistance in the laboratory: Isabel Kelly, Emily Gulson, Daniel Conley, Gerd Masselink, Rafael Almar, Ad Reniers, Peter Troch, David Gallach-Sanchez, Robert McCall, Ian Turner, Tom Baldock, Peter Ganderton, Tom Beuzen, Gwyn Hennessey, Huub Rijpers and Aril Pandya.

References

Aagaard, T. and Greenwood, B. (1995). Suspended sediment transport and morphological response on a dissipative beach. *Continental Shelf Ressources* 15, 1061—1086.

Al-Lashi, R. S., Gunn, S. R., and Czerski, H. (2016). Automated Processing of Oceanic Bubble Images for measuring Bubble Size Distributions underneath Breaking Waves. *Journal of Atmospheric and Oceanic Technology* 338, 1701—1714.

Battjes, J. A. (1974). Surf similarity. *14th International Conference of Coastal Engineering*, pp. 466–480.

Blanchard, D. C. (1963). The electrification of the atmosphere by particles from bubbles in the sea. *Progress in Oceanography* 1, pp. 73 –202.

Blenkinsopp, C. E. and Chaplin, J. R. (2007). Void fraction measurements in breaking waves. Vol. 463. 2088. Proceedings of the Royal Society of London Series A - Mathematical Physical and Engineering Sciences, 3151—3170.

Blenkinsopp, C. E. and Chaplin, J. R. (2008). The effect of relative crest submergence on wave breaking over submerged slopes. *Coastal Engineering*, 967—974.

Blenkinsopp, C. E. and Chaplin, J. R. (2010). Bubble size measurements in breaking waves using optical fiber phase detection probes. *IEEE Journal of Oceanic Engineering* 35, 2, 388—401.

Bonmarin, P. (1989). Geometric Properties of Deep-Water Breaking Waves. *Journal of Fluid Mechanics* 209, 405—433.

Bonneton, P., Bruneau, N., Castelle, B., and Marche, F. (2010). Large-scale vorticity generation due to dissipating waves in the surf zone. *Discrete and Continuous Dynamical Systems - Series B* 13(4), 729—738.

Cox, D. T. and Shin, S. (2003). Laboratory Measurements of Void Fraction and Turbulence in the Bore Region of Surf Zone Waves. *Journal of Engineering Mechanics*, 1197—1205.

Czerski, H., Twardowski, M., Zhang, X., and Vagle, S. (2011). Resolving size distributions of bubbles with radii less than 30 m with optical and acoustical methods. *Journal of Geophysics Research* 116.

Deane, G. B. (2016). The performance of high-frequency Doppler sonars in actively breaking wave crests. *IEEE Journal of Oceanic Engineering* 41, 1028—1034.

Deane, G. B. and Stokes, M. D. (1999). Air Entrainment Processes and Bubble Size Distributions in the Surf Zone. *Journal of Physical Oceanography* 29, 1393—1403.

Deane, G. B. and Stokes, M. D. (2002). Scale Dependence of Bubble Creation Mechanisms in Breaking Waves. *Nature* 418, 839—844.

Deane, G. (1997). Sound Generation and Air Entrainment By Breaking Waves in the Surf Zone. *Journal of the Acoustic Society of America* 102, 2671—2689.

Galvin, C. J. (1968). Breaker Type Classification on Three Laboratory Beaches. *Journal of Geophysical Research* 73, 3651—3659.

Galvin, C. J. (1969). Breaker Travel and Choice of Design Wave Height. *Journal of the Waterways and Harbours Division, ASCE, WW2* 95, 175—200.

Govender, K., Alport, M. J., Mocke, G., and Michallet, H. (2002). Video measurements of fluid velocities and water levels in breaking waves. *Physica Scripta* T97, 152—159.

Hoefel, F. and Elgar, S. (2003). Wave induced sediment transport and sandbar migration. *Nature* 299(5614), 1885—1887.

Jansen, P. C. M. (1986). Laboratory Observations of the Kinematics in the Aerated Region of Breaking Waves. *Coastal Engineering* 9, 453—477.

Kiger, K. T. and Duncan, J. H. (2012). Air-Entrainment Mechanisms in Plunging Jets and Breaking Waves. *Annual Review of Fluid Mechanics* 44 (1), pp. 563–596.

Lamarre, E. and Melville, W. K. (1991). Air Entrainment and Energy Dissipation in Breaking Waves. *Nature* 351, 469—472.

Landrini, M., Colagrossi, A., Greco, M., and Tulin, M. P. (2007). Griddless simulations of splashing processes and near-shore bore propagation. *Journal of Fluid Mechanics* 591, 183—213.

Leifer, I., Leeuw, G. D., and Cohen, L. H. (2003). Optical Measurement of Bubbles: System. *Journal of Atmospheric and Oceanic Technology* 20, 1317—1332.

Leifer, I., Patro, R. K., and Bowyer, P. (2000). A Study on the Temperature Variation of Rise Velocity for Large Clean Bubbles. *Journal of Atmospheric and Oceanic Technology* 17, 1392—1402.

Longuet-Higgins, M. S. and Cokelet, E. D. (1976). The Deformation of Steep Surface Waves on Water. A Numerical Method of Computation. *Proceedings of the Royal Society of London*. A, 1—26.

Lopez De San Roman-Blanco, B., Coates, T. T., Holmes, P., Chadwick, A. J., Bradbury, A., Baldock, T. E., Pedrozo-Acuna, A., Lawrence, J., and Grüne, J. (2006). Large scale experiments on gravel and mixed beaches: experimental procedure, data documentation and initial results. *Coastal Engineering* 53, 349—362.

Ma, G., Shi, F., and Kirby, J. T. A polydisperse two-fluid model for surf zone bubble simulation. *Journal of Geophysical Research: Oceans* 116 (C5) ().

Martins, K., Blenkinsopp, C., Power, H. E., Bruder, B., Puleo, J. A., and Bergsma, E. (2017a). High-resolution monitoring of wave transformation in the surf zone using a LiDAR scanner array. *Coastal Engineering* 128, 37—43.

Mead, S. T. and Black, K. (2001). Predicting the breaking intensity of surfing waves. *Special Issue of the Journal of Coastal Research on Surfing*, 103—130.

Medwin, H. (1970). In-Situ Acoustic Measurements of Bubble Populations in Coastal Ocean Waters. *Journal of Geophysical Research* 75, 599—611.

Melville, M. K. (1996). The Role of Surface-Wave Breaking in Air-Sea Interaction. *Annual Review of Fluid Mechanics* 28 (1), pp. 279–321.

Miller, R. L. (1976). Role of Vortices in Surf Zone Prediction: Sedimentation and Wave Forces. *Beach and Nearshore Sedimentation, Society of Economic Paleantologists and Mineralogists, Special Publication* 24.

Nadaoka, K. (1986). "A Fundamental Study on Shoaling and Velocity Field Structure of Water Waves in the Nearshore Zone". PhD thesis. Tokyo Institute of Technology, Tokyo.

Nadaoka, K., Hino, A., and Koyano, Y. (1989). Turbulent Flow Field Structure of Breaking Waves in the Surf Zone. *Journal of Fluid Mechanics* 204, 359—387.

Peregrine, D. H. (1981). The Fascination of Fluid Mechanics. *Journal of Fluid Mechanics* 106, 59—80.

Robertson, B. (2013). Wave vortex parameters as an indicator of breaking intensity. *International Journal of Physical and Mathematical Sciences* (1), pp. 47–54.

Serdula, C. D. and Loewen, M. R. (1998). Experiments Investigating the Use of Fibre-Optic Probes for Measuring Bubble-Size Distributions. *IEEE Journal of Oceanic Engineering* 23, 385—399.

Smith, E. R. and Kraus, N. C. (1991). Laboratory Study of Wave Breaking over Bars and Artificial Reefs. *Journal of Waterway, Port, Coastal and Ocean Engineering* 117, 307—325.

Smith, E. R. and Kraus, N. C. (2016). X-ray PTV measurement of solitary waves. Vol. 367. 18th International Symposium on the Application of Laser and Imaging Techniques to Fluid Mechanics, 2604—2612.

Smith, J. A. (2005). Acoustically observed bubble cloud evolution under deep-water breaking waves. *Journal of Atmospheric and Oceanic Technology* 338, 1701—1714.

Smith, J. A. (2014). A Bistatic Phased-Array Doppler Sonar for wave-current Research. *Journal of Atmospheric and Oceanic Technology* 31, 1628—1641.

Stockdon, H. F., Holman, R. A., Howd, P. A., and Sallenger, A. H. (2006). Empirical parameterization of setup, swash, and runup. *Coastal Engineering* 53, 573—588.

Stokes, M. D. and Deane, G. B. (1999). A New Optical Instrument for the Study of Bubbles at High Void Fractions Within Breaking Waves. *IEEE Journal of Oceanic Engineering* 24, 300—311.

Szczuka, J. (1989). Acoustic detection of gas bubbles in the sea. *Oceanologia* 28, 103—113.

Tallent, J. R., Yamashita, T., and Tsuchiya, Y. (1990). *Transformation Characteristics of Breaking Water Waves*. A Torum OT Gudmestad. Kluwer Academic Publishers, 509—524.

Vagle, S. and Farmer, D. M. (1992). The Measurement of Bubble-Size Distributions by Acoustical Backscatter. *Journal of Atmospheric and Oceanic Technology* 9 (5), pp. 630–644.

Vagle, S. and Farmer, D. M. (1998). A Comparison of Four Methods for Bubble Size and Void Fraction Measurements. *IEEE Journal of Oceanic Engineering* 23, 211—222.

Zheng, K., Sun, Z., Sun, J., Zhang, Z., Yang, G., and Zhou, F. (2009). Numerical simulations of water wave dynamics based on SPH methods. *Journal of Hydrodynamics* 21, 843—850.

de Leeuw, G. and Leifer, I. (2002). Bubbles Outside the Plume During the LUMINY Wind-Wave Experiment. *Gas Transfer at Water Surfaces* 127, 295—301.

List of publications and presentations

Journal Publications:

C.E. Blenkinsopp, **P.M. Bayle**, D. Conley, G. Masselink, E Gulson, I. Kelly, R. Almar, I.L. Turner, T.E. Baldock, T. Beuzen, R. McCall, H. Rijper, A. Reniers, P. Troch, D. Gallach-Sanchez, O. Bryan, A. Hunter, G. Hennessey, P. Ganderton, M. Kudella, S. Schimmels (In review). High-resolution, prototype-scale laboratory measurements of nearshore wave processes and morphological evolution of a sandy beach with and without a dynamic cobble berm revetment. Scientific Data.

P.M. Bayle, C.E. Blenkinsopp, K. Martins, G. Kaminsky, H. Weiner and D. Cottrell (In review). High-resolution measurements of a dynamic cobble berm revetment during a spring tidal cycle: swash zone morphodynamics. *Coastal Engineering*.

P.M. Bayle, C.E. Blenkinsopp, K. Martins, G. Kaminsky, H. Weiner and D. Cottrell (In review). Behaviour and performance of a dynamic cobble berm revetment during a spring tidal cycle in North Cove, Washington State, USA. *Coastal Engineering*.

P.M. Bayle, T. Beuzen, C.E. Blenkinsopp, T.E. Baldock, and I.L. Turner (In review). A new approach for scaling beach profile evolution and sediment transport rates in distorted laboratory models. *Coastal Engineering*.

P.M. Bayle, C.E. Blenkinsopp, D. Conley, G. Masselink, T. Beuzen and R. Almar (2020). Performance of a dynamic cobble berm revetment for coastal protection, under increasing water level. *Coastal Engineering*, 159.
DOI: 10.1016/j.coastaleng.2020.103712

P. M. Bayle, T. Beuzen, C. E. Blenkinsopp, T.E. Baldock, and I.L. Turner (2020). Beach Profile Changes under Sea Level Rise in Laboratory Flume Experiments at Different Scale. *Journal of Coastal Research 95(sp1)*, 192-196.
DOI: 10.2112/SI95-038.1.

K. Martins, P. Bonneton, **P.M. Bayle**, C.E. Blenkinsopp, A. Mouragues, H. Michallet (2020). Surf Zone Wave Measurements from Lidar Scanners: Analysis of Non-hydrostatic Processes. *Journal of Coastal Research 95(sp1)*, 1189-1194.
DOI: 10.2112/SI95-231.1

O. Bryan, **P.M. Bayle**, C.E. Blenkinsopp, and A.J. Hunter (2019). Breaking Wave Imaging using Lidar and Sonar, IEEE Journal of Oceanic Engineering.
doi: 10.1109/JOE.2019.2900967

Conference Proceedings:

C.E. Blenkinsopp, **P.M. Bayle**, D. Conley, G. Masselink, E. Gulson, I. Kelly, R. Almar, I.L. Turner, T.E. Baldock, T. Beuzen, R. McCall, H. Rijper, A.Reniers, P. Troch, D. Gallach-Sanchez, A. Hunter, O, Bryan, G. Hennessey, P. Ganderton, S. Schimmels, M. Kudella (2019). Dynamic Coastal Protection: Resilience of Dynamic Revetments(DynaRev). *Proceedings of the HYDRALAB+Joint User Meeting, Bucharest, May2019*.
DOI:

P.M. Bayle, C.E. Blenkinsopp, D. Conley and G. Masselink (2018). Coastal Adaptation Under Sea Level Rise: Prototype scale Measurements and Modelling of a Dynamic Cobble Berm Revetment. *Coastal Engineering Proceedings, 1(36)*, risk.64.
DOI: 10.9753/icce.v36.risk.64.

Presentations at conferences or seminars:

P.M. Bayle et *al*. Beach Profile Changes under Sea Level Rise in Laboratory Flume Experiments at Different Scale. Presentation at SCARC19, Bari, Italy (Sept. 2019).

P.M. Bayle et *al*. Coastal Adaptation Under Sea Level Rise: Prototype scale Measurements and Modelling of a Dynamic Cobble Berm Revetment. Presentation at the Hydralab+ Joint User meeting, Bucharest, Romania (May 2019).

P.M. Bayle et *al*. Coastal Adaptation Under Sea Level Rise: Prototype scale Measurements and Modelling of a Dynamic Cobble Berm Revetment. Presentation at the Plymouth Coastal Observatory annual meeting, Exeter, UK (October 2018).

P.M. Bayle et *al*. Coastal Adaptation Under Sea Level Rise: Prototype scale Measurements and Modelling of a Dynamic Cobble Berm Revetment. Presentation at ICCE 2018, Baltimore, USA (August 2018).

P.M. Bayle, C.E. Blenkinsopp. Coastal adaptation under Sea Level Rise using soft engineering. Presentation at YCSEC 2018, Hull, UK (March 2018).

P.M. Bayle, C.E. Blenkinsopp. Coastal adaptation under Sea Level Rise using soft engineering. Micro-Engineering presentation in Cardiff, UK (May 2017).

P.M. Bayle, C.E. Blenkinsopp. Coastal adaptation under Sea Level Rise using soft engineering. Poster at YCSEC 2017, Bath, UK (April 2017).

P.M. Bayle, C.E. Blenkinsopp. Coastal adaptation under Sea Level Rise using soft engineering. Presentation at the WISE Industry day, at HR Wallingford, UK (March 2017).

Awards and scholarships:

2019: Bursary support for the Washington field experiment, from Santander Bank.

Appendix B.

2019: Abstract prize at Acoustic science competition for the UKAN first Anniversary 2019, Bath.

2017: Poster prize at the YCSEC 2017, Bath.

2015-2019: Water Informatics: Science & Engineering (WISE) Centre for Doctoral Training (CDT) scholarship to carry research as a PhD student.